

# **Experimental and Numerical Investigations of Simultaneously Developing Laminar-Turbulent Transitional Regime of Mixed Convection Flows in a Vertical Tube**

A Thesis Submitted  
In Partial Fulfillment of the Requirements  
for the Degree of

**Doctor of Philosophy**

by

**“Somenath Gorai”**

**(2017MEZ0025)**



**DEPARTMENT OF MECHANICAL ENGINEERING  
INDIAN INSTITUTE OF TECHNOLOGY ROPAR**

January 2024

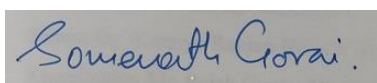
Somenath Gorai: *Experimental and Numerical Investigations of Simultaneously Developing Laminar-Turbulent Transitional Regime of Mixed Convection Flows in a Vertical Tube*

Copyright © 2024 by Indian Institute of Technology Ropar  
All Rights Reserved

*DEDICATED*  
*TO*  
*MY BELOVED PARENTS*  
*Sri Ram Chandra Gorai and Smt. Sushila Gorai*

## DECLARATION

I declare that this work entitled “Experimental and Numerical Investigations of Simultaneously Developing Laminar-Turbulent Transitional Regime of Mixed Convection Flows in a Vertical Tube” has not previously been accepted in substance for any degree and is not being simultaneously submitted in candidature for any other degree. This thesis is being submitted in partial fulfilment of the requirements for the degree of Ph.D in Mechanical Engineering. This thesis is the result of my own independent investigation, except where otherwise stated. I have acknowledged all the other sources by stating the references explicitly. I declare that any idea/data/fact/source stated in my thesis has not been fabricated/falsified/misrepresented. All the principles of academic honesty and integrity have been followed. I understand that any violation of the above will be cause for disciplinary action by the Institute and can also evoke penal action from the sources which have thus not been properly cited or from whom proper permission has not been taken when needed. I hereby give consent for my thesis, if accepted, to be available online in the Institute’s Open Access repository and for inter-library loan, and for the title and abstract to be made available to outside organizations.



Signature

Name: Somenath Gorai

Entry Number: 2017MEZ0025

Program: Doctor of Philosophy (Ph.D.)

Department: Mechanical Engineering

Indian Institute of Technology Ropar,

Rupnagar, Punjab-140001

Date: 05-01-2024



## ACKNOWLEDGMENTS

I would like to express my sincere gratitude to my thesis advisors, Dr. Devranjan Samanta and Prof. Sarit Kumar Das (IIT Madras), for their continuous support, valuable suggestions, and guidance throughout my research work and Ph.D life at the Indian Institute of Technology Ropar. Working with them has given me great learning opportunities. This thesis would never have become a reality without their support and guidance.

I am thankful to my Doctoral Committee members, Prof. Navin Kumar, Dr. Himanshu Tyagi, Dr. Ranjan Das from the Mechanical Engineering Department, and Dr. Vishwajeet Mehandia from the Chemical Engineering Department, for their constructive feedback, insightful suggestions, and encouragement throughout this course of research. I would like to thank all the staff at IIT Ropar for providing the necessary resources and facilities. I am thankful to the MHRD, Govt. of India, for providing the scholarship during my tenure.

I would like to acknowledge the eminent professors from HTTP Lab, Prof. Arvind Pattamatta and Prof. C. Balaji, who shared their equipment to perform the experiments at IIT Madras. I owe my sincere gratitude to Mr. Sagaya Rajesh and other technicians at HTTP Lab for their enormous effort to build the experimental set-up precisely.

I am grateful to all my colleagues and fellow researchers, especially Dr. Nilamani Sahoo, Dr. Soumya Ranjan Mishra, Mr. Gudlavalleti V V S Vara Prasad, Mr. Khusro Kamaluddin, Mr. Pulak Gupta, Mr. Rahul Kumar, Mr. Manglesh Singh, Mr. Simranjeet Singh at IIT Ropar, and Dr. Pyarimohan Dehury, Dr. Nithya Murugesan, Dr. Allwyn Jhonson, Dr. Akash A R, Mr. Rishi Ramakrishnan L, Mr. Supratim Saha, Mr. Navdeep Malik at IIT Madras for their stimulating discussions, shared resources, and exchange of ideas at tea that enriched my research experience by shaping my perspectives and refining my knowledge.

My deepest gratitude goes to my parents, Sri Ram Chandra Gorai and Smt. Sushila Gorai, for their unwavering support, patience, and understanding throughout this journey. Their encouragement and belief in my capabilities have been my driving forces in overcoming challenges and reaching this milestone. I have no words to express my gratitude to my wife Kakoli Gorai and beloved son Master Keshav Gorai for their unconditional love and sacrifice.

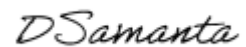
I would like to take this opportunity to express my deep sense of gratitude to my sisters, in-laws, and all those who have contributed, directly or indirectly. Your support has been indispensable, and I am truly humbled and honoured to have had you by my side on this academic expedition.

Finally, I am indebted to Almighty God for giving me knowledge, strength, good health, patience, and showing the right path in life.

Somenath Gorai

## CERTIFICATE

It is certified that the work contained in the thesis titled “**Experimental and Numerical Investigations of Simultaneously Developing Laminar-Turbulent Transitional Regime of Mixed Convection Flows in a Vertical Tube**” by **Somenath Gorai** has been carried out under my/our supervision and that this work has not been submitted elsewhere for the award of any degree.



**Signature of the Supervisor**

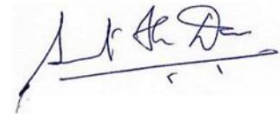
Dr. Devranjan Samanta

Department of Mechanical Engineering

Indian Institute of Technology Ropar

Rupnagar, Punjab-140001, India

Date: 5<sup>th</sup> January 2024



**Signature of the Supervisor**

Prof. Sarit K. Das

Department of Mechanical Engineering

Indian Institute of Technology Madras

Chennai, Tamil Nadu-600036, India

Date: 5<sup>th</sup> January 2024

## LAY SUMMARY

Two essential parameters in today's life are how to get "more" with "less" investment. The "more" I am talking about is the higher heat transfer rate we want and the "less" is the minimum effort needed to achieve it. The maximum heat being transferred with minimum work is nothing but the aim of my present thesis. The device that transfers the heat either to cool or heat is called heat exchanger. It basically absorbs heat from one fluid and rejects to the other or vice versa. To achieve this, we can increase the flow rate or the mixing of the fluid particles to transfer more heat. There are two ways to increase the flow rate: either by increasing the velocity of the fluid or by increasing the heat supply. The increase in heat supply will change the fluid's properties in such a way that there is less resistance to it and the velocity of the fluid increases. At low flow rates, the velocity is low, and the fluid flow takes place layer-by-layer, such as water at the edge before it falls in a water fall or the smoke initially coming out of the incense stick. At higher flow rates, the fluid layer mixes, and haphazard flow takes place, such as foamy water flowing in a high stream river or smoke coming out of incense sticks afterwards. At some intermediate flow rate, the flow is layer by layer for some time and then becomes haphazard. For example, in a waterfall, the water at the edge is clear, and transparent but at the immediate downstream, it transforms into milky white foam. The layer-by-layer flow and the mixing can be visualized in laboratory-level experiments by sending a dye (used a potassium permanganate in the present study) into the fluid. The device I built consists of a smooth tube (stainless steel 316L) of diameter 10 mm and length 1.3 m fixed vertically through which water is sent from a storage tank. The water gets heated in the tube by supplying electricity to the tube (like an emersion rod), and then the heated water comes out of the tube. This heated water goes to another cooling device called a "chiller," where it gets cooled. The cooled water is again sent to the tube, and the cycle repeats. The flow resistance is measured through pressure sensors, and the heat carrying ability is analysed through temperature sensors. After that, the measured data are interpreted to quantify the amount of flow resistance and the heat being transferred. It has been found that the pressure drop and heat transfer are optimal at intermediate flows. So, in industries, device named as "heat exchanger" will perform better when it operates at an intermediate flow regime called the transitional regime. The outcome of the present research work will be beneficial wherever there is a fluid

flow subjected to the involvement of heating or cooling, where higher heat transfer with minimum work is the prime concern.

## ABSTRACT

Combined free and forced convection, most often called mixed convection, has practical importance in many engineering applications like heat exchangers, solar energy systems, cooling of electronic equipment, extraction of geothermal energy, and many areas because of its varying nature of heat transfer. This present study investigates the heat transfer, pressure drop, and flow characteristics of buoyancy-assisting (heated upward) and opposing (heated downward) flows of water in the simultaneously hydrodynamically and thermally developing laminar-turbulent transitional regime of mixed convection in a vertical tube. To accomplish this, both numerical and experimental investigations were carried out for the range of Reynolds number, ( $10^2 \leq Re \leq 1.5 \times 10^4$ ), Grashof number ( $10^3 \leq Gr \leq 10^8$ ), Richardson number ( $0.01 \leq Ri \leq 1.5$ ) and Prandtl number ( $3 \leq Pr \leq 7$ ) in a vertical tube with a length-to-diameter ( $L/D$ ) ratio of  $\leq 500$ . 2D axisymmetric, steady-state simulations were performed by employing a SIMPLE/Coupled scheme for pressure-velocity coupling in momentum equations and a second-order UPWIND scheme for solving convective terms. Numerical results show that buoyancy plays a significant role in laminar-turbulent transitions between assisting and opposing flows. In the case of laminar mixed convection, it can be inferred from the velocity profile that the velocity gradient is sharper near the walls in assisting flow. In contrast, in the case of opposing flow, the velocity gradient is sharper at a distance from the wall. With increasing  $Ri$ , both  $f$  and  $Nu$  exhibit increasing and decreasing trend for buoyancy-aided and opposed flows, respectively. It is worth mentioning that the developing region exhibits higher  $Nu$  compared to fully developed states for both aided and opposed flows. The effect of heat flux on the entry length is also analyzed in buoyancy-assisting and opposing flows. The hydrodynamic development length ( $L_h$ ) increases as we increase the  $Ri$  for both assisting and opposing flow, but the thermal entry length ( $L_t$ ) decreases in the case of assisting flow in contrast to the opposing flow. In contrast, in turbulent mixed convection, there is not much of a difference between buoyancy-aiding and opposing flows due to the dominance of turbulence. It has been observed that the pressure drop (quantified by  $f$ ) and heat transfer (quantified by  $Nu$ ) both are higher in buoyancy-opposing flow than buoyancy-assisting flow. The entry length is also short, and the flow is developed early. The hydrodynamically fully developed conditions in buoyancy-assisting and opposing flow were achieved by  $L/D \sim 21$  and  $\sim 17$  and the thermally

developed condition by  $L/D \sim 25$  and  $\sim 20$ , respectively. The laminar-turbulent transitional regime shows a compromise between pressure drop and heat transfer. The increase in  $Re$  and  $Gr$  keeping  $Ri$  constant first increases  $f$  and then decreases, whereas the  $Nu$  increases in both buoyancy assisting and opposing flow. Furthermore, the mixed convection experimental set-up was built to perform experiments in the laminar, transitional, and lower ranges of turbulent regimes for aiding and opposing flows. The effects of varying  $Gr$  and  $Re$ , at fixed  $Ri$  on pressure drop and heat transfer were investigated for both buoyancy-assisting and buoyancy-opposing flows. Experimental results showed that the average  $f$  decreases with the increase in  $Re$  in the laminar regime, increased in the transitional regime and decreased again with the further increase in  $Re$  in the turbulent regime. The average  $Nu$  increases continuously with the increase in  $Re$  in all laminar, transitional, and turbulent regimes. The inception of transition occurs earlier in the opposing flow as compared to the assisting flow for the same  $Re$  and  $Gr$ . It has also been observed that the transition is delayed with the increase in  $Ri$  in both flows. The numerical results were also compared with my experiments. Finally, correlations were developed to quantify the friction factor,  $f = f(Re, Gr)$ , Colburn  $j$ -factor,  $f/j = f(Re, Gr, Pr)$ , and Nusselt number,  $Nu = f(Re, Gr, Pr, L/D)$  in developing and fully developed regime of laminar, transitional, and turbulent mixed convection under both the flow conditions.

**Keywords:** Mixed convection; Developing flow; Transitional regime; Buoyancy-aiding and opposing flow; Vertical tube

## LIST OF PUBLICATIONS

### *Journal papers*

1. **Gorai, S.,** Das, S.K. & Samanta, D. (2022). Numerical investigations on the difference between aiding and opposing flows in the developing regime of laminar mixed convection in vertical tubes, *Numerical Heat Transfer, Part A: Applications*, 84(4), 1-25, Taylor and Francis.  
DOI: <https://doi.org/10.1080/10407782.2022.2105600>
2. **Gorai, S.,** Samanta, D., & Das, S. K. (2023). Heat Transfer in Simultaneously Developing Turbulent Mixed Convection Flows in Vertical Tubes, *Heat Transfer Engineering*, 45(22), Taylor and Francis.  
DOI: <https://doi.org/10.1080/01457632.2023.2289226>
3. **Gorai, S.,** Samanta, D., & Das, S. K. (2023). Transitional Mixed Convection for Buoyancy-assisting and Opposing Flows in a Vertical Tube-A Numerical Study, *Thermal Science and Engineering Progress, Elsevier*. [Manuscript ID: TSEP-D-23-03893, Under Review]
4. **Gorai, S.,** Samanta, D., & Das, S. K. (2023). Experimental investigations of heat transfer in simultaneously developing transitional regime of mixed convection flows in a vertical tube. *Journal of Heat and Mass Transfer, ASME*. [Manuscript ID: HT-23-1385, Revision pending]
5. **Gorai, S.,** Samanta, D., & Das, S. K. (2023). Heat transfer investigations in the developing regime of mixed convection for buoyancy-aiding and opposing flows in a vertical tube and its transition. *International Journal of Heat and Mass Transfer, Elsevier*. [Submitted]

### *Conference papers*

1. **Gorai, S.,** Samanta, D., & Das, S. K. (2021). Numerical Investigation of Buoyancy-assisted and-opposed flows in the Laminar Regime of Mixed Convection through a Vertical Channel, *ISHMT Digital Library*. Begell House Inc., IIT Madras, Chennai, Tamil Nadu, India. DOI: [10.1615/IHMT-2021.1290](https://doi.org/10.1615/IHMT-2021.1290)
2. **Gorai, S.,** Samanta, D., & Das, S. K. (2023). Flow instability in buoyancy-assisted and opposed flows through a vertical pipe in the laminar regime of mixed convection- A numerical study, *ASTFE Digital Library*, Begell House Inc., University of Maryland, USA. DOI : [10.1615/TFEC2023.fit.046071](https://doi.org/10.1615/TFEC2023.fit.046071)



3. **Gorai, S.**, Samanta, D., & Das, S. K. (2023). Numerical Investigation of Transitional Mixed Convection for Buoyancy-Assisting and Opposing Flows in a Vertical Tube, *International Heat Transfer Conference Digital Library*, Begell House Inc., Cape Town, South Africa. DOI: [10.1615/IHTC17.270-20](https://doi.org/10.1615/IHTC17.270-20)

#### ***Book Chapters***

1. **Gorai, S.**, Das, S.K. (2020). Studies on Mixed Convection and Its Transition to Turbulence—A Review. In: Runchal, A. (eds) 50 Years of CFD in Engineering Sciences. *Springer*, Singapore. DOI: [https://doi.org/10.1007/978-981-15-2670-1\\_10](https://doi.org/10.1007/978-981-15-2670-1_10)

#### ***Publications outside the thesis work***

1. Shelar, H., **Gorai, S.**, and Samanta, D. (2022). “Application of Machine Learning to Predict Hydrodynamic and Thermal Parameters in Laminar Mixed Convection Flows through Vertical Pipes, *ISME Journal of Thermofluids*, 8(2), 31-41. DOI: <https://isme.iitd.ac.in/journals/thermofluids/index.php/announce/viewarticle/59>

## TABLE OF CONTENTS

DECLARATION .....	iv
ACKNOWLEDGMENTS .....	v
CERTIFICATE .....	vii
LAY SUMMARY .....	viii
ABSTRACT .....	x
LIST OF PUBLICATIONS .....	xii
TABLE OF CONTENTS .....	xiv
LIST OF FIGURES .....	xxi
LIST OF TABLES .....	xxxix
Notations and Abbreviations .....	xxxix
Chapter 1 .....	35
Introduction .....	35
1.1 Overview of mixed convection .....	35
1.2 Non-dimensional numbers .....	36
1.2.1 Rayleigh number .....	36
1.2.2 Richardson number .....	37
1.2.3 Graetz number .....	37
1.2.4 Friction factor .....	38
1.2.5 Nusselt number .....	38
1.2.6 Colburn $j$ -factor .....	38
1.2.7 Buoyancy parameter .....	39
1.3 Flow regimes .....	39
1.3.1 Laminar flow .....	39
1.3.2 Turbulent flow .....	39
1.3.3 Laminar-turbulent transitional flow .....	40
1.4 Developing and fully developed flow .....	40
1.4.1 Hydrodynamic and thermal entrance length .....	43

<b>1.5 Mixed convection criteria and flow regime maps.....</b>	<b>44</b>
<b>1.5.1 Free, forced, and mixed convection regime in a vertical tube.....</b>	<b>48</b>
<b>1.6 Applications of mixed convection.....</b>	<b>48</b>
<b>1.7 Organization of the thesis .....</b>	<b>49</b>
<b>1.8 Conclusions .....</b>	<b>50</b>
<b>Chapter 2.....</b>	<b>51</b>
<b>Literature Review and Objectives .....</b>	<b>51</b>
<b>2.1 Laminar mixed convection .....</b>	<b>51</b>
<b>2.1.1 Analytical studies on laminar mixed convection .....</b>	<b>51</b>
<b>2.1.2 Computational studies on laminar mixed convection .....</b>	<b>52</b>
<b>2.1.3 Experimental studies on laminar mixed convection.....</b>	<b>54</b>
<b>2.2 Turbulent mixed convection.....</b>	<b>55</b>
<b>2.2.1 Analytical studies on turbulent mixed convection.....</b>	<b>56</b>
<b>2.2.2 Computational studies on turbulent mixed convection .....</b>	<b>56</b>
<b>2.2.3 Experimental studies on turbulent mixed convection.....</b>	<b>57</b>
<b>2.3 Transitional mixed convection .....</b>	<b>59</b>
<b>2.3.1 Analytical studies on transitional mixed convection .....</b>	<b>59</b>
<b>2.3.2 Computational studies on transitional mixed convection.....</b>	<b>59</b>
<b>2.3.3 Experimental studies on Transition.....</b>	<b>61</b>
<b>2.4 Summary and research scope.....</b>	<b>62</b>
<b>2.5 Objectives of the present study .....</b>	<b>63</b>
<b>2.6 Scope of the present work.....</b>	<b>64</b>
<b>2.7 Conclusions .....</b>	<b>65</b>
<b>Chapter 3.....</b>	<b>67</b>
<b>Numerical Methodology and Validation .....</b>	<b>67</b>
<b>3.1 Introduction .....</b>	<b>67</b>
<b>3.2 Physical model .....</b>	<b>67</b>
<b>3.3 Mathematical formulation for laminar mixed convection .....</b>	<b>68</b>

<b>3.3.1 Numerical procedure .....</b>	<b>69</b>
<b>3.3.2 Validation of laminar model.....</b>	<b>72</b>
3.3.2.1 <i>Hydrodynamic validation.....</i>	72
3.3.2.2 <i>Thermal validation.....</i>	73
<b>3.4 Mathematical formulation for transitional mixed convection .....</b>	<b>73</b>
<b>3.4.1 Numerical procedure .....</b>	<b>75</b>
<b>3.4.2 Validation of transitional model .....</b>	<b>77</b>
<b>3.5 Mathematical formulation for turbulent mixed convection.....</b>	<b>77</b>
<b>3.5.1 Numerical procedure .....</b>	<b>79</b>
<b>3.5.2 Comparison of various turbulence models .....</b>	<b>80</b>
<b>3.5.3 Hydrodynamic and thermal validation .....</b>	<b>82</b>
<b>3.6 Conclusions .....</b>	<b>83</b>
<b>Chapter 4.....</b>	<b>85</b>
<b>Experimental Set-up and Procedure .....</b>	<b>85</b>
<b>4.1 Introduction .....</b>	<b>85</b>
<b>4.2 Experimental set-up and components .....</b>	<b>85</b>
4.2.1 Flow calming section .....	86
4.2.2 Test section.....	88
4.2.3 Mixer section.....	90
4.2.4 Visualization section.....	91
4.2.5 Instrumentation.....	92
4.2.5.1 <i>Thermocouples .....</i>	92
4.2.5.2 <i>Resistance temperature detector (RTD).....</i>	93
4.2.5.3 <i>Differential pressure transducer (DPT).....</i>	93
4.2.5.4 <i>Flowmeter .....</i>	93
4.2.5.5 <i>Power supply.....</i>	94
4.2.5.6 <i>Data acquisition system (DAQ) .....</i>	95
4.2.6 Centrifugal pump and syringe pump .....	96

<b>4.2.7 Chiller unit .....</b>	<b>96</b>
<b>4.3 Data reduction method.....</b>	<b>98</b>
<b>4.4 Experimental procedure .....</b>	<b>100</b>
<b>4.5 Uncertainties .....</b>	<b>102</b>
<b>4.6 Validation .....</b>	<b>103</b>
<b>4.6.1 Hydrodynamic validation .....</b>	<b>103</b>
<b>4.6.2 Thermal validation .....</b>	<b>104</b>
<b>4.6.3 Laminar forced convection .....</b>	<b>105</b>
<b>4.6.4 Turbulent forced convection .....</b>	<b>107</b>
<b>4.6.5 Transitional forced convection .....</b>	<b>108</b>
<b>4.7 Conclusions .....</b>	<b>110</b>
<b>Chapter 5.....</b>	<b>111</b>
<b>Laminar Mixed Convection.....</b>	<b>111</b>
<b>5.1 Introduction .....</b>	<b>111</b>
<b>5.2 Numerical results on laminar mixed convection .....</b>	<b>111</b>
<b>5.2.1 Buoyancy-assisted flow .....</b>	<b>112</b>
5.2.1.1 <i>Influence of heat flux (<math>q</math>).....</i>	112
5.2.1.2 <i>Influence of <math>Ri</math> .....</i>	114
5.2.1.3 <i>Influence of <math>Re</math> .....</i>	117
<b>5.2.2 Buoyancy-opposed flow.....</b>	<b>120</b>
5.2.2.1 <i>Influence of heat flux .....</i>	120
5.2.2.2 <i>Influence of <math>Ri</math> .....</i>	122
5.2.2.3 <i>Influence of <math>Re</math> .....</i>	124
<b>5.3 Comparison between buoyancy-assisted and buoyancy-opposed flow.....</b>	<b>128</b>
<b>5.4 Friction factor and Nusselt number correlations .....</b>	<b>130</b>
<b>5.5 Experimental results on laminar mixed convection .....</b>	<b>134</b>
<b>5.5.1 Average pressure drop and heat transfer in simultaneously developing laminar flows.....</b>	<b>134</b>

<b>5.5.2 Local heat transfer in the developing laminar mixed convection flow.....</b>	<b>137</b>
<b>5.5.3 Effect of <math>Ri</math> on heat transfer .....</b>	<b>138</b>
5.5.3.1 <i>Influence of <math>Ri</math> through visualization .....</i>	141
<b>5.6 Comparison between numerical and experimental laminar mixed convection results.....</b>	<b>143</b>
<b>5.6.1 Pressure drop and heat transfer comparisons.....</b>	<b>143</b>
<b>5.7 Conclusions .....</b>	<b>145</b>
<b>APPENDIX A .....</b>	<b>147</b>
<b>Additional plots related to laminar mixed convection numerical results .....</b>	<b>147</b>
<b>Chapter 6.....</b>	<b>157</b>
<b>Transitional Mixed Convection.....</b>	<b>157</b>
<b>6.1 Introduction .....</b>	<b>157</b>
<b>6.2 Numerical results on transitional mixed convection .....</b>	<b>157</b>
<b>6.2.1 Buoyancy-assisting Flow.....</b>	<b>158</b>
6.2.1.1 <i>Fixed <math>Ri</math> and varying <math>Gr</math>, <math>Re</math> .....</i>	158
<b>6.2.2 Buoyancy-opposing Flow .....</b>	<b>162</b>
6.2.2.1 <i>Fixed <math>Ri</math> and varying <math>Gr</math>, <math>Re</math> .....</i>	162
<b>6.3 Comparison between buoyancy-assisting and opposing flows.....</b>	<b>166</b>
<b>6.4 Experimental results on transitional mixed convection.....</b>	<b>169</b>
<b>6.4.1 Average pressure drop and heat transfer in the transitional mixed convection flow .....</b>	<b>170</b>
<b>6.4.2 Friction factor and Nusselt number correlations .....</b>	<b>172</b>
<b>6.4.3 Local heat transfer in the developing transitional mixed convection flow .....</b>	<b>173</b>
<b>6.4.4 Flow visualization in laminar, transitional, and turbulent mixed convection flow .....</b>	<b>174</b>
<b>6.5 Comparison between numerical and experimental transitional mixed convection results .....</b>	<b>176</b>
<b>6.5.1 Heat transfer in the developing regime of transitional mixed convection flows .....</b>	<b>176</b>

<b>6.6 Conclusions .....</b>	<b>177</b>
<b>Chapter 7.....</b>	<b>179</b>
<b>Turbulent Mixed Convection .....</b>	<b>179</b>
<b>7.1 Introduction .....</b>	<b>179</b>
<b>7.2 Numerical results on turbulent mixed convection.....</b>	<b>179</b>
<b>7.2.1 Flow regime plot .....</b>	<b>180</b>
<b>7.2.2 Buoyancy-assisted flow .....</b>	<b>180</b>
7.2.2.1 <i>Fixed Gr and varying Re, Ri .....</i>	<i>181</i>
7.2.2.2 <i>Fixed Ri and varying Re, Gr .....</i>	<i>182</i>
<b>7.2.3 Buoyancy-opposed flow.....</b>	<b>185</b>
7.2.3.1 <i>Fixed Gr and varying Re, Ri .....</i>	<i>185</i>
7.2.3.2 <i>Fixed Ri and varying Re, Gr .....</i>	<i>186</i>
<b>7.2.4 Comparison between buoyancy-assisted and buoyancy-opposed flow.....</b>	<b>187</b>
7.2.4.1 <i>Fixed Gr and varying Re, Ri .....</i>	<i>187</i>
7.2.4.2 <i>Fixed Ri and varying Gr, Re .....</i>	<i>188</i>
<b>7.2.5 Entry length comparison .....</b>	<b>189</b>
<b>7.2.6 Friction factor and Nusselt number correlations .....</b>	<b>191</b>
<b>7.3 Experimental results on turbulent mixed convection .....</b>	<b>193</b>
<b>7.3.1 Average pressure drop and heat transfer in the fully developed turbulent flow .....</b>	<b>194</b>
<b>7.3.2 Local heat transfer in the turbulent mixed convection flow.....</b>	<b>196</b>
<b>7.4 Comparison between numerical and experimental turbulent mixed convection results.....</b>	<b>198</b>
<b>7.4.1 Heat transfer comparison in turbulent mixed convection .....</b>	<b>198</b>
<b>7.5 Conclusions .....</b>	<b>199</b>
<b>Chapter 8.....</b>	<b>201</b>
<b>Summary and Conclusions .....</b>	<b>201</b>
<b>8.1 Introduction .....</b>	<b>201</b>
<b>8.2 Summary of the present work .....</b>	<b>201</b>

<b>8.3 Major conclusions .....</b>	<b>203</b>
<b>8.4 Future scope and recommendations .....</b>	<b>204</b>
<b>REFERENCES/BIBLIOGRAPHY .....</b>	<b>207</b>
<b>APPENDIX B.....</b>	<b>215</b>
<b>Uncertainty Analysis and Calibration of Instruments.....</b>	<b>215</b>
<b>B.1 General form of uncertainty analysis equation .....</b>	<b>215</b>
<b>B.2 Calibration of RTD and thermocouples .....</b>	<b>215</b>
<b>B.3 Calibration of DPT .....</b>	<b>217</b>
<b>B.4 Calibration of Coriolis mass flowmeter .....</b>	<b>218</b>
<b>B.5 Calibration of alignment of the set-up .....</b>	<b>218</b>
<b>B.6 Measurement of surface roughness.....</b>	<b>219</b>



## LIST OF FIGURES

<b>Figure 1.1</b> The schematic representations of free, forced and mixed convection (Cengel and Ghajar [9]) .....	36
<b>Figure 1.2</b> The intermittent character of the disturbance in terms of flashes ( P. G. Drazin [11]) .....	40
<b>Figure 1.3</b> Schematic of the hydrodynamic and thermal boundary layers and entrance lengths for (a) hydrodynamically developing isothermal flow, (b) hydrodynamically developing flow followed by thermally developing flow, and (c) simultaneously hydrodynamically and thermally developing flow (Everts <i>et al.</i> [12]). .....	42
<b>Figure 1.4</b> Regimes of free, forced, and mixed convection for flow through vertical tubes ( $0.01 < PrD/L < 1$ ) (taken from Metais and Eckert [3]).....	45
<b>Figure 1.5</b> Regimes of free, forced, and mixed convection for flow through horizontal tubes ( $0.01 < PrD/L < 1$ ) (taken from Metais and Eckert [3]).....	46
<b>Figure 1.6</b> Flow regime map for flow in horizontal tubes with three different inlet configurations and uniform heat flux condition (taken from Ghajar and Tam [14]) ...	46
<b>Figure 1.7</b> Flow regime map for developing and fully developed flow as a function of $Re$ and $Ri^*(x/D)$ in a horizontal tube (taken from Everts and Meyer [13]).....	47
<b>Figure 1.8</b> Flow regime map for developing and fully developed flow as a function of $Re$ and $Ra^*/Gz$ in a horizontal tube (taken from Everts and Meyer [13]).....	47
 <b>Figure 2.1</b> Predicted flow regime map for combined free and forced convection in a vertical tube (taken from Tanaka <i>et al.</i> [29]).....	53
 <b>Figure 3.1</b> Schematic diagram of (a) buoyancy-assisting and (b) buoyancy-opposing flow.....	68
<b>Figure 3.2</b> (a) 2D axisymmetric model (b) structured mesh with fine grids near the tube wall .....	70
<b>Figure 3.3</b> Optimization of (a) grids and (b) bias factor (BF) with % error in centerline velocity and temperature at $L/D=450$ for $Re=250$ and $Ri=1.0$ .....	72
<b>Figure 3.4</b> Comparison of fully developed $f$ with the (a) Hagen-Poiseuille flow (b) assisting and opposing flow of laminar mixed convection with Meyer <i>et al.</i> [99] .....	72
<b>Figure 3.5</b> Comparison of local $Nu$ (a) assisting and opposing flow of laminar forced convection results at a heat flux $4.3 \text{ kW/m}^2$ and $Re=1050$ with Bashir <i>et al.</i> [98] and (b)	

assisting and opposing flow of laminar mixed convection results at a heat flux of 6.5 kW/m <sup>2</sup> and $Re=1600$ with Meyer <i>et al.</i> [99] .....	73
<b>Figure 3.6</b> Comparison of transition $\kappa - \kappa l - \omega$ and transition SST model for same $Re$ and $Ri$ .....	76
<b>Figure 3.7</b> Comparison of local $Nu$ variation with numerical results of Abraham <i>et al.</i> [109] .....	77
<b>Figure 3.8</b> The universal velocity profile $u^+$ vs. $y^+$ plot for $Re = 6500$ and fixed $Ri = 0.16$ at $L/D = 140$ .....	81
<b>Figure 3.9</b> Comparison of average fully developed (a) $f$ and (b) $Nu$ of various turbulence models with the standard available correlations and experimental results at $Ri = 0.001$ .....	83
<b>Figure 4.1</b> Schematic diagram of the mixed convection experimental set-up .....	86
<b>Figure 4.2</b> (a) Schematic and (b) photographic view of the calming section.....	87
<b>Figure 4.3</b> (a) Assembled calming section and its (b) sub-components.....	88
<b>Figure 4.4</b> (a) Schematic and (b) photographic view of the test section with thermal and pressure sensors arrangement.....	89
<b>Figure 4.5</b> (a) Test section and its (b) sub-components with thermocouple arrangement .....	90
<b>Figure 4.6</b> (a) Schematic of the mixer section with splitter plates and its (b) photographic view .....	90
Figure 4.7 Mixer section and its design .....	91
<b>Figure 4.8</b> (a) Pictorial view of the visualization section with camera and (b) its subcomponents.....	92
<b>Figure 4.9</b> (a) Flowmeter display unit mounting and (b) its connection to the flowline .....	94
<b>Figure 4.10</b> Direct Current (DC) power source with its connections and the control unit .....	95
<b>Figure 4.11</b> (a) Data logger switch unit and (b) data acquisition software interface ..	95
<b>Figure 4.12</b> (a) Syringe pump for dye injection and (b) centrifugal pump for main line flow.....	96
<b>Figure 4.13</b> (a) Chiller unit (b) inside view of the insulated tank and (c) PID controller .....	97
<b>Figure 4.14</b> Mixed convection experimental set-up with individual components for (a) aiding and (b) opposing flow .....	101

<b>Figure 4.15</b> (a) Hydrodynamic ( $f$ vs. $Re$ ) validation plot for aiding and opposing flow with zero heat flux .....	104
<b>Figure 4.16</b> (a) Thermal ( $Nu$ vs. $Re$ ) validation plot for aiding and opposing flow with negligible heat flux .....	105
<b>Figure 4.17</b> Laminar forced convection validation plot ( $Nu$ vs. $Re$ ) for aiding flow at heat flux ( $q$ ) of $950 \text{ W/m}^2$ .....	106
<b>Figure 4.18</b> Axial variation of (a) wall ( $T_w$ ) and mean ( $T_m$ ) temperature and (b) wall and mean temperature difference ( $T_w - T_m$ ) at $Re = 300$ at heat flux ( $q$ ) of $450 \text{ W/m}^2$ in laminar forced convection for aiding flow .....	107
<b>Figure 4.19</b> Local (a) $Nu$ vs. $L/D$ and (b) $Nu$ vs. $1/Gz$ variation for $Re = 300$ at heat flux of $450 \text{ W/m}^2$ in laminar forced convection for aiding flow .....	107
<b>Figure 4.20</b> Thermal ( $Nu$ vs. $Re$ ) validation plot for aiding and opposing laminar, transitional, and turbulent mixed convection at heat flux ( $q$ ) of $8000 \text{ W/m}^2$ .....	108
<b>Figure 4.21</b> Thermal ( $Nu$ vs. $Re$ ) validation plot of transitional mixed convection regime for aiding flow at heat flux ( $q$ ) of $4.5 \text{ kW/m}^2$ .....	109
<b>Figure 5.1</b> (a) Centreline velocity and (b) velocity profile at $L/D = 500$ with different heat flux ( $q$ ) $0 \text{ kW/m}^2$ , $1 \text{ kW/m}^2$ and $2 \text{ kW/m}^2$ at $Re = 250$ . Magnified view of the velocity profiles in $0.5 \leq r/R \leq 0.70$ are provided in Figure A.1. Developing and developed velocity profiles and their magnified view for one case $q = 2 \text{ kW/m}^2$ is also provided in Figure A.2. ....	113
<b>Figure 5.2</b> (a) Centreline temperature and (b) non-dimensional temperature profile with different heat flux ( $q$ ) $0 \text{ kW/m}^2$ , $1 \text{ kW/m}^2$ and $2 \text{ kW/m}^2$ at $Re = 250$ .....	113
<b>Figure 5.3</b> (a) Local $C_f$ plot, Enlarged view of Figure 5.1(b) adjacent to the wall i.e. $0.7 \leq r/R \leq 1$ are presented in A.3; (b) local $Nu$ vs. $1/Gz$ plot with different heat flux ( $q$ ) $0 \text{ kW/m}^2$ , $1 \text{ kW/m}^2$ and $2 \text{ kW/m}^2$ at $Re = 250$ . The corresponding wall ( $T_w$ ) and mean ( $T_m$ ) temperature variation plot for one case is presented in Figure A.4 .....	114
<b>Figure 5.4</b> (a) Centreline velocity and (b) velocity profile at $L/D = 500$ for $Re = 250$ and $Ri = 0 - 1.5$ . Magnified view of the velocity profiles in $0.5 \leq r/R \leq 0.70$ are provided in Figure A.5. ....	115
<b>Figure 5.5</b> (a) Centerline temperature (b) non-dimensional temperature profile at $Re = 250$ and $Ri = 0.125 - 1.5$ .....	116
<b>Figure 5.6</b> Variation of (a) local $C_f$ and (b) local $Nu$ at $Re = 250$ and $Ri = 0.125 - 1.5$ .....	116

<b>Figure 5.7</b> (a) Velocity profile and (b) non-dimensional temperature profile at $L/D = 500$ for $Re = 500, 750$ and $1000$ at $Ri = 0.1$ .....	117
<b>Figure 5.8</b> (a) Local $C_f$ plot and (b) local $Nu$ plot at $Ri = 0.1$ and $Re = 500, 750$ and $1000$ . Magnified view of local $Nu$ plot for $4 \leq Nu \leq 5$ is provided in Figure A.6. ....	118
<b>Figure 5.9</b> (a) Developing and (b) fully developed $Nu$ plot with increasing $Re$ at different $Ri$ .....	118
<b>Figure 5.10</b> Fully developed $f$ and Colburn $j$ -factor plot for varying $Re$ at $L/D = 500$ with different $Ri$ . Magnified view of Colburn $j$ -factor plot for $800 \leq Re \leq 1000$ is provided in A.7.....	119
<b>Figure 5.11</b> Comparison between developing Colburn $j$ -factor for (a) varying $Re$ and $L/D$ at fixed $Ri = 0.1$ (b) varying $Re$ and $Ri$ at fixed $L/D$ [Magnified view of Colburn $j$ -factor plot for $800 \leq Re \leq 1000$ is provided in Figure A.8].....	120
<b>Figure 5.12</b> (a) Centerline velocity and (b) velocity profile at $L/D = 500$ with different heat flux ( $q$ ) $0 \text{ kW/m}^2$ , $1 \text{ kW/m}^2$ and $2 \text{ kW/m}^2$ at $Re = 250$ . Magnified view of the velocity profiles in $0.5 \leq r/R \leq 0.70$ are provided in Figure A.1. Corresponding developing and developed velocity profiles and their magnified view for one case $q = 2 \text{ kW/m}^2$ is also provided in Figure A.9.....	121
<b>Figure 5.13</b> (a) Centerline temperature and (b) non-dimensional temperature profile with different heat flux ( $q$ ) $0 \text{ kW/m}^2$ , $1 \text{ kW/m}^2$ and $2 \text{ kW/m}^2$ at $Re = 250$ .....	121
<b>Figure 5.14</b> (a) Local skin friction plot and (b) Local $Nu$ plot with different heat flux ( $q$ ) $0 \text{ kW/m}^2$ , $1 \text{ kW/m}^2$ and $2 \text{ kW/m}^2$ at $Re = 250$ . Enlarged view of Figure 5.12(b) adjacent to the wall i.e., $0.7 \leq r/R \leq 1$ are presented in A.3 and the corresponding wall ( $T_w$ ) and mean ( $T_m$ ) temperature variation plot for various cases are presented in Figure A.4.....	122
<b>Figure 5.15</b> (a) Centerline velocity and (b) velocity profile at $L/D = 500$ for $Ri = 0.0 - 1.5$ at $Re = 250$ . Magnified view of the velocity profiles in $0.5 \leq r/R \leq 0.70$ are provided in Figure A.5. ....	123
<b>Figure 5.16</b> (a) Centerline temperature (b) non-dimensional temperature profile for $Ri = 0.25 - 1.5$ at $Re = 250$ .....	123
<b>Figure 5.17</b> Variation of (a) local $C_f$ and (b) local $Nu$ plot at $Re = 250$ and $Ri = 0.125 - 1.5$ .....	124
<b>Figure 5.18</b> (a) Velocity profile and (b) non-dimensional temperature profile at $L/D = 500$ for $Re = 500, 750$ and $1000$ at $Ri = 0.1$ .....	125

<b>Figure 5.19</b> Variation of (a) local $C_f$ plot and (b) local $Nu$ plot at $Re = 500, 750$ and $1000$ and $Ri = 0.1$ . Magnified view of local $Nu$ plot for $4 \leq Nu \leq 5$ is provided in Figure A.6.....	126
<b>Figure 5.20</b> (a) Developing and (b) fully developed $Nu$ plot with increasing $Re$ at different $Ri$ .....	126
<b>Figure 5.21</b> Fully developed Colburn $j$ -factor plot for varying $Re$ at $L/D = 500$ with different $Ri$ . Magnified view of Colburn $j$ -factor plot for $800 \leq Re \leq 1000$ is provided in Figure A.7.....	127
<b>Figure 5.22</b> Comparison between developing Colburn $j$ -factor for (a) varying $Re$ and $L/D$ at fixed $Ri = 0.1$ (b) varying $Re$ and $Ri$ at fixed $L/D$ [Magnified view of Colburn $j$ -factor plot for $800 \leq Re \leq 1000$ is provided in Figure A.8]. .....	127
<b>Figure 5.23</b> Comparison between local (a) $C_f$ and (b) $Nu$ for assisting and opposing flow at $Re = 250$ and $Ri = 0.5, 1.0, 1.5$ .....	128
<b>Figure 5.24</b> Comparison between fully developed (a) $f$ and (b) $Nu$ for assisting and opposing flow at $Re = 250$ and $Ri = 0.125 - 1.5$ . Similar trends were observed at $Re = 350, 500$ and $750$ (See Figure A.13). .....	129
<b>Figure 5.25</b> Comparison of hydrodynamic and thermal entry length for assisting and opposing flow at $Re = 250$ and different $Ri$ . .....	130
<b>Figure 5.26</b> (a) & (b) Fully developed friction factor correlation plot with $Re$ , (c) & (d) fully developed friction factor correlation plot with $Ri$ , and (e) & (f) fully developed $Nu$ correlation plot with $Ri$ for assisting and opposing flows, respectively .....	131
<b>Figure 5.27</b> Deviation of correlation and numerical data of $f$ and $Nu$ for (a) Eqs. 5.3 & 5.6 (b) Eqs. 5.4 & 5.7 and (c) Eqs. 5.5 & 5.8 .....	133
<b>Figure 5.28</b> Deviation of correlation and numerical data of $Nu$ at fixed $Re$ and varying $Ri$ for Eq. 5.9 in developing (a & c) and Eq. 5.10 in fully developed flows (b & d) .	133
<b>Figure 5.29</b> (a) Average $f$ vs. $Re$ comparison plot with magnified plot for (b) aiding and (b) opposing flow of laminar mixed convection with varying $Re, Gr$ at different $Ri$ . .....	135
<b>Figure 5.30</b> Average $Nu$ vs. $Re$ comparison plot for laminar mixed convection with varying $Re, Gr$ at different $Ri$ .....	137
<b>Figure 5.31</b> Local (a) $Nu$ vs. $L/D$ and (b) $Nu$ vs. $Gz$ plot for laminar mixed convection at fixed $Ri=0.1$ in aiding flow for different $Re$ . .....	138
<b>Figure 5.32</b> Local (a) $Nu$ vs. $L/D$ and (b) $Nu$ vs. $Gz$ plot for laminar mixed convection at fixed $Ri=0.1$ in opposing flow.....	138

<b>Figure 5.33</b> Local $Nu$ vs. $L/D$ plot for laminar mixed convection at fixed $Ri=0.1-1.5$ in (a) aiding and (b) opposing flow at $Re=500$ .....	139
<b>Figure 5.34</b> Local $Nu$ vs $L/D$ plot for laminar mixed convection at varying $Ri=0.1-1.5$ in (a) aiding and (b) opposing flow at $Re=700$ along with wall and mean fluid temperature variation in (c) aiding and (d) opposing flow for $Ri=0.75$ .....	140
<b>Figure 5.35</b> Average $Nu$ vs $Ri$ plot for laminar mixed convection at fixed $Re=500$ and $700$ in (a) aiding and (b) opposing flow .....	140
<b>Figure 5.36</b> Flow patterns at fixed $Re=1000$ for (a) $Ri=0.1$ (laminar) (b) $Ri=0.5$ (transitional) (c) $Ri=1.0$ (quasi-turbulent) and (c) $Ri=1.5$ (turbulent) in aiding flow	142
<b>Figure 5.37</b> Flow patterns at fixed $Re=1000$ for (a) $Ri=0.1$ (laminar) (b) $Ri=0.5$ (transitional) (c) $Ri=1.0$ (quasi-turbulent) and (c) $Ri=1.5$ (turbulent) in opposing flow .....	142
<b>Figure 5.38</b> Local $f$ and $Nu$ vs. $Re$ comparison plot at $L/D=121$ for (a) & (b) aiding and (c) & (d) opposing laminar mixed convection at fixed $Ri=0.1$ .....	144
<b>Figure 5.39</b> Local $Nu$ (numerical vs. experimental) comparison plots in (a) aiding and (b) opposing flow for laminar mixed convection at fixed $Ri$ .....	145
 <b>Figure A.1</b> Magnified view of (a) Figure 5.1(b) and (b) Figure 5.12(b) within region $0.5 \leq r/R \leq 0.70$ .....	147
<b>Figure A.2:</b> (a) Velocity profile and (b) magnified velocity near the walls ( $0.95 \leq r/R \leq 1$ ) at different axial length (for Figure 5.1(b) at $q= 2 \text{ kW/m}^2$ ).....	147
<b>Figure A.3:</b> Magnified view of (a) Figure 5.1 b) and (b) Figure 5.12(b) adjacent to the wall i.e., $0.7 \leq r/R \leq 1$ , based upon which the friction factor was defined .....	148
<b>Figure A.4:</b> Wall temperature ( $T_w$ ) and mean temperature ( $T_m$ ) variation at different axial length (for Figure 5.3(b) and 5.14(b) at $q= 2 \text{ kW/m}^2$ ) for (a) assisting and (b) opposing flow.....	148
<b>Figure A.5:</b> Magnified view of (a) Figure 5.4(b) and (b) Figure 5.15(b).....	148
<b>Figure A.6:</b> Magnified view of (a) Figure 5.8(b) and (b) Figure 5.19(b).....	149
<b>Figure A.7:</b> Magnified view of (a) Figure 5.10 and (b) Figure 5.21 .....	149
<b>Figure A.8:</b> Enlarged view of (a) Figure 5.11(b) and (b) Figure 5.22(b) .....	149
<b>Figure A.9:</b> (a) Velocity profile and (b) magnified velocity near the walls ( $0.95 \leq r/R \leq 1$ ) at different axial length (for Figure 5.12(b) at $q= 2 \text{ kW/m}^2$ ).....	150
<b>Figure A.10:</b> Local $C_f$ and $Nu$ plot corresponding to different $Ri$ at $Re = 350$ for (a, c) assisting and (b, d) opposing flow (numerical instability observed after $Ri = 1.0$ )..	150

<b>Figure A.11:</b> Local $C_f$ and $Nu$ plot corresponding to different $Ri$ at $Re = 500$ for (a, c) assisting and (b, d) opposing flow (numerical instability observed after $Ri = 0.75$ )	151
<b>Figure A.12:</b> Local $C_f$ and $Nu$ plot corresponding to different $Ri$ at $Re = 750$ for (a, c) assisting and (b, d) opposing flow (numerical instability observed after $Ri = 0.5$ )	152
<b>Figure A.13:</b> Fully developed $f$ vs. $Ri$ and $Nu$ vs. $Ri$ plots corresponding to (a, b) $Re = 350$ (c, d) 500 and (e, f) 750 for assisting and opposing flow (numerical instability observed after $Ri = 1.0$ for $Re = 350$ , after $Ri = 0.75$ for $Re = 500$ and after $Ri = 0.5$ for $Re = 750$ )	153
<b>Figure A.14:</b> Comparison of (a) velocity and (b) non-dimensional temperature ( $T_{\text{nondim}}=(T-T_i)/qD/k$ , $r_{\text{nondim}}=r/R$ ) profiles for varying viscosity at $Ri=0.1$ and $Re=500$ in aiding flow. Due to the decrease in viscosity with the increase in temperature, velocity near the wall increases as compared to the velocity when the viscosity is constant. To conserve the mass the increase in velocity near the wall gets compensated with the decrease of it at the centre. Thus, the heat is being carried away by the fluid resulting in lower temperature gradient. This ultimately increases the friction factor and decreases the Nusselt number.	154
<b>Figure A.15:</b> Comparison of (a) velocity and (b) non-dimensional temperature profiles for varying viscosity at $Ri=0.1$ and $Re=500$ in opposing flow. Due to opposing effect of free convection the increase in the velocity near the wall and decrease at the centre is less as compared to aiding flow. Thus, the pressure drop also increases in opposing flow. The temperature gradient is indiscernible in case of varying viscosity with temperature as compared to the constant viscosity. However, there is an increase of temperature at the core which results in decrease of heat transfer.	154
<b>Figure 6.1</b> (a) Centerline velocity and (b) velocity profile at $L/D=150$ for fixed $Ri=0.1$ and varying $Re$ and $Gr$ in aiding flow	158
<b>Figure 6.2</b> (a) Centerline temperature and (b) non-dimensional temperature profile at $L/D=150$ for fixed $Ri=0.1$ and varying $Re$ and $Gr$ in aiding flow	159
<b>Figure 6.3</b> (a) Coefficient of skin friction ( $C_f$ ) and (b) local $Nu$ axial plot at fixed $Ri=0.1$ and varying $Re$ and $Gr$ in aiding flow	160
<b>Figure 6.4</b> (a) Radial turbulent kinetic energy ( $\kappa$ ) at $L/D=150$ and (b) axial turbulent eddy frequency ( $\omega$ ) plot at fixed $Ri=0.1$ and varying $Re$ and $Gr$ in aiding flow	161
<b>Figure 6.5</b> Axial (a) intermittency ( $\gamma$ ) and (b) momentum thickness Reynolds number ( $Re\theta$ ) plot at the centreline (i.e, $r/R=0.5$ ) for fixed $Ri=0.1$ and varying $Re$ and $Gr$ in aiding flow	162

<b>Figure 6.6</b> (a) Centerline velocity and (b) velocity profile at $L/D=150$ for fixed $Ri=0.1$ and varying $Re$ and $Gr$ in opposing flow .....	163
<b>Figure 6.7</b> (a) Centerline temperature and (b) non-dimensional temperature profile at $L/D=150$ for fixed $Ri=0.1$ and varying $Re$ and $Gr$ in opposing flow .....	163
<b>Figure 6.8</b> (a) Coefficient of skin friction ( $C_f$ ) and (b) local $Nu$ plot at fixed $Ri=0.1$ and varying $Re$ and $Gr$ in opposing flow .....	164
<b>Figure 6.9</b> (a) Radial turbulent kinetic energy at $L/D=150$ ( $\kappa$ ) and (b) axial turbulent eddy frequency ( $\omega$ ) plot at fixed $Ri=0.1$ and varying $Re$ and $Gr$ in opposing flow ..	165
<b>Figure 6.10</b> Axial (a) intermittency ( $\gamma$ ) and (b) momentum thickness Reynolds number ( $Re\theta$ ) plot at the centreline (i.e, $r/R=0.5$ ) for fixed $Ri=0.1$ and varying $Re$ and $Gr$ in opposing flow .....	166
<b>Figure 6.11</b> Comparison of (a) centerline velocity and (b) outlet velocity profile in assisting and opposing case at $Re=2500$ and $Ri=0.1$ .....	167
<b>Figure 6.12</b> Comparison of (a) centerline temperature and (b) outlet non-dimensional temperature profile in assisting and opposing case at $Re=2500$ and $Ri=0.1$ .....	167
<b>Figure 6.13</b> Comparison local $C_f$ and $Nu$ in assisting and opposing case at $Re=2500$ and $Ri=0.1$ .....	168
<b>Figure 6.14</b> Comparison of turbulent kinetic energy at $L/D=150$ and turbulent eddy frequency profile at outlet in assisting and opposing case at $Re=2500$ and $Ri=0.1$ ..	168
<b>Figure 6.15</b> Comparison of intermittency and $Re\theta$ in assisting and opposing case at $Re=2500$ and $Ri=0.1$ .....	169
<b>Figure 6.16</b> (a) Average $f$ vs. $Re$ comparison plot and magnified view for (b) aiding and opposing flow of transitional mixed convection with varying $Re$ , $Gr$ at different $Ri$ .....	171
<b>Figure 6.17</b> (a) Average $Nu$ vs. $Re$ comparison plot and magnified plot for (b) aiding and opposing flow of transitional mixed convection with varying $Re$ , $Gr$ at different $Ri$ .....	172
<b>Figure 6.18</b> Local (a) $Nu$ vs. $L/D$ and (b) $Nu$ vs. $Gz$ plot for transitional mixed convection at fixed $Ri=0.1$ in aiding flow .....	173
<b>Figure 6.19</b> Local (a) $Nu$ vs. $L/D$ and (b) $Nu$ vs. $Gz$ plot for transitional mixed convection at fixed $Ri=0.1$ in opposing flow .....	174
<b>Figure 6.20</b> Flow patterns for (a) laminar ( $Re=969$ ) (b) transitional ( $Re=2438$ ) and (c) turbulent ( $Re=3814$ ) mixed convection at fixed $Ri=0.1$ in aiding flow .....	175



<b>Figure 6.21</b> Flow patterns for (a) laminar ( $Re=977$ ) (b) transitional ( $Re=2264$ ) and (c) turbulent ( $Re=3394$ ) mixed convection at fixed $Ri=0.1$ in opposing flow .....	176
<b>Figure 6.22</b> Local $Nu$ (numerical vs. experimental) comparison plots for transitional mixed convection at fixed $Ri$ .....	177
<b>Figure 7.1</b> Comparison of the present mixed convection data on the flow regime map of Metais and Eckert [3] applicable for a vertical tube ( $0.01 < PrD/L < 1$ ) .....	180
<b>Figure 7.2</b> (a) Outlet velocity profile and (b) fully developed $f$ at $L/D = 150$ for varying $Re, Ri$ at fixed $Gr=4.07 \times 10^6$ .....	181
<b>Figure 7.3</b> Non-dimensional outlet temperature profile and (b) fully developed $Nu$ plot at fixed $Gr=4.07 \times 10^6$ and varying $Re, Ri$ .....	182
<b>Figure 7.4</b> Radial variation of (a) $\kappa$ and (b) $\varepsilon$ profile at a fixed $L/D = 150$ for varying $Re, Ri$ at fixed $Gr=4.07 \times 10^6$ .....	182
<b>Figure 7.5</b> (a) Velocity profile at $L/D = 150$ and (b) fully developed $f$ plot for varying $Re, Gr$ at fixed $Ri = 0.16$ .....	184
<b>Figure 7.6</b> (a) Non-dimensional outlet temperature profile and (b) fully developed $Nu$ plot for varying $Re, Gr$ at fixed $Ri = 0.16$ .....	184
<b>Figure 7.7</b> Variation of radial (a) $\kappa$ and (b) $\varepsilon$ profile at a fixed $L/D = 150$ for varying $Re, Gr$ at fixed $Ri = 0.16$ .....	185
<b>Figure 7.8</b> (a) Fully developed $f$ (b) $Nu$ variation for varying $Re, Ri$ at fixed $Gr=4.07 \times 10^6$ .....	186
<b>Figure 7.9</b> Variation of fully developed (a) $f$ and (b) $Nu$ at fixed $Ri = 0.16$ and varying $Re, Gr$ .....	187
<b>Figure 7.10</b> Comparison between fully developed (a) $f$ and (b) $Nu$ for varying $Re$ and $Ri$ at fixed $Gr$ in assisting and opposing flow .....	188
<b>Figure 7.11</b> Comparison between fully developed (a) $f$ and (b) $Nu$ at $L/D = 50$ for varying $Gr$ and $Re = 5000 - 20000$ at fixed $Ri$ in assisting and opposing flow ....	189
<b>Figure 7.12</b> Comparison of the ratio of (a) friction factor ( $f/f_o$ ) and (b) Nusselt number ( $Nu/Nu_o$ ) of mixed and forced convection in assisting and opposing flow .....	189
<b>Figure 7.13</b> Local skin friction coefficient ( $C_f$ ) and Nusselt number ( $Nu$ ) variation axially for assisting and opposing flow (a) at fixed $Gr$ and varying $Re, Ri$ (b) at fixed $Ri$ and varying $Re, Gr$ .....	190

<b>Figure 7.14</b> Comparison of hydrodynamic and thermal entry length for assisting and opposing flow (a) at fixed $Gr$ and varying $Re$ , $Ri$ and fixed $Re$ and varying $Gr$ , $Ri$ (b) at fixed $Ri$ and varying $Re$ , $Gr$ .....	191
<b>Figure 7.15</b> Deviation of correlation and numerical data for (a) $f$ (b) $Nu$ and (c) $f/j$ .....	193
<b>Figure 7.16</b> Average $f$ vs. $Re$ comparison plot in turbulent mixed convection with varying $Re$ , $Gr$ at different $Ri$ .....	195
<b>Figure 7.17</b> Average $Nu$ vs. $Re$ comparison plot in turbulent mixed convection with varying $Re$ , $Gr$ at different $Ri$ .....	196
<b>Figure 7.18</b> Local (a) $Nu$ vs. $L/D$ and (b) $Nu$ vs. $Gz$ plot for turbulent mixed convection at fixed $Ri=0.1$ in aiding flow .....	197
<b>Figure 7.19</b> Local (a) $Nu$ vs. $L/D$ and (b) $Nu$ vs. $Gz$ plot for turbulent mixed convection at fixed $Ri=0.1$ in opposing flow .....	198
<b>Figure 7.20</b> Local $Nu$ (numerical vs. experimental) comparison plots in (a) aiding and (b) opposing flow of turbulent mixed convection at fixed $Ri$ .....	199
 <b>Figure B.1:</b> Calibration of T-type thermocouples and PT 100.....	216
<b>Figure B.2:</b> Comparison of Differential Pressure Transmitter (DPT) with digital manometer.....	217
<b>Figure B.3:</b> Flowmeter vs. manual readings calibration plot .....	218
<b>Figure B.4:</b> Vertical and horizontal alignment of the experimental test-rig .....	219
<b>Figure B.5:</b> Surface roughness measured at ten different locations of inside surface of the SS 316 L tube .....	219

## LIST OF TABLES

<b>Table 3.1</b> Optimization of grids with $L/D = 500$ at $Ri = 1$ and $Re = 250$ .....	71
<b>Table 3.2</b> Optimization of bias factor with $31 \times 30001$ grid size at $Ri = 1$ and $Re = 250$ .....	71
<b>Table 3.3</b> Optimization of grids at $Ri = 0.001$ and $Re = 20000$ for $\Delta T = 0.8^\circ\text{C}$ with $L/D = 140$ .....	79
<b>Table 3.4</b> Optimization of bias factor with $301 \times 7501$ grid size at $Ri = 0.001$ and $Re =$ $20000$ with $L/D = 140$ .....	80
 <b>Table 4.1</b> List of the instruments, their operating ranges, and associated uncertainties .....	103
 <b>Table 5.1</b> Range of the coefficients, constants and exponents present in Eqs. (5.9) and (5.10) .....	132
 <b>Table 6.1</b> Range of the coefficients and exponents present in Eqs. (6.2) and (6.3) ..	173
 <b>Table 7.1</b> Range of the coefficients and exponents present in Eqs. (7.1), (7.2), and (7.3) .....	192
 <b>Table B.1:</b> Sample data generated from the calibration report of a T-type thermocouple .....	216
<b>Table B.2:</b> Sample data generated from the calibration report of a PT100 .....	217

## Notations and Abbreviations

### *Abbreviations*

AWF	Analytical Wall Functions
BF	Bias Factor
CFD	Computational Fluid Dynamics
DPT	Differential Pressure Transducer
DNS	Direct Numerical Simulations
FD	Fully Developed
FVM	Finite Volume Method
GIT	Grid Independency Test
LES	Large Eddy Simulation
LRV	Lower Range Value
OAR	Open Area Ratio
PIV	Particle Image Velocimetry
RANS	Reynolds-Averaged-Navier-Stokes
RNG	Renormalisation Group
SIMPLE	Semi-Implicit Pressure Linked Equations
SST	Shear Stress Transport
TBL	Thermal Boundary Layer
TDR	Turbulent Dissipation Rate ( $\text{m}^2/\text{s}^3$ )
TFC	Turbulent Forced Convection
TEF	Turbulent Eddy Frequency ( $\text{s}^{-1}$ )
TKE	Turbulent Kinetic Energy ( $\text{m}^2/\text{s}^2$ )
UHF	Uniform Heat Flux
URV	Upper Range Value
UWT	Uniform Wall Temperature

### *Nomenclature*

$a$	coefficient used in Eq. (5.9), (7.1)
$A$	intercept in Eq. (5.10)
$A_s$	surface area ( $\text{m}^2$ )
$b$	coefficient used in Eq. (7.2)
$B$	coefficient in Eq. (5.10)
$Bo$	Buoyancy parameter ( $Gr/Re^{3.425}Pr^{0.8}$ )
$B$	von-Karman constant ( $\approx 5.2$ )
$c$	coefficient used in Eq. (7.3)
$C_f$	skin friction coefficient ( $ \tau_w /\frac{\rho u_m^2}{2}$ )
$C_p$	specific heat at constant pressure ( $\text{J/kg K}$ )
$D$	diameter of the tube ( $\text{m}$ )
$f$	friction factor ( $8 \times  \tau_w /\rho u_m^2$ )
$Gr$	Grashof number based on heat flux ( $g\beta D^4 \dot{q}/\nu^2 k$ )
$Gr^*$	$Gr \times Nu$
$Gr_q$	Grashof number based on heat flux ( $g\beta D^4 \dot{q}/\nu^2 k$ )
$Gr_M$	solulal Grashof number ( $g\beta_M D^3(\omega_2 - \omega_1)/\nu^2$ )
$Gr_T$	thermal Grashof number ( $g\beta_T D^3(T_2 - T_1)/\nu^2$ )
$Gz$	Graetz number ( $RePrD/L$ )
$h$	heat transfer coefficient ( $\text{Wm}^2\text{-K}$ )
$I$	turbulence intensity ( $\sqrt{u'^2}/u_{avg}$ ), current (A)
$j$	Colburn $j$ -factor ( $Nu/RePr^{1/3}$ )
$k$	thermal conductivity ( $\text{W/m-K}$ )
$L$	the axial length of the tube ( $\text{m}$ )
$L_h$	hydrodynamic entrance length ( $\text{m}$ )

$L_t$	thermal entrance length (m)	$V$	voltage (V)
$m$	exponent used in Eq. (7.1)	$v$	transverse velocity (m/s)
$n$	exponent used in Eq. (5.9), (7.2)	$x$	axial direction
$Nu$	Nusselt number ( $hD/k$ )	$y$	radial direction
$o$	exponent used in Eq. (7.3)	$y^+$	radial nondimensional distance from the wall ( $yv/u_\tau$ )
$p$	pressure (Pa), coefficient used in Eq. (6.2)	$z$	transverse coordinate (m)
$\bar{p}$	mean pressure (Pa)	<b>Greek Symbols</b>	
$P$	pressure (Pa)	$\alpha$	thermal diffusivity (m <sup>2</sup> /s)
$Pr$	Prandtl number ( $\mu C_p/k$ )	$\beta$	thermal expansion coefficient (K <sup>-1</sup> )
$q$	exponent used in Eq. (6.2)	$\epsilon$	eddy diffusivity (m <sup>2</sup> /s)
$Q$	heat rate (W)	$\varepsilon$	turbulent dissipation rate ( $C_\mu^{3/4} \frac{k^{3/2}}{D}$ )
$\dot{q}$	heat flux (W/m <sup>2</sup> )	$\gamma$	intermittency
$r$	axial coordinates (m), coefficient used in Eq. (6.3)	$\Gamma$	effective diffusivity (Pa-s)
$R$	radius of the tube (m)	$\kappa$	turbulent kinetic energy ( $3/2 (u_{avg} I)^2$ )
$R^2$	a statistical measure of goodness of fit	$\mu$	dynamic viscosity (Pa-s)
$Ra$	Rayleigh number ( $Gr \times Pr$ )	$\nu$	kinematic viscosity (m <sup>2</sup> /s)
$Ra$	surface roughness ( $\mu\text{m}$ )	$\omega$	specific dissipation rate (1/s)
$Re$	Reynolds number ( $\rho u_m D/\mu$ )	$\Omega$	vorticity (rad)
$Re_\theta$	momentum thickness Reynolds number ( $\rho u_m \theta/\mu$ )	$\sigma$	turbulent Prandtl number, uncertainty
$Ri$	Richardson number ( $Gr/Re^2$ )	$\rho$	density (kg/m <sup>3</sup> )
$s$	exponent used in Eq. (6.3)	$\tau$	shear stress
$T$	temperature (K)	<b>Subscripts</b>	
$u$	axial velocity (m/s)	$avg$	average
$U$	velocity at the tube inlet (m/s)	$b$	bulk
$u_\tau$	friction velocity ( $\sqrt{\tau_w/\rho}$ )	$c$	critical
		$e$	Electrical

<i>exp</i>	experimental
<i>g</i>	gauge
<i>H, th</i>	thermal
<i>i</i>	inlet
$\infty$	ambient
<i>l</i>	laminar
<i>m</i>	mean
<i>M</i>	momentum
<i>o</i>	forced, outlet
<i>p</i>	constant pressure
<i>s</i>	surface, solid
<i>t</i>	turbulent
$\theta$	momentum thickness
<i>trans</i>	transition
<i>w</i>	wall, water
<i>z</i>	axial direction
<b><i>Superscripts</i></b>	
'	fluctuations
$-, \sim$	average or mean value
<b><i>Other symbols</i></b>	
$\sim$	approximately

### 1.1 Overview of mixed convection

Mixed convection is the combined form of natural and forced convection heat transfer, which has been a subject matter of study of researchers in the field of nuclear reactors, solar energy systems, heat exchangers, supercritical boilers, cooling of electronic devices, extraction of geothermal energy, and many more areas because of its varying nature as a heat transfer phenomenon. At the interface of natural and forced convection this mode of heat transfer can be categorized into either aiding (buoyancy force and fluid flow are in the same direction) or opposing (buoyancy force and fluid flow are in the opposite direction), which decides whether the enhancement or impairment of heat transfer will take place. The study of mixed convection is essential as the regime exhibits enhanced heat transfer ability compared to individual free and forced convection [1]. The flow characteristics and heat transfer in mixed convection were dependent on various factors like the flow regime (developing or fully developed) [2], pipe orientation (horizontal or vertical) [3], boundary condition (constant heat flux or constant wall temperature) [3], flow type (laminar or turbulent) [4] and the flow direction (upward or downward) [1]. In the early understanding of convective heat transfer, forced and free convective heat transfer were studied separately, and any intermixing of these two was ignored. The simultaneous effects of buoyancy forces and externally applied inertia forces are responsible for this mixed regime (Figure 1.1). When attention was given to such possibilities, it was initially limited to laminar and transitional flow studies and later extended to turbulent flows. It is obvious that the heat transfer will be higher in combined free and forced convection as compared to free convection alone. Compared to the forced convection, in aiding flow, the free convection effect is added to the forced flow and enhances the heat transfer. In contrast, it opposes the forced flow and impairs heat transfer. But this is true for laminar mixed convection only. In the case of turbulent mixed convection, the reverse happens because more turbulence in opposing flows eventually increases the heat transfer. Detailed reviews on mixed convection till date can be found in review articles [1], [5]–[8].

## 1.2 Non-dimensional numbers

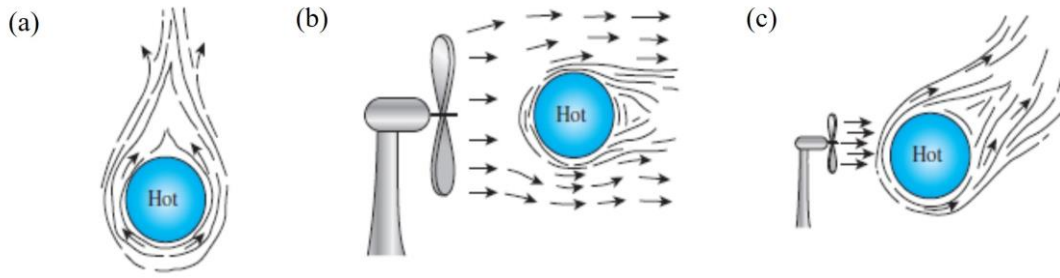


**Figure 1.1** The schematic representations of free, forced and mixed convection (Cengel and Ghajar [9])

## 1.2 Non-dimensional numbers

In this section, we are going to discuss the non-dimensional numbers useful in the hydrodynamic and thermal analysis of mixed convection flows. The key dimensionless numbers involved in mixed convection are used to quantify the effect of different parameters such as velocity of the working fluid, heat flux through the walls, length, and diameter of the tube collectively. The dimensionless number (Reynolds number) related to velocity determines the regime of the forced convection to be laminar or turbulent. Similarly, the dimensionless number (Grashof number) based on heat flux describes whether the free convection is laminar or turbulent. These dimensionless numbers are also combined into a new number (Richardson number) to quantify them relative to each other.

### 1.2.1 Rayleigh number

Rayleigh number ( $Ra$ ) can be represented as the product of Grashof number ( $Gr^* = \frac{g\beta D^3(T_s - T_\infty)}{\nu^2}$ ) and Prandtl number ( $Pr = \frac{\mu C_p}{k}$ ), where  $T_s$ , is the surface temperature and  $T_\infty$ , is the temperature of the fluid at a far distance from the surface. Rayleigh number determines whether the free convection will become laminar ( $Ra > 10^9$ ) and turbulent ( $Ra < 10^9$ ). The Grashof number quantifies the ratio of buoyancy force to the viscous force. The temperature difference ( $T_s - T_\infty$ ) is not always known in constant heat flux conditions. In that case, a modified Grashof number ( $Gr$ ) is used, which is obtained as the product of Nusselt number ( $Nu$ ) and  $Gr^*$ .

$$Gr = Nu \times Gr^* \quad (1.1)$$

The ratio of momentum diffusivity to thermal diffusivity is called the Prandtl number, named after the German Physicist Ludwig Prandtl. In 1904, he introduced the theory of boundary layers. The relative thickness and growth of the hydrodynamic and thermal



boundary layers can be explained by  $Pr$ . For  $Pr > 1$ , the hydrodynamic boundary layer thickness ( $\delta_h$ ) is higher than that of the thermal boundary layer ( $\delta_t$ ), and the reverse is true when  $Pr < 1$ .

### 1.2.2 Richardson number

Richardson number ( $Ri$ ), the ratio of buoyancy force and inertia force, quantifies the relative magnitude of free and forced convection. It is named after the name of Lewis Fry Richardson, originally a mathematician.

$$Ri = \frac{\text{Buoyancy force}}{\text{Inertia force}} = \frac{Gr}{Re^2} \quad (1.2)$$

Reynolds number ( $Re = \frac{\rho u_m D}{\mu}$ ) is a ratio of inertia force to viscous force.  $Re$  governs the forced convection to be laminar or turbulent.  $Ra$  determines whether the natural convection is laminar or turbulent. For external flow, both natural and forced convections are present. The relative importance of each mode of heat transfer is determined by the  $Ri$  values. The  $Ri$  is present in the non-dimensional momentum equation for a vertical hot plate subjected to natural convection.

In general, when  $Ri \gg 1$ , free convection dominates; conversely, forced convection dominates when  $Ri \ll 1$ . For the case  $Ri \approx 1$ , both buoyancy and inertia forces are equally significant. This situation where both the free and forced convection effects are equally dominant is referred to as mixed convection.

### 1.2.3 Graetz number

A dimensionless number called Graetz number ( $Gz$ ) named after a German Physicist, Leo Graetz, is a dimensionless number used in heat transfer and fluid dynamics to characterize the relative importance of convection and conduction in a fluid flow system. It is defined as the product of  $Re$  and  $Pr$ . The Graetz length, also known as the Graetz number is a characteristic length scale that indicates how far a fluid needs to travel in a channel or pipe to achieve thermal equilibrium with the surrounding medium. It's a concept often used in situations involving laminar flow and convective heat transfer.

$$Gz = RePr \frac{D}{x} \quad (1.3)$$

When a fluid flows through a pipe, heat is transferred between the fluid and the walls of the conduit due to the temperature difference. The Graetz length is defined as the distance along the flow direction that the fluid needs to travel in order to achieve a

## 1.2 Non-dimensional numbers

temperature distribution that is close to the fully developed temperature profile. The local values of  $Nu$  are typically presented graphically in terms of the inverse of this dimensionless parameter ( $1/Gz$ ). When the  $1/Gz$  value assumes  $\sim 0.05$ , the flow can be termed fully developed in both constant heat flux and wall temperature boundary conditions. Therefore, when  $1/Gz$  is greater than 0.05, the local  $Nu$  approach their fully developed values of 4.364 in constant heat flux and 3.66 in constant surface temperature.

### 1.2.4 Friction factor

Pressure drop is a quantity of interest in the pipe flow analysis because it is used for estimation of friction factor  $f$ . The friction factor  $f$  is an indicator of the power requirements of the fan or pump to maintain the flow. The pressure drop for all types of fully developed internal flows (laminar or turbulent flows, circular or noncircular pipes, smooth or rough surfaces, horizontal or inclined pipes) can be expressed as

$$\Delta P_L = f \frac{L}{D} \frac{\rho u_{avg}^2}{2} \quad (1.4)$$

Here, the  $f$  is known as the Darcy friction factor, named after the French Engineer Henry Darcy.

### 1.2.5 Nusselt number

The Nusselt number is the ratio of heat transfer by convection to heat transfer by conduction. The heat transfer through the fluid layer is by convection while in motion and conduction while in rest. That is why the heat transfer enhances through a fluid with increased fluid motion. Hence the lowest possible value of  $Nu$  is one in the case of pure heat conduction. It is named after the German physicist Wilhelm Nusselt. For a circular tube, the  $Nu$  can be calculated as follows:

$$Nu = \frac{Q_{conv}}{Q_{cond}} = \frac{hD}{k_s} \quad (1.5)$$

### 1.2.6 Colburn $j$ -factor

Like friction factor ( $f$ ), another nondimensional number called Colburn  $j$ -factor is named after an American engineer, Allan Philip Colburn. In forced and mixed convection analysis, we are primarily interested in determining  $f$  and  $Nu$ . Therefore, it is desirable to have a relation between  $f$  and  $Nu$  so that one can be calculated when the other is available. Such relations are developed based on the similarity between momentum and heat transfers in boundary layers. These are known as *Reynold's analogy* and *Chilton-Colburn analogy*. It is expressed as

$$j = \frac{Nu}{RePr^{1/3}} \quad (1.6)$$

### 1.2.7 Buoyancy parameter

The Buoyancy parameter ( $Bo = \frac{Gr}{Re^{3.425}Pr^{0.8}}$ ) is used to determine the onset of the heat transfer impairment and recovery zone for buoyancy aiding and enhancement in buoyancy opposing turbulent mixed convection flow of flat channels or vertical tubes subjected to constant heat flux conditions.

## 1.3 Flow regimes

The fluid flow is generally classified as laminar, transitional, and turbulent regimes. The criteria to decide the different regime is in terms of  $Re$  in the case of forced convection and  $Ra$  in case of free convection. A flow regime plot (Figure 1.3) between  $Re$  and  $GrPrD/L$  has been produced by Metais and Eckert [3] for flow through a vertical tube with constant heat flux and constant wall temperature conditions. It demarcates the free, forced, and mixed convection regions with laminar, transition, and turbulent flow regimes.

### 1.3.1 Laminar flow

Osborne Reynolds [10] performed the dye experiment by injecting a thin filament of dye into the water at the inlet in a glass tube. The experimental apparatus consists of different test sections of diameter 1 inch, ½ inch, and ¼ inch and 4 feet 6 inches long glass tube fitted with trumpet mouthpieces so that water might enter without disturbance. The experiment showed that at sufficient low velocity, the dye streak formed a straight line and reached the tube exit without mixing.

### 1.3.2 Turbulent flow

As Reynolds [10] increased the flow velocity, the dye diffused downstream and the whole tube section was coloured. This flow regime marked by the rapid mixing of dye is denoted as turbulent flow. On viewing the tube by the light of an electric spark, the mass of colour resolved itself into a mass of visible curls called eddies. At this, the fluid motion was highly unstructured, random, and zigzag which indicates the fluctuations in the velocity. These eddies are responsible for enhanced mixing. Since the boundary layer grows much faster compared to the laminar flow, the entry length is much shorter than the laminar flows.

## 1.3 Flow regimes

### 1.3.3 Laminar-turbulent transitional flow

The intermediate flow, where the laminar and turbulent flows coexist termed a transitional flow regime. The flow switches between laminar and turbulent flow. Reynolds [10] defined this situation as “*Another phenomenon very marked in the smaller tubes, was the intermittent character of the disturbance. The disturbance would suddenly come on through a certain length of the tube and pass away and then come on again, giving the appearance of flashes, and these flashes would often commence successively at one point in the pipe.*” The appearance when the flashes succeeded each other rapidly was as shown in Figure 1.1.

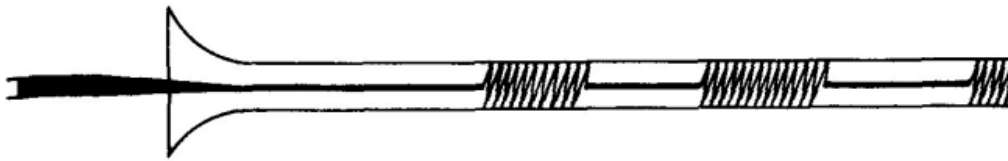


**Figure 1.2** The intermittent character of the disturbance in terms of flashes ( P. G. Drazin [11])

## 1.4 Developing and fully developed flow

The pipe flow can be said to be fully developed when the flow is both hydrodynamically and thermally fully developed. For a flow to be fully developed hydrodynamically and thermally, the velocity profile ( $u(r)$ ) and nondimensional temperature profile ( $\theta(r)$ ) will not change in the axial direction respectively. At thermally fully developed conditions, the difference between wall ( $T_w$ ) and mean temperature ( $T_m$ ) in axial direction will become constant for a constant heat flux boundary condition. The region in which both the velocity and dimensionless temperature profiles remain unchanged along the axial difference is called hydrodynamically and thermally developed respectively. The mathematical expressions for hydrodynamically and thermally fully developed flow are mentioned in Eqs 1.7 and 1.8 [9]. In the developing region, the velocity and nondimensional temperature profile goes on varying until they achieve the axially invariant profiles i.e., the fully developed state. Due to the very thin boundary layer in the developing regime, the momentum and heat diffusion is more, resulting a higher value of  $f$  and  $Nu$ .

The fully developed flow can be expressed as:

$$\text{Hydrodynamic fully developed condition: } \frac{\partial u(r,x)}{\partial x} = 0 \text{ or } u = u(r) \quad (1.7)$$

$$\text{Thermally fully developed condition: } \frac{\partial \left[ \frac{T_w(x) - T(r,x)}{T_w(x) - T_m(x)} \right]}{\partial x} = 0 \text{ or } \frac{\partial \theta}{\partial x} = 0 \quad (1.8)$$

where 'x' is the axial and 'r' is the radial direction.

In Figure 1.3, the schematic of velocity and temperature profiles in the developing and fully developed flow regions has been indicated. The difference in entry lengths in case of hydrodynamically developing followed by thermally developing and simultaneously hydrodynamically and thermally developing flow for constant heat flux boundary conditions is also presented.

## 1.4 Developing and fully developed flow

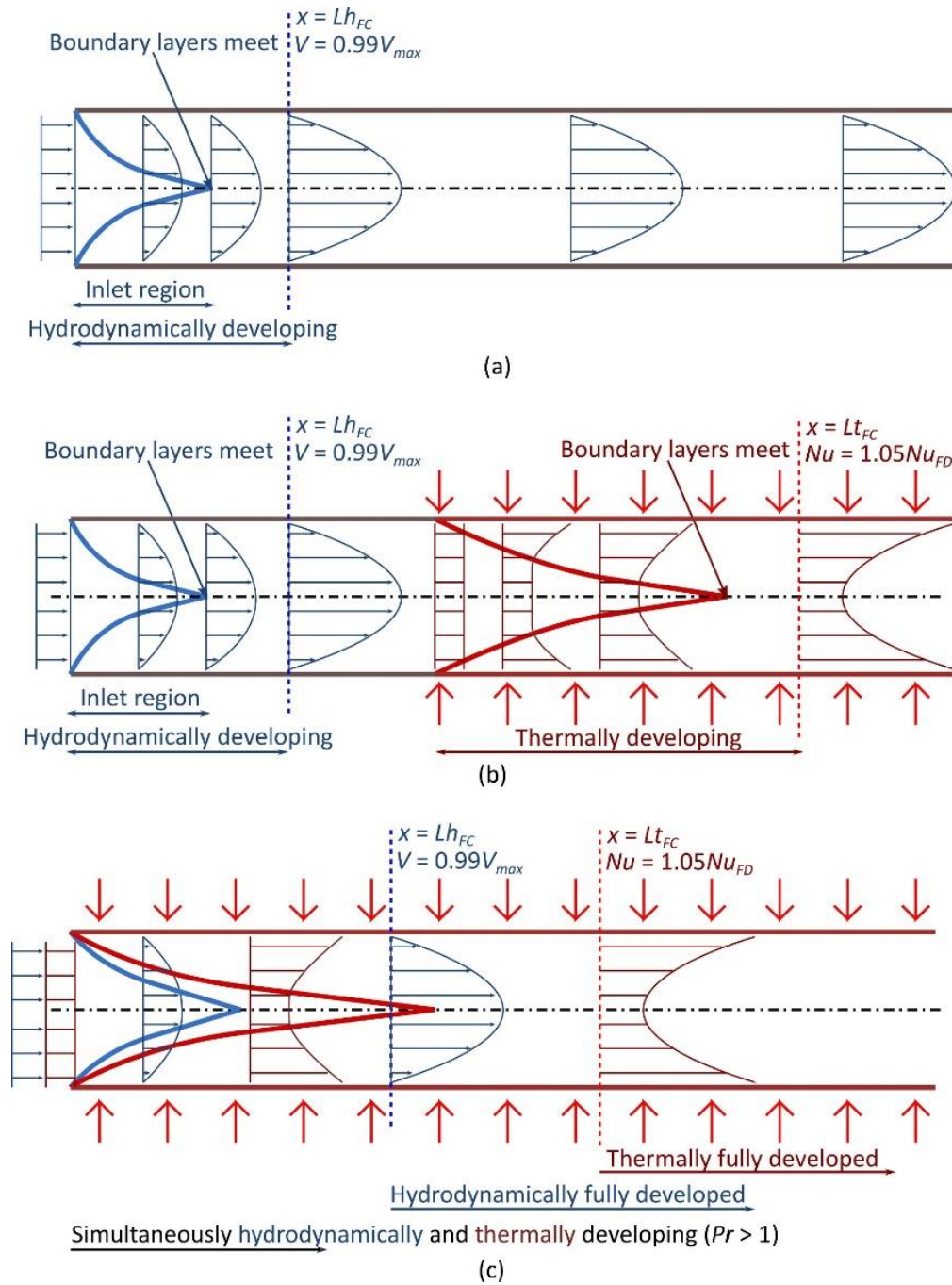


**Figure 1.3** Schematic of the hydrodynamic and thermal boundary layers and entrance lengths for (a) hydrodynamically developing isothermal flow, (b) hydrodynamically developing flow followed by thermally developing flow, and (c) simultaneously hydrodynamically and thermally developing flow (Everts *et al.* [12]).

In simultaneously developing flow, the hydrodynamic and thermal boundary layer both grow simultaneously. The entrance length in simultaneously developing flow will either increase or decrease compared to the hydrodynamically developed and thermally developing flow depending on the type of mixed convection: aiding, opposing, and transverse.

### 1.4.1 Hydrodynamic and thermal entrance length

The hydrodynamic entry length is the axial distance till which the hydrodynamic boundary layer continues to grow before it becomes steady. In the same way, the point till the thermal boundary layer develops is called the thermal entry length. The velocity profile and nondimensional temperature profile become axially invariant beyond the entry lengths.

When a flow through a tube takes place, the fluid in contact with the tube surface assumes zero velocity with no-slip boundary conditions. The fluid particles in the above layer have some velocity and increase towards the center of the tube. This growth in the boundary layer takes place gradually and meets at the center of the tube. This leads to the formation of a hydrodynamic boundary layer, called boundary layer thickness (Figure 1.2(a)).

Similarly, when a fluid at a uniform temperature enters the tube at some higher temperature, the fluid in contact with the surface (heated with constant heat flux) is assumed almost at wall temperature. Due to this, the fluid present at the center of the tube is different from the fluid present adjacent to the tube wall. This difference leads to the convection heat transfer in the transverse direction and the development of a thermal boundary layer. The thickness of the thermal boundary layer increases with the flow progress in axial direction. When it meets the center of the tube (Figure 1.2(b)), the flow is said to be thermally fully developed. The hydrodynamic and thermal entrance length are essential parameters for fluid flow in a tube with heat transfer. Because whether the friction factor and heat transfer coefficient are dependent (developing flow) or independent (fully developed flow) of the axial location. These are calculated from the tube inlet and dependent on the Reynolds number ( $Re$ ) and tube diameter ( $D$ ) for hydrodynamic entry length ( $L_h$ ) in a forced laminar flow. For forced convection laminar flow, along with  $Re$  and  $D$ , the Prandtl number ( $Pr$ ) also decides the thermal entry length ( $L_t$ ).

$$L_h = 0.05 ReD \quad (1.9)$$

$$L_h = 0.05 RePrD \quad (1.10)$$

For a turbulent flow, the hydrodynamic and thermal entry length is same for  $Pr = 1$  and can be obtained as

## 1.5 Mixed convection criteria and flow regime maps

$$L_h = L_t \approx 10D \quad (1.11)$$

### 1.5 Mixed convection criteria and flow regime maps

Combined free and forced convection, popularly known as mixed convection, is characterized by a nondimensional number called the Richardson number ( $Ri$ ). The  $Ri$  is derived through the process of nondimensionalizing the momentum equation that is relevant to the flow across a vertical hot plate. Even though the  $Ri$  is obtained for the case of a vertical plate, it is one of the mixed convection criteria in circular ducts to decide the impact of free convection over forced convection. The mixed convection flow regime generally falls in a range of  $0.1 \leq Ri \leq 10$  (Cengel and Ghajar [9], Everts and Meyer [13]) observed through the experiments. For  $Ri=0.1$ , the free convection is one tenth of the forced convection and when  $Ri=10$ , it is ten times stronger than forced convection, the flow can be considered in mixed convection.

Flow regime maps are crucial graphs to determine whether the free convection is dominant (mixed convection) or the free convection effect is negligible (forced convection). These flow regime maps are a plot between  $Re$  in the ordinate against  $GrPrD/L$  or sometimes  $Ra$  in the abscissa. The first flow regime map was developed by Metais and Eckert [3] (Figures 1.3 and 1.4) which was applicable for fully developed flow in horizontal and vertical tubes. They considered length-to-diameter ratio to determine the flow regime and provided separate maps for horizontal and vertical tubes valid for a condition of  $0.01 < PrD/L < 1$ . The boundaries of the forced and free convection regimes are established in such a way that the actual heat flow under the combined effect of the forces does not diverge by more than 10% from the heat flux that would be induced by the external forces alone or the body forces alone. The map demarcates the free, forced, and mixed convection regions along with their laminar, turbulent, and transitional flow regimes. Followed by it, Ghajar and Tam [14] obtained a flow regime map (Figure 1.5) that is applicable for high  $Pr$  fluids (ranging between 23 to 140) with constant heat flux condition for a horizontal tube only. Their regime map could be used for three different inlet geometries: square-edged, re-entrant, and bell-mouth inlet. A recent work by Everts and Meyer [13] developed a flow regime map (Figures 1.6 and 1.7) for a horizontal tube subjected to constant heat flux boundary conditions. This map is developed for fully developed and developing flows for both low and high  $Pr$  fluids. They obtained the flow regime plots to decide the mixed



convection criteria by considering both conditions as 1. when 10 % higher heat transfer is obtained than the pure free or forced convection, 2. with a range of  $Ri$  in between 0.1 and 10, the free convection is ten times lower and higher than the forced convection. The developing regime is also analyzed by taking the length-to-diameter ( $x/D$ ) ratio into the abscissa of the graph.

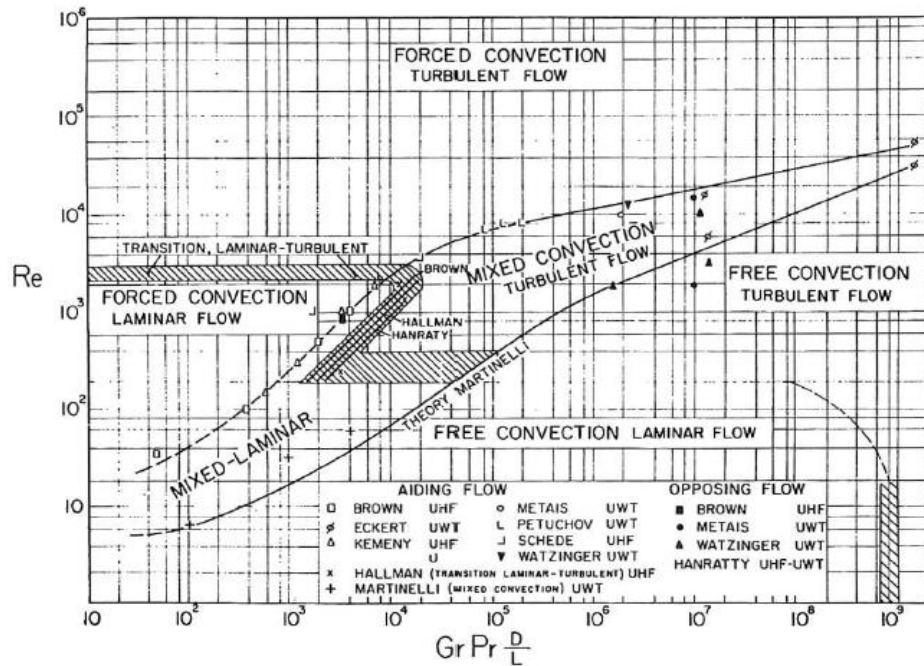


**Figure 1.4** Regimes of free, forced, and mixed convection for flow through vertical tubes ( $0.01 < PrD/L < 1$ ) (taken from Metais and Eckert [3])

## 1.5 Mixed convection criteria and flow regime maps

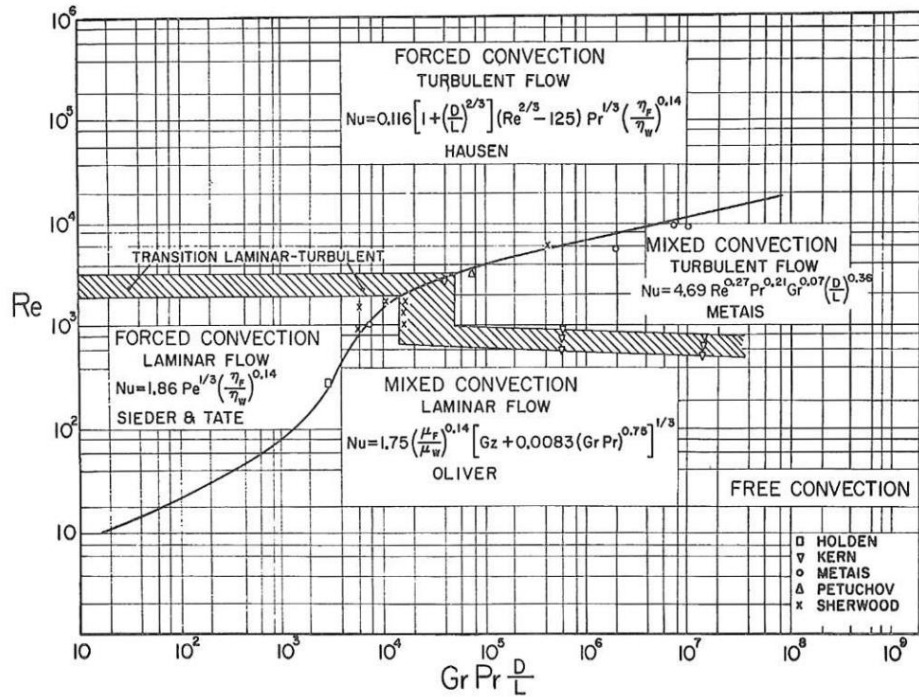


**Figure 1.5** Regimes of free, forced, and mixed convection for flow through horizontal tubes ( $0.01 < PrD/L < 1$ ) (taken from Metais and Eckert [3])

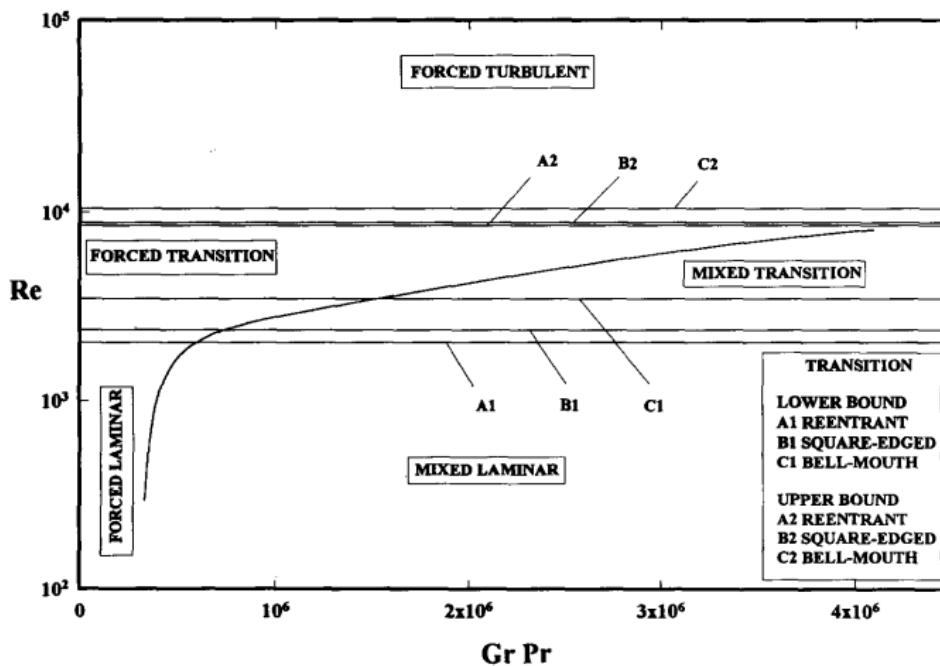


**Figure 1.6** Flow regime map for flow in horizontal tubes with three different inlet configurations and uniform heat flux condition (taken from Ghajar and Tam [14])

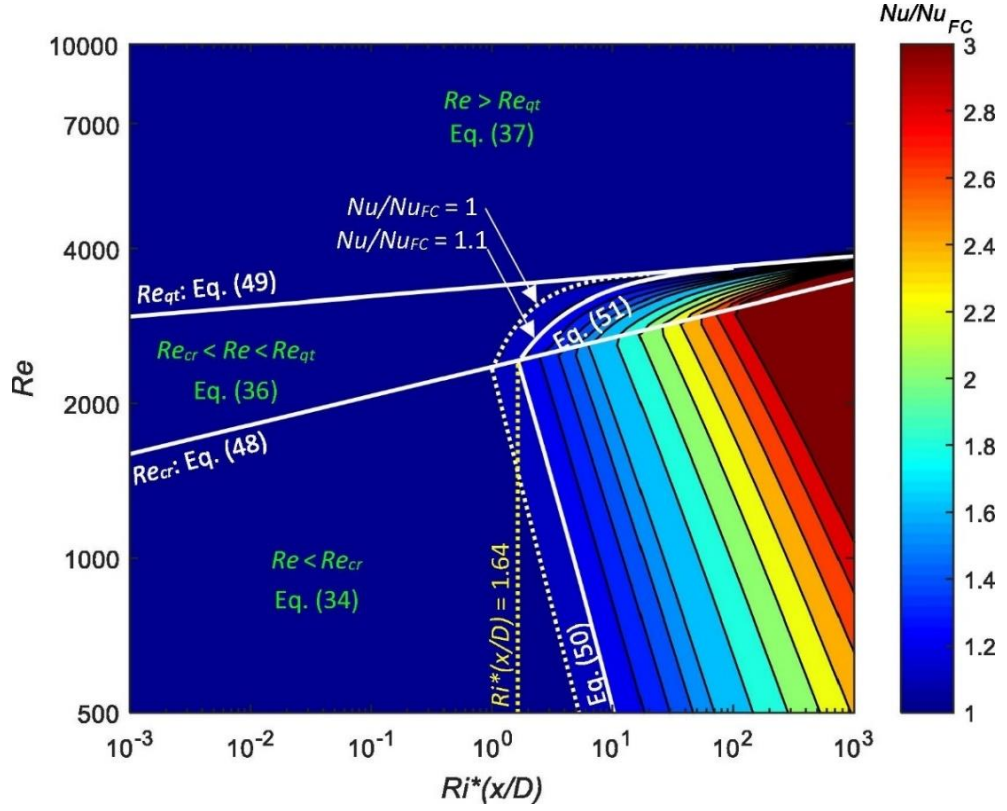


**Figure 1.7** Flow regime map for developing and fully developed flow as a function of  $Re$  and  $Ri^*(x/D)$  in a horizontal tube (taken from Everts and Meyer [13])

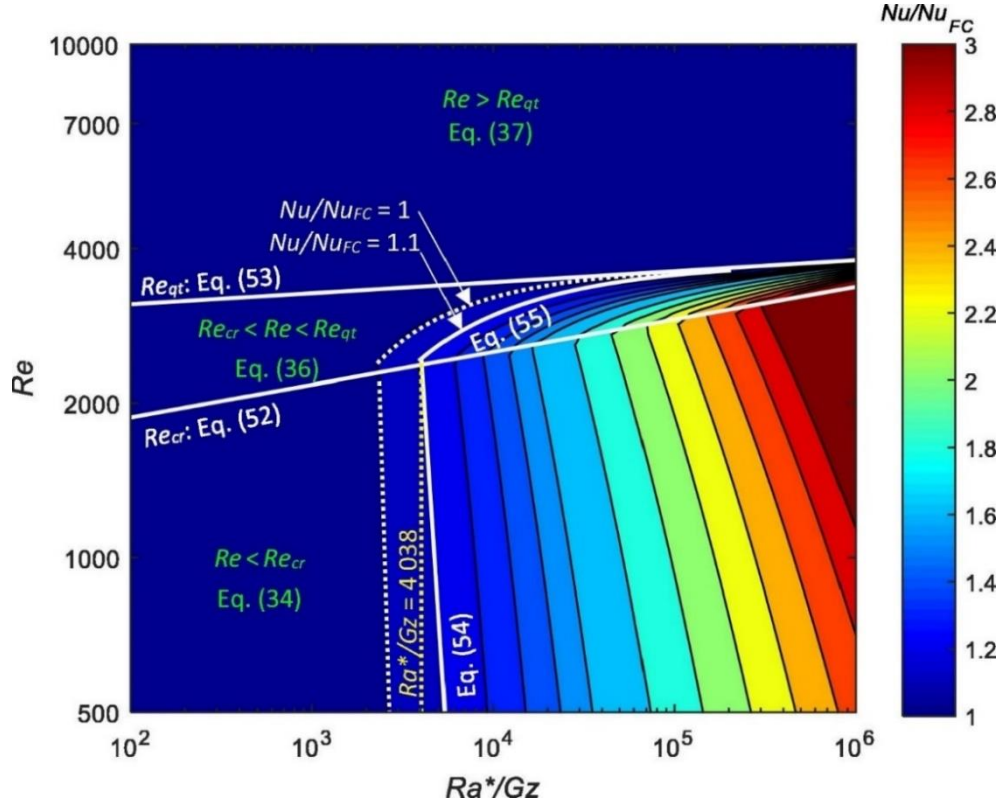


**Figure 1.8** Flow regime map for developing and fully developed flow as a function of  $Re$  and  $Ra^*/Gz$  in a horizontal tube (taken from Everts and Meyer [13])

## 1.5 Mixed convection criteria and flow regime maps

### 1.5.1 Free, forced, and mixed convection regime in a vertical tube

Free convection, characterized by  $Ra$ , when it is less than  $10^9$ , will behave like the laminar flow, and above which the flow becomes turbulent. The intermediate  $Ra$  near  $10^9$  lies in the transitional flow regime. Similarly, when  $Re$  is less than 2300 for a pipe, the flow is laminar, and above 4000, it will be turbulent. For  $2300 < Re < 4000$ , the flow undergoes a transition from laminar to turbulent. Likewise, for combined free and forced convection, when both  $Ra$  as well as  $Re$  are in the laminar zone, the mixed convection is said to be in pure laminar, and when both are in the turbulent zone, it is the case of pure turbulent mixed convection. The only flow regime map given by Metais and Eckert [3] (Figure 1.3) is applicable for a vertical tube subjected to uniform wall temperature and uniform heat flux conditions. The flow regime map depicts that even for low  $Re$  the flow can become turbulent at a considerable heat flux. The possible cases when either free convection is in laminar and forced convection is in a turbulent regime or vice-versa, the type of mixed convection still needs to be explored in detail. It has been explored in the present work, and details will be discussed in further chapters.

## 1.6 Applications of mixed convection

Fluid flow with heat transfer occurs in many industrial applications, such as pressurized water nuclear reactors, supercritical boilers, solar collectors, cooling of electronic equipment, extraction of geothermal energy, and heat exchangers. The process is called forced convection when the fluid motion is induced by some external means (fan, blower, pump, etc.). If it arises from an external force field (for example, gravitational, electric, and magnetic forces) acting on density gradients induced by the transport process, it is called free (or natural) convection. In real life, flow is driven simultaneously by external means and by a force field acting on density gradients, called mixed (or combined) convection. Due to the varying nature and enhanced heat transfer ability of mixed convection, it has significant importance in heat exchangers. In the design aspect of a heat exchanger, two critical parameters are. pressure drop and heat transfer rates. In laminar flow, both the pressure drop and the heat transfer coefficient are lower. In turbulent flow, although the heat transfer coefficient is higher compared to laminar case, the pressure drop is also higher. The higher pressure drop implies higher pumping power and not favourable from the viewpoints of energy requirements. Hence, after observing the pros and cons of the pressure drop and heat transfer coefficients in

the laminar and turbulent flow regimes, there must be a compromise between pressure drop and heat transfer in the transitional flow regime. Although heat exchangers usually operate in the laminar regime, the possibility to optimising the heat transfer with a minimum pressure drop in the transitional mixed convection regime leads us to investigate it further.

### 1.7 Organization of the thesis

The thesis is organized as follows:

- A brief introduction to the fundamentals of mixed convection, different flow regimes, its various types, and critical dimensionless parameters are discussed in Chapter 1.
- Chapter 2 provides a detailed literature survey on the theoretical, numerical, and experimental aspects of mixed convection flows through a pipe, duct, or channel. Based on the literature survey, research gaps were identified, and the objectives were defined.
- The numerical procedure, grid independence test, and validation of the numerical models in laminar, turbulent, and transitional mixed convection are presented in Chapter 3.
- The detailed experimental set-up design, procedure, data reduction technique, uncertainty analysis, and validation are explained in Chapter 4.
- The numerical and experimental results in the simultaneously developing laminar mixed convection regime and their comparison are discussed in Chapter 5.
- In Chapter 6, the numerical and experimental analysis of the laminar-turbulent transitional regime of mixed convection and their comparisons in terms of pressure drop and heat transfer are presented.
- Chapter 7 describes the numerical and experimental results and their comparison for the simultaneously developing turbulent mixed convection flows.
- The summary of the present work, concluding remarks, and its future scope are presented in Chapter 8.

## 1.8 Conclusions

## 1.8 Conclusions

An overview of mixed convection, followed by the relevant non-dimensional parameters, was discussed. The importance of developing flow and different flow regimes were also explained. The application, motivation, and the chapter-wise organization of the thesis are elucidated. The present thesis aims to investigate the pressure drop and heat transfer phenomena in the simultaneously hydrodynamically and thermally developing laminar, transitional, and turbulent mixed convection flows in a vertical tube subjected to a constant heat flux boundary condition. Furthermore, it investigates the effect of Grashof number ( $Gr$ ), Reynolds number ( $Re$ ), and Richardson number ( $Ri$ ) on the pressure drop and heat transfer for both buoyancy-assisting and buoyancy-opposing flows. In addition to it, the effect of heat flux (hence  $Gr$ ) on the entrance length for both buoyancy-aided and opposed flows have been explored. Apart from these, the correlations of friction factor ( $f$ ) and Nusselt number ( $Nu$ ) with the governing parameters like  $Re$ ,  $Gr$  and  $Ri$  applicable for developing as well as developed flow have been produced in laminar, transitional, and turbulent flow regimes. Finally, the numerical results were validated with my experimental results.

### Literature Review and Objectives

---

This chapter focuses on the previous analytical, computational, and experimental studies of mixed convection in vertical and horizontal pipes, channels, and ducts. Based on the literature survey I have highlighted the research gaps and identified the research scope and objectives of the thesis. I have categorized the literature survey as (i) laminar (ii) turbulent, and (iii) transitional mixed convection.

#### 2.1 Laminar mixed convection

It can be safely said that when both Reynolds number,  $Re$  (for forced convection) and Rayleigh number,  $Ra$  (for natural convection) are in the laminar regime, the mixed convection is also laminar. The distortion of the velocity field and the pattern of the convection in the fluid decides the heat transfer enhancement or impairment in the case of aiding and opposing laminar mixed convection.

##### 2.1.1 Analytical studies on laminar mixed convection

In laminar flow, variations of density and viscosity with temperature affect the flow dynamics and heat transfer rate. From the mid-20<sup>th</sup> century, Martinelli and Boelter [15], Hallman [16], Hanratty *et al.* [17], Morton [18], and many others started analyzing fully developed laminar mixed convection flow models. They could only describe the variation of density and viscosity for a fully developed model during heating and cooling in a vertical tube with the isothermal wall. After that with the emergence of computers, attempts were made to obtain solutions for the developing flow. Rosen and Hanratty [19] used the boundary layer integral method and power series to obtain the temperature and velocity profiles following earlier work by Pigford [20]. Chen *et al.* [21] suggested that the buoyancy effect and forced flow enhance the heat transfer by ~20 percent for both pure forced and pure free convection. Boulama and Galanis [22] also presented exact analytical solutions for upward fully developed steady-state laminar mixed convection flow between two vertical parallel plates. The velocity profile, temperature profile, friction coefficient, and Nusselt number results show that in the uniform wall temperature (UWT) case, it depends on a single parameter called combined buoyancy

## 2.1 Laminar mixed convection

parameter:  $(Gr_T + Gr_M)/Re$  and in uniform heat flux (UHF) case it depends on three parameters:  $Gr_T/Re$ ,  $Gr_M/Re$ , and  $q_1/q_2$ . Solutions also revealed that the UHF case is valid when the net heating effect is positive. The various plots depict that there is a significant improvement in the heat transfer rate near the walls due to the buoyancy effect. The flow reversal phenomena and heat transfer characteristics of the fully developed laminar flow mixed convection in vertical heated channels were analyzed analytically by Cheng *et al.* [20]. The velocity distribution, temperature distribution as well as Nusselt number ( $Nu$ ) variation exhibit a flow reversal near the colder wall within the channel below the threshold value of  $Re/Gr$  ( $\approx 2.5 \times 10^4$ ). Analytical solutions for mixed convection in a vertical micro-channel along with numerical results using Lattice Boltzmann Method (LBM) were obtained by Avramenko *et al.* [21]. The velocity profiles, temperature profiles, and Nusselt number variations showed that the effect of the Knudsen number ( $Kn$ ) was more pronounced near the wall. The increase in  $Kn$ , attributed to the increase in temperature on the wall and deteriorating heat transfer. In contrast, near the centreline, Rayleigh number ( $Ra$ ) effect was more substantial. This is because higher Rayleigh numbers increase the velocity gradient at the wall, exhibiting a point of minimum velocity at the centerline of the channel.

### 2.1.2 Computational studies on laminar mixed convection

Numerical solutions of heat transfer for the upward flow of air by taking variable physical properties with uniform wall temperature were obtained by Boulama and Galanis [22]. The numerical models for developing mixed convection flow taking account of variations of density and viscosity was also developed by Lawrence and Chato [26] and by Marner and McMillan [27] for the same boundary conditions. An interesting result was presented, which indicates that the local Nusselt value increases near the point of maximum velocity distortion (the point where minimum centerline velocity is obtained after deviation from the parabolic velocity profile) with the thermal entry length and then decreases further downstream as the fluid and wall temperature difference minimizes. Zeldin and Schmidt [28] used an iterative method and solved the full elliptic equations to avoid marching procedures. They inferred that the velocity profile differs from the forced convection and the maximum velocity may not occur at the centreline ( $r \approx 0.85$ , if  $r = 0$  at the centerline). In buoyancy-aiding flow, the velocity near the wall increases due to the difference in the wall and fluid temperature and decreases at the center. Hence the heat transfer coefficient increases, and the



velocity profile changes significantly from parabolic shape. In buoyancy-opposing flow, the velocity reduces near the wall, and hence heat transfer decreases. The velocity gradient at the wall approaches zero causing flow reversal locally. Tanaka *et al.* [29] predicted a fully developed upward flow by  $\kappa - \varepsilon$  turbulence model in a heated vertical pipe and compared with experimental results of nitrogen gas as a test fluid. The hot-wire measurements in the experiments demonstrate a complete laminarization at  $Re=3000$ . A numerically predicted regime for mixed convection was plotted between the Reynolds number ( $Re$ ) and Grashof number ( $Gr$ ). The upper left part (Figure 2.1) represents the forced convection regime, and the lower right part (Figure 2.1) endorses natural convection. Various analytical investigations demonstrate that pressure drop is significantly affected by heat transfer and vice versa. Semi-empirical correlations for pressure drop were developed by Joye [30]. The equations are valid for laminar, constant wall temperature boundary conditions in vertical, internal aiding flows. The measurement of pressure drop is quite difficult in vertical mixed convection, particularly for liquids. Hence a correction factor needs to be applied due to the density difference of fluid in the manometer and the conduit.

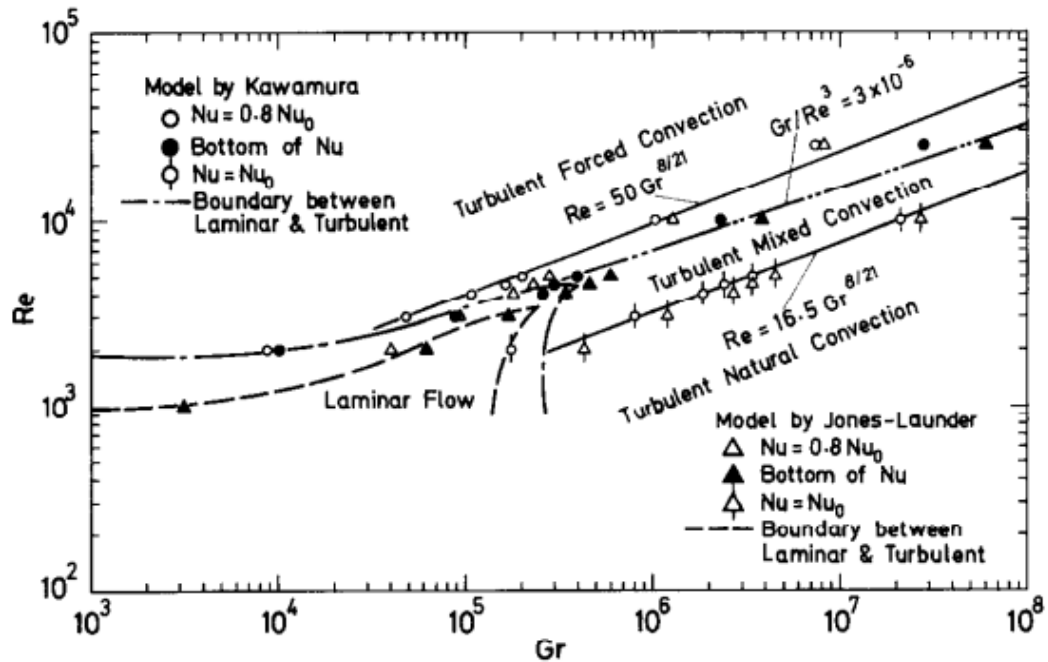


**Figure 2.1** Predicted flow regime map for combined free and forced convection in a vertical tube (taken from Tanaka *et al.* [29])

Compound effects of shear and buoyancy for mixed convection in a 2D enclosure were numerically studied by Onyejekwe [31]. It was found that the core flow is sensitive to the boundary conditions and the movement of the walls. Under the effect of aiding

## 2.1 Laminar mixed convection

buoyancy, mixed convection flow and heat transfer around a long cylinder of the square cross-section were investigated in the vertical open configuration by Sharma *et al.* [32]. The local and average  $Nu$  were calculated to make a thorough study of heat transfer and it was observed that it increases with the increase in  $Ri$  and/or  $Re$ . The mixed convection distorts the streamline and isotherms and increases the drag coefficient, increasing the heat transfer rate. Al-asadi *et al.* [33] illustrated the characteristics of heat transfer and fluid flow in an inclined circular pipe for nanofluids. They found that the wall shear stress and velocity increases as the  $Re$  increases, while the surface temperature decreases. Furthermore, they inferred that the surface temperature increases as the inclination angle increases, and the heat transfer is enhanced in assisting flow compared to opposing flow. Many problems which were very difficult to solve analytically became simple with the advent of powerful computers and various software packages like ANSYS-Fluent, COMSOL Multiphysics, OpenFOAM, etc. Among various research works on laminar mixed convection, one was by Balaji *et al.* [34]. They obtained correlations for the average Nusselt number by a general methodology called Asymptotic Computational Fluid Dynamics (ACFD) to disturb the limiting solutions of forced and natural convection. This methodology was first developed by Gersten and Herwig [35]. Because of its asymptotic correctness, this approach worked well and was also physically consistent. In coaxial double duct heat exchangers, an experimental and numerical study of mixed convection with flow reversal was carried out by Mare *et al.* [36]. Velocity vectors of water in a vertical parallel ascending flow in a heat exchanger were determined by Particle Image Velocimetry (PIV) technique experimentally. They were in excellent agreement with the numerical results. Both numerical and experimental observations showed that the flow reversal occurs simultaneously in the inner tube and the annulus for heating and for cooling of the flow, which must be avoided for affecting the flow stability and heat transfer. Fu *et al.* [37] also numerically investigated the reversal of mixed flow in three-dimensional vertical rectangular channel. The compressibility of fluid was considered, which means the Boussinesq approximation is no longer valid. They found that at high  $Ri$ , the natural convection governs the flow and thermal field, ultimately triggering the flow reversal mechanisms.

### 2.1.3 Experimental studies on laminar mixed convection

Any experimental work in natural convection is difficult to perform due to the low range of velocities. This is even more complex in mixed convection because of the free

convection effect that is induced along with forced flows. Since earlier studies didn't measure all the wall temperatures, which causes problems in determining the Nusselt number accurately. Hallman [38] carried out experimental study on laminar mixed convection in a vertical tube of test section approximately ~36 inches in length with 58 thermocouples. The aim was to examine the transition, limiting case for pure laminar forced convection and the thermal entrance effects. This study concluded that the solutions are applicable at far from the entrance for positive values of  $Ra$  and may be for small negative  $Ra$  value. However not much could be obtained from experiments regarding transition to turbulent flow for large negative Rayleigh number and the unsteady case. Joye [39] compared the existing correlations with his experimental investigation for opposing flow in mixed convection in a vertical tube for various  $Gr$  and a range of  $Re$  (700 – 25000). The mixed convection region exists between  $Re$  values of 4,000 and 10,000. Correlations for  $Nu$  presented by [40] for opposing flow, predicted quite similar results except for the region  $Re < 4000$ . It was observed that  $Nu$  reduces as the  $Gr$  reduces in this range of  $Re$ . To study the local and average heat transfer for hydrodynamically fully developed, thermally developing and fully developed laminar air flow inside a horizontal circular cylinder, an experiment was conducted by Mohammed and Salman [41]. They found that the  $Nu$  increases as the heat flux increases. It was also concluded that free convection reduces the heat transfer at low  $Re$  and enhances for higher  $Re$ .

### 2.2 Turbulent mixed convection

Contrary to laminar mixed convection, when the Rayleigh number for free convection and Reynolds number for forced convection, both are in the turbulent regime, it is said to be turbulent mixed convection. The effects of buoyancy can be speculated very easily in laminar case whereas it is not so straightforward in turbulent flows. Detailed reviews were presented by Jackson *et al.* [1], Jackson [42], and Galanis and Behzadmehr [5] on turbulence and heat transfer characteristics in vertical passages.

## **2.2 Turbulent mixed convection**

### **2.2.1 Analytical studies on turbulent mixed convection**

Polyakov [43] discussed analytically the growth of secondary free convection currents in forced turbulent flows in horizontal pipes with weak thermo-gravitational effects. The results were compared with experimental data obtained for water flow and air flow, where substantial thermo-gravitational influence was present on turbulent flow and the heat exchange. The overall resistance to the momentum and heat transport in turbulent forced and mixed convective flows was treated by employing “wall functions” to the thin near-wall viscosity affected sub-layer by Craft *et al.* [44]. Wall functions are of different types, its purpose is to solve the differential equations across the sub-layer with some algebraic formulae or low-cost routes. Their aim was to accurately model the flow in viscosity-affected-sub-layer region in a suitable form for use in CFD. Suga *et al.* [45] improved the performance of analytical wall-functions (AWF) developed by Craft *et al.* [46] while predicting the turbulent heat transfer for recirculating and impinging flows. To account the variations of parameters they introduced a functional behavior into the coefficient of eddy viscosity of AWF which was also validated for different flows.

### **2.2.2 Computational studies on turbulent mixed convection**

Supercritical boilers in power plants and supercritical water in cooling nuclear reactors make turbulent mixed convection essential to study. Studies on supercritical pressure found huge loss of heat transfer for upward flow near critical point in heated tubes. The effect was named “pseudo-boiling” and thought it to be like film-boiling. Through experiments by Shitsman [47], [48] and Jackson *et al.* [49], it became clear that the effect is due to buoyancy and not due to film-boiling. The localized heat impairment is not only limited to fluids at supercritical pressure, but can occur also for liquids and gases at normal pressure alike the experimental results by Hall and Price [50], Steiner [51], Kenning *et al.* [52] and Fewster [53] etc. An early study by Hsu and Smith [54] showed unpredicted patterns and mentioned that the heat transfer coefficient in upward heated turbulent mixed convection is less as compared to forced convection alone. In fact, for downward flow in heated tubes, buoyancy force enhances the turbulent properties causing a higher heat transfer coefficient than the forced flow alone. In conclusion, as the buoyancy becomes more and more dominant, heat transfer for upward flow also increases with the same heat transfer coefficients for these two cases. Studies on turbulent mixed convection with water and air, show less indication of the influence of buoyancy on heat transfer. Using a variety of computational formulations and turbulence models, attempts were made to simulate buoyancy-induced turbulent

convective heat transfer in vertical tubes by Tanaka *et al.* [55]. They used modified Reichardt's eddy diffusivity model. Walklate [56] used both  $\kappa - \varepsilon$  models and mixing-length models to simulate the experiments of Carr *et al.* [57]. He found that the low  $Re$   $\kappa - \varepsilon$  models performed better than the mixing-length and standard  $\kappa - \varepsilon$  models. Launder and Spalding [58] numerically predicted a turbulent flow and recommended that turbulence models are best served as per the computational economy, range of applicability, and physical reality. Skiadaressis and Spalding [59] and Abdelmeguid and Spalding [60] predicted the flow and heat transfer characteristics for the turbulent flow of air in the developing and fully developed region of a circular horizontal pipe. They compared the numerical results with experimental data reported by [61] and [62] in fully developed flow and found them to be fairly good in agreement. Jackson *et al.* [40] examined low  $Re$   $\kappa - \varepsilon$  turbulence model of Launder and Sharma [63] for turbulent mixed convection of a developing air flow in vertical tubes. It was in good agreement with the experimental heat transfer data and flow profile measurements. It was also suggested that the low  $Re$  two-equation models make the simplest formulation for turbulent mixed convection flows. Further, Mikielwicz [64] carried out a relative study of the performance of various turbulence models and found that the low  $Re$   $\kappa - \varepsilon$  turbulence model as the most suitable model. After the 1980's, for better results, several upgraded turbulence models have been used. Large Eddy Simulations (LES) and Direct Numerical Simulations (DNS) are few of those methods. Kasagi and Nishimura [65] conducted one of the earliest studies of mixed convection in vertical channels with DNS. Simulations obtained with fixed  $Re$  and varying  $Gr$  provided detailed information with visualization than could be obtained with experiments. Later You *et al.* [66] conducted DNS study for at moderately low Reynolds number (2650) in a vertical heated tube with uniform physical properties and Boussinesq approximation. Kim *et al.* [67] assessed the performance of different turbulence models in buoyancy-aided turbulent mixed convection through vertical tubes and compared their results with the DNS results of You *et al.* [66].

### 2.2.3 Experimental studies on turbulent mixed convection

Despite the effort from Eckert and Diaguila [68], Brown and Gauvin [69], and Petukhov and Strigin [61] till 1970, the effect of buoyancy in vertical flows on heat transfer for turbulent flow was still unclear. Thereafter, Carr *et al.* [57] carried out experiments for aiding air flow in a vertical pipe and velocity profile, temperature profile and turbulence

## 2.2 Turbulent mixed convection

quantities using hot-wire anemometry. It was found that with increasing heat flux, the free convection effect causes distortion (the position of maximum velocity moving from the tube center to a position near the wall) in the flow structure. In addition, with increase in heat flux, decrease in turbulent shear stress, and increase in the width of viscous sublayer were also observed. Vilemas *et al.* [65] performed an experimental investigations of local heat transfer in a vertical gas-cooled tube for turbulent mixed convection. Correlations were obtained to calculate local heat transfer along the tube for weak and strong buoyancy effects, but these are unable to provide much information in the intermediate region. Parlattan *et al.* [71] investigated friction factor and heat transfer coefficient experimentally in aiding and opposing turbulent mixed convection conditions for flowing water in a vertical tube. Jackson *et al.* [72] investigated the turbulent mixed convection effect in a vertical heated pipe with sodium as a working fluid. The behaviour in results were found to be opposite to a high Prandtl number fluid such as mercury. The heat transfer is enhanced in aiding flow and impaired in opposing flow. Celata *et al.* [73] investigated the forced and mixed convective flow of water upwards in a heated pipe experimentally. The results confirm that the heat transfer deterioration takes place in an upward heated flow due to the laminarization effect in near-wall region. The heat transfer decreases as the length to diameter ratio increases. This reduction is maximum when the buoyancy parameter ( $Bo$ ) is near to unity. Ghajar and his co-workers [74]–[77] performed extensive experiments on horizontal tubes to find out the effect of different inlet geometries and heating on friction factor and heat transfer in the transitional and turbulent regimes. Aicher and Martin [71] summarizes experimental results for both aiding and opposing flow conditions and furnishes own experimental results influencing length-to-diameter ratio on heat transfer in vertical tubes. Finally, they provided a new empirical correlation that provides better results than all available correlations. Few studies [79], [80] worked on the prediction of heat transfer by Artificial Neural Network (ANN) to get a more accurate correlation. Following Ghajar's work, Meyer and his co-workers [81]–[83] performed experiments mostly on horizontal tubes and in a few cases on vertical tubes to analyze the effect of inlet geometries and heating on the pressure drop as well as heat transfer in laminar, transitional, quasi-turbulent and turbulent flow regimes. The quasi-turbulent regime is the end of the transitional and prior to the start of the turbulent flow regime. The flow characteristics in quasi-turbulent regime are not exactly same as turbulent flows. The friction factor

and Nusselt number in the quasi-turbulent flow regime are overpredicted by the existing friction factor and heat transfer correlations of turbulent flow.

### 2.3 Transitional mixed convection

It can be said that the fluid flow and heat transfer characteristics in laminar and turbulent mixed convection are reasonably well understood theoretically, numerically, and experimentally. Literature available where the transition from laminar to turbulent mixed convection occurred is scarce. However, with the effort of a few researchers' various numerical models and correlations has been developed to know about the heat transfer behaviour and its characteristics in this regime.

#### 2.3.1 Analytical studies on transitional mixed convection

Since transition is a phenomenon which can be observed just beyond or close to a certain critical parameter, no such analytical formulation can be made. Hence the studies concentrated on results of simulations and experiments only.

#### 2.3.2 Computational studies on transitional mixed convection

Numerical studies by Behzadmehr *et al.* [84], [85] for upward mixed convection of air flow in a long vertical tube were conducted for two values of  $Re = 1000$  and  $1500$ , and a range of Grashof number ( $Gr \leq 10^8$ ) by using low  $Re$   $\kappa - \varepsilon$  turbulence model with Boussinesq approximations. Corresponding to laminar-turbulent transition and laminarization of the flow, two critical  $Gr$  were identified for each  $Re$ . The critical values observed from laminar to turbulent condition i.e.  $Gr = 8 \times 10^6$  for  $Re = 1000$  and  $Gr = 2 \times 10^6$  for  $Re = 2000$ , were in good agreements with the study of Metais and Eckert [3]. Finally, for  $Gr = 7 \times 10^7$  the fully developed flow field became turbulent for  $Re = 1500$  and laminar for  $Re = 1000$ . This transition from turbulent to laminar is called relaminarization and was due to the laminarization of buoyancy induced acceleration. A correlation had been developed for fully developed upward mixed convection in vertical tubes with uniform heat flux which was valid for both laminar and turbulent conditions within a range:  $1000 \leq Re \leq 1500$ . Tam and Ghajar [86] examined many experimental works and collected data points to know in detail the heat transfer behavior in the transition region under a uniform wall heat flux boundary condition for plain horizontal tubes. Also, many correlations were

### 2.3 Transitional mixed convection

recommended for different regimes to predict the heat transfer. Among them Tam and Ghajar [79] provided the most accurate correlation as indicated below in Eqs. (2.1)-(2.3), following a popular correlation obtained by Churchill [87] mentioned in Eq. (2.4). Finally, a flow regime map was presented to determine the boundary between forced and mixed convection in horizontal tubes having different inlet configurations.

$$Nu_{trans} = Nu_l + \{\exp[(a - Re)/b] + Nu_t^c\}^c \quad (2.1)$$

$$Nu_l = 1.24 \left[ \left( \frac{RePrD}{x} \right) + 0.025(GrPr)^{0.75} \right]^{1/3} \left( \frac{\mu_b}{\mu_w} \right)^{0.14} \quad (2.2)$$

$$Nu_t = 0.023Re^{0.8}Pr^{0.385} \left( \frac{X}{D} \right)^{-0.0054} \left( \frac{\mu_b}{\mu_w} \right)^{0.14} \quad (2.3)$$

$$Nu^{10} = Nu_t^{10} + \left[ \frac{\exp[(2200-Re)/365]}{Nu_{tc}^2} + \frac{1}{Nu_t^2} \right]^{-5} \quad (2.4)$$

Poskas *et al.* [88] used turbulence transition models with ANSYS-Fluent and investigated the opposing mixed convection heat transfer in an inclined flat channel. The numerical modelling results were in good agreement with the experimental heat transfer results of Poskas *et al.* [89], performed with the same boundary conditions. They reported the presence of asymmetrical velocity profiles in the channel due to formation of vortices. The parameters responsible for this was not only the buoyancy parameter alone but also the length of the channel. As the influence of buoyancy parameter becomes stronger, the instability increases, and the flow becomes turbulent. The author had performed modelling using different laminar and transitional turbulence models:  $\kappa - \kappa_l - \omega$ , Shear Stress Transport (SST) and Reynolds stress- $\omega$  model. After the analysis it was concluded that in case of laminar model for low and high  $Re$  number the vortices are formed at the beginning of the heated part and diminished downstream the channel. Abdollahzadeh *et al.* [90] used RANS models for numerical simulations of laminar-turbulent transition in convection heat transfer. They compared different turbulence models used for the simulation of transition heat transfer in mixed convection between two flat plates. The effects of inlet velocity, inclination angle, heated wall temperature and Richardson number on the flow features and heat transfer rate were studied in detail. It was found that the increase in inlet velocity initially promotes the transition and further increase of it delays the transition. Also increase in inclination angle delays the transition point whereas increase of wall temperature and Richardson number accelerates it. When inclination increases, the magnitude of buoyancy force which causes a delay in transition.



### 2.3.3 Experimental studies on Transition

Based on the experimental results, Kemeny and Somers [91] concluded that the transition occurs normally, either by a reversal in wall temperature or a smaller rise in temperature than expected as the distance from the entry increases. Metais and Eckert [3] provided a flow regime plot between  $Re$  and  $GrPrD/L$  based on the available experimental data to demarcate laminar, turbulent, and transitional regimes for free, forced, and mixed convection flows in a vertical tube. This is applicable for both uniform heat flux and uniform wall temperature boundary conditions. Barozzi *et al.* [92] reported experimentally and numerically the effects of sharp entry and transition effects for laminar combined convection in vertical tubes. They also investigated a possible criterion of transition based on the axial location of minimum Nusselt number. Ghajar and his co-workers [74]–[77] investigated extensively the effect of different inlet geometry, heating and Prandtl number ( $Pr$ ) on the laminar-turbulent transition of mixed convection in a horizontal tube. It was found that the transition was delayed for smoother inlet geometries as well as increasing the heat fluxes. Flow regimes demarcating the boundary between forced and mixed convection was also shown for different inlet configurations (re-entrant, square-edged, and bell mouth). Grassi and Testi [93] performed experiments for developing upward flow in a circular duct under transitional mixed convection. Heat transfer loss was observed due to laminarization of the turbulent flow, which was characterized by two non-dimensional numbers, Graetz number ( $Gz$ ) and Grashof number. The heat transfer along the tube showed a non-monotonic, transitional behaviour with minimum at laminarized zone. Behzadmehr *et al.* [94] performed an experimental study to investigate the onset of laminar-turbulent mixed convection transition phenomena in a vertical heated tube. This article dealt with the nature of temperature and velocity variations using experimental data obtained at  $Re=1000, 1300$ , and  $1600$  for a wide range of  $Gr$ . Observing the average temperature at the center of the tube, a point of deviation was detected for a value of  $Gr/Re > 1500$  indicating the periodic thermal instability. In a vertical flat channel the local opposing mixed convection heat transfer was experimentally investigated by Poskas *et al.* [89] with symmetrical heating in a laminar–turbulent transition region. The results showed that there was a notable increase in heat transfer with the air pressure and the heat transfer was much more intense in the vortex flow region than it was in the case of turbulent forced convection.

## 2.4 Summary and research scope

Poskas *et al.* [95] investigated experimentally buoyancy opposing mixed convection heat transfer at different air pressures (0.1-0.4 MPa) in a vertical flat channel in the transition region. They found that the critical Reynolds number increases with the increase in buoyancy.

Following Ghajar's work, Meyer and his co-workers [2], [96]–[98] experimentally investigated the heat transfer characteristics of simultaneously developing and fully developed flow in the laminar, transitional, quasi-turbulent, and turbulent regime of mixed convection flows through horizontal tubes. It was observed that the  $Re$  at which the transition started was independent of the axial position and that the transition occurred at the same time over the entire tube length. However, the end of transition was dependent on axial position and occurred earlier as the flow approached fully developed. Apart from that, another finding was that the free convection effect aids a faster transition from laminar to turbulent. It was also said that heat transfer characteristics observed were much different in developing flow as that of fully developed flow. Bashir [97], Bashir *et al.* [98] and Meyer *et al.* [99] investigated the heat transfer and pressure drop in forced and mixed convection respectively in a vertical tube. It was found that for fully developed vertical flow the transition was delayed as compared to the horizontal flow, where the secondary flow caused earlier transition. However, their study was focussed on fully developed flow only. The hydrodynamic and thermal behaviour in a vertical tube will be different from that of horizontal tubes. Having said that, the friction factor, and the heat transfer phenomenon in a simultaneously hydrodynamically and thermally developing transitional regime of mixed convection flow through a vertical tube is still elusive.

## 2.4 Summary and research scope

Heat transfer by combined forced and natural convection, commonly known as mixed convection occurs both in natural and engineered systems. Due to its complex nature and limited applicability the studies in mixed convection are few and far between in literature. The detailed literature survey provides a comprehensive overview of the compelling research in the field of mixed convection over half a century because of the enhanced heat transfer ability of combined free and forced convection as compared to that of free and forced convection alone. This Chapter covers analytical, numerical, and experimental studies associated with laminar and turbulent mixed convection in detail.

Apart from that, numerical and experimental studies related to laminar-turbulent transition are also discussed. The first observation is that there is ample amount of analytical as well as experimental work present associated to laminar and turbulent mixed convection. However, an acceptable and concrete criterion corresponding to the laminar-turbulent transition in mixed convection is still difficult to find. Detailed reviews in mixed convection till date were presented by Jackson *et al.* [37], Galanis and Behzadmehr [5], Poskas and Poskas [100], Dawood *et al.* [101], Ghajar *et al.* [7], and Everts and Meyer [6] leads to the research scope to work further.

Literature available for the transition from laminar to turbulent mixed convection are very less in number. Also, analytical formulation can't be made for laminar-turbulent transition, hence studies were focused on computational and experimental observations of this phenomenon. Thus, it can be said that the physics of flow and heat transfer in laminar mixed convection is reasonably well understood. However, in comparison the studies on turbulent mixed convection appear to be less conclusive. The search for an appropriate wall function remained the dream of all researchers in this field. It appears that there does not exist any universal wall function since the two regimes of forced and natural convection are physically quite different processes and their interaction does not have any general feature. On the other hand, using brute force computing such as LES and DNS are also not bringing any better understanding of turbulent mixed convection at higher Reynolds numbers. Even for low Reynolds number a huge computational power and time is needed. Under the circumstances experiments appears to be the way out where the flow features and vortex characteristics can be revealed through advanced experimental techniques such as interferometry or PIV. A clear and acceptable criterion behind laminar-turbulent conversion of mixed convection for simultaneously hydrodynamically and thermally developing flow in a vertical tube is still evasive. The experimental studies are often in patches with limited ranges of Rayleigh, Reynolds, and Richardson numbers. There is a need to carry out comprehensive experiments with wide range of these parameters for both aiding and opposing flows to indicate any absolute criteria for the transition.

### 2.5 Objectives of the present study

The main objectives based on the gap identified from the literature survey are as follows:

## 2.5 Objectives of the present study

1. To analyse the effect of  $Re$ ,  $Gr$  and  $Ri$  numerically on the fluid flow and heat transfer in the simultaneously developing regime of laminar mixed convection flows in a vertical tube.
2. To investigate numerically the heat transfer, pressure drop, and flow characteristics in the turbulent mixed convection regime, considering assisting and opposing buoyancy effects.
3. To numerically investigate the flow characteristics in the transitional mixed convection regime with assisting and opposing buoyancy effects.
4. To design and build an experimental set-up to perform experiments in the developing regime of laminar, transitional, and turbulent mixed convection flows through a smooth vertical tube to investigate the effect of free convection on pressure drop and heat transfer.
5. Experimental investigation of heat transfer and pressure drop in the laminar-turbulent transitional regime of mixed convection for both aiding and opposing flows.
6. To study the effect on hydrodynamic and thermal entry length with the variation of  $Gr$ ,  $Re$ , and  $Ri$  in the laminar, transitional, and turbulent regimes for both buoyancy-aided and opposed mixed convection flows.
7. To develop correlations of  $f$  and  $Nu$  with the governing parameters such as  $Re$ ,  $Gr$ ,  $Pr$ ,  $Ri$  in the laminar, transitional, and turbulent regime of mixed convection flow in a vertical tube.

## 2.6 Scope of the present work

The aim of the present work is to reveal the physics of the simultaneously developing laminar-turbulent transitional regime of mixed convection flow through a vertical pipe subjected to constant heat flux boundary condition. Instead of a complex geometry a circular tube is used for the present numerical as well as experimental study which is commonly used in heat exchangers in industries. Based on the efficacy of the different numerical models and the computational resources available, the present numerical study was restricted to two- and three-equation RANS models. The 2D steady-state simulations were preferred over the 3D and transient simulations to reduce computational power while compromising the properties of the fluid invariant with respect to time. In numerical simulations, the length of the test section is not a matter of

concern, and a length-to-diameter ( $L/D$ ) ratio of 1000 is also considered for validation in the laminar mixed convection study. However, as per the availability of different tube materials on the market, a smooth stainless-steel (SS) tube of grade 316 L was chosen to avoid any corrosion over the period. The SS tube of length 1.3 m and diameter 0.01 m is chosen so that a length-to-diameter ratio of 130 will undergo developing flow, which is the prime focus of the present work. In addition to that, it will be sufficient to obtain the hydrodynamically fully developed condition for the validation of the experimental set-up. The present experiments are with normal water as the working fluid, which is normally used in the industries due to its high specific heat. The heating of the test section was done by the Joule heating method for which a low-voltage and high-current DC source was used. The experimental set-up was limited to performing the experiments of simultaneously developing forced, and mixed convection flow through a vertical tube with constant heat flux boundary conditions for a specified range of  $Re=500$  to  $15000$ ,  $Gr=10^3$  to  $10^8$ ,  $Ri=0$  to  $1.5$ , and  $Pr=3$  to  $7$ . Both assisting and opposing flow experiments can be performed with a provision to measure the inlet and outlet water temperature (using two PT 100), the tube wall temperatures (using eleven T-type thermocouples), the axial pressure drop between the inlet and outlet (using DPT) and the inside chiller water temperature. Apart from this, the flow behaviour (laminar, transitional, or turbulent) can also be visualized by sending a dye to the tube inlet. The visualization technique used here can provide data qualitatively rather than quantitatively.

### 2.7 Conclusions

In this chapter, the existing analytical, numerical, and experimental investigations in laminar, turbulent, and transitional mixed convection studies are discussed in detail. Based on the literature survey, the research scope was highlighted, and the objectives of the present work have been defined. At the end of the chapter, the scope of the present work is also explained.



# Numerical Methodology and Validation

---

### 3.1 Introduction

In this chapter, the numerical procedure to study the flow characteristics and heat transfer behaviour in the developing and fully developed regime of laminar, transitional, and turbulent mixed convection in a vertical tube considering the buoyancy-assisting and -opposing effects have been described. The governing and transport equations applicable for different models have been discussed. The numerical scheme used to solve by the laminar, transitional, and turbulence numerical models are explained here. Finally, the grid independency test followed by the validation of the numerical models in the laminar, transitional, and turbulent forced and mixed convection flows are presented.

### 3.2 Physical model

A vertical tube of diameter ( $D$ ) 0.01 m and length ( $L$ ) 5 m with negligible thickness has been modelled for the laminar mixed convection analysis as shown in Figure 3.1. The length-to-diameter ratio ( $L/D = 500$ ) was found to be sufficient for attaining the fully developed condition in the laminar flow. Since the entry length in case of turbulent flows is much shorter than that of laminar flow, the length-to-diameter ratio has been reduced from 500 to 150 for the simulation of turbulent flows. This will reduce the domain size and further the computational effort. As our focus was on developing flow, hence  $L/D$  of 150 has also been considered for the simultaneously developing transitional regime simulations. Because of the uniform heating from the side walls, both hydrodynamic and thermal boundary layers grow simultaneously from the entry of the tube. The geometry is symmetrical about the  $y$ -axis. The mirror image of the velocity and temperature profiles of the simulated portion will represent the complete profile of the tube. In case of buoyancy-assisting, the flow is in the upward direction against gravity (Figure 3.1(a)). In contrast, the flow is in downward direction along the gravity in buoyancy-opposing flow with heating from the side walls (Figure 3.1(b)). In Figure 3, positive  $x$ -direction is against the gravity and  $y$ -direction is along the transverse section

### 3.2 Physical model

of the pipe flow. The velocity components  $u$  and  $v$  are along the  $x$  and  $y$  directions respectively.

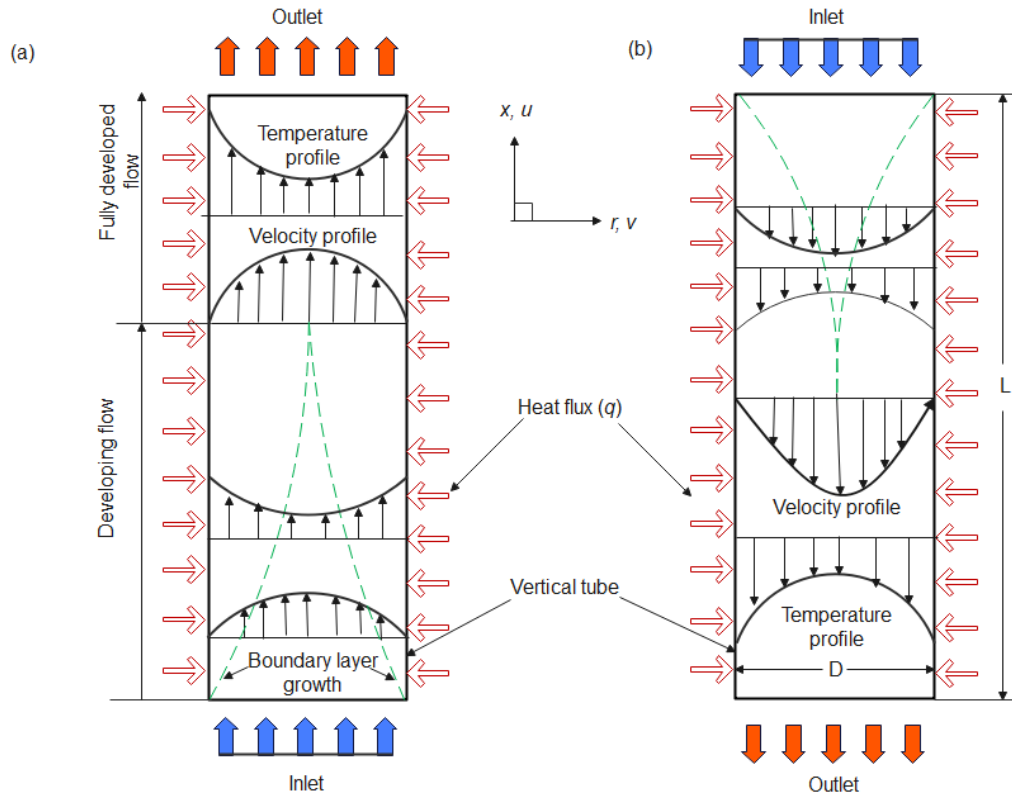


**Figure 3.1** Schematic diagram of (a) buoyancy-assisting and (b) buoyancy-opposing flow

### 3.3 Mathematical formulation for laminar mixed convection

The mathematical formulation for a steady state two-dimensional axisymmetric vertical tube with uniform wall heat flux boundary condition for a laminar flow is being discussed here. The working fluid was water, and the flow was assumed to be incompressible (Eqs. 3.1 and 3.2). Boussinesq approximation has been considered for the simulations. Thus, fluid properties were constant except the density in the body force term (last term in Eq. (3.3)) of momentum equation. The heat flux from the tube walls increases the fluid temperature near the walls. Consequently, the increase in temperature causes the decrease in density and induces the buoyancy effect. Hence, the buoyancy effect is implemented by use of the Eq. (3.5). At the inlet, the velocity is uniform across the tube cross section. At the exit, the pressure outlet boundary condition with zero-gauge pressure was implemented. Since the velocity at the outlet is unknown, this boundary condition is applied. The present study will highlight the results of simultaneously



hydrodynamically and thermally developing as well as fully developed flow through a vertical tube.

The governing equations in cylindrical coordinates for two-dimensional, steady, and incompressible flow are expressed as follows:

**Continuity equation:**

$$\frac{\partial(ur)}{\partial r} + r \frac{\partial v}{\partial z} = 0 \quad (3.1)$$

**Momentum equations:**

$$\text{Radial direction: } \rho \left( u \frac{\partial u}{\partial r} + v \frac{\partial u}{\partial z} \right) = -\frac{\partial p}{\partial r} + \mu \left( \frac{\partial^2 u}{\partial r^2} + \frac{1}{r} \frac{\partial u}{\partial r} - \frac{u}{r^2} + \frac{\partial^2 u}{\partial z^2} \right) \quad (3.2)$$

$$\text{Axial direction: } \rho \left( u \frac{\partial v}{\partial r} + v \frac{\partial v}{\partial z} \right) = -\frac{\partial p}{\partial z} + \mu \left( \frac{\partial^2 v}{\partial r^2} + \frac{1}{r} \frac{\partial v}{\partial r} + \frac{\partial^2 v}{\partial z^2} \right) - \rho g_z \quad (3.3)$$

**Energy equation:**

$$\rho c_p \left( u \frac{\partial T}{\partial r} + v \frac{\partial T}{\partial z} \right) = k \left( \frac{1}{r} \frac{\partial T}{\partial r} + \frac{\partial^2 T}{\partial r^2} + \frac{\partial^2 T}{\partial z^2} \right) \quad (3.4)$$

**Equation of state:**

$$\rho = \rho_i [1 - \beta(T - T_i)] \quad (3.5)$$

Boundary conditions applicable as per the problem statement are:

Inlet: Uniform inlet velocity,  $u = U_i$ ,  $v = 0$ ,  $T = T_i$  at  $z = 0$  and  $r = 0$  to  $R$ ;  $r = 0$  at centre and  $r = R$  at the wall.

Outlet: Pressure outlet boundary condition with  $p_g = 0$  at  $z = L$  and  $r = 0$  to  $R$

Tube walls: Constant heat flux,  $\dot{q} = Q_e/A_s$  at  $r = R$  and  $z = 0$  to  $L$

Tube axis: Symmetry condition,  $\frac{\partial u}{\partial r} = 0$ ,  $\frac{\partial v}{\partial r} = 0$ ,  $\frac{\partial T}{\partial r} = 0$  at  $r = 0$  and  $z = 0$  to  $L$

### 3.3.1 Numerical procedure

Before studying the influence of various parameters  $Re$ ,  $Gr$  and  $Ri$  on fluid flow and heat transfer characteristics, the 2D-axisymmetric computational domain with structured grids has been modelled in the Computational Fluid Dynamics (CFD) solver. The two-dimensional axisymmetric geometry of 1 mm wall thickness was modelled in the commercial software ANSYS-Fluent [102] as shown in Figure 3.2 (a). The thickness is negligible by considering the tube material as copper for which the temperature drops from the outer to the inner wall is minimal due to its high thermal conductivity. The meshing and subsequent simulation of one half of the vertical tube is sufficient for our studies in the laminar regime due to its symmetrical behaviour. Axial spacing between grids is uniform throughout the domain. Along the radial direction, the meshing was performed non-uniformly with finer grids near the walls for more

### 3.3 Mathematical formulation for laminar mixed convection

accurate simulations of velocity and temperature profiles at the wall boundary (Figure 3.2(b)).

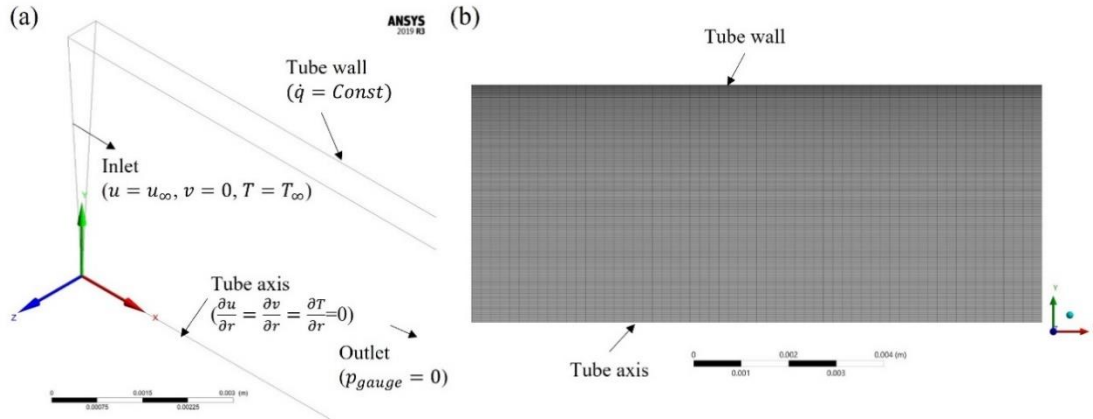


**Figure 3.2** (a) 2D axisymmetric model (b) structured mesh with fine grids near the tube wall

The steady state was applied in the pressure-based solver. The gravity direction is in the negative  $x$ -direction as per the coordinate system illustrated in Figure 3.2. The flow was laminar and incompressible. The inlet velocity was selected as per the  $Re$  we wanted to simulate. Water properties were taken at atmospheric pressure and at an inlet temperature of 20 °C. For  $100 \leq Re \leq 2300$ , the length-to-diameter ratio ( $L/D$ ) of 1000 was used to compare the results in the fully developed state. The  $Gr$  based on constant heat flux varies from  $10^3$  to  $7.935 \times 10^6$ . The corresponding  $Ri$  lies in between 0.1 to 1.5. The numerical solution is presented by solving the governing equations utilizing Finite Volume Method (FVM). In FVM, the partial differential terms of the governing equations are solved across a small volume surrounded by each node. The convective and diffusive terms are solved by second order UPWIND method while Semi-Implicit Pressure Linked Equations (SIMPLE) scheme is employed to solve pressure-velocity coupling. In upwind scheme, the upstream variables are used to calculate the derivatives in the flow field. That means the set of datapoints taken from the flow directions are used to calculate the derivatives more precisely. The semi-implicit method for pressure-linked equations usually refers to the pressure correction method. An initial value of pressure is considered, and the velocities are solved. Then these velocities are substituted in the conservation equation to satisfy. Upon solving, the difference is added to the velocities and substituted back into the momentum equations and solved for the pressure [103]. The pressure value is then corrected in the momentum equation, and the velocities are solved again. This process repeats till the continuity

equation is satisfied. These governing equations are solved till the convergence criteria are reached. The convergence criteria were set to  $10^{-4}$ ,  $10^{-5}$  and  $10^{-7}$  for continuity, momentum, and energy equation respectively [104].

**Grid Independence Test (GIT):** The grid independence test was conducted for four different grids as presented in Table 3.1. Input parameters affecting the computational domain are number of divisions in axial and radial directions and the radial bias factor. The bias factor can be defined as the ratio of the largest grid size to the smallest grid size. The output parameters have been taken as local centreline velocity and temperature at  $L/D = 450$ . The error considered in the output parameter is limited to 0.1 %. The optimum grid in radial and axial direction is found to be  $31 \times 30001$  ( $r \times z$ ). After obtaining suitable grids in axial and radial directions, the bias factor has been optimized. In Table 3.2, the bias factor of 15 in radial direction is found sufficient to counter the steep gradients in velocity and temperature profiles near to the tube walls considering less than 0.1 % error in the output parameters. From the grid independence study,  $31 \times 30001$  grid size with bias factor 15 has been chosen for further simulations.

**Table 3.1** Optimization of grids with  $L/D = 500$  at  $Ri = 1$  and  $Re = 250$

Sl. No.	Grid size ( $r \times z$ )	BF	Nodes	Elements	Centerline velocity (m/s)	% Error	Centerline temperature (K)	% Error
1	11×10001	5	110011	100000	0.037907	-	323.29	-
2	21×20001	5	420021	400000	0.038052	0.38	323.236	0.017
3	<b>31×30001</b>	5	930031	900000	0.038103	0.13	323.224	0.004
4	41×40001	5	1640041	1600000	0.038069	0.09	323.223	0.000

**Table 3.2** Optimization of bias factor with  $31 \times 30001$  grid size at  $Ri = 1$  and  $Re = 250$

Sl. No.	Grid size ( $r \times z$ )	BF	Nodes	Elements	Centerline velocity (m/s)	% Error	Centerline temperature (K)	% Error
1	31×30001	5	930031	900000	0.038103		323.224	-
2	31×30001	10	930031	900000	0.038264	0.421	323.223	0.000
3	31×30001	<b>15</b>	930031	900000	0.038303	0.102	323.223	0.000
4	31×30001	20	930031	900000	0.038302	0.002	323.226	0.001

The GIT has also been shown in a plot (Figure 3.3) between % error in the local centerline velocity and temperature with the increase in grid size. From Figures 3.3(a) and (b), it can be seen that the decrease in % error after grid size  $31 \times 30001$  is minimal.

### 3.3 Mathematical formulation for laminar mixed convection

Hence the grid size of  $31 \times 30001$  with a bias factor of 15 is considered as the optimum mesh.

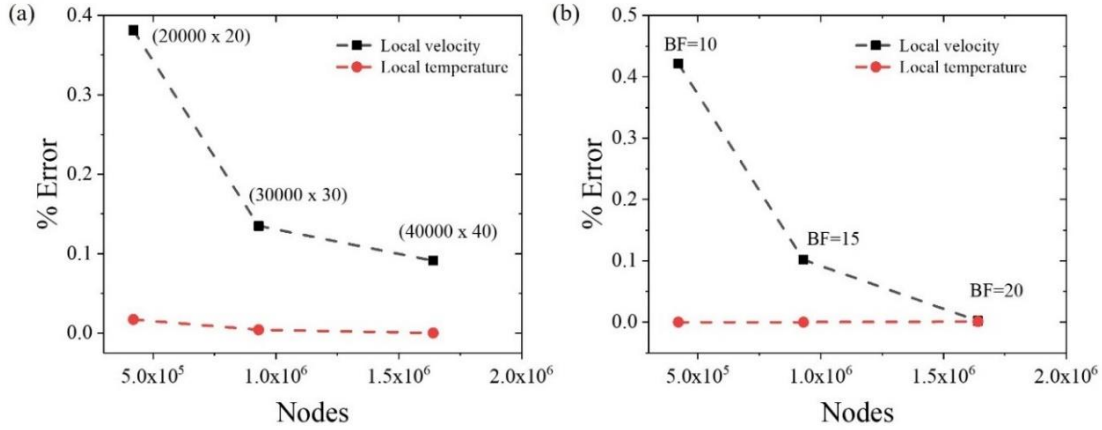


**Figure 3.3** Optimization of (a) grids and (b) bias factor (BF) with % error in centerline velocity and temperature at  $L/D=450$  for  $Re=250$  and  $Ri=1.0$ .

#### 3.3.2 Validation of laminar model

##### 3.3.2.1 Hydrodynamic validation

The fully developed friction factor  $f$  results obtained from the numerical model have been validated with the theoretical values of Hagen-Poiseuille flow ( $f = 64/Re$ ) [105] and the experimental data of Meyer *et al.* [99]. The validation results of buoyancy-aided and -opposed laminar tube flows are shown in Figure 3.4. The maximum deviation of friction factors is 1.3 % (Figure 3.4 (a)) for Hagen-Poiseuille flow and less than 2 % and 1 % for assisting and opposing flow (Figure 3.4 (b)) of laminar mixed convection respectively.

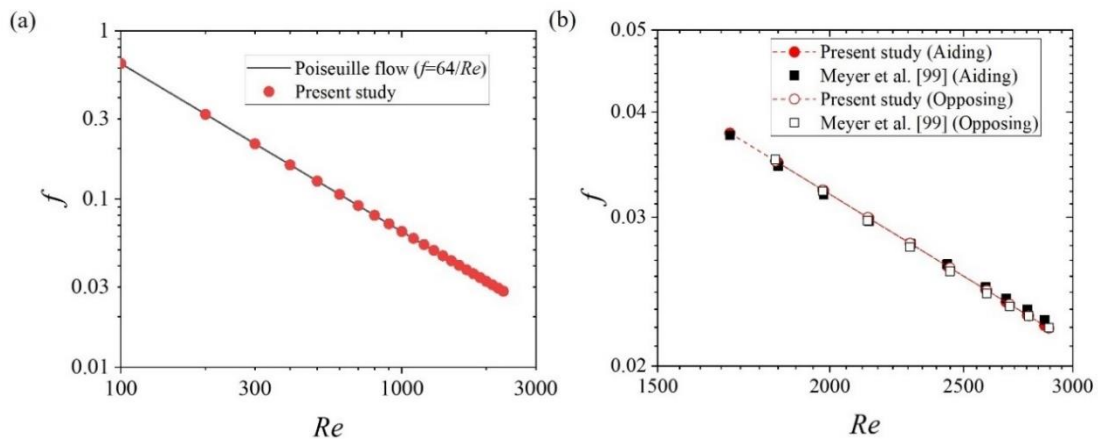


**Figure 3.4** Comparison of fully developed  $f$  with the (a) Hagen-Poiseuille flow (b) assisting and opposing flow of laminar mixed convection with Meyer *et al.* [99]

### 3.3.2.2 Thermal validation

The heat transfer results were compared with the  $Nu$  value for laminar fully developed forced convection flow at constant heat flux ( $Nu \approx 4.364$ ) [9] and the experimental outcomes of Bashir *et al.* [98] (Figure 3.5 (a)). The average fully developed  $Nu$  obtained in between  $L/D = 475$  and  $L/D = 858$  in Figure 3.5 (a) is 4.404 and 4.358 for upward and downward flow respectively, which is within 1 % of the value 4.364. The mixed convection results were also compared with the experimental results of Meyer *et al.* [99] in Figure 3.4 (b). The results are in satisfactory agreement with a maximum deviation of 5 %.

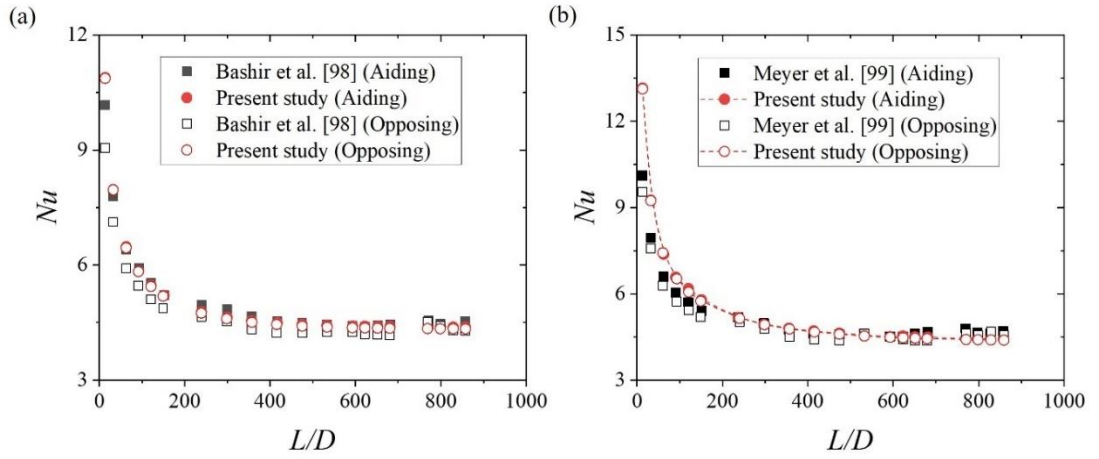


**Figure 3.5** Comparison of local  $Nu$  (a) assisting and opposing flow of laminar forced convection results at a heat flux 4.3 kW/m<sup>2</sup> and  $Re=1050$  with Bashir *et al.* [98] and (b) assisting and opposing flow of laminar mixed convection results at a heat flux of 6.5 kW/m<sup>2</sup> and  $Re=1600$  with Meyer *et al.* [99]

## 3.4 Mathematical formulation for transitional mixed convection

The mathematical formulation for a steady state two-dimensional axisymmetric vertical tube with uniform wall heat flux boundary condition for a transitional mixed convection flow is discussed here. The working fluid and the assumptions are like the laminar case. Except these, a vertical tube of diameter ( $D$ ) 0.01 m and length ( $L$ ) 1.5 m with a wall thickness of 0.001 m has been modelled for the analysis. The length-to-diameter ratio ( $L/D = 150$ ) will attain the developing flow in laminar and transitional mixed convection [106]. At the inlet, the turbulence intermittency is kept at 1 across the tube cross section and other boundary conditions are same as that of laminar flow.

### 3.4 Mathematical formulation for transitional mixed convection

The two-dimensional axisymmetric geometry modelled in ANSYS-Fluent [102] as shown in Figure 3.2. It consists of a vertical tube of radius 0.005 m and length of 1.5 m with wall thickness of 0.001 m as copper has been considered the tube material in the simulations.

The governing equations are expressed as follows:

$$\text{Continuity equation: } \frac{\partial(u_i)}{\partial x_i} = 0 \quad (3.6)$$

$$\text{Momentum equations: } \rho \left( u_j \frac{\partial(u_i)}{\partial x_j} \right) = -\frac{\partial p}{\partial x_i} + \frac{\partial}{\partial x_j} \left( (\mu + \mu_t) \frac{\partial u_i}{\partial x_j} \right) \pm \rho_i g_i \quad (3.7)$$

$$\text{Energy equation: } u_j \frac{\partial T}{\partial x_j} = (\alpha + \alpha_t) \frac{\partial}{\partial x_j} \left( \frac{\partial T}{\partial x_j} \right) \quad (3.8)$$

$$\text{Equation of state: } \rho_i = \rho_\infty [1 - \beta(T - T_\infty)] \quad (3.9)$$

In order to simulate the transition stage, we have adopted the transition SST model [88]. This model is a four equation model and blending of  $\kappa - \omega$  SST model [102] with the other two transport quantities: one for intermittency ( $\gamma$ ) and one for the transition onset momentum-thickness Reynolds number ( $Re_\theta$ ) as follows.

$$\frac{\partial(\rho \kappa u_j)}{\partial x_j} = \frac{\partial}{\partial x_j} \left[ \Gamma_\kappa \frac{\partial \kappa}{\partial x_j} \right] + \widetilde{G}_\kappa - Y_\kappa + S_\kappa \quad (3.10)$$

$$\frac{\partial(\rho \omega u_j)}{\partial x_j} = \frac{\partial}{\partial x_j} \left[ \Gamma_\omega \frac{\partial \omega}{\partial x_j} \right] + G_\omega - Y_\omega + D_\omega + S_\omega \quad (3.11)$$

$$\frac{\partial(\rho \gamma u_j)}{\partial x_j} = \frac{\partial}{\partial x_j} \left[ \left( \mu + \frac{\mu_t}{\sigma_\gamma} \right) \frac{\partial \gamma}{\partial x_j} \right] \frac{\partial \gamma}{\partial x_j} + P_{\gamma 1} - E_{\gamma 1} + P_{\gamma 2} - E_{\gamma 2} \quad (3.12)$$

$$\frac{\partial(\rho \widetilde{Re}_{\theta t} u_j)}{\partial x_j} = \frac{\partial}{\partial x_j} \left[ \sigma_{\theta t} (\mu + \mu_t) \frac{\partial \widetilde{Re}_{\theta t}}{\partial x_j} \right] + P_{\theta t} \quad (3.13)$$

Where,  $\widetilde{G}_\kappa = \min(G_\kappa, 10\rho\beta^*\kappa_\omega)$ ;  $G_\kappa = -\rho \overline{u'_i u'_j} \frac{\partial u_i}{\partial x_j}$ ,  $G_\omega = \frac{\alpha}{\nu_t} \widetilde{G}_\kappa$ ,  $\nu_t = C_\mu \frac{\kappa^2}{\varepsilon}$ ,  $\Gamma_\kappa = \mu + \frac{\mu_t}{\sigma_\kappa}$ ,  $\Gamma_\omega = \mu + \frac{\mu_t}{\sigma_\omega}$ ,  $Y_\kappa = \rho\beta^*\kappa_\omega$ ;  $\beta^* = 0.09$ ,  $Y_\omega = \rho\beta\omega^2$ ,  $\mu_t = \frac{\rho\kappa}{\omega} \cdot \frac{1}{\max[\frac{1}{\alpha^*}, \frac{S \times F_2}{a_1 \omega}]}$ ,  $\alpha_t = \frac{\nu_t}{Pr_t}$ ,  $Pr_t = 0.85$ ,  $\sigma_\gamma = 1.0$ ,  $P_{\gamma 1} = 2F_{length}\rho S[F_{onset}\gamma]^{c_{\gamma 3}}$ ,  $c_{\gamma 3} = 0.5$ ,  $S$  = strain rate magnitude,  $F_{length} = f(\widetilde{Re}_{\theta t})$ ,  $E_{\gamma 1} = \gamma P_{\gamma 1}$ ,  $P_{\gamma 2} = (2c_{\gamma 1})\rho\Omega\gamma F_{turb}$ ,  $c_{\gamma 1} = 0.03$ ,  $E_{\gamma 2} = c_{\gamma 2}\gamma P_{\gamma 2}$ ,  $c_{\gamma 2} = 50$ ,  $F_{turb} = e^{-\left(\frac{Re_t}{4}\right)^4}$ ,  $\sigma_\kappa = \frac{1}{F_1/\sigma_{\kappa,1} + (1-F_1)/\sigma_{\kappa,2}}$ ,  $\sigma_\omega = \frac{1}{F_1/\sigma_{\omega,1} + (1-F_1)/\sigma_{\omega,2}}$ ,  $S_{ij} = \frac{1}{2} \left( \frac{\partial u_j}{\partial x_i} + \frac{\partial u_i}{\partial x_j} \right)$ ,  $\alpha^* = \alpha_\infty^* \left( \frac{\alpha_0^* + Re_t/R_\kappa}{1 + Re_t/R_\kappa} \right)$ ,  $Re_t = \frac{\rho\kappa}{\mu\omega}$ ,  $R_\kappa = 6$ ,  $\alpha_0^* = \frac{\beta_i}{3}$ ,  $\beta_i = 0.072$ ,  $\widetilde{Re}_{\theta t} = f(I, \lambda)$ ,  $\sigma_{\theta t} = 2.0$ ,  $P_{\theta t} = c_{\theta t} \frac{\rho}{t} (Re_{\theta t} - \widetilde{Re}_{\theta t})(1 - F_{\theta t})$ ,  $c_{\theta t} = 0.03$ ,  $t = \frac{500\mu}{\rho u^2}$ ,  $F_{\theta t} = \min \left( \max \left( F_{wake} e^{\left(-\frac{\gamma}{\delta}\right)^4}, 1.0 - \left( \frac{\gamma - 1/50}{1.0 - 1/50} \right)^2 \right), 1.0 \right)$ ,  $F_{wake} =$

$$e^{\left(-\frac{Re_\omega}{1E+5}\right)^4}, \quad Re_\omega = \frac{\rho\omega y^2}{\mu}, \quad \delta = \frac{50\Omega y}{u}\delta_{BL}, \quad \delta_{BL} = \frac{15}{2}\theta_{BL}, \quad \theta_{BL} = \frac{\widetilde{Re_{\theta t}}\mu}{\rho u}, \quad I = \text{turbulent}$$

intensity,  $\lambda$  = scaler measure of the streamwise pressure gradient,  $F_1, F_2$  are blending functions,  $D_\omega$ =cross-diffusion term,  $S_\kappa = S_\omega = 0$  (there are no source terms)

Boundary conditions applicable are:

Inlet: Uniform inlet velocity,  $u = U_\infty, v = 0, T = T_\infty, \gamma = 1$  at  $x = 0$  and  $r = 0$  to  $R$ ;  $r = 0$  at centre and  $r = R$  at the wall.

Outlet: Pressure outlet boundary condition with  $p_g = 0$  at  $x = L$  and  $r = 0$  to  $R$

Tube walls: Constant heat flux,  $\dot{q} = Q_e/A_s, Re_\theta = 0$  at  $r = R$  and  $x = 0$  to  $L$

Tube axis: Symmetry condition,  $\frac{\partial u}{\partial r} = 0, \frac{\partial v}{\partial r} = 0, \frac{\partial T}{\partial r} = 0$  at  $r = 0$  and  $x = 0$  to  $L$

### 3.4.1 Numerical procedure

Following the same procedure as that of the laminar case, the grid independence test was conducted for four different grids  $31 \times 3001$ ,  $51 \times 5001$ ,  $101 \times 7501$ , and  $151 \times 10001$  ( $r \times z$ ). The error considered in the output parameter was limited to 0.1 %. The optimum grid was found to be  $101 \times 7501$ . After obtaining suitable grids in axial and radial directions, the bias factor has been optimized. The bias factor of 5 and 10 in the axial and radial direction respectively was found sufficient to counter the steep gradients in the developing and near the tube walls region.

In the present study, two transition models have been used to compare the results. The transition  $\kappa - \kappa_l - \omega$  (three-equation) and transition SST (four equation) models are compared [88] for the same case at  $Re = 2000$  and  $Ri = 0.1$ . The transition  $\kappa - \kappa_l - \omega$  model [107], an eddy viscosity type model, consists of transport equations for turbulent kinetic energy ( $\kappa$ ), laminar kinetic energy ( $\kappa_l$ ), and inverse of turbulent time scale ( $\omega$ ). This model is used to predict boundary layer development and calculate the transition onset. It can be beneficial to effectively address the transition from laminar to turbulent boundary layer. The transition SST model [108] is a coupling of  $\kappa - \omega$  SST and two other transport quantities named intermittency ( $\gamma$ ) and momentum thickness Reynolds number ( $Re_\theta$ ). This is used to model turbulent flows where significant proportion of the boundary layer is laminar. During the transition state, the flow switches between laminar and turbulent state intermittently [9]. To quantify the intermittent nature of the flow at a given location, the intermittency factor  $\gamma$  denotes the percentage of time the flow is laminar and turbulent. It varies from 0 to 1, for laminar  $\gamma = 0$  and for turbulent it is  $\gamma = 1$ . The transport equation (Eq. 3.12) for intermittency

### 3.4 Mathematical formulation for transitional mixed convection

comprises of production as well as destruction terms. The production term controls the length of the transition region, and the destruction term allows the boundary layer to laminarise by dissipating the intermittency fluctuations. The  $Re_\theta$  is the measure of the distance from the leading edge to the point where transition occurs. It indicates the onset of transition to turbulence. The Eq. 3.13 is linked with the intermittency equation. It consists of a production term ( $P_{\theta t}$ ) based on momentum thickness which is a correlation of blending functions ( $F_{\theta t}$ ,  $F_{length}$ ). These are calculated at each cell. When these blending functions past a threshold value, the production term ( $P_\gamma$ ) in the intermittency transport equation is switched on. The  $Re_\theta$  and its initial value is calculated using empirical correlations based on the turbulent intensity ( $I$ ). The meshing ensures the  $y^+$  value near to the tube wall throughout the length is below 1. The coupling of pressure-velocity in momentum equations was solved by the coupled scheme and second order UPWIND was used for solving the convective and dissipative terms. The convergence criteria were set to  $10^{-4}$ ,  $10^{-6}$ , and  $10^{-9}$  for continuity, momentum, and energy equations respectively. Turbulent kinetic energy ( $\kappa$ ), intermittency ( $\gamma$ ), and momentum thickness Reynolds number ( $Re_\theta$ ) were set to  $10^{-6}$  and specific dissipation rate ( $\omega$ ) convergence criteria was set to  $10^{-8}$ . It has been found that the transition SST model is able to predict the fluctuations better in the transitional regime as compared to the transition  $\kappa - \kappa_l - \omega$  model. It has also been found that the local  $Nu$  plot obtained in the transition SST model was similar to the results of Abraham *et al.* [109]. The comparison plot of various transition models as shown in Figure 3.6 describes the variation of  $Nu$  axially for different  $Re$  at fixed  $Ri$ .

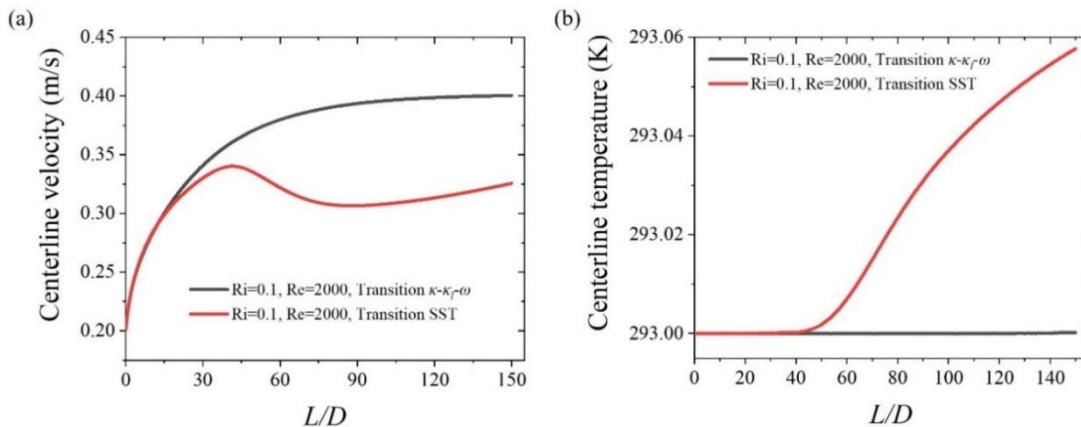


**Figure 3.6** Comparison of transition  $\kappa - \kappa_l - \omega$  and transition SST model for same  $Re$  and  $Ri$



### 3.4.2 Validation of transitional model

Following the robustness of different transition models used in [88], two transition models has been compared in the present study (Figures 3.2(a), (b)). It was found that the fluctuations in centerline velocity and temperature have been captured well by the transition SST model as compared to the transition  $\kappa - \omega$  model. The local  $Nu$  plot as shown in Figure 3.7 doesn't match exactly but showing similar behaviour of  $Nu$  variation. Hence the transition SST model was used for further simulations. Furthermore, the transition SST model results at different  $Re$  are validated with the results of Abraham *et al.* [109]. It decreases in the entrance region, takes a plateau like shape indicating the transition and then becomes steady once the flow is developed.

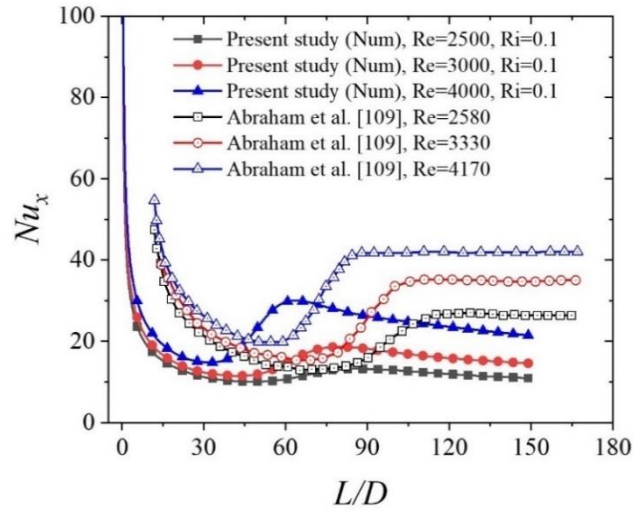


**Figure 3.7** Comparison of local  $Nu$  variation with numerical results of Abraham *et al.* [109]

### 3.5 Mathematical formulation for turbulent mixed convection

The working fluid, boundary conditions, and the governing equations are same as the laminar case used for the study of turbulent mixed convection. Similar to the transitional model, an axisymmetric vertical pipe of diameter ( $D$ ) 0.01 m and length ( $L$ ) 1.5 m has been modelled for the analysis. Apart from the governing equations of continuity, momentum, and energy, the turbulence models solve additional transport equations. The turbulence model used for the simulation is  $\kappa - \varepsilon$  have two additional equations: (a) Turbulent kinetic energy ( $\kappa$ ) and (b) Turbulent dissipation rate ( $\varepsilon$ ). The turbulence intensity ( $I$ ) is kept at 1 % [102] and the corresponding hydraulic diameter is mentioned in the inlet and outlet boundary conditions as 0.01 m. Turbulence intensity ( $\sqrt{u'^2}/u_{avg}$ ) is the ratio of

### 3.5 Mathematical formulation for turbulent mixed convection

root-mean-square of the velocity fluctuations ( $u', v'$ ) and their mean flow velocity ( $u_{avg}, v_{avg}$ ). The present study will highlight the results of simultaneously hydrodynamically and thermally developing as well as fully developed turbulent flow through a vertical tube.

The governing equations [110] are expressed as follows:

#### Continuity equation:

$$\frac{\partial(\bar{u})}{\partial x} + \frac{1}{r} \frac{\partial(r\bar{v})}{\partial r} = 0 \quad (3.14)$$

#### Momentum equations:

$$\text{Axial direction: } \bar{u} \frac{\partial \bar{u}}{\partial x} + \bar{v} \frac{\partial \bar{u}}{\partial r} = -\frac{1}{\rho} \frac{\partial \bar{p}}{\partial x} + \frac{1}{r} \frac{\partial}{\partial r} \left[ r(\nu + \epsilon_M) \frac{\partial \bar{u}}{\partial r} \right] \pm g_x \quad (3.15)$$

$$\text{Radial direction: } \bar{u} \frac{\partial \bar{v}}{\partial x} + \bar{v} \frac{\partial \bar{v}}{\partial r} = -\frac{1}{\rho} \frac{\partial \bar{p}}{\partial r} + \frac{1}{r} \frac{\partial}{\partial r} \left[ r(\nu + \epsilon_M) \frac{\partial \bar{v}}{\partial r} \right] \quad (3.16)$$

#### Energy equation:

$$\bar{u} \frac{\partial \bar{T}}{\partial x} + \bar{v} \frac{\partial \bar{T}}{\partial r} = \frac{1}{r} \frac{\partial}{\partial r} \left[ r(\alpha + \epsilon_H) \frac{\partial \bar{T}}{\partial r} \right] \quad (3.17)$$

#### Equation of state:

$$\rho = \rho_i [1 - \beta(\bar{T} - T_i)] \quad (3.18)$$

Boundary conditions applicable as per the problem statement are:

Inlet: Uniform inlet velocity,  $\bar{u} = U_i, \bar{v} = 0, \bar{T} = T_i$  at  $x = 0$  and  $r = 0$  to  $R$ ;  $r = 0$  at the center and  $r = R$  at the wall

Outlet: Pressure outlet boundary condition with  $p_g = 0$  at  $x = L$  and  $r = 0$  to  $R$

Tube walls: Constant heat flux,  $\dot{q} = Q_e/A_s$  at  $r = R$  and  $x = 0$  to  $L$

Tube axis: Symmetry condition,  $\frac{\partial \bar{u}}{\partial r} = 0, \frac{\partial \bar{v}}{\partial r} = 0, \frac{\partial \bar{T}}{\partial r} = 0$  at  $r = 0$  and  $x = 0$  to  $L$

The turbulent kinetic energy (TKE) which is defined as the mean kinetic energy of eddies per unit mass. It is expressed as the average of the square of the velocity fluctuations:  $\kappa = \frac{1}{2}(\overline{u'^2} + \overline{v'^2})$ . Also, the turbulent dissipation rate (TDR) is the rate at which these eddies get dissipated in terms of heat per unit time. The turbulent transport equations for TKE ( $\kappa$ ) and TDR ( $\epsilon$ ) in the realizable  $\kappa - \epsilon$  model is expressed by the following equations [102]:

$$\frac{\partial(\kappa u_j)}{\partial x_j} = \frac{\partial}{\partial x_j} \left[ \left( \nu + \frac{\nu_t}{\sigma_\kappa} \right) \frac{\partial \kappa}{\partial x_j} \right] + G_\kappa + G_b - \epsilon - Y_M + S_\kappa \quad (3.19)$$

$$\frac{\partial(\epsilon u_j)}{\partial x_j} = \frac{\partial}{\partial x_j} \left[ \left( \nu + \frac{\nu_t}{\sigma_\epsilon} \right) \frac{\partial \epsilon}{\partial x_j} \right] + C_1 S \epsilon - C_2 \frac{\epsilon^2}{\kappa + \sqrt{\nu \epsilon}} + C_{1\epsilon} \frac{\epsilon}{\kappa} C_{3\epsilon} G_b + S_\epsilon \quad (3.20)$$

Where,  $G_\kappa = -\overline{u_i' u_j'} \frac{\partial u_i}{\partial x_j}$ ,  $G_b = -g_i \frac{\beta}{\rho} \frac{v_t}{Pr_t} \frac{\partial T}{\partial x_i}$ ,  $v_t = C_\mu \frac{\kappa^2}{\varepsilon}$ ,  $C_1 = \max \left[ 0.43, \frac{\eta}{\eta+5} \right]$ ,  $\eta = S \frac{\kappa}{\varepsilon}$ ,  $S = \sqrt{2S_{ij}S_{ij}}$ ,  $S_{ij} = \frac{1}{2} \left( \frac{\partial u_j}{\partial x_i} + \frac{\partial u_i}{\partial x_j} \right)$ ,  $C_2 = 1.9$ ,  $C_\mu = 0.09$ ,  $Pr_t = 0.85$ ,  $\sigma_\kappa = 1$ ,  $\sigma_\varepsilon = 1.2$ ,  $C_{1\varepsilon} = 1.44$ ,  $C_{3\varepsilon} = 1$ ,  $Y_M = 0$  (since the flow is incompressible),  $S_\kappa = S_\varepsilon = 0$  (there are no source terms)

### 3.5.1 Numerical procedure

The geometry, boundary conditions, tube material and are same as that of transitional simulations. The geometry is symmetrical about the  $x$ -axis and the gravity is acting along the negative  $x$ -axis. Following the protocol of previous studies for symmetric flow in channels [88], [111] one-half of the tube is being simulated. The structured meshing was done with uniform mesh in axial and non-uniform mesh in the radial direction with fine grids near the walls as shown in Figure 3.2(b). The coupled scheme is used for solving pressure-velocity coupling and the second order UPWIND scheme is used for solving various energy and heat dissipation equations. The convergence in case of coupled scheme is faster as compared to the SIMPLE scheme because it solves the momentum and pressure-based continuity equation together. The convergence criteria are set to  $10^{-6}$ ,  $10^{-6}$ , and  $10^{-9}$  for continuity, momentum, and energy equation respectively. Turbulent kinetic energy ( $\kappa$ ) and turbulent dissipation rate ( $\varepsilon$ ) transport equations convergence criteria were set at  $10^{-6}$  [112]. The grid independence test was completed on achieving the convergence criteria of the solutions. It was conducted for four different grids as presented in Table 3.3.

**Table 3.3** Optimization of grids at  $Ri = 0.001$  and  $Re = 20000$  for  $\Delta T = 0.8^\circ\text{C}$  with  $L/D = 140$

Grid size ( $r \times z$ )	Bias factor	Nodes	Elements	Centerline velocity (m/s)	% Error	Centerline temperature (K)	% Error
101×3001	10	303101	300000	2.37563		293.186	
201×5001	10	1005201	1000000	2.36838	0.305	293.179	0.002
301×7501	10	2257801	2250000	2.36419	0.177	293.179	0.000
401×10001	10	5010501	5000000	2.36206	0.090	293.179	0.000

The error considered in the output parameter was limited to 0.1 %. The optimum grid was found to be 301×7501 ( $y \times x$ ). After obtaining suitable grids in axial and radial directions, the bias factor has been optimized. In Table 3.4, the bias factor of 10 in the radial direction was found sufficient to counter the steep gradients in velocity and temperature profiles near the tube walls. From the grid independence study, 301×7501 grid size with bias factor 10 has been chosen for further simulations.

### 3.5 Mathematical formulation for turbulent mixed convection

**Table 3.4** Optimization of bias factor with 301×7501 grid size at  $Ri = 0.001$  and  $Re = 20000$  with  $L/D = 140$

Grid size ( $r \times z$ )	Bias factor	Nodes	Elements	Centerline velocity (m/s)	% Error	Centerline temperature (K)	% Error
<b>301×7501</b>	<b>10</b>	2257801	2250000	2.36419		293.179	
<b>301×7501</b>	15	2257801	2250000	2.36473	0.023	293.18	0.0003
<b>301×7501</b>	20	2257801	2250000	2.36518	0.019	293.18	0.0000

The computational domain has been modelled in the appropriate pressure-based solver. In numerical simulations the nondimensional distance from the wall,  $y^+$  remains less than one throughout the tube length for all the range of  $5000 \leq Re \leq 20000$  and at least 10 grids are present within the viscous sublayer  $0 \leq y^+ \leq 5$ . The purpose of making fine grids closest to the walls is that the linear region in the universal velocity profile is used for the estimation of the friction factor. The inlet velocity is selected as per the  $Re$ . Inlet water properties are taken at atmospheric pressure and an inlet temperature of 20 °C. For  $5000 \leq Re \leq 6500$ , the flow regime is in turbulent mixed convection and the flow attains a fully developed state. The  $Gr$  based on heat flux varies from  $2.14 \times 10^6$  to  $6.88 \times 10^6$ . The corresponding  $Ri$  lie between 0.09 to 0.16.

#### 3.5.2 Comparison of various turbulence models

In the present study, one, two, and three equation turbulence models were used to compare the results in terms of friction factor ( $f$ ) and Nusselt number ( $Nu$ ). Spalart-Almaras (one-equation),  $\kappa - \varepsilon$  and  $\kappa - \omega$  (two-equation) and  $\kappa - \kappa_l - \omega$  (three-equation) models were compared for the extreme case at  $Re = 6500$  and  $Ri = 0.16$ . In the universal velocity profile plot (a plot between axial nondimensional velocity ( $u^+$ ) vs. radial dimensionless distance from wall ( $y^+$ )), the turbulence models such as Spalart-Almaras, Realizable  $\kappa - \varepsilon$ , Standard  $\kappa - \varepsilon$ , RNG  $\kappa - \varepsilon$ , Standard  $\kappa - \omega$ ,  $\kappa - \omega$  SST, and Transition  $\kappa - \kappa_l - \omega$  were used for the comparison (Figure 3.8). The Spalart-Allmaras model [113] was developed in 1994 specifically for aerodynamics and turbomachinery applications which are subjected to adverse pressure gradients. It is the simplest one equation model that solves only one additional equation which is a modified form of turbulent kinematic viscosity ( $\tilde{\nu}$ ). The modified form of turbulent kinematic viscosity ( $\tilde{\nu}$ ) is identical to the turbulent kinematic viscosity ( $\nu_t$ ) except in the near wall (viscous sub-layer) region. The two-equation  $\kappa - \varepsilon$  turbulence models were developed by Launder and Spalding [114] in 1972 and further improved with the advancement of time. These the simplest “complete models” of turbulence that solves

two additional transport equations  $\kappa$  and  $\varepsilon$  to determine the turbulent velocity and length scales independently. The robustness, economy, and reasonable accuracy make standard  $\kappa - \varepsilon$  model popular in the industrial flow and heat transfer simulations. Further improvements of these two models led to the development of Renormalization Group (RNG)  $\kappa - \varepsilon$  and realizable  $\kappa - \varepsilon$  model.

The RNG  $\kappa - \varepsilon$  model was developed by a rigorous statistical theory known as “renormalization group theory [115]” and has few advancements in comparison to standard  $\kappa - \varepsilon$  model. The benefits are as follows: (a) an additional term has been added in the  $\varepsilon$  equation to improve the accuracy, (b) it is also applicable for swirling flows, and (c) unlike other  $\kappa - \varepsilon$  models, the realizable  $\kappa - \varepsilon$  model uses an analytical formula to calculate turbulent Prandtl number instead of a constant value as provided by other models. The realizable  $\kappa - \varepsilon$  model is relatively a recent development and has improvements such as: (1) A new formulation for the turbulent viscosity and (2) A new transport equation of dissipation rate ( $\varepsilon$ ) derived from an exact equation for the transport of the mean-square vorticity fluctuation.

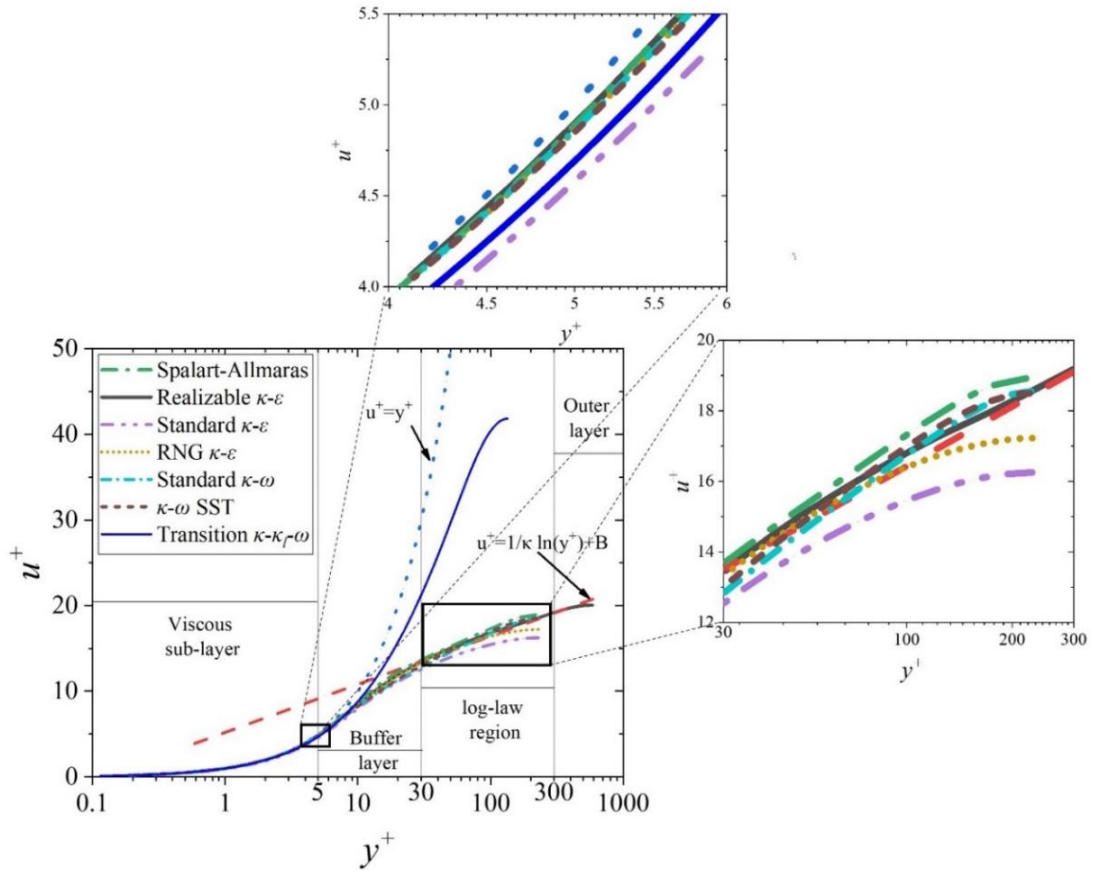


**Figure 3.8** The universal velocity profile  $u^+$  vs.  $y^+$  plot for  $Re = 6500$  and fixed  $Ri = 0.16$  at  $L/D = 140$

### 3.5 Mathematical formulation for turbulent mixed convection

The term “realizable” means that the model satisfies certain mathematical constraints on the Reynolds stresses, consistent with the physics of the turbulent flows [116]. Neither the standard  $\kappa - \varepsilon$  model nor the RNG  $\kappa - \varepsilon$  is satisfying the earlier mentioned mathematical constraints. This model has superior performance for flows involving rotations, boundary layers under adverse pressure gradients, separation, and recirculation. Other two-equation models; 1. Standard  $\kappa - \omega$  model developed in 1988 is applicable for near wall-bounded flows and free shear flows and thus gives better accuracy than standard  $\kappa - \varepsilon$  model 2. Shear Stress Transport (SST)  $\kappa - \omega$  model was developed in 1994 which is the effective blending of  $\kappa - \varepsilon$  and  $\kappa - \omega$  model. It accounts the robust and accurate formulation of the  $\kappa - \omega$  model in the near wall region and free stream independence of the  $\kappa - \varepsilon$  model in the far field. In addition to this, it incorporates a damped cross-diffusion derivative term in the  $\omega$  equation and the turbulent viscosity is modified to account for the transport of the turbulent shear stress. Further, the transition  $\kappa - \kappa_t - \omega$  model is also compared to deal with presence of any transitional phenomena in the specified range of present study. It is used to predict the boundary layer development and to calculate the onset of transition.

Figure 3.8 delineates that the realizable  $\kappa - \varepsilon$  model produces the best match with the velocity profile in the viscous sublayer and log-law region. The enhanced wall treatment consideration ensures the  $y^+$  value near to the tube wall throughout the length is below 1. It has also been found that the fully developed  $f$  and  $Nu$  using the realizable  $\kappa - \varepsilon$  model was nearest to the theoretical as well as experimental results as compared to the other models. The comparison plot of various turbulence models as shown in Figure 3.9 describes the variation of  $f$  and  $Nu$  with  $Re$  at fixed  $Ri$ .

#### 3.5.3 Hydrodynamic and thermal validation

The fully developed friction factor ( $f$ ) results obtained using the realizable  $\kappa - \varepsilon$  model have been compared in Figure 3.9(a) with the correlations of Blasius [105], Petukhov [9], Filonenko [83], and the experimental data of Allen and Eckert [117], Everts [118], Meyer and Abolarin [81], Bashir and Meyer [82]. The average deviation of friction factors is 1.7 % with Blasius [105], 0.94 % with Petukhov [9], 2.60 % with Filonenko [83], and 5 % with the experimental results [117], [118], [81], and [82] respectively.

The heat transfer results obtained from the numerical model were compared in Figure 3.10(b) in terms of Nusselt number ( $Nu$ ) with the correlations of Dittus-Boelter [9], Meyer *et al.* [83] applicable for fully developed turbulent forced convection flow at

constant heat flux conditions and the experimental outcomes of Meyer and Abolarin [81], Everts [118], Bashir and Meyer [82], Bashir *et al.* [98]. The average fully developed  $Nu$  obtained in between  $L/D = 45$  and  $L/D = 150$  shows deviation of 16.2 % with Dittus-Boelter [9], 25.9 % with Meyer *et al.* [83], 23.0 % with Everts [118], 19.8 % with Bashir *et al.* [98] and less than 30 % with the experimental existing data of Meyer and Abolarin [81], Bashir and Meyer [82] on turbulent mixed convection flows. Such a deviation maybe due to these two reasons: (a) the results are obtained from a 2D axisymmetric domain instead of a 3D one, which can produce more accurate results and (b) there is a considerable deviation among the existing correlations when they were compared to each other [19, 33].

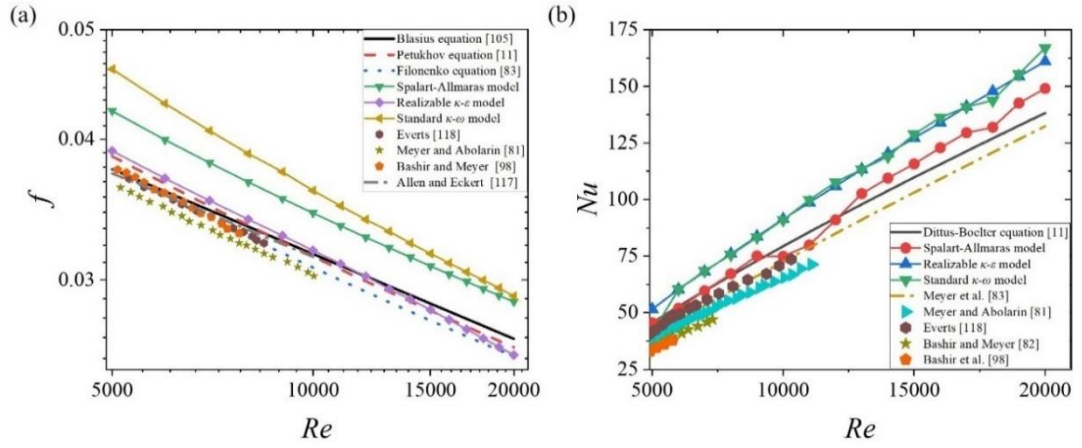


**Figure 3.9** Comparison of average fully developed (a)  $f$  and (b)  $Nu$  of various turbulence models with the standard available correlations and experimental results at  $Ri = 0.001$

### 3.6 Conclusions

Thus, the numerical methodology followed in the present work for analysing laminar, transitional, and turbulent mixed convection flows were explained in detail. Followed by the numerical procedure, the GIT was performed to optimise the grids with fine grids near the wall. The numerical models and their comparisons for better performance were also discussed. Laminar model was used for the study of laminar mixed convection flow regime. For the laminar-turbulent transitional mixed convection analysis, two numerical models; transition  $\kappa - \kappa_l - \omega$  and transition SST were compared. The transition SST model was selected over transition  $\kappa - \kappa_l - \omega$  model to get more accurate results. Among different turbulence models such as

### 3.6 Conclusions

Spalart-Almaras, Realizable  $\kappa - \varepsilon$ , Standard  $\kappa - \varepsilon$ , RNG  $\kappa - \varepsilon$ , Standard  $\kappa - \omega$ ,  $\kappa - \omega$  SST, and Transition  $\kappa - \kappa_l - \omega$ ; the realizable  $\kappa - \varepsilon$  turbulence model with enhanced wall treatment produces the best match in turbulent mixed convection analysis. Further, the result of each numerical model is validated with the theory as well as existing experiments of forced and mixed convections.



### Experimental Set-up and Procedure

---

#### 4.1 Introduction

The purpose of this chapter is to discuss in detail the experimental set-up used to determine the pressure drop and heat transfer in a vertical tube at different heat fluxes and flow rates. The design and fabrication of the experimental set-up calibration, and procedure to perform the experiments are explained here. The data reduction technique, validation of the set-up, and uncertainty analysis of the components are discussed. The hydrodynamic and thermal validation results for developing and fully developed flows in laminar, transitional, and turbulent regimes are also demonstrated.

#### 4.2 Experimental set-up and components

The schematic of the experimental set-up is shown in Figure 4.1. It is a closed circuit that consists of a pump (a centrifugal self-priming pump) that takes water from a storage tank of capacity 225 litres and sends it to the test section (a smooth tube of stainless steel 316 L). Before the test section, water passes through a flow straightening part called the calming section, which makes the flow straight at the entry to the test section. The purpose of this calming section is to create a uniform flow at the square-edged entry. The Coriolis mass flow meter used for measuring the flow discharge was fixed before the calming section, where the set mass of water flows to the test section and the remaining water is sent back to the storage tank through a bypass valve. The water gets heated in the test section by the Joule effect. For heating the test section, a three-phase DC power source is connected to the ends of the test section, and power is supplied. The heated water then passes through the mixer, where the hot water gets mixed, and the average water temperature at the outlet is recorded by the RTD sensor (PT 100). One visualization provision has been made after the outlet to see the changes in flow due to the changes in the heat supply and the flow rate. The hot water passes through the 1.5 tonne of refrigeration (TR) chiller unit, where it gets cooled and stored in the tank, whose temperature is continuously

## 4.2 Experimental set-up and components

monitored with an RTD. The inlet water temperature is recorded by another RTD just before entry to the test section. One dye flow arrangement is also made to send dye for visualization purposes. A 20-gauge needle is bent at  $90^\circ$  and fixed at the calming section so that the tip of the needle will be positioned exactly at the centre and at the entry point of the test section. One syringe pump is used to send dye into the flow line at the same velocity as the main line flow. In total, eleven thermocouples are attached to the test section, and two pressure taps are brazed to connect a differential pressure transducer to measure the pressure drop across the tube. All the thermal and pressure sensor readings are logged in the Data Acquisition System (Keysight 9270) connected to a desktop.

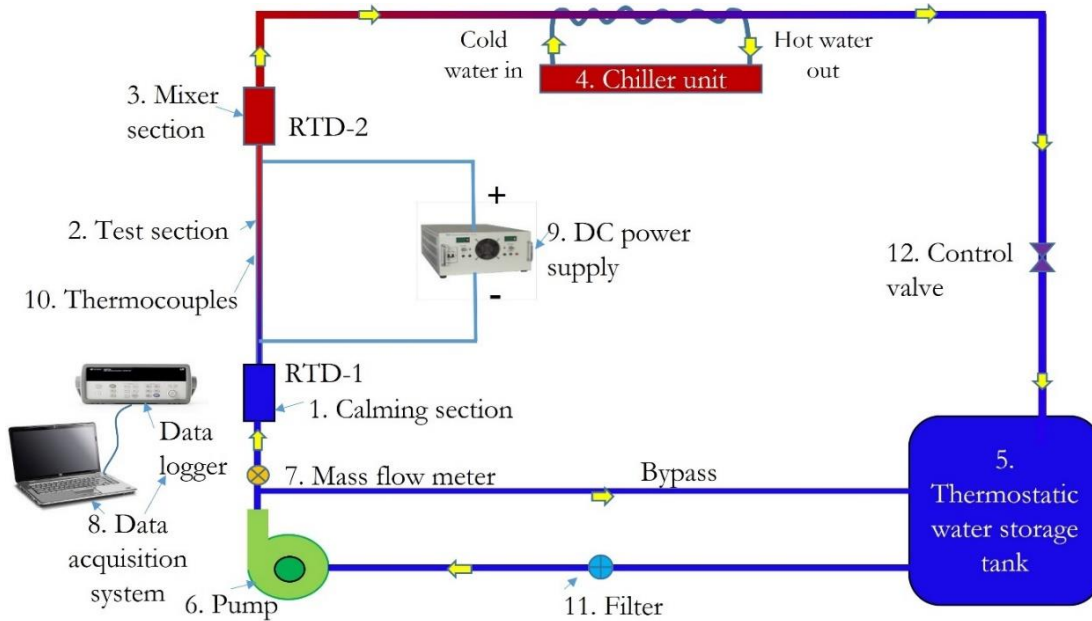


**Figure 4.1** Schematic diagram of the mixed convection experimental set-up

### 4.2.1 Flow calming section

The flow-calming section is a flow straightening part made up of a transparent material named acrylic. The schematic and photographic views of the calming section are shown in Figures 4.2(a) and (b). The assembled part and its subcomponents are provided in Figures 4.3(a) and (b). A circular hollow tube of inner diameter 90 mm and outer diameter 118 mm is formed from a solid rod of diameter 120 mm and length 600 mm. The calming section consists of three perforated plates (OAR of 29) with 37 holes of diameter 10 mm at a circular pitch of  $15^\circ$ . These plates are attached to the flanges to connect tightly. The section was made leakproof by placing O-rings (3 mm in diameter) in between the flanges to arrest water. The flanges are tightened by means of helical screws (M8×1) and springs of sufficient length. Before the end of the calming section, two wire meshes (OAR of 68) are tightly packed with soda straws (6 mm in diameter

and 100 mm in length), followed by the perforated plates. An acetal disc (diameter 120 mm and width 30 mm) is bolted to the calming section. The acetal disc is also connected to the test section. The purpose of this acetal disc is two-fold: (i) to provide sufficient insulation to the calming section from the heat generated in the test section by the electrical power supply and (ii) to make an arrangement for a square-edged inlet. The square-edge inlet is the provision at the inlet to the test section with a reduction in diameter from the calming to the test section [118]. In the current experimental setup, the ratio of calming section to test section diameter is kept at 9. A provision for the dye injection has been made; one needle is placed at the end of the calming section and before the entry to the test section. One RTD is also fixed at the end of the calming section to measure the average inlet water temperature.

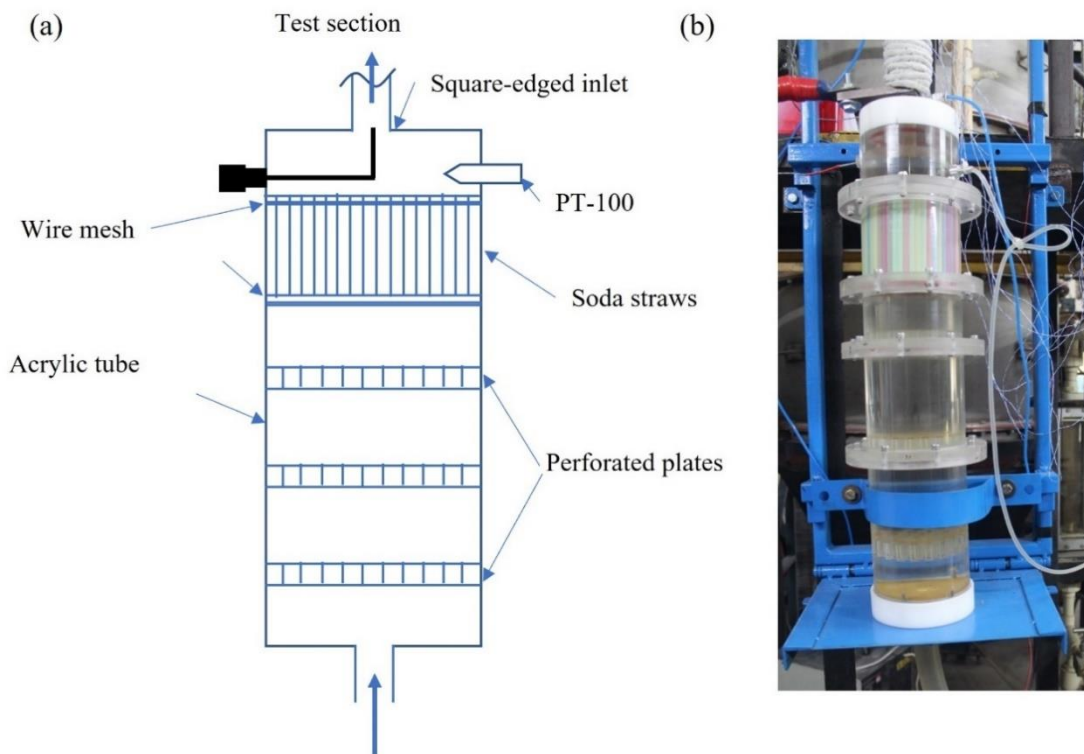


**Figure 4.2** (a) Schematic and (b) photographic view of the calming section

## 4.2 Experimental set-up and components

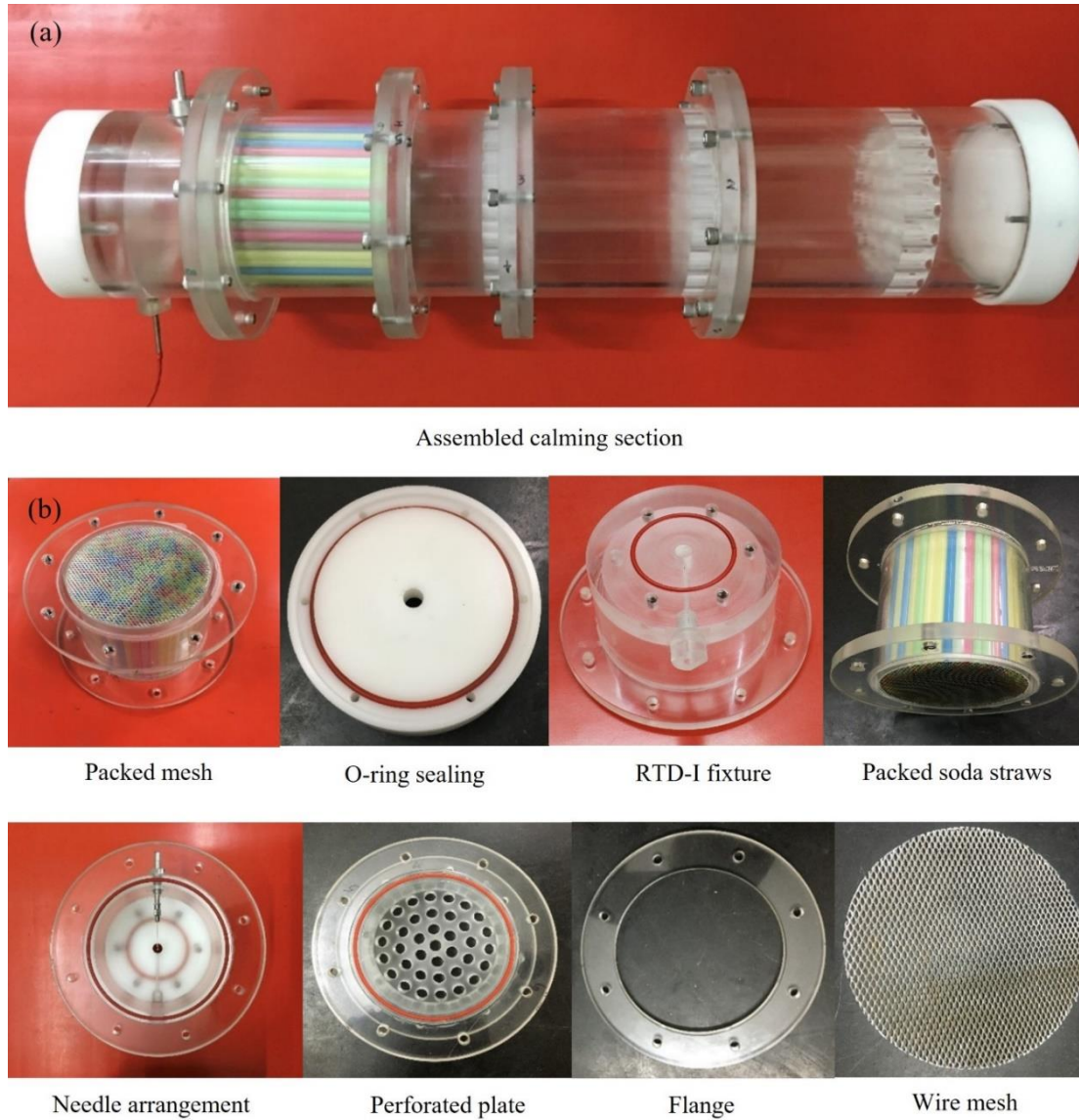


**Figure 4.3** (a) Assembled calming section and its (b) sub-components

### 4.2.2 Test section

A smooth stainless-steel tube of inner diameter 10 mm, outer diameter 12 mm, and length 130 mm was used as the test section. The schematic showing the thermal sensor arrangement with the assembled photographic view is shown in Figures 4.4(a) and (b). The 316 L grade of stainless-steel tube is used for experimental purposes to avoid corrosion of the material in the long run. Both ends of the test section are brazed with two male fittings to be fitted with the acetal disc. Two copper bars ( $l \times b \times h$  of  $95 \times 30 \times 10$  in mm) are brazed at both sides at 125 mm apart to connect the positive and negative cables of the DC power source, as displayed in Figure 4.5(a). Pressure tapings made of brass tube (4 mm hole) are brazed at the inlet and outlet of the test section after making a hole of 1.5 mm on the stainless-steel tube. These pressure tapings are connected by

means of pneumatic tubes (4 mm in diameter) to the diaphragm-based differential pressure transducer to record the pressure drop. Eleven T-type thermocouples are attached at a gradually increasing distance from the inlet to the test section over a single layer of Kapton tape to electrically insulate the sensors, as shown in Figure 4.5(b).

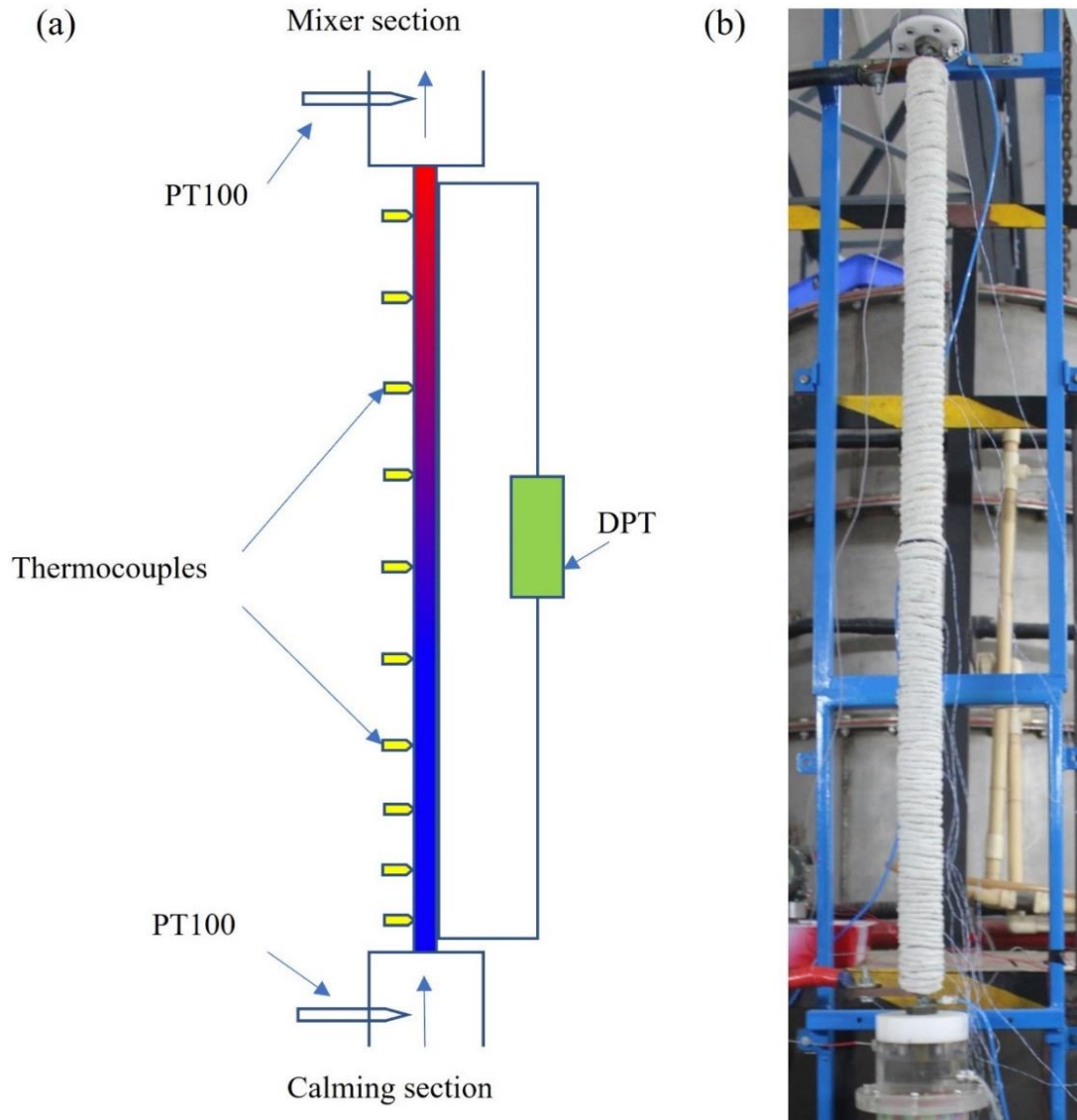


**Figure 4.4** (a) Schematic and (b) photographic view of the test section with thermal and pressure sensors arrangement



## 4.2 Experimental set-up and components

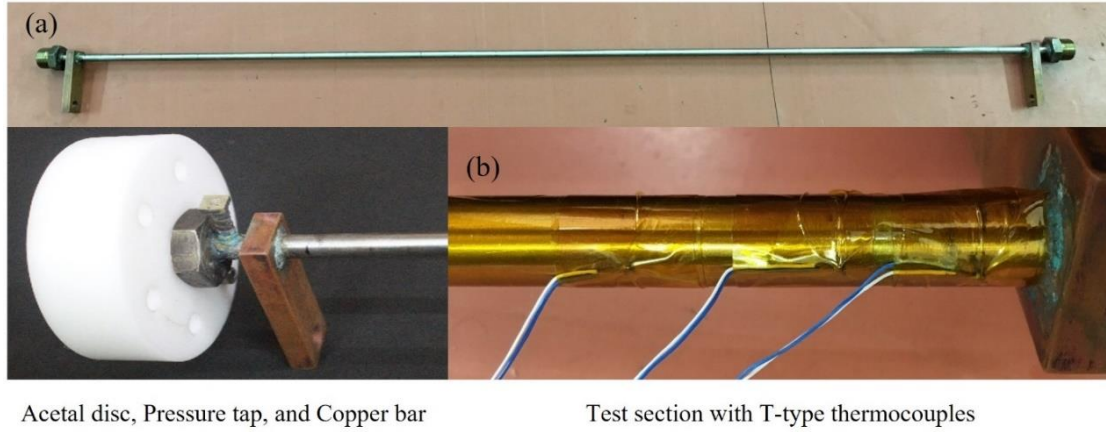


**Figure 4.5** (a) Test section and its (b) sub-components with thermocouple arrangement

### 4.2.3 Mixer section

The schematic and actual diagram of the mixer section is presented in Figures 4.6(a) and (b). The mixer section is made up of an acetal cylinder of diameter 120 mm and length 100 mm. It consists of four splitter plates or baffles ( $l \times b$  of  $15 \times 9$  in mm) bonded and placed  $90^\circ$  to each other as shown in Figure 4.7 at the entry of the mixer section to mix the heated water coming out of the test section so that the average water temperature can be measured by the RTD fixed at the end portion of the mixer section.

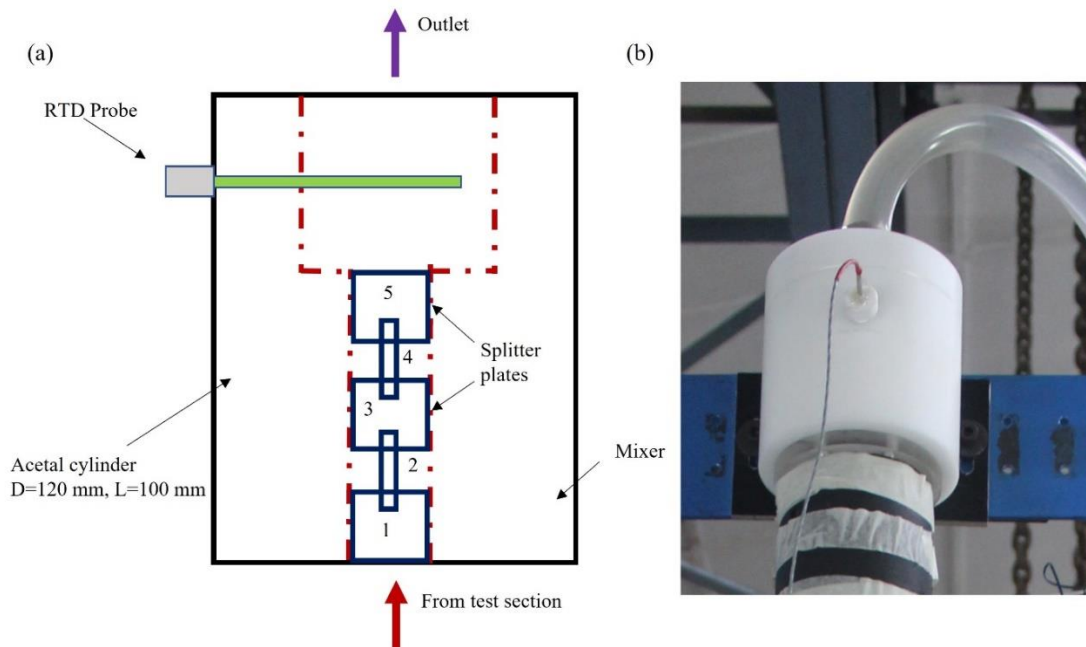


**Figure 4.6** (a) Schematic of the mixer section with splitter plates and its (b) photographic view

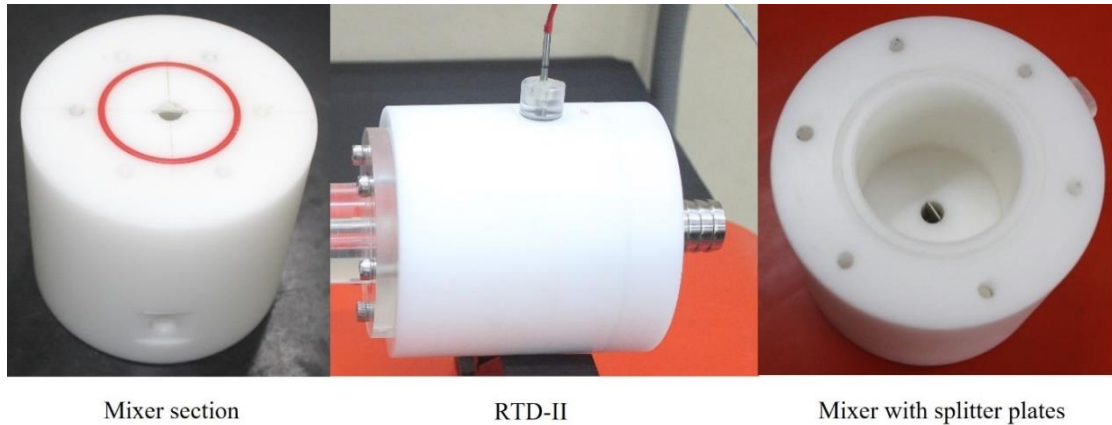


**Figure 4.7** Mixer section and its design

### 4.2.4 Visualization section

The most important and difficult stage of the experimental set-up fabrication was to provide a transparent section to visualize the flow. The aim was to put a transparent part having high temperature resistance which is challenging because it is to be connected to the high temperature end of test section. It can be seen in Figure 4.8(a), after the test section and before the mixer section one transparent tube (length 200 mm and diameter 50 mm) of acrylic is fitted by means of flanges (bonded over the transparent acrylic tube). Two ends are bolted on the acetal disc fitted to the test section and the mixer section as shown in Figure 4.8(b). The transparent tube is drilled with hole of 10 mm diameter same as the test section to maintain the flow of water coming out of the test section. To prevent leakage, the fittings are provided with O-rings at both the ends of the transparent tube.

## 4.2 Experimental set-up and components

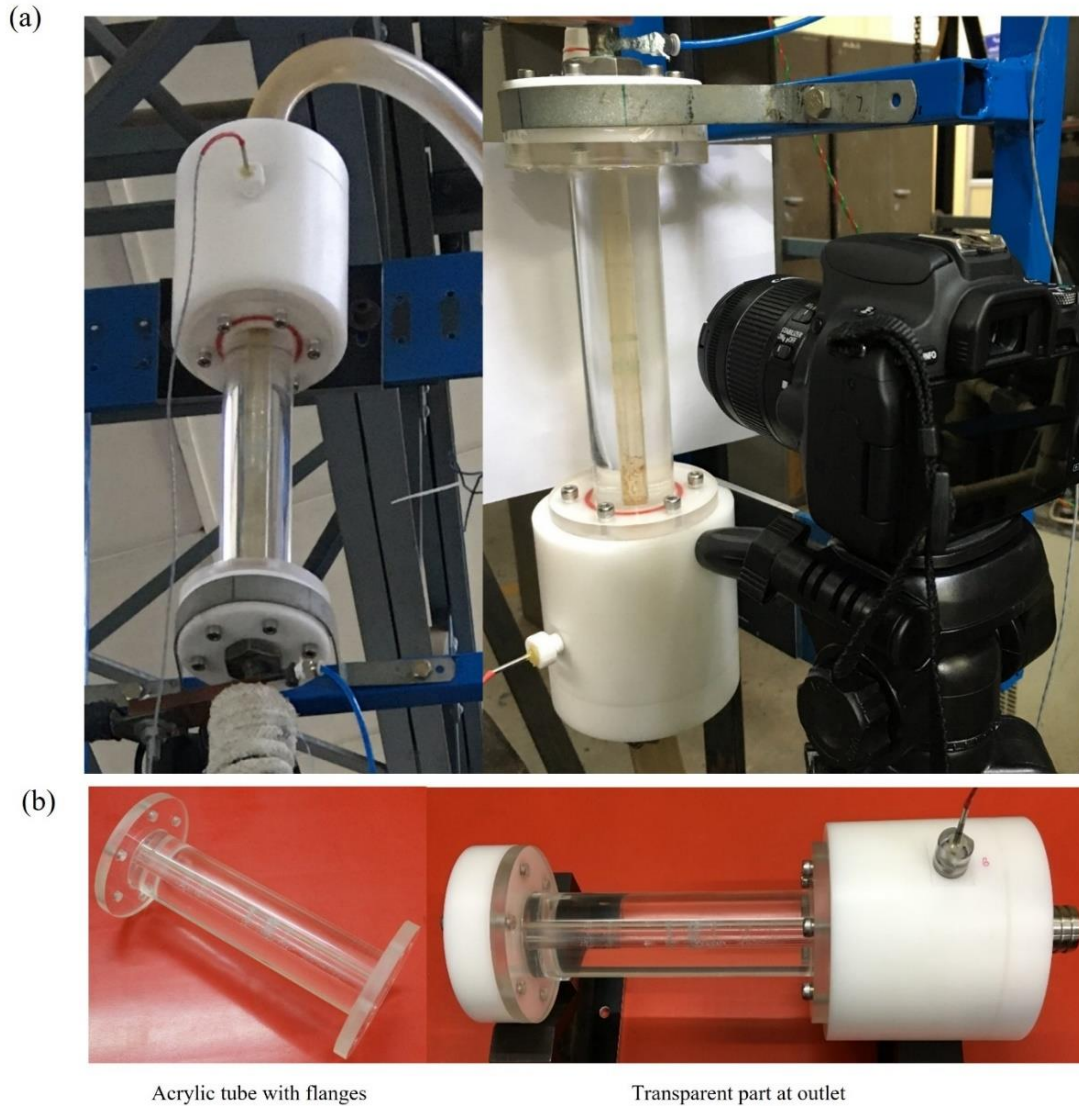


**Figure 4.8** (a) Pictorial view of the visualization section with camera and (b) its subcomponents

### 4.2.5 Instrumentation

The various instruments used in the experiments, such as thermocouples, RTDs, differential pressure transducer, flowmeter, power source, data logger etc., are discussed in this section.

#### 4.2.5.1 Thermocouples

T-type thermocouples of the bead type are used for the measurement of the tube's outer surface temperature. The bead diameter is 1 mm, and the wire diameter is 0.25 mm. The extension wire is of length 2 m, and the outer diameter ranges from 0.5 mm to 1 mm. The range of the T-type thermocouples is from 0 to 350 °C, with an accuracy of 0.2 °C. In total, 11 thermocouples are attached to the outer surface of the test section at a



gradually increasing axial distance from the inlet. At the inlet, thermocouples are placed at a closer distance as compared to the later part of the test section to counter the sharp variation of the flow variables in the developing flow regime. Before placing the thermocouples, the whole test section was covered with one layer of an electrically insulated and thermally conducting Kapton tape (width 2 inches and thickness 0.06 mm).

### 4.2.5.2 Resistance temperature detector (RTD)

The average water temperature at the inlet and exit of the test section is measured by means of the three-wire RTD (PT100). One is fitted at the entry of the test section in the calming section and the other one in the mixer section. The PT100 used in present experiments are of pencil type probes of 3 mm diameter and 100 mm length with an accuracy of 0.1 °C. The extension wire is of 3 meter in length so that it can be connected to the data logger. The data logger available for data acquisition was compatible with two-wire and four-wire RTD's. Hence, a three-wire RTD was connected to the data logger after making a provision for four-wire type of RTD by aiding one dummy connection.

### 4.2.5.3 Differential pressure transducer (DPT)

A differential pressure transducer (Yokogawa, Model No. EJA110E-JHS4J-912EB) of the diaphragm type is used to measure the pressure drop across the test section. The capsule used was H-type, with a pressure drop measurement range of -500 kPa to 500 kPa. The span of measurement was set from 0 Pa (Lower Range Value: LRV) to 5000 Pa (Upper Range Value: URV). The accuracy of the differential pressure transducer was  $\pm 0.055$  % of the span. As per the user manual, the higher-pressure side (H) is connected at the inlet of the test section, and the lower pressure side (L) is connected at the exit of the test section.

### 4.2.5.4 Flowmeter

A Coriolis mass flow meter (EMERSON, Model: 1700R12ABFEZCZ) with a flow range of 0 to 450 kg/hr is used to send water to the test section. It is placed exactly before the calming section and after the pump. The display unit and the sensor with core processor are displayed in Figures 4.9(a) and (b). The micro motion mass flow meter was calibrated by stopwatch and bucket method, and the accuracy found was 1.54 % in the laminar range (= 0–2300), 2.54 % in the transitional range (=2300-5000), and 1.10

## 4.2 Experimental set-up and components

% in the turbulent regime ( $= 5000\text{--}15000$ ). Due to the vertical orientation of the flow, the minimum flow rate possible is  $3\text{ kg/hr}$  ( $Re \approx 300$ ) in aiding flow and  $5\text{ kg/hr}$  ( $Re \approx 500$ ) in opposing flow.

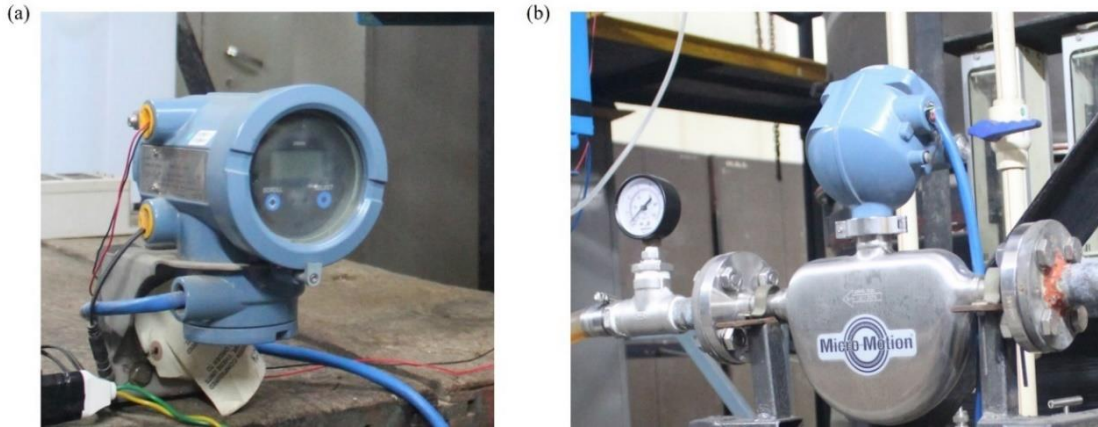


**Figure 4.9** (a) Flowmeter display unit mounting and (b) its connection to the flowline

### 4.2.5.5 Power supply

The electrical power input was given by a low-voltage and high-current Direct Current (DC) power source (Suppususee Technologies Private Limited, Chennai) of capacity  $8.4\text{ kW}$ . The equipment and its connections are illustrated in Figure 4.10. The voltage and current ranges were  $0\text{--}24\text{ Volts}$  and  $0\text{--}350\text{ amps}$ , respectively. The uncertainty is  $0.1\text{ V}$  and  $1\text{ A}$ , which leads to  $0.1\%$  of the nominal power. The direct current input is given to heat the test section (a stainless-steel tube of  $ID = 10\text{ mm}$  and  $OD = 12\text{ mm}$ ) of length  $1.3\text{ m}$ . A high-current DC power source utilizing the Joule's effect as the working principle is used for the heating of the test section. This is essential because with high current, the resistance will be low, and hence the heating will be greater. Even though the maximum current is  $350\text{ A}$ , sometimes it has been observed that the electrical resistivity changes during the experiments due to the change in temperature. Therefore, the input currents continuously need to be adjusted to ensure that constant heat flux is obtained throughout the experiments.



**Figure 4.10** Direct Current (DC) power source with its connections and the control unit

### 4.2.5.6 Data acquisition system (DAQ)

The data acquisition switch unit (Keysight 9270) along with a 20-channel multiplexer (34970A) is used to log the data measured by the flowmeter, thermal, and pressure sensors. The display unit and the interface for the data collection are displayed in Figures 4.11(a) and (b). The data was recorded every 5 seconds until the steady state was reached, and the average of 20 measurements was considered for the data interpretation.

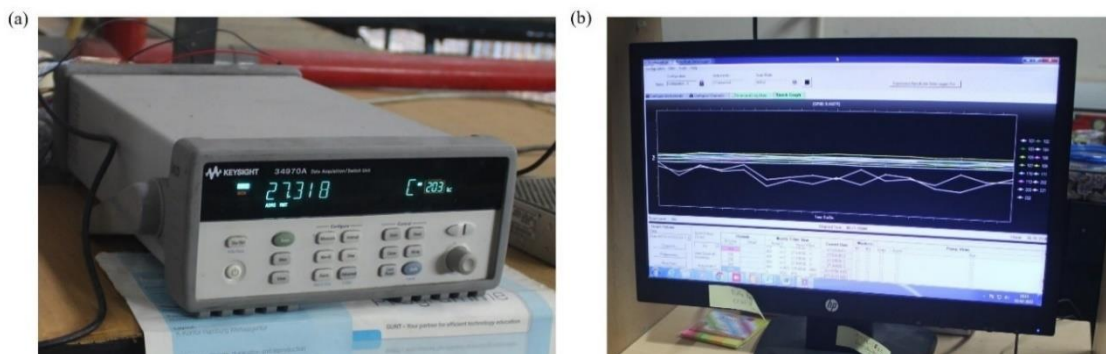


**Figure 4.11** (a) Data logger switch unit and (b) data acquisition software interface

The extension wires of the thermal sensor were connected to the high and low sides of the multiplexer channels, which takes the input as a potential difference and gives a digital output in terms of the unit set as °C. The pressure sensors are connected to the

## 4.2 Experimental set-up and components

high and low terminals of the channel through electrical wires, which take input as a current in milliamperes (mA) and give output as set in Pascal (Pa). Similarly, the flowmeter sensor unit is also connected to the channel, which take input as a current and provide digital output in terms of the flow rate of the set unit in kg/hr.

### 4.2.6 Centrifugal pump and syringe pump

A syringe pump (Figure 4.12(a), New Era, Model: NE-300) is used to send dye into the main flow line. The dye flow rate is set (in ml/min) so that the velocity remains same as that of the main line flow rate. Potassium permanganate of 0.1M-0.2M solution was used as a dye to visualize the flow. A syringe of 60 ml capacity was used and set at different required flow rates. The dye is sent at the inlet of the test section to avoid any disturbances in the flow characteristics. A centrifugal pump (Figure 4.12(b), self-priming mini master II) of capacity 0.5 HP is used to send water from the water storage tank to the test section. The achievable head range is 6–30 m with a flow rate of 2600–600 lph. The centrifugal pump, which takes water from the tank and sends it to the test section, is followed by the mass flowmeter. The flow is controlled by a needle valve (1" BSP, SS 316), and the excess amount of water flows back to the storage tank through a bypass valve.

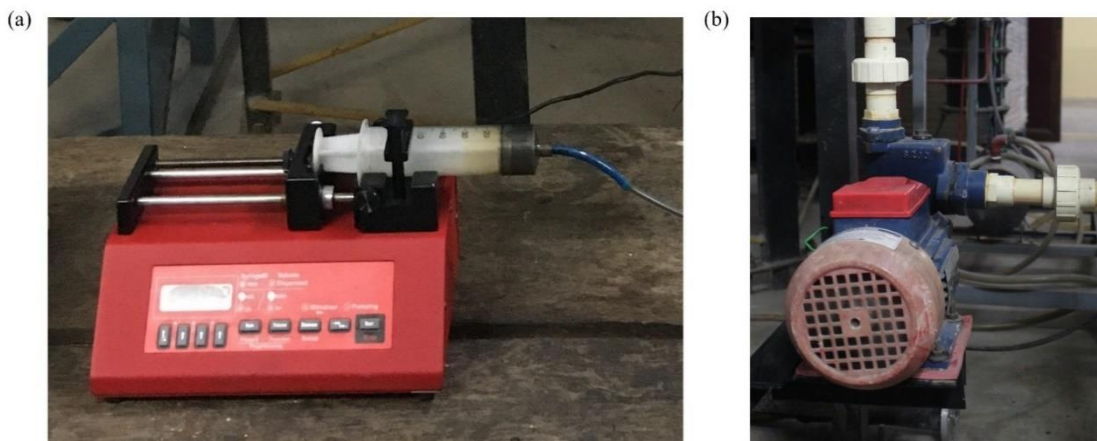


**Figure 4.12** (a) Syringe pump for dye injection and (b) centrifugal pump for main line flow

### 4.2.7 Chiller unit

A 1.5 TR chiller with compressor unit and insulated tank (Figure 4.13(a)) is used to cool the heated water coming out of the test section. Refrigerant (R-22) filled in copper coils (Figure 4.13(b)) surrounded with water absorbs the heat from the water and maintains the temperature. The water temperature is monitored through a Proportional-Integral-



## Chapter 4: Experimental Set-up and Procedure

Derivative (PID) controller (Figure 4.13(c)), where the temperature is indicated by a PT100 dipped into the chiller unit. The controller is semi-automatically set so that the chiller unit will automatically cut off once the water temperature reaches the set value and then restart when the water temperature becomes higher by 1 °C above the set value.

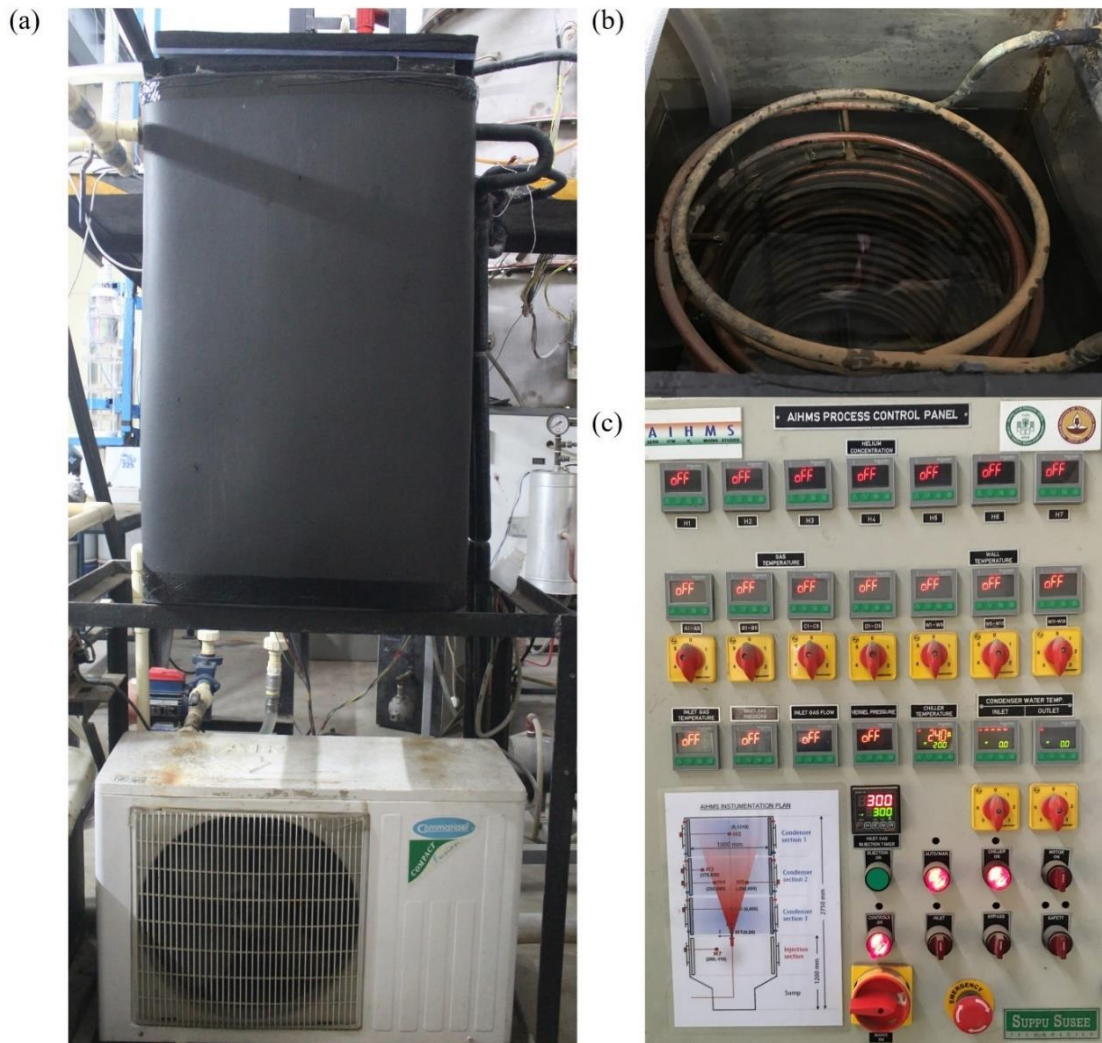


**Figure 4.13** (a) Chiller unit (b) inside view of the insulated tank and (c) PID controller

### 4.3 Data reduction method

### 4.3 Data reduction method

The data logged from the data logger are temperatures, mass flow rate, and pressure drops to determine the local and average pressure drops and heat transfer coefficients. These are essentially quantifying the friction factor ( $f$ ) and Nusselt number ( $Nu$ ). The detailed method used for the data reduction is discussed here.

The bulk fluid temperature ( $T_b$ ) can be obtained by calculating the algebraic mean of the inlet ( $T_i$ ) and outlet ( $T_o$ ) average fluid temperatures. The inlet temperature of water is maintained at 20 °C at atmospheric pressure. Because of the constant heat flux boundary condition, the average axial fluid temperature increases linearly. The local bulk fluid temperature ( $T_b(x)$ ) at an axial location  $x$  can also be calculated as Eq. (4.2). Once the bulk fluid temperature is known, the non-dimensional parameters are recalculated by taking the fluid properties at the bulk fluid temperature.

$$T_b = \frac{(T_i + T_o)}{2} \quad (4.1)$$

$$T_b(x) = T_i + \frac{(T_o - T_i)}{L} \left( \frac{L(x)}{2} \right) \quad (4.2)$$

$$Re_b = \frac{\rho_b u_m D}{\mu_b} = \frac{4\dot{m}}{\pi \mu_b D} \quad (4.3)$$

$$Gr_b = \frac{g \beta_b \dot{q} D^4}{\nu_b^2 k_b} \quad (4.4)$$

$$Ri_b = \frac{Gr_b}{(Re_b)^2} \quad (4.5)$$

$$Ra_b = Gr_b \times Re_b \quad (4.6)$$

$$Pr_b = \frac{\mu_b c_{p_b}}{k_b} \quad (4.7)$$

$$Gz_b = Re_b Pr_b D / L \quad (4.8)$$

The electrical heat input ( $Q_e$ ) is obtained from the voltage and current as indicated by the DC power supply. The amount of heat carried away by water ( $\dot{Q}_w$ ) can be determined if the inlet and outlet water temperatures are known. The heat flux ( $\dot{q}$ ) can be obtained by dividing the heat absorbed ( $\dot{Q}_w$ ) by water to the inner surface area ( $A_s$ ) of the tube.

$$Q_e = V \times I \quad (4.9)$$

$$\dot{Q}_w = \dot{m}C_{pb}(T_o - T_i) \quad (4.10)$$

$$\dot{q} = \frac{Q_w}{A_s} = \frac{Q_w}{\pi DL} \quad (4.11)$$

The heat transfer rate to the water was used to calculate the heat flux because it is more accurate as there is always some heat loss to the surroundings. The test section was insulated with 45 mm thick insulation by ceramic fiber ropes (5 mm in diameter) having a thermal conductivity of 0.13 W/m-K. The heat lost to the surroundings can be obtained by the energy balance (EB) equation as written in Eq. (4.12). The energy balance equation shows a non-zero value and some amount of heat lost to the ambient air; hence, the electrical heat input is always higher than the heat transfer rate to the water.

$$EB = \left| \frac{Q_e - Q_w}{Q_e} \right| \times 100 = \left| \frac{V \times I - \dot{m}C_{pb}(T_o - T_i)}{V \times I} \right| \times 100 \quad (4.12)$$

$$Q_{lost} = Q_e - \dot{Q}_w \quad (4.13)$$

The inner wall temperature was obtained after subtracting the temperature drop from the outer tube surface to the inner wall. The thermal resistance due to the thickness of the tube is determined by considering the heat conduction through a circular cylinder of outer ( $D_o$ ) and inner diameter ( $D_i$ ) for a specified heated length of  $L$ . If the thermal conductivity of the tube material (SS 316 L has 16.3 W/m-K) is known, the temperature drops across the tube wall ( $\Delta T$ ) can be determined as follows:

$$R_{th} = \frac{\ln(D_o/D_i)}{2\pi kL} \quad (4.14)$$

$$\dot{Q}_w = \frac{\Delta T}{R_{th}} \quad (4.15)$$

The inner surface temperature of the stainless-steel tube is obtained after deducting the temperature drop from the outer tube surface temperature. The mean temperature of water will linearly increase due to the constant heat supply from the tube wall and can be expressed as Eq. (4.17).

$$T_{w,i}(x) = T_{w,o}(x) - \Delta T = T_{w,o}(x) - \dot{Q}_w \times R_{th} \quad (4.16)$$

$$T_m(x) = T_i + (T_o - T_i) \frac{x}{L} \quad (4.17)$$

#### 4.4. Experimental procedure

The local heat transfer coefficient ( $h_x$ ) can be determined from the convective heat transfer equation at an axial location,  $x$ . The average heat transfer coefficient ( $\bar{h}$ ) then can be determined by the length integral from inlet to the outlet. Consequently, the local Nusselt number ( $Nu_x$ ) and average Nusselt number ( $\overline{Nu}$ ) can also be obtained. Furthermore, the heat transfer can also be analysed by another dimensionless number called Colburn  $j$ -factor and expressed as Eq. (4.22).

$$h_x = \frac{\dot{q}}{(T_w(x) - T_m(x))} \quad (4.18)$$

$$\bar{h} = \frac{1}{L} \int_0^L h_x dx \quad (4.19)$$

$$Nu_x = \frac{h_x D}{k_b} \quad (4.20)$$

$$\overline{Nu} = \frac{\bar{h} D}{k_b} \quad (4.21)$$

$$j = \frac{Nu}{Re Pr^{1/3}} \quad (4.22)$$

The experimental pressure drops ( $\Delta p_{exp}$ ) were measured from the differential pressure transducer. The offset value in the DPT can be either added or subtracted based on the negative or positive error present in the instrument, respectively. Further, the friction factor can be calculated by the experimentally measured pressure drop ( $\Delta p_{exp}$ ) between two pressure taps separated by an axial length ( $L(x)$ ) and the mass flow rate ( $\dot{m}$ ) or mean velocity ( $v$ ) of the working fluid.

$$\Delta p_{exp} = \Delta p_{measured} \pm \Delta p_{offset} \quad (4.23)$$

$$\bar{f} = \frac{2\Delta p_{exp} D}{L(x) \rho_b v^2} = \frac{\pi^2 \rho_b \Delta p_{exp} D}{8\dot{m}^2 L(x)} \quad (4.24)$$

#### 4.4 Experimental procedure

The experiments were performed under normal temperature and pressure conditions. The experimental set-up was built in such a way that buoyancy-aiding and buoyancy-opposing mixed convection experiments could be performed with a change in the orientation of the set-up (Figures 4.14(a) and (b)).



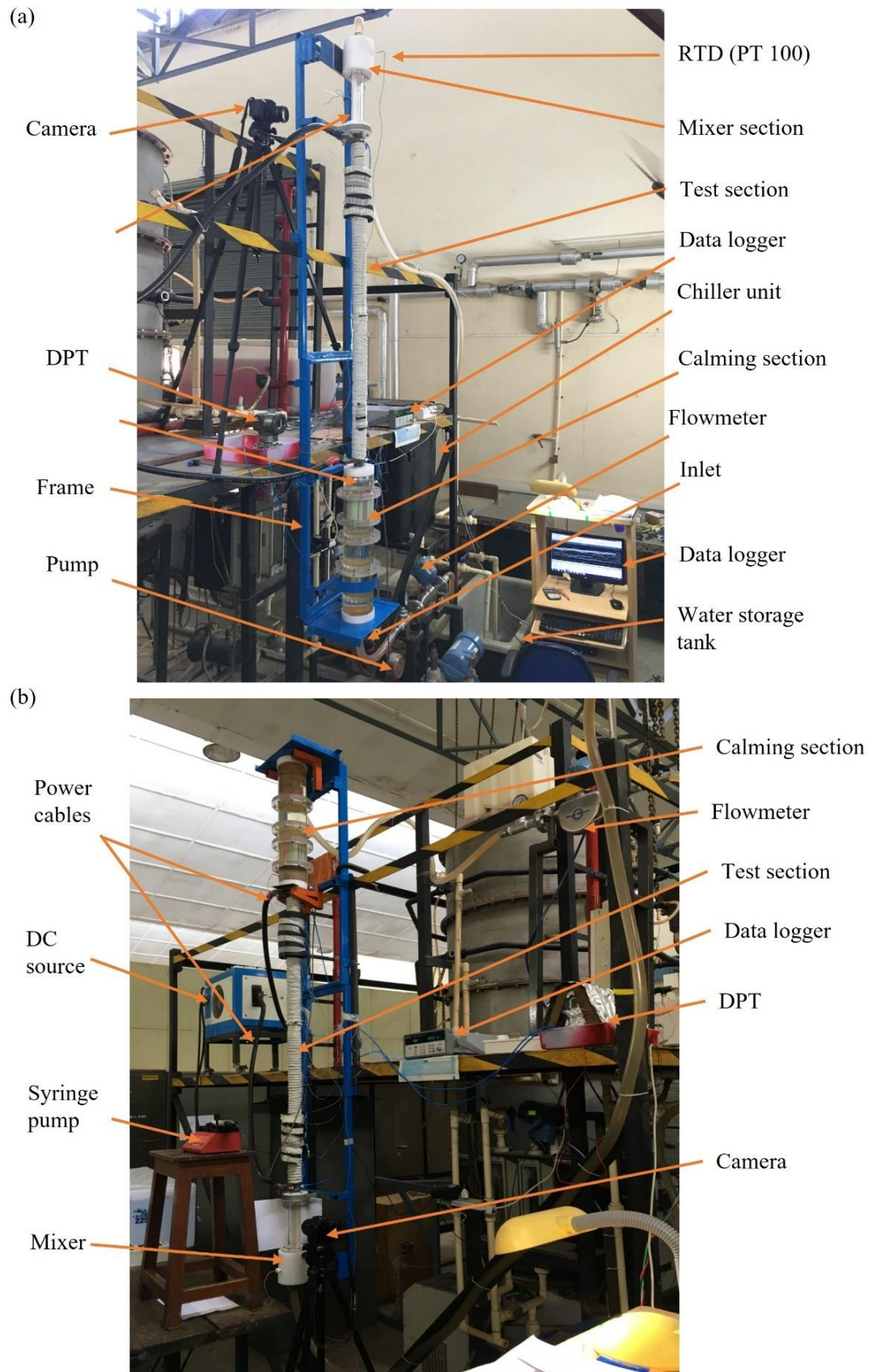


**Figure 4.14** Mixed convection experimental set-up with individual components for (a) aiding and (b) opposing flow

#### 4.4. Experimental procedure

Normal water was the working fluid. Water was sent to the inlet of the test section at 20°C at normal atmospheric pressure. As shown in the figures, initially the water was pumped after venting so that air bubbles do not get trapped inside the pipeline. Thereafter, the cycle runs for 10–15 minutes until the steady state was reached. Steady-state conditions were assumed once there was negligible variation in temperature, pressure drop, and flow rate for at least 20 cycles (100 seconds). Once the steady state was reached, the readings were recorded in the data logger. The average of the last 20 cycles of data points is considered for the analysis. Although the average time taken to reach steady state is around 40–45 minutes in laminar flow, 15–20 minutes for turbulent flow, and even more than an hour in the case of a transitional flow regime. Basically, the time taken to reach the steady state depends on both the mass flow rate and the heat flux. More heat flux and a lower flow rate will take longer than a high flow rate and low heat flux. The experiments were run in increasing order of mass flow rate and in reverse order of flow rate to see the hysteresis loss. Even though the hysteresis loss is small in the turbulent regime, moderate in the laminar regime, and a little higher in the transitional regime, it was decided to run the experiments in the order of increasing flow rate because it takes longer to reach steady state in the opposite order and there are more runs. The experiments can be performed for a minimum of  $Re = 300$  and a maximum of  $Re = 15000$  in aiding flow and  $Re = 500 - 15000$  in opposing flow. The flow rates were adjusted by controlling the needle valve, and the heating was controlled by regulating the voltage and current in the DC power supply. Once the steady state was reached, the dye was sent through the syringe pump and the flow patterns were visualized by a Digital Single Lens Reflex (DSLR, Canon EOS 300D) camera.

#### 4.5 Uncertainties

The experimental uncertainties were calculated as per the method suggested by Venkateshan [119] for the measured and derived quantities. The details of the uncertainty calculations are discussed in Appendix B. However, the list of equipment, the range of measurements, and their accuracies are listed in Table 4.1. Based on these accuracies, the uncertainties are obtained for the derived parameters.

**Table 4.1** List of the instruments, their operating ranges, and associated uncertainties

Equipment/Quantity	Range	Uncertainty
Thermocouples (T-type)	0 – 150 °C	±0.11 °C
RTD (PT 100)	0 – 100 °C	±0.11 °C
Coriolis mass flowmeter	0-450 LPH	1.1-2.54 %
DPT	0-5000 Pa	±0.055 % of span
DC Source (Voltage)	0-24 V	±0.1 V
DC Source (Current)	0-350 A	±1 A
$f$	-	2.3-14.6 %
$Nu$	-	9.1-20.7 %

The uncertainties calculated for the Reynolds number based on the mass flow rate is 1.1 % in the laminar, 2.54 % in the transitional and 1.54 % in the turbulent regime. The Nusselt number uncertainties are higher, and it is 9.1 % in the laminar, 20.7 % in the transitional and 13.2 % in the turbulent regime.

## 4.6 Validation

The validation of the experimental results for the simultaneously developing forced and mixed convection flow regime was done hydrodynamically as well as thermally. For thermal validation constant heat flux boundary condition was considered.

### 4.6.1 Hydrodynamic validation

The experimental set-up was first validated for the cold-run case, both in aiding and opposing flows (Figure 4.15). The friction factor ( $f$ ) results are compared for values varying  $Re$  from 494 to 15053 at zero heat flux ( $q \dot{=} 0 \text{ W/m}^2$ ). The fully developed flow results are compared with the Poiseuille equation [105] and Blasius equation [105] in the laminar and turbulent flow regimes. Since the focus of the current experiments is on developing flows, the results of the laminar developing flow are compared to the correlations of Shah [120] and Tam *et al.* [77], and the results of the turbulent developing flow are compared to the correlations of Phillips [121]. Thereafter, the present results are also compared with the existing experimental results of Everts [118] for laminar, transitional, and turbulent flows which is applicable for a horizontal tube. The results of this study compare well with Shah's correlation [120], Poiseuille's equation [105], Tam *et al.*'s correlation [77], Blasius' correlation [105], and Phillips'

## 4.6 Validation

correlation [121]. The largest difference is 7.6% with Shah's correlation [120], 27.8% with Poiseuille's equation [105], 18.8% with Tam *et al.*'s correlation [77], 8.8% with Blasius' correlation [105], and 13% with Phillips' correlation [121]. The reason for a higher deviation from the Poiseuille equation in the laminar flow and a relatively closer agreement with the Blasius equation in the turbulent flow is expected. This is because the present experiments in the laminar flow regime ( $Re = 500$  to  $2300$ ) are mainly in the developing regime, while the experiments in the turbulent flow regime ( $5000 < Re < 15000$ ) fall in the fully developed region. Based on the hydrodynamic entry length for a laminar pipe flow ( $\frac{L}{D} \geq 100$ ), the length required to be fully developed is 1 m for a pipe diameter of 10 mm. In the present study, the pressure taps are situated at the entry and exit of the tube, which indicates that most of the laminar regime is developing. The fully developed flow is only possible with high Reynolds numbers where the flow becomes turbulent, and the entry length is short. In general, the hydrodynamic entry length for a turbulent flow is  $L_h = 10D$ . In this aspect, it can be said that the experimental set-up is well suited for doing experiments in the simultaneously hydrodynamically and thermally developing flow regime of a vertical tube.

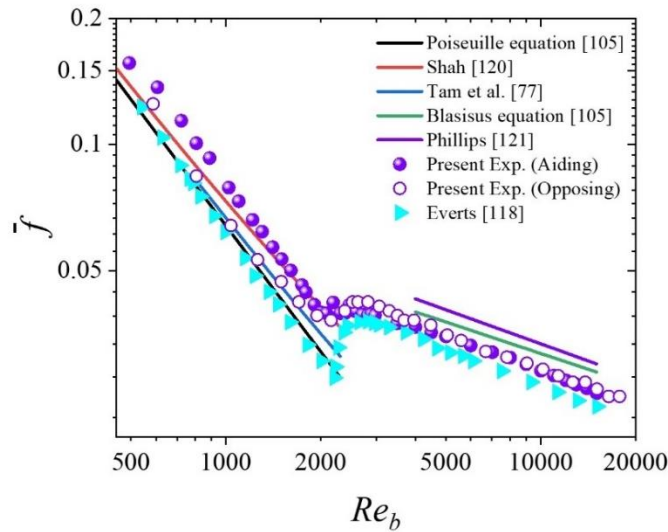


**Figure 4.15** (a) Hydrodynamic ( $f$  vs.  $Re$ ) validation plot for aiding and opposing flow with zero heat flux

### 4.6.2 Thermal validation

The heat transfer results were validated in terms of Nusselt numbers ( $Nu$ ) with varying Reynolds numbers ( $Re$ ) at different fixed Richardson numbers ( $Ri$ ). For forced convection experiments, the  $Ri$  was kept lower than 0.05. At the same time, it was also to be kept in mind that the inlet and outlet temperature difference should not be too small

so that it goes beyond the uncertainty limit of the measuring instruments. The aiding and opposing flow comparison results are presented in Figure 4.16. Laminar forced convection  $Nu$  was compared with the Nusselt number obtained from the correlation of Shah and London [122] and turbulent forced convection  $Nu$  with the correlation given by Gnielinski [123], Ghajar and Tam [75], which are applicable for a developing flow, and Dittus-Boelter [9], Sieder-Tate [83], and Meyer *et al.* [83], which are applicable for fully developed flows. The average deviation with the correlation of Shah and London [122] is 5.2%, Dittus-Boelter [9] is 6.9%, Gnielinski [123] is 16.9%, Ghajar and Tam [75] are 13.1%, Sieder-Tate [83] is 14.93%, and Meyer *et al.* [83] is 18%. The experimental results were also compared with my simulations, and they were found to be well in agreement with an average deviation of 7.8%. In the present validation, the experiments were also conducted for laminar, transitional, and turbulent regimes by varying  $Re$  and  $Gr$  keeping the  $Ri$  fixed value at 0.05. The range of heat flux for  $Re_b=537$  to 17248 at  $Ri = 0.05$  is 333 W/m<sup>2</sup> to 124201 W/m<sup>2</sup> in aiding flow, and for  $Re_b = 767$  to 12978 at  $Ri = 0.05$ , it is 624 W/m<sup>2</sup> to 116794 W/m<sup>2</sup> in opposing flow.

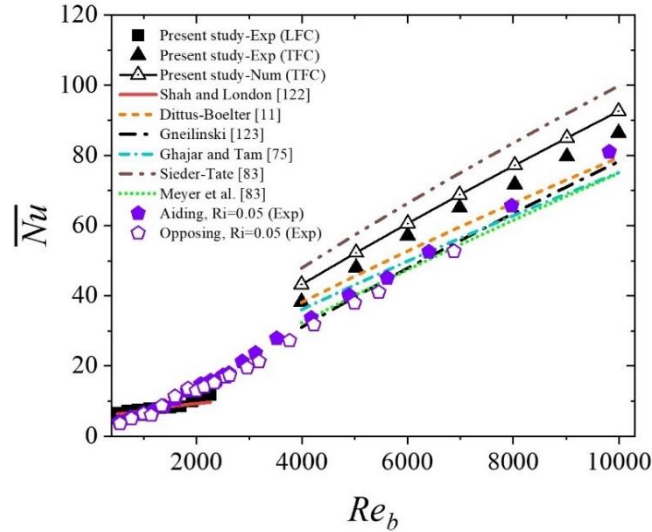


**Figure 4.16** (a) Thermal ( $Nu$  vs.  $Re$ ) validation plot for aiding and opposing flow with negligible heat flux

#### 4.6.3 Laminar forced convection

To maintain forced convection with uniform heat flux in a laminar flow, the heat flux is to be kept low so that the free convection effect becomes negligible. The average  $Nu$  is calculated for a range of  $Re_b$  varying from 508 to 2267 (Figure 4.17) at a very low heat flux of 950 W/m<sup>2</sup>. For the specified heat flux, the difference between inlet and outlet water temperatures varies between 2.4 °C and 0.5 °C, respectively. The nondimensional

## 4.6 Validation

hydrodynamic ( $L_h/D$ ) and thermal ( $L_t/D$ ) entry lengths required to be 25 and 170 for a tube of diameter,  $D = 0.01$  m when  $Re=500$  and  $Pr=6.8$ . Hence, the present experimental phase will mostly lie in the developing regime with  $Re = 500$  and above. Therefore, the results are compared with the correlation given by Shah and London [122] for developing flows. It has been found that the average deviation is 5.2% until  $Re=1922$ , and beyond that, the results deviate from Shah and London's [122] correlation.

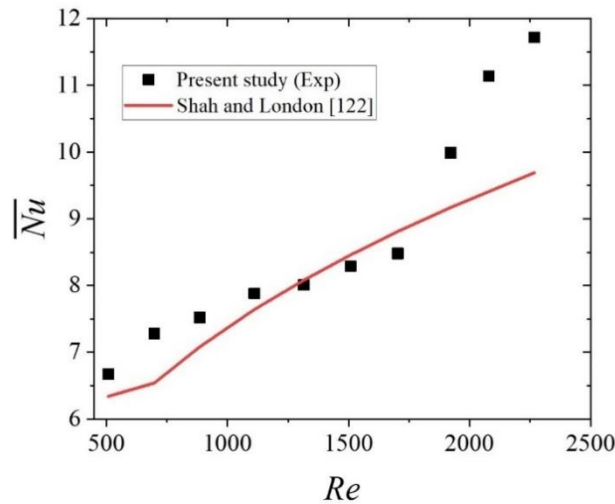


**Figure 4.17** Laminar forced convection validation plot ( $Nu$  vs.  $Re$ ) for aiding flow at heat flux ( $\dot{q}$ ) of  $950 \text{ W/m}^2$

To get the  $Nu$  value for fully developed flow conditions, it is possible at very low  $Re$  such as 300 at a heat flux of  $450 \text{ W/m}^2$  (as shown in Figure 4.18). At this condition, the nondimensional thermal entry length ( $L_t/D$ ) required to be fully developed is 105; hence, the last thermocouple station can be considered the fully developed region, and the local  $Nu$  at that length can be assumed to be fully developed. In that case, the wall and mean temperature variation are shown to ensure that the flow is still developing or has reached a fully developed condition. It is found that the last temperature reading can be taken as the fully developed value.



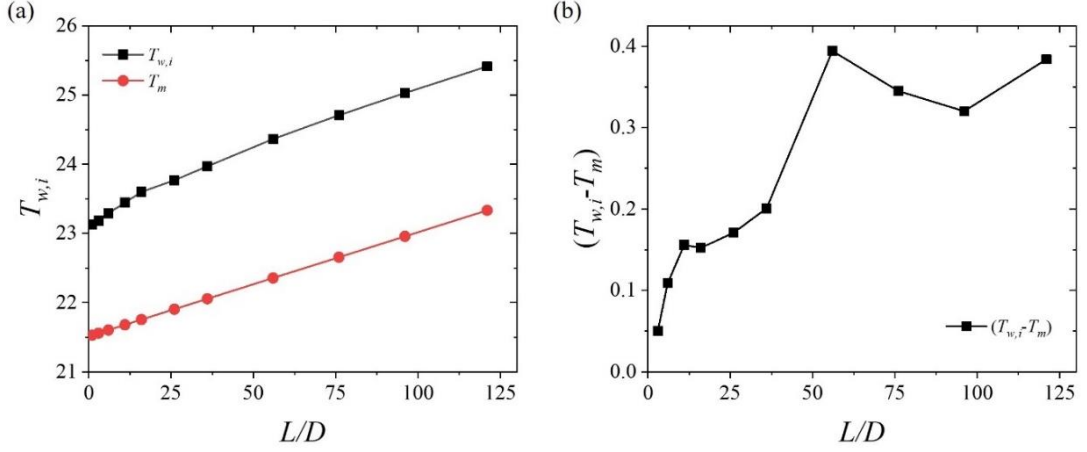


**Figure 4.18** Axial variation of (a) wall ( $T_w$ ) and mean ( $T_m$ ) temperature and (b) wall and mean temperature difference ( $T_w - T_m$ ) at  $Re = 300$  at heat flux ( $\dot{q}$ ) of  $450 \text{ W/m}^2$  in laminar forced convection for aiding flow

The  $Nu$  value for fully developed flow that can be achieved in the experiment is 3.89 (Figure 4.19), which is deviating by  $\sim 12.5\%$  from the theoretical  $Nu$  value of 4.364 obtained for incompressible, laminar, fully developed flow through a circular pipe subjected to constant heat flux conditions.

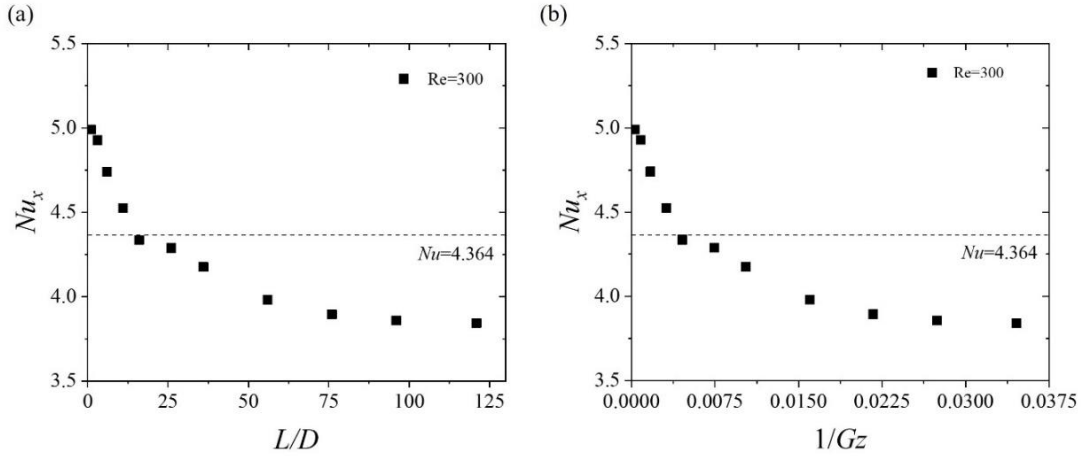


**Figure 4.19** Local (a)  $Nu$  vs.  $L/D$  and (b)  $Nu$  vs.  $1/Gz$  variation for  $Re = 300$  at heat flux of  $450 \text{ W/m}^2$  in laminar forced convection for aiding flow

#### 4.6.4 Turbulent forced convection

To keep the free convection effect to a minimum, the heat flux is maintained at a lower value so that the  $Ri$  remains less than 0.1. In the present study of turbulent forced convection (Figure 4.20), the  $Re_b$  varying from 3992 to 9993 at a heat flux of  $8000 \text{ W/m}^2$ , for which  $Ri$  varies from 0.017 to 0.003. The inlet and outlet water temperature differences obtained for this flow range are  $2.5^\circ\text{C}$  to  $0.9^\circ\text{C}$ . Since the thermal entry length in the turbulent mixed convection is found to be within  $L/D \sim 20$  [110], the fully

## 4.6 Validation

developed condition can be easily achieved. The average  $Nu$  is compared with the popular correlations of Dittus-Boelter [9], Sieder-Tate [83] for fully developed flows, and Gnielinski [123], Ghajar and Tam [75], and Meyer *et al.* [83] for developing flows. The average deviation found with Dittus-Boelter [9] is 6.99%, Sieder-Tate [83] is 14.93%, Gnielinski [123] is 16.9%, Ghajar and Tam [75] is 13.09%, and Meyer *et al.* [83] is 18%. Till date, the Gnielinski [123] correlation has been found to be the most reliable correlation for the present study. The experimental results were also compared with the present numerical results, and a 7.8% deviation was found.

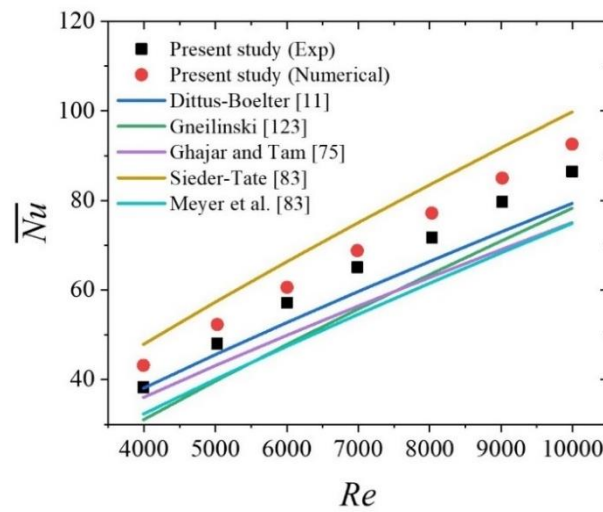


**Figure 4.20** Thermal ( $Nu$  vs.  $Re$ ) validation plot for aiding and opposing laminar, transitional, and turbulent mixed convection at heat flux ( $\dot{q}$ ) of  $8000 \text{ W/m}^2$

### 4.6.5 Transitional forced convection

To validate the transitional regime, the heat flux must lie between laminar and turbulent forced convection heat fluxes, keeping in mind that  $Ri$  should be less than 0.1. The range of bulk Reynolds numbers ( $Re_b$ ) from 2013 to 3960 at a heat flux of  $4500 \text{ W/m}^2$  is used for the validation of transitional forced convection results (Figure 4.21). This range has been decided for validation based on the observation of the  $f$  vs.  $Re$  plot (Figure 4.15) for the no-heat flux run of experiments. In this specified range of parameters, the  $Ri$  varies from 0.038 to 0.01. The inlet and outlet water temperature differences were limited to  $2.8^\circ\text{C}$  and  $1.4^\circ\text{C}$  for the specified range of heat flux. There are many correlations available for laminar and turbulent forced convection flows as compared to transitional forced convection flows. The first correlation in the transitional flow regime was given by Hausen [124] based on the experimental data of Sider and Tate [83]. However, Bertsche *et al.* [125] and many others found that their experimental data



deviated from the correlation given by Hausen [126] in 1959. In the late 20<sup>th</sup> century, the correlations given by Gnielinski [123] and Churchill [87] for forced convections were applicable to developing and fully developed conditions of transitional flow. Churchill tried to propose a single correlation to obtain a heat transfer coefficient that is applicable for the entire flow regime: laminar, transitional, and turbulent. The accuracy gets compromised in it, in contrast to Gnielinski's [123] correlation, which is particularly applicable for transitional and turbulent flow regimes (for  $Re > 8000$ ). Tam and Ghajar [86] mentioned that the correlation proposed by Churchill taking 249 experimental data points with a 20% deviation can be more accurate if more data in the transitional regime is obtained in the future. Till date, Gnielinski's [127] correlation is a better all-round correlation to calculate the heat transfer coefficient in forced convection for the transitional and turbulent flow regimes. A comprehensive work by Taler [126] had proposed a new correlation to find the heat transfer coefficient for transitional and turbulent flow regimes that is applicable for both constant heat flux and constant surface temperature boundary conditions with air ( $Pr = 0.7$ ) as the working fluid.

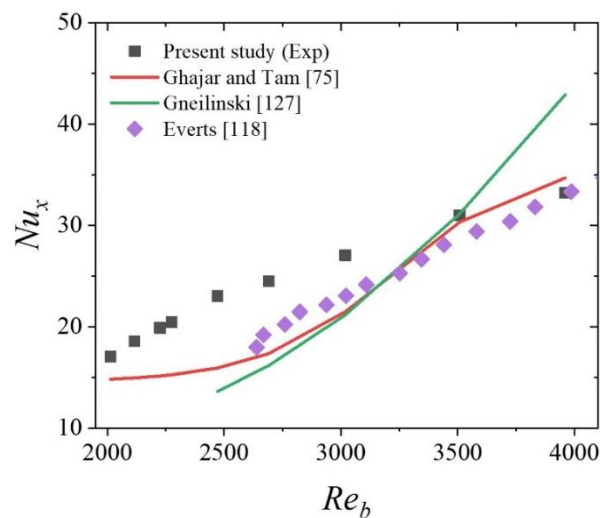


**Figure 4.21** Thermal ( $Nu$  vs.  $Re$ ) validation plot of transitional mixed convection regime for aiding flow at heat flux ( $\dot{q}$ ) of  $4.5 \text{ kW/m}^2$

The average  $Nu$  is validated with the correlations of Ghajar and Tam [75], Gnielinski [127], and the experimental results of Everts [118]. The maximum deviation of 27%

## 4.7 Conclusions

with Ghajar and Tam [75] and 44% with Gnielinski [127] is obtained because these correlations are developed for air or water flow through long horizontal tubes. The experimental data of Everts [118] is also for fully developed flows through a horizontal tube.

## 4.7 Conclusions

The experimental set-up, individual components, data reduction method, experimental procedure, and uncertainty analysis have been explained in detail. The design and fabrication of each component were described with a schematic as well as an assembled photographic view of the part. The experimental set-up was built as per the flexibility to run and suitability of conducting experiments both in aiding and opposing flows. The measurement techniques of pressure drop, temperature, mass flow rate, and electrical power were documented. The uncertainty of the measured and derived quantities was obtained and tabulated. Finally, the experimental results for aiding and opposing, developing and developed flows of laminar, transitional, and turbulent regimes were presented. The laminar, transitional, and turbulent flows were validated against the existing available correlations based on the experimental data for developing and fully developed flows. Due to length constraint the experimental regime of the laminar and transitional flows was limited in the developing flow regime, whereas the turbulent flow measurements could be performed in fully developed states. The present friction factor results are in good agreement with the correlation given by Shah [120], with an average deviation of 7.6% in the laminar flow and an average deviation of 8.8% with the correlation of Blasius [105]. Similarly, the average Nusselt numbers are deviating by 5.2% with the correlation of Shah and London [122] in the laminar regime and 16.9% with the Gnielinski [123] correlation in the turbulent regime. The transitional regime study in a vertical tube was rare, and the present results were compared with the correlations of Ghajar and Tam [75], Gnielinski [127], and the experimental results of Everts [118] available for horizontal tubes. The validation plot well indicates that when the transition starts, it (Figure 4.16) becomes stagnant for an increase, and then by the end of the transition, it continuously increases with a further increase of  $Re$ .

#### 5.1 Introduction

In this chapter, numerical study is conducted to analyse the flow characteristics and heat transfer behaviour in the developing and fully developed regime of laminar mixed convection in a vertical tube considering the buoyancy-assisting and -opposing effects. The aim is to investigate the effect of  $Gr$ ,  $Re$  and  $Ri$  on the pressure drop and heat transfer through a vertical tube subjected to constant heat flux from the walls for both buoyancy-assisting and -opposing flows. In addition to the fully developed state, the thermal and hydrodynamic features in the developing region are also presented. The variation of hydrodynamic and thermal entry length with the variation of  $Gr$  is explored for both buoyancy-aided and opposed cases. Finally, the correlations of friction factor ( $f$ ) and Nusselt number ( $Nu$ ) with the governing parameters like  $Re$ ,  $Gr$  and  $Ri$  which are applicable for developing as well as developed flow is discussed.

#### 5.2 Numerical results on laminar mixed convection

Mixed convection in a vertical tube with test fluid water was characterized by different parameters like  $Re$ ,  $Gr$  and  $Ri$ . After the grid independence test, the simulations were performed with optimum grid size. The  $L/D$  ratio was decreased from 1000 to 500 in further simulations for two reasons. Besides reducing the computational time, the  $L/D$  was reduced to avoid the possibility of exceeding boiling temperature at ambient atmospheric pressure. For example: with the present domain of study at  $Ri = 1$ ,  $Re = 250$ , inlet temperature ( $T_i = 20\text{ }^{\circ}\text{C}$ ) and constant heat flux ( $\dot{q}=1838\text{ kW/m}^2$ ), the outlet water temperature reaches  $55\text{ }^{\circ}\text{C}$  at  $L/D = 500$ . For the same conditions, the outlet temperature will be  $110\text{ }^{\circ}\text{C}$  at  $L/D = 1000$ . The heat transfer, pressure drop and flow characteristics were analysed with the range of parameters  $100 \leq Re \leq 2300$ ,  $10^3 \leq Gr \leq 7.935 \times 10^6$ ,  $0.1 \leq Ri \leq 1.5$  and  $Pr = 7$  for both assisting and opposing flows.

## 5.2 Numerical results on laminar mixed convection

### 5.2.1 Buoyancy-assisted flow

#### 5.2.1.1 Influence of heat flux ( $\dot{q}$ )

Figures 5.1(a) and (b) show the centreline velocity along tube length and velocity profiles in fully developed region respectively for three different cases of heat flux:  $\dot{q}=0$  kW/m<sup>2</sup>, 1 kW/m<sup>2</sup> and 2 kW/m<sup>2</sup> at  $Re = 250$  and  $Ri = 0.27, 0.54$  and  $1.09$ . From Figure 5.1(a), it was observed that the centreline velocity in both developing and fully developed flow decreases with increasing heat flux. Moreover, the nature of evolution of centreline velocity along  $L/D$  in presence of wall heat flux is different from no heat flux condition. In no heat flux condition, the centerline velocity goes on increasing along the length and then assumes a steady state value. However, for both the cases of non-zero heat flux, centreline velocity assumes a peak value and then settles down to a lower value in fully developed region. Initially as the fluid enters, its centreline velocity increases and reaches to a maximum due to no slip boundary condition. However, with increase in  $L/D$ , due to considerable free convection effect induced by wall heat flux, velocity adjacent to the tube wall is enhanced. In order to conserve the mass flow rate, centreline velocity is decreased. The decrease in centreline velocity is by  $\sim 15\%$  at  $\dot{q}=1$  kW/m<sup>2</sup> to  $\sim 26\%$  at  $\dot{q}=2$  kW/m<sup>2</sup> as compared to the ideal parabolic profile ( $\dot{q} = 0$ ). Due to symmetric nature of the problem, the velocity profile in one half of the tube section for different magnitudes of heat flux was presented in Figure 5.1(b). The velocity profile is the usual parabolic profile for no heat flux condition. This is in accordance with the velocity profiles observed in previous experimental studies [93]. For the fully developed state, the velocity profile no longer changes along the axial length. Also, the  $L/D$  over which the fully developed state is attained, increases from  $\sim 17$  for  $\dot{q}=0$  kW/m<sup>2</sup> to  $\sim 82$  and  $\sim 128$  for  $\dot{q}=1$  kW/m<sup>2</sup> and  $2$  kW/m<sup>2</sup> respectively (Figure 5.1(a)). With increase of heat flux, the velocity profiles undergo evolution along the tube length for a greater distance, thereby increasing the entry length.

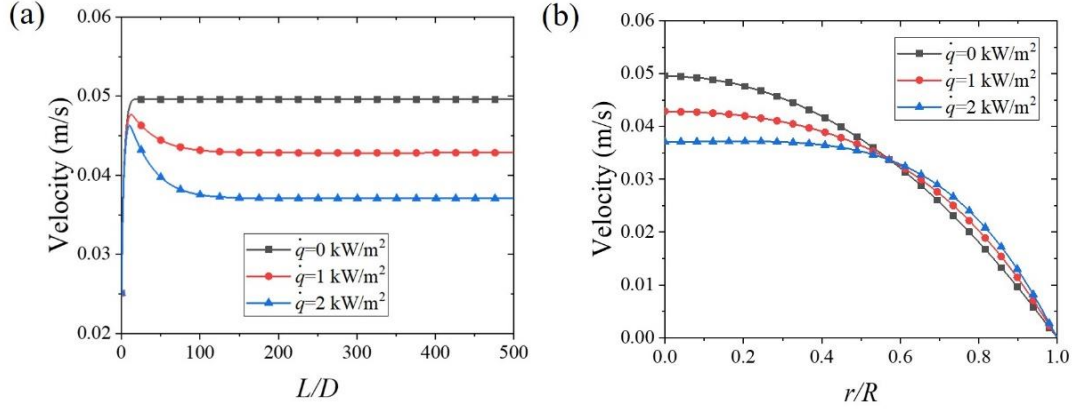


**Figure 5.1** (a) Centreline velocity and (b) velocity profile at  $L/D = 500$  with different heat flux ( $\dot{q}$ ) 0 kW/m<sup>2</sup>, 1 kW/m<sup>2</sup> and 2 kW/m<sup>2</sup> at  $Re = 250$ . Magnified view of the velocity profiles in  $0.5 \leq r/R \leq 0.70$  are provided in Figure A.1. Developing and developed velocity profiles and their magnified view for one case  $\dot{q}=2$  kW/m<sup>2</sup> is also provided in Figure A.2.

Subsequently the centerline temperature and the non-dimensional temperature profile across the tube section for thermally developed flow are plotted in Figures 5.2(a) and (b) respectively. As expected, with the increasing wall heat flux, centerline temperature increases along the tube length. Also, the difference between the inlet and bulk fluid temperature increases. Hence, the temperature gradient increases with increasing the wall heat flux (Figure 5.2(b)).

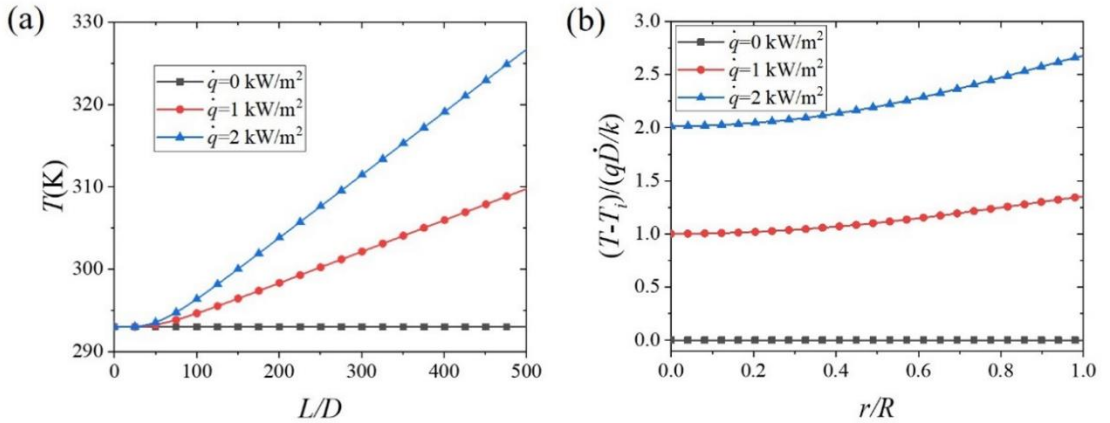


**Figure 5.2** (a) Centreline temperature and (b) non-dimensional temperature profile with different heat flux ( $\dot{q}$ ) 0 kW/m<sup>2</sup>, 1 kW/m<sup>2</sup> and 2 kW/m<sup>2</sup> at  $Re = 250$

The local skin friction coefficient ( $C_f$ ) increases with increasing the heat flux (Figure 5.3(a)). Compared to the no heat flux case the fully developed  $f$  increases by  $\sim 25\%$  and  $\sim 47\%$  at  $\dot{q}=1$  kW/m<sup>2</sup> and 2 kW/m<sup>2</sup> respectively. The increasing trend is due to the

## 5.2 Numerical results on laminar mixed convection

higher velocity gradients caused by the assisting effect of free convection in presence of higher heat flux (refer Figure A.3). The inverse of a non-dimensional number called Graetz number ( $Gz$ ) determines the thermal entrance length for hydrodynamically fully developed and thermally developing flow [12]. Contrary to forced convection case where thermally developed flow is attained for  $1/Gz = 0.05$ , our mixed convection cases showed evidence of developing flow beyond  $1/Gz = 0.05$ . The variation of local  $Nu$  with  $1/Gz$  (Figure 5.3(b)) shows an increase in local  $Nu$  with the increase of heat flux. The fully developed  $Nu$  increases by  $\sim 8\%$  and  $\sim 16\%$  at  $\dot{q}=1 \text{ kW/m}^2$  and  $2 \text{ kW/m}^2$  respectively as compared to the no heat flux case. The increasing trend of  $Nu$  with increasing heat flux is due to the higher heat diffusion induced by the free convection effect at higher heat fluxes. As the heat flux increases, the thermal boundary layer also grows faster due to free convection effect that will lead to higher  $Nu$  in the developing region.

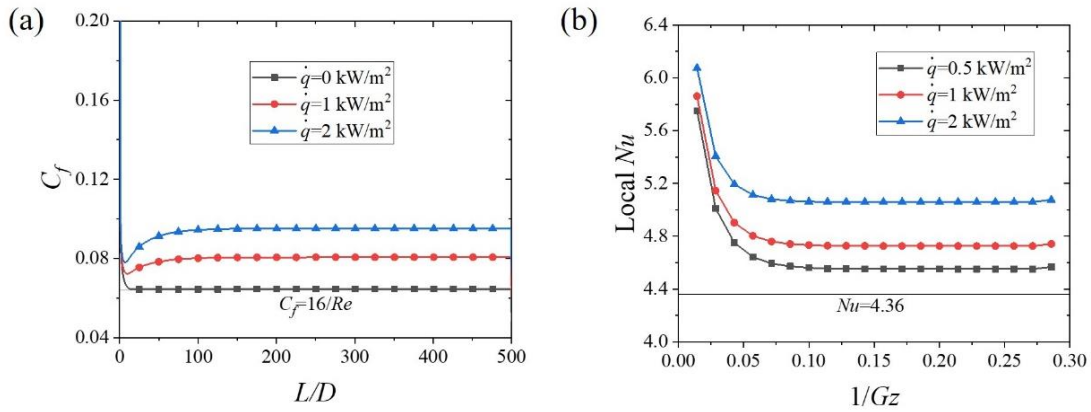


**Figure 5.3** (a) Local  $C_f$  plot, Enlarged view of Figure 5.1(b) adjacent to the wall i.e.  $0.7 \leq r/R \leq 1$  are presented in A.3; (b) local  $Nu$  vs.  $1/Gz$  plot with different heat flux ( $\dot{q}$ )  $0 \text{ kW/m}^2$ ,  $1 \text{ kW/m}^2$  and  $2 \text{ kW/m}^2$  at  $Re = 250$ . The corresponding wall ( $T_w$ ) and mean ( $T_m$ ) temperature variation plot for one case is presented in Figure A.4

### 5.2.1.2 Influence of $Ri$

Richardson number ( $Ri = Gr/Re^2$ ) is a non-dimensional number denoting the ratio of buoyancy force to the inertia force. Therefore,  $Ri$  plays a significant role in understanding the impact of free convection on forced convection. The influence of  $Ri$  on mixed convection can be understood with the various flow profiles and thermal plots for a range of  $Ri = 0 - 1.5$  [13] at fixed  $Re$ . Since the modified  $Gr$  contains the heat flux term in the numerator, variation of heat flux leads to variation of  $Ri$  at a constant  $Re$ . At  $Ri \sim 0$  (negligible heat flux), forced convection is dominant and usually the role

of free convection is neglected. At  $Ri = 1.5$  (buoyancy force is 50 % higher than the inertia force), free convection will have significant role. The centreline velocity variation and velocity profile have been plotted in this range to understand the impact of buoyancy effects. Figure 5.4(a) shows decrease in centreline velocity in assisting flow with the increase of  $Ri$  from 0 to 1.5 at  $Re = 250$ . The decreasing trend of centerline velocity is more evident in Figure 5.4(b). The maximum velocity at  $Ri = 1.5$  decreases up to ~34 % as compared to the case when  $Ri \sim 0$  for fixed  $Re = 250$ . With increasing  $Ri$ , the buoyancy effect is more predominant and consequently accelerating the flow near the wall compared to the cases at lower  $Ri$ . This phenomenon is expected as  $Ri$  as well as buoyancy effects will increase with  $Gr$  for fixed  $Re$ . This behaviour is identical to Figure 5.1(b) where the centerline velocity decreases with increasing wall heat flux.

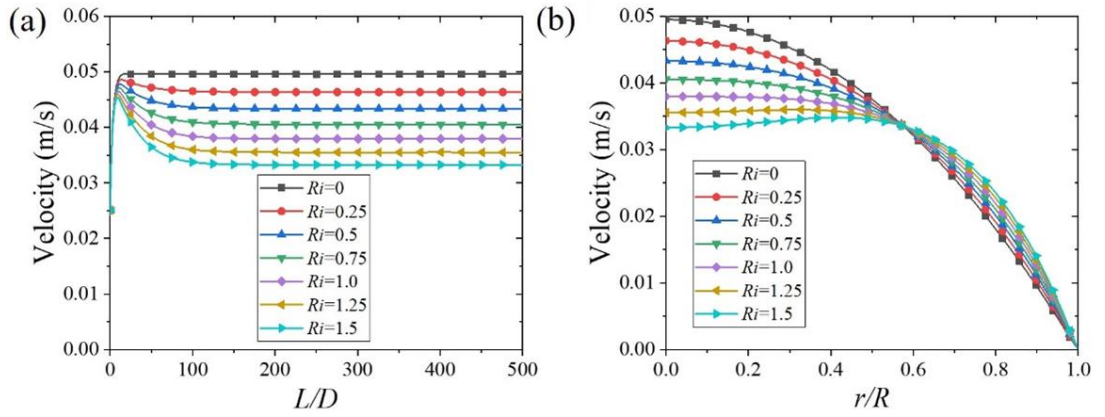


**Figure 5.4** (a) Centreline velocity and (b) velocity profile at  $L/D = 500$  for  $Re = 250$  and  $Ri = 0 - 1.5$ . Magnified view of the velocity profiles in  $0.5 \leq r/R \leq 0.70$  are provided in Figure A.5.

In the similar way the centreline temperature variation along the length and the dimensionless temperature profile have been plotted as shown in Figure 5.5(a) and (b) respectively. The centreline temperature (Figure 5.5(a)) as well as the temperature gradient (Figure 5.5(b)) near the tube wall increases with increasing  $Ri$ . This trend is like earlier observations presented in Figures 5.2(a) and (b) where centreline temperature and temperature gradient are increasing with increasing wall heat flux respectively.

## 5.2 Numerical results on laminar mixed convection

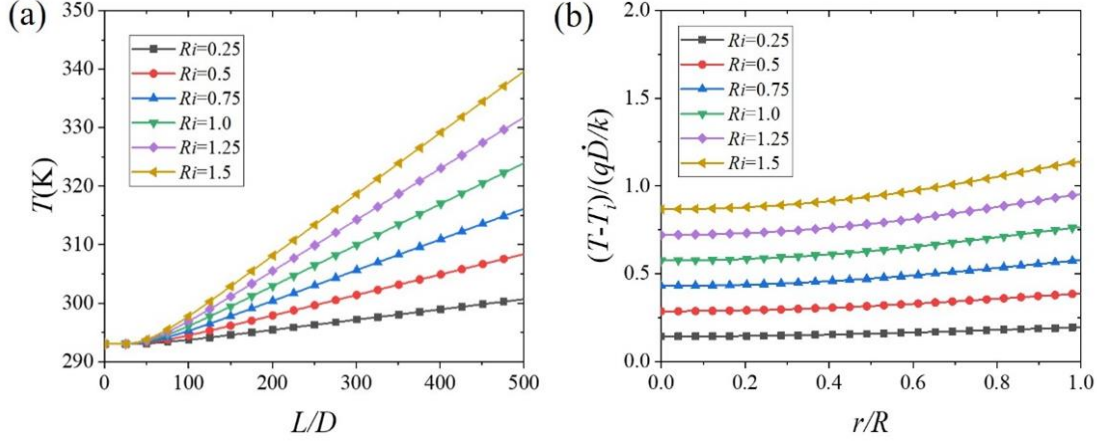


**Figure 5.5** (a) Centerline temperature (b) non-dimensional temperature profile at  $L/D = 500$  for  $Re = 250$  and  $Ri = 0.125 - 1.5$

Subsequently based on the velocity and temperature profile, the local  $C_f$  and  $Nu$  for various  $Ri$  (Figure 5.6) have been calculated. From the plot, it is evident that both the local  $C_f$  and local  $Nu$  are increasing with increasing  $Ri$ . The local  $C_f$  increases up to  $\sim 65\%$  whereas the local  $Nu$  increases by  $\sim 22\%$  at  $Ri = 1.5$  for fixed  $Re = 250$ . With the increasing velocity gradient near the wall, the friction factor increases with increasing  $Ri$ . Consequently, the heat transfer is also increasing simultaneously because of significant free convection effect with the increase of  $Ri$ . This produces increasing trend of local  $Nu$  with increasing the  $Ri$ . Similar trends of friction factor and Nusselt number dependence on  $Ri$  were also observed for  $Re = 350, 500$  and  $750$  (Figure A.10, A.11 and A.12).

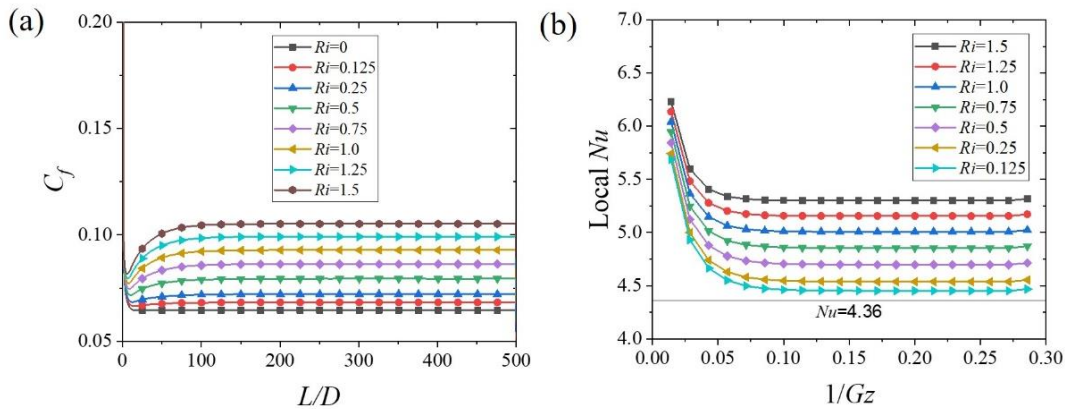


**Figure 5.6** Variation of (a) local  $C_f$  and (b) local  $Nu$  at  $Re = 250$  and  $Ri = 0.125 - 1.5$



### 5.2.1.3 Influence of $Re$

In this section the effect of  $Re$  in laminar regime have been quantified. Simulations are performed keeping the  $Ri$  constant as 0.1 and varying  $Re = 500, 750$  and  $1000$  with appropriate changes in the  $Gr$ . Here the effect of  $Re$  on the flow as well as heat transfer has been explained with various plots of velocity, temperature, local  $C_f$  and local  $Nu$ . It is clear in Figure 5.7(a), that the fluid velocity increases as the  $Re$  increases from 500 to 1000 at a fixed  $Ri$ . The reduction in centreline velocity compared to the no heat flux case i.e., the classical parabolic profile case increases with the increase of  $Re$ . The reduction in maximum velocity is  $\sim 7\%$  and  $\sim 13\%$  for  $Re = 500$  and  $1000$  respectively. For a fixed  $Ri$ , increase in  $Re$  results in increase of  $Gr$  and consequently increase of heat flux. This higher  $Gr$  increases the free convection effect and the temperature difference between the inlet and bulk fluid. Hence, the temperature gradient is also increasing for higher  $Re$  that can be seen in Figure 5.7(b).

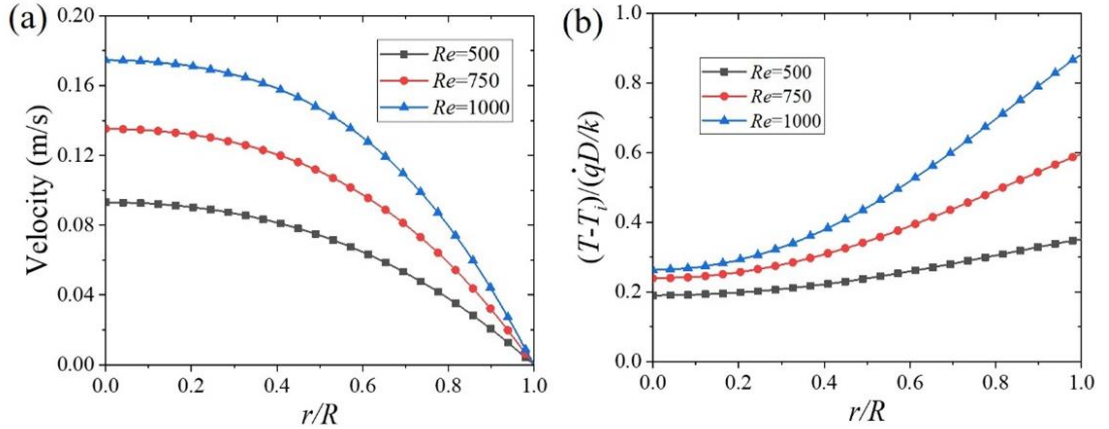


**Figure 5.7** (a) Velocity profile and (b) non-dimensional temperature profile at  $L/D = 500$  for  $Re = 500, 750$  and  $1000$  at  $Ri = 0.1$

Based on the velocity profiles at different locations, the local  $C_f$  values are calculated. Although, the local  $C_f$  decreases with increase of  $Re$  at a fixed value of  $Ri$  (Figure 5.8(a)), the local  $C_f$  values of laminar mixed convection are higher than the  $C_f$  of ideal parabolic velocity profile by  $10\%$  and  $20\%$  for  $Re = 500$  and  $1000$  respectively. This increase is because of the increase in velocity gradient adjacent the wall due to the higher  $Gr$  corresponding to the  $Re$  to keep  $Ri = 0.1$ . The local  $Nu$  at a fixed  $Ri$  in Figure 5.8(b) increases with the increase in  $Re$  since the free convection effect increases with the corresponding increase in  $Gr$ . The increment of  $Nu$  from the fully developed forced

## 5.2 Numerical results on laminar mixed convection

convection ( $Nu = 4.36$ ) is higher by  $\sim 4\%$  and  $\sim 8\%$  at  $Re = 500$  and  $1000$  respectively. Hence the rate of heat transfer increases with  $Re$  at a fixed  $Ri$ .

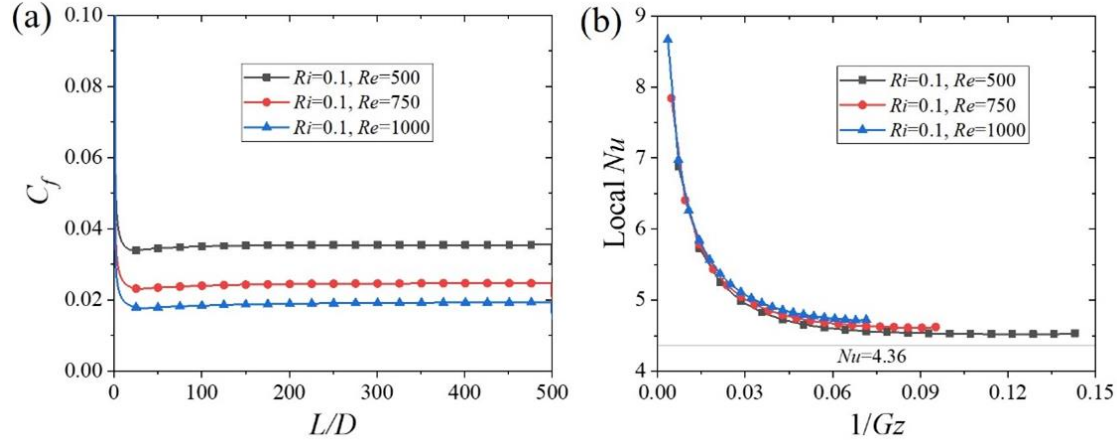


**Figure 5.8** (a) Local  $C_f$  plot and (b) local  $Nu$  plot at  $Ri = 0.1$  and  $Re = 500, 750$  and  $1000$ . Magnified view of local  $Nu$  plot for  $4 \leq Nu \leq 5$  is provided in Figure A.6.

In Figures 5.9(a) and (b) the variation of local  $Nu$  with respect to  $Re$  at different  $Ri$  has been plotted for developing and fully developed regime. It has been observed that the local  $Nu$  exhibits increasing trend with  $Re$  as well as  $Ri$ . For  $Ri = 0.2$ , the developing  $Nu$  is greater by  $\sim 30\%$  from that of the fully developed  $Nu$  at  $Re = 1000$  because of the increasing thermal boundary layer in the developing regime. These two plots clearly describe that the heat transfer in the developing flow is always higher as that of the fully developed flow.

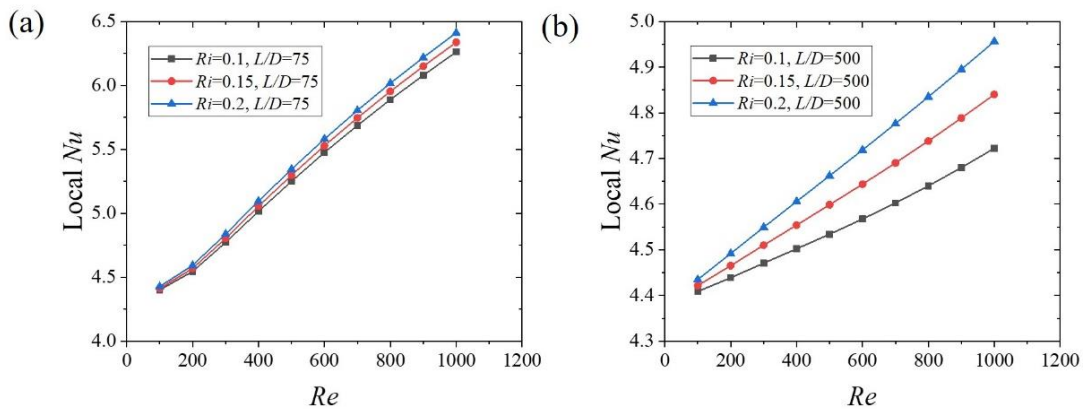


**Figure 5.9** (a) Developing and (b) fully developed  $Nu$  plot with increasing  $Re$  at different  $Ri$

The heat transfer characteristics is further analysed with another dimensionless number called Colburn  $j$ -factor ( $j = \frac{Nu}{Re.Pr^{1/3}}$ ). The purpose is to compare the heat transfer and

pressure drop together for varying  $Re$  in laminar mixed convection regime. The plot in Figure 5.10 compares the fully developed  $f$  and Colburn  $j$ -factors at a fixed  $Ri$  as a function of  $Re$ . The  $f$  and  $j$  both decreases with increasing  $Re$ , which is expected because of inverse proportionality. Furthermore, at a fixed  $Re$ , the  $f$  and  $j$  both increases with increase in  $Ri$ . That means the pressure drop as well as heat transfer increases with the increase of  $Ri$  as already shown in Figures 5.6(a) and (b) respectively.

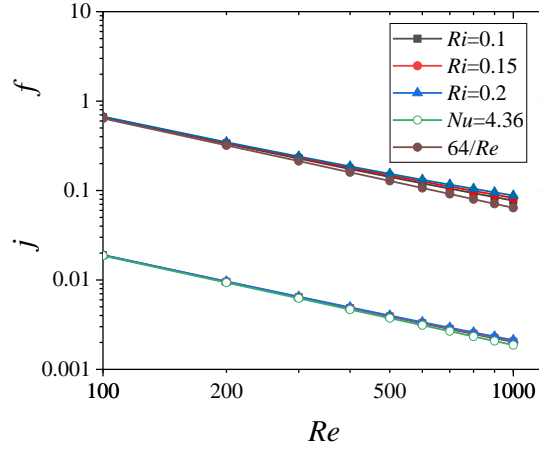


**Figure 5.10** Fully developed  $f$  and Colburn  $j$ -factor plot for varying  $Re$  at  $L/D = 500$  with different  $Ri$ . Magnified view of Colburn  $j$ -factor plot for  $800 \leq Re \leq 1000$  is provided in A.7.

In similar way, two more plots of Colburn  $j$ -factor have been obtained: Figure 5.11(a) is for increasing axial length at fixed  $Ri$  and Figure 5.11(b) is for increasing  $Ri$  at fixed axial length. In former case the  $j$ -factor decreases with the increase of axial length at a fixed  $Ri$  and approaches to the Colburn  $j$ -factor based on  $Nu = 4.36$  whereas the latter one reports the same idea as explained in Figure 5.10.

## 5.2 Numerical results on laminar mixed convection

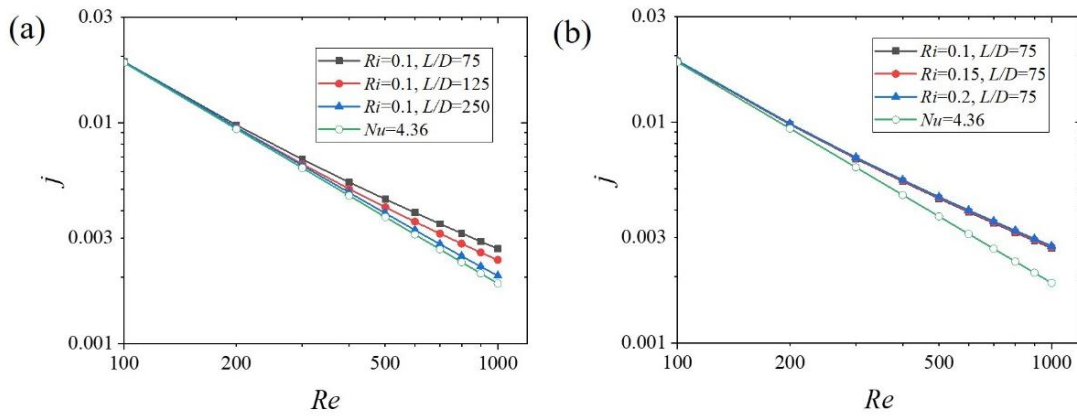


**Figure 5.11** Comparison between developing Colburn  $j$ -factor for (a) varying  $Re$  and  $L/D$  at fixed  $Ri = 0.1$  (b) varying  $Re$  and  $Ri$  at fixed  $L/D$  [Magnified view of Colburn  $j$ -factor plot for  $800 \leq Re \leq 1000$  is provided in Figure A.8].

### 5.2.2 Buoyancy-opposed flow

#### 5.2.2.1 Influence of heat flux

The influence of heat flux in case of buoyancy-opposed flows can be described with varying the heat flux  $0 \text{ kW/m}^2$ ,  $1 \text{ kW/m}^2$  and  $2 \text{ kW/m}^2$  and hence corresponding  $Ri = 0.27, 0.54$  and  $1.09$  at  $Re = 250$  like the buoyancy-assisted case. In buoyancy aided cases (Figure 5.1(a)), the centreline velocity first increases in developing region and then decreases to a steady state value. On the contrary, for buoyancy opposed case, the centreline velocity continuously increases and eventually becomes steady at fully developed flow condition (Figure 5.12(a)). Also, unlike buoyancy aided case (Figure 5.1(a)), the centreline velocity in the developed region increases with heat flux. As the fluid enters, the centreline velocity increases due to the no slip condition. Afterwards with the increase in  $L/D$ , because of the opposing buoyancy effect velocity near the wall decreases with increasing the heat flux. In order to conserve the mass flow rate across a tube cross section, the centreline velocity increases with increasing heat flux (Figure 5.12(b)). The velocity profile for non-zero heat flux cases in Figure 5.12(b) shows decrease in velocity near the tube wall and an increase at the centre of the tube to fulfil the continuity equation. The velocity increment compared to the no heat flux case increases with increasing heat flux i.e.  $\sim 15\%$  and  $\sim 34\%$  at  $\dot{q} = 1 \text{ kW/m}^2$  and  $2 \text{ kW/m}^2$  respectively. It is also evident from Figure 5.12(a); the development length increases from  $\sim 17$  at  $\dot{q} = 0 \text{ kW/m}^2$  to  $\sim 89$  and  $\sim 161$  with increase of heat flux at  $1 \text{ kW/m}^2$  and  $2 \text{ kW/m}^2$  respectively.

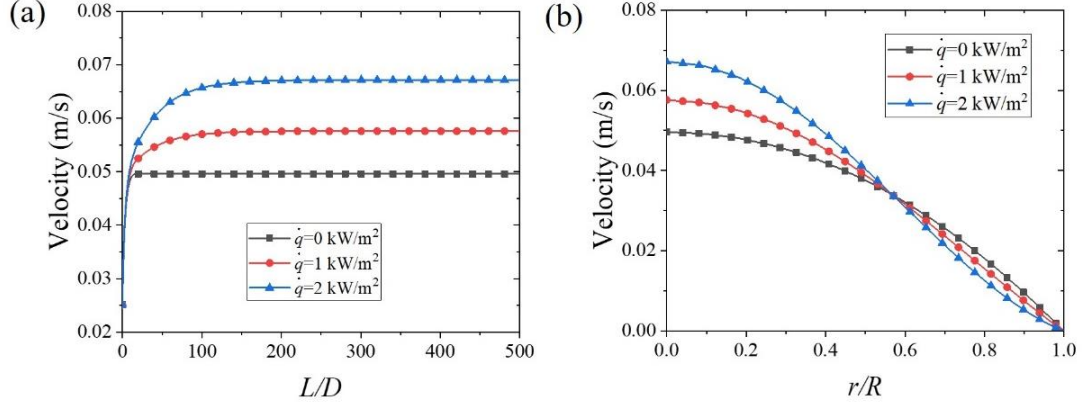


**Figure 5.12** (a) Centerline velocity and (b) velocity profile at  $L/D = 500$  with different heat flux ( $\dot{q}$ ) 0 kW/m<sup>2</sup>, 1 kW/m<sup>2</sup> and 2 kW/m<sup>2</sup> at  $Re = 250$ . Magnified view of the velocity profiles in  $0.5 \leq r/R \leq 0.70$  are provided in Figure A.1. Corresponding developing and developed velocity profiles and their magnified view for one case  $\dot{q} = 2$  kW/m<sup>2</sup> is also provided in Figure A.9.

Subsequently, the centreline temperature and the nondimensional temperature profile for three different heat fluxes have been plotted. The centreline temperature increases with the increase in heat flux. The difference in temperature gradient in Figures 5.13(a) and (b) clearly indicates the influence of heat flux. The gradient increases with the increase of heat flux because of the increase in inlet and the bulk fluid temperature difference due to the significant free convection effect caused by higher heat flux.

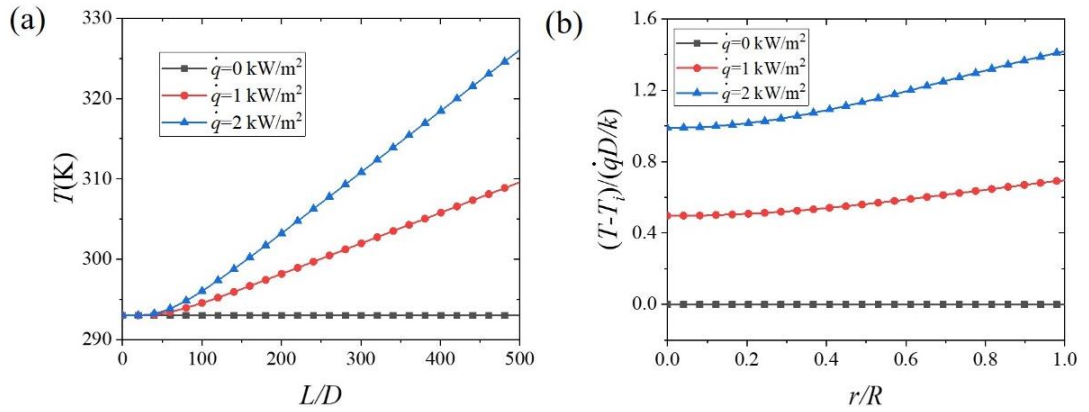


**Figure 5.13** (a) Centerline temperature and (b) non-dimensional temperature profile with different heat flux ( $\dot{q}$ ) 0 kW/m<sup>2</sup>, 1 kW/m<sup>2</sup> and 2 kW/m<sup>2</sup> at  $Re = 250$

Figure 5.14(a) indicates decrease of local  $C_f$  at higher heat flux. As the heat flux increases, the free convection effect pushes the velocity towards the centre which changes the velocity profile with decreasing gradient near the wall. Hence, the

## 5.2 Numerical results on laminar mixed convection

decreasing trend of  $C_f$  with increasing heat flux has been observed. Compared to no heat flux case, the fully developed  $f$  reduces by  $\sim 28\%$  and  $\sim 60\%$  at  $\dot{q}=1\text{ kW/m}^2$  and  $2\text{ kW/m}^2$  respectively. The local  $Nu$  plot in Figure 5.14(b) signifies that the heat transfer also decreases as the heat flux increases. The fully developed  $Nu$  reduces by  $\sim 8\%$  and  $\sim 17\%$  at  $\dot{q}=1\text{ kW/m}^2$  and  $2\text{ kW/m}^2$  respectively as compared to the no heat flux case. In buoyancy-opposing flow the upward motion due to free convection effect opposes the downward forced flow which basically reduces the velocity near the wall and hence diminishes the heat diffusion from the wall towards the centre. Thus, the opposing free convection effect impedes the heat transfer as the heat flux increases.

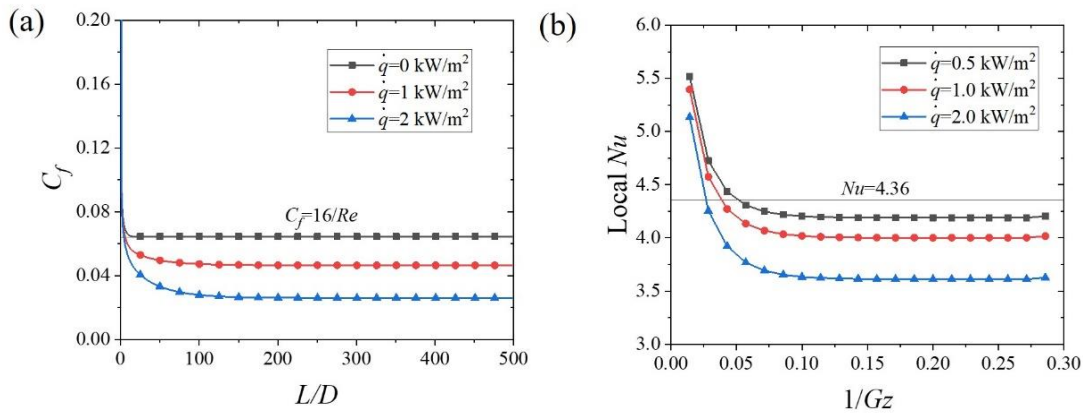


**Figure 5.14** (a) Local skin friction plot and (b) Local  $Nu$  plot with different heat flux ( $\dot{q}$ )  $0\text{ kW/m}^2$ ,  $1\text{ kW/m}^2$  and  $2\text{ kW/m}^2$  at  $Re = 250$ . Enlarged view of Figure 5.12(b) adjacent to the wall i.e.,  $0.7 \leq r/R \leq 1$  are presented in A.3 and the corresponding wall ( $T_w$ ) and mean ( $T_m$ ) temperature variation plot for various cases are presented in Figure A.4.

### 5.2.2.2 Influence of $Ri$

Like buoyancy-assisted flow, the influence of  $Ri$  in case of buoyancy-opposed flows are identified with the hydrodynamic and thermal results for a range of  $Ri = 0 - 1.5$  at fixed  $Re = 250$ . The results are opposite in nature in buoyancy-opposed flow as compared to buoyancy-assisted flow (Figures 5.4(a), (b)). The centreline velocity and velocity profile as shown in Figures 5.15(a) and (b) shows that the velocity at the centre of the tube increases whereas it decreases at the tube wall. With increasing  $Ri$ , increasing buoyancy effects decelerates the velocity near the wall to a higher extent and as a result, the centreline velocity accelerates. The maximum velocity increment at  $Ri = 1.5$  is almost  $50\%$  compared to the no heat flux case i.e.,  $Ri = 0$  for  $Re = 250$ .



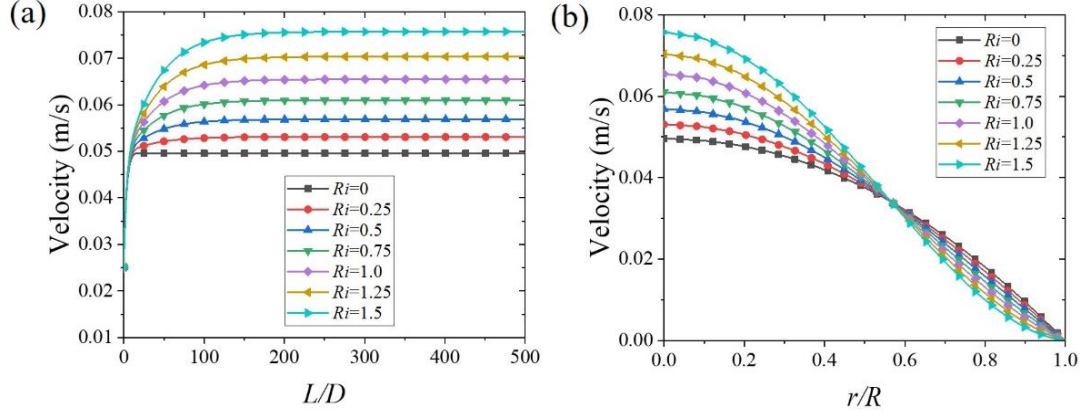


**Figure 5.15** (a) Centerline velocity and (b) velocity profile at  $L/D = 500$  for  $Ri = 0.0 - 1.5$  at  $Re = 250$ . Magnified view of the velocity profiles in  $0.5 \leq r/R \leq 0.70$  are provided in Figure A.5.

The centerline temperatures and the nondimensional temperature profiles with varying  $Ri$  are presented in Figures 5.16(a) and (b) respectively. The centreline temperature increases along the axial length with increasing  $Ri$ . Furthermore, the temperature gradient increases with increasing  $Ri$ . This is because of the added difference in inlet and bulk fluid temperature at higher  $Ri$ . At fixed  $Re = 250$ , as the  $Ri$  increases, the corresponding  $Gr$  also increases and hence the free convection effect increases due to which the difference in inlet and bulk fluid temperature increases and therefore the temperature gradient near the wall also increases. However, it must be noted that the thermal gradient is lesser in case of buoyancy-opposed cases compared to the buoyancy-aided cases.

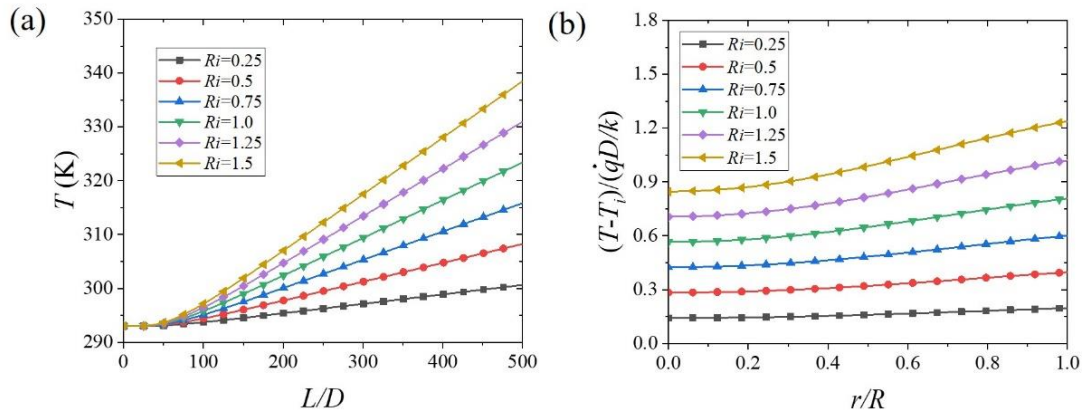


**Figure 5.16** (a) Centerline temperature (b) non-dimensional temperature profile for  $Ri = 0.25 - 1.5$  at  $Re = 250$

## 5.2 Numerical results on laminar mixed convection

The variation of local  $C_f$  plot shown in Figures 5.17(a) is just opposite to the assisted flow (Figure 5.6(a)). Due to decreasing velocity gradient near the tube wall with increasing  $Ri$  (Figure 5.15(b)), the friction factor values for fully developed condition decreased. The local  $Nu$  plot in Figure 5.17(b) is also showing an opposite trend of the buoyancy-assisted case (Figure 5.6(b)) i.e., it decreases with the increase of  $Ri$ . The local  $C_f$  decreases up to  $\sim 87\%$  whereas the local  $Nu$  decreases by  $\sim 25\%$  at  $Ri = 1.5$  compared to  $Ri \sim 0$  for fixed  $Re = 250$ . Similar to the effect of heat flux (section 5.2.1), due to the increasing buoyancy effect with increasing  $Ri$ , the velocity gradient near the wall keeps on decreasing in comparison to the pure laminar flow. This results in the decreasing trend of local  $Nu$  values with increasing  $Ri$  hence the heat transfer gets impaired. For the buoyancy-assisted flow, the local  $C_f$  and  $Nu$  magnitudes are higher than the  $Ri = 0$  case whereas these are lower than the  $Ri = 0$  case for the buoyancy-opposed flow. Similar trends were observed for both buoyancy-assisted and -opposed cases for  $Re = 350, 500$  and  $750$  (A.10, A.11 and A.12).

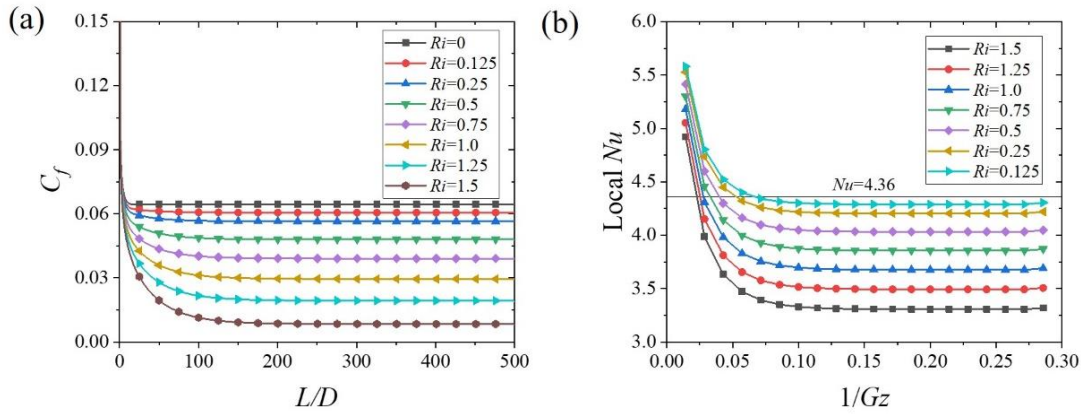


**Figure 5.17** Variation of (a) local  $C_f$  and (b) local  $Nu$  plot at  $Re = 250$  and  $Ri = 0.125 - 1.5$

### 5.2.2.3 Influence of $Re$

Like the buoyancy-assisted case, here the influence of  $Re$  on pressure drop and heat transfer is observed by varying  $Re$  from 500 to 1000 and keeping the  $Ri$  constant at 0.1. The velocity, temperature, local  $C_f$ ,  $Nu$  and Colburn  $j$ -factor plots for varying  $Re$  will be discussed in this section. The velocity profile shows that the fluid velocity increases as the  $Re$  increases from 500 to 1000 at fixed  $Ri$ . In buoyancy-opposing flow the velocity near the wall decreases because of the opposing effect of free convection whereas the velocity at the centre increases to satisfy the continuity. However, the maximum velocity (Figure 5.18(a)) is higher as compared to the laminar parabolic flow.



The maximum velocity is  $\sim 4\%$  higher at  $Re = 500$  and is  $\sim 7\%$  higher at  $Re = 1000$  compared to the classical parabolic flow. In order to keep  $Ri$  constant, when  $Re$  is increased, there is increase in  $Gr$ . Higher  $Gr$  results in higher free convection effects, thereby causing the increase in inlet and bulk fluid temperature and hence the temperature gradient increases with increasing  $Re$  (Figure 5.18(b)).

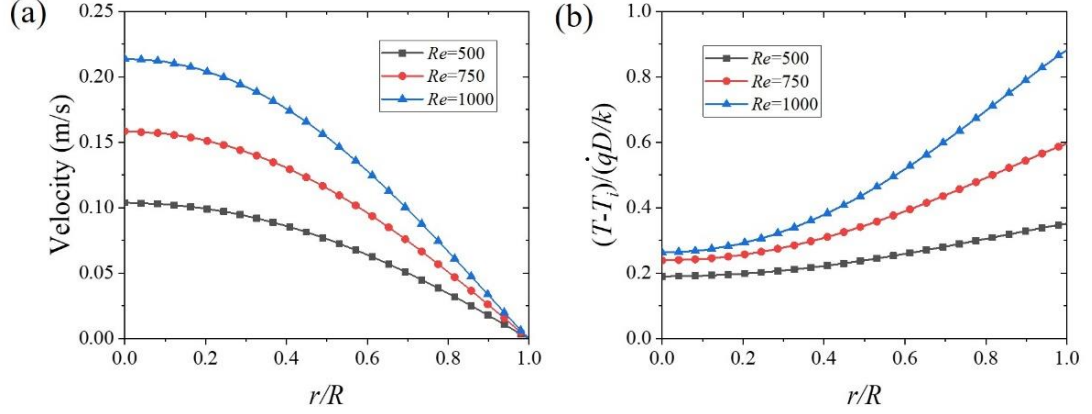


**Figure 5.18** (a) Velocity profile and (b) non-dimensional temperature profile at  $L/D = 500$  for  $Re = 500, 750$  and  $1000$  at  $Ri = 0.1$

Subsequently, the local  $C_f$  and  $Nu$  values for increasing  $Re$  have been obtained. In accordance with the decreasing velocity gradient for increasing  $Re$  (Figure 5.18(a)), the local  $C_f$  exhibited decreasing trend with the increase of  $Re$  (Figure 5.19(a)). The local  $C_f$  here is lower by  $8.5\%$  at  $Re = 500$  and by  $17\%$  at  $Re = 1000$  as that of the  $C_f$  for parabolic velocity profile. From the velocity profile (Figure 5.18(a)) it is evident that the velocity gradient near the wall decreases and hence that results in the decrease of local  $C_f$ . The decrease in velocity gradient near the wall reduces the heat diffusion from wall that results into decrease in heat transfer. Thus, the local  $Nu$  at a fixed  $Ri$  also decreases with the increase in  $Re$  from 500 to 1000 can be seen in Figure 5.19(b). It is lower by  $\sim 2\%$  at  $Re = 500$  and by  $\sim 3\%$  at  $Re = 1000$  from the fully developed forced convection  $Nu$  as indicated in the diagram.

## 5.2 Numerical results on laminar mixed convection

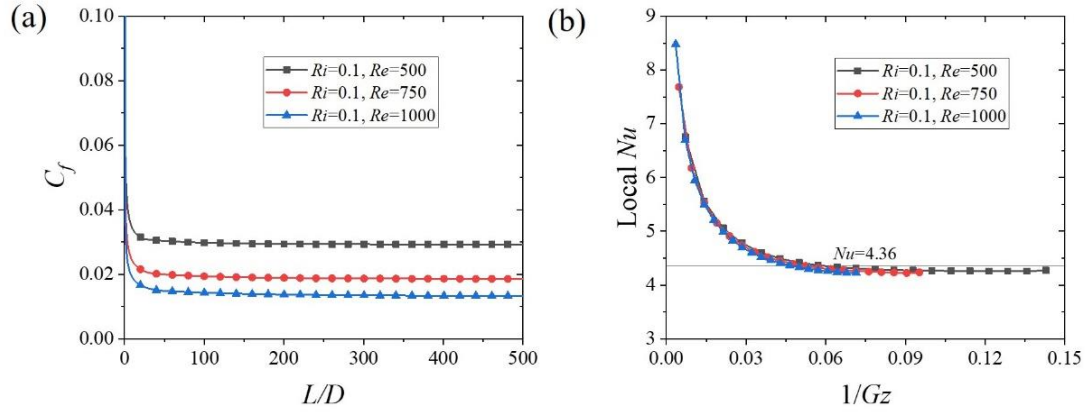


**Figure 5.19** Variation of (a) local  $C_f$  plot and (b) local  $Nu$  plot at  $Re = 500, 750$  and  $1000$  and  $Ri = 0.1$ . Magnified view of local  $Nu$  plot for  $4 \leq Nu \leq 5$  is provided in Figure A.6.

Local  $Nu$  Vs  $Re$  at different  $Ri$  for the developing and the fully developed region have been plotted in Figures 5.20(a) and (b) respectively. In the developing regime, the local  $Nu$  is increasing with the increase of  $Re$  at fixed  $Ri$  whereas it decreases in fully developed regime. To ensure this trend the local  $Nu$  against  $L/D$  have been plotted for  $Re = 500, 750$  and  $1000$ , reached the same conclusions. This is due to the thinnest thermal boundary layer present in the developing regime which makes the free convection effect significant. Furthermore, at fixed  $Re$  the fully developed  $Nu$  decreases as the  $Ri$  increases which is also seen in Figure 5.17(b).

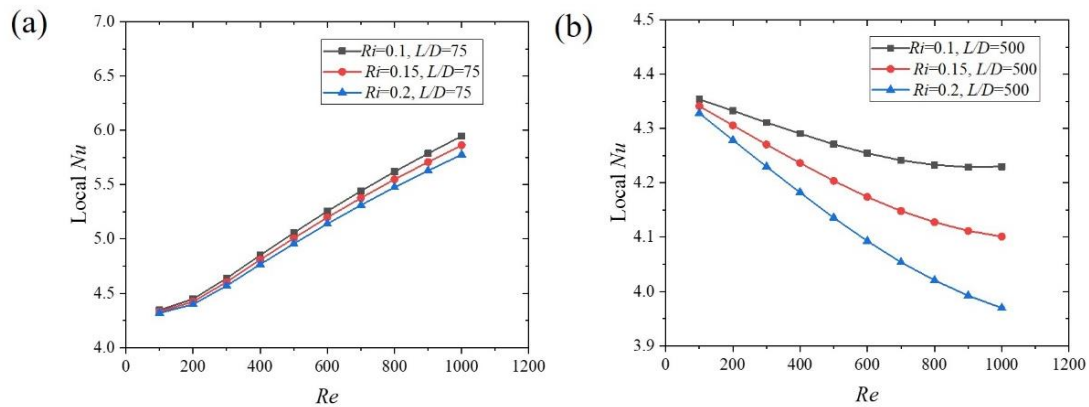


**Figure 5.20** (a) Developing and (b) fully developed  $Nu$  plot with increasing  $Re$  at different  $Ri$

The heat transfer characteristics is examined by Colburn  $j$ -factor similarly as explained in assisting flow. It is obvious that for fully developed flow, the  $f$  and  $j$  both decreases with the increase of  $Re$  because of inverse proportionality. It further decreases with the

increase of  $Ri$  at a fixed  $Re$  in opposing flow. In comparison to the Colburn  $j$ -factor corresponding to  $Nu = 4.36$ , it decreases for higher  $Ri$  which specifies the reduction of heat transfer with the increase of  $Ri$  (Figure 5.21).

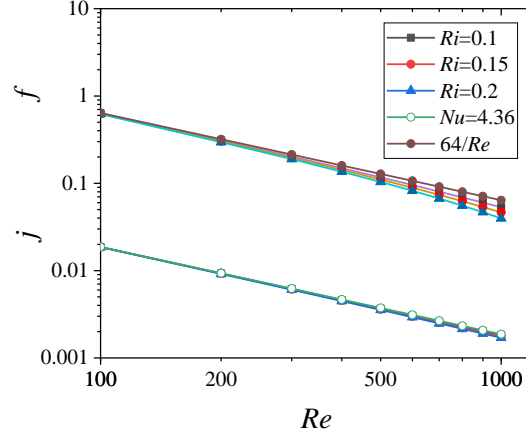


**Figure 5.21** Fully developed Colburn  $j$ -factor plot for varying  $Re$  at  $L/D = 500$  with different  $Ri$ . Magnified view of Colburn  $j$ -factor plot for  $800 \leq Re \leq 1000$  is provided in Figure A.7.

Two separate plots of Colburn  $j$ -factor, Figure 5.22(a) at a fixed  $Ri$  and different axial location and Figure 5.22(b) at different  $Ri$  and fixed axial location. In former case as the flow progresses towards fully developed, the  $j$ -factor approaches the forced convection at fixed  $Ri$  whereas in developing regime it is showing the same trend with magnitude higher than the  $j$ -factor based on  $Nu = 4.36$  with the increase in  $Ri$  signifying pronounced heat transfer.

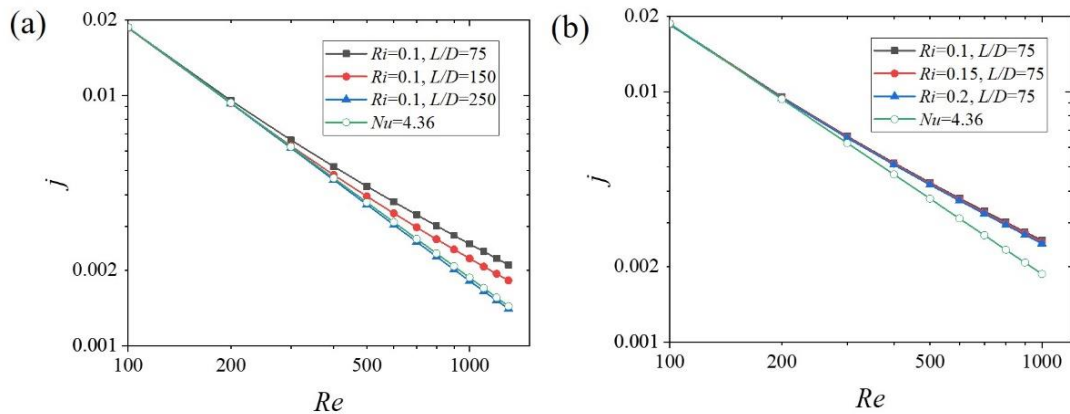


**Figure 5.22** Comparison between developing Colburn  $j$ -factor for (a) varying  $Re$  and  $L/D$  at fixed  $Ri = 0.1$  (b) varying  $Re$  and  $Ri$  at fixed  $L/D$  [Magnified view of Colburn  $j$ -factor plot for  $800 \leq Re \leq 1000$  is provided in Figure A.8].

### 5.3 Comparison between buoyancy-assisted and buoyancy-opposed flow

### 5.3 Comparison between buoyancy-assisted and buoyancy-opposed flow

In this section the comparative analysis of the buoyancy-assisting and opposing flows in the laminar regime of mixed convection is explained. Figures 5.23(a) and (b) represents the local  $C_f$  and  $Nu$  variation in the developing and fully developed regime for  $Ri = 0.5, 1.0$  and  $1.5$  at fixed  $Re = 250$ . The values of  $Ri$  are chosen in such a way that the free convection effect is just lower, equal and above the forced convection effect. The local  $C_f$  plot clearly demarcates that the friction factor ( $f = 4C_f$ ) is higher in assisting and lower in opposing mixed convection as that of the fully developed friction factor ( $64/Re$ ) for laminar flow (refer Figure 5.24(a)). On the same context, the local  $Nu$  is higher for assisted and lower in opposed mixed convection as compared to the fully developed  $Nu = 4.36$  for uniform heat flux (refer Figure 5.24(b)). The trend is increasing in assisting and decreasing in opposing flow and furthermore at a particular  $Ri$  for same  $Re$ , it is higher in assisting flow as that of the opposing flow.

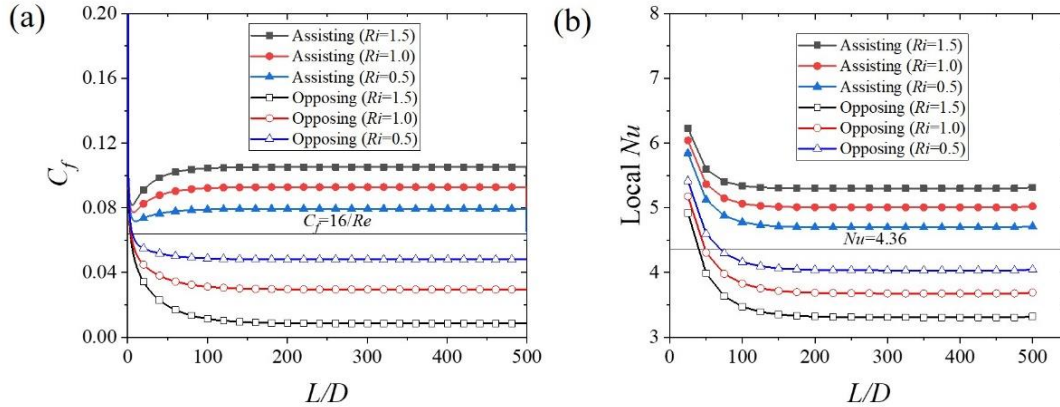


**Figure 5.23** Comparison between local (a)  $C_f$  and (b)  $Nu$  for assisting and opposing flow at  $Re = 250$  and  $Ri = 0.5, 1.0, 1.5$ .

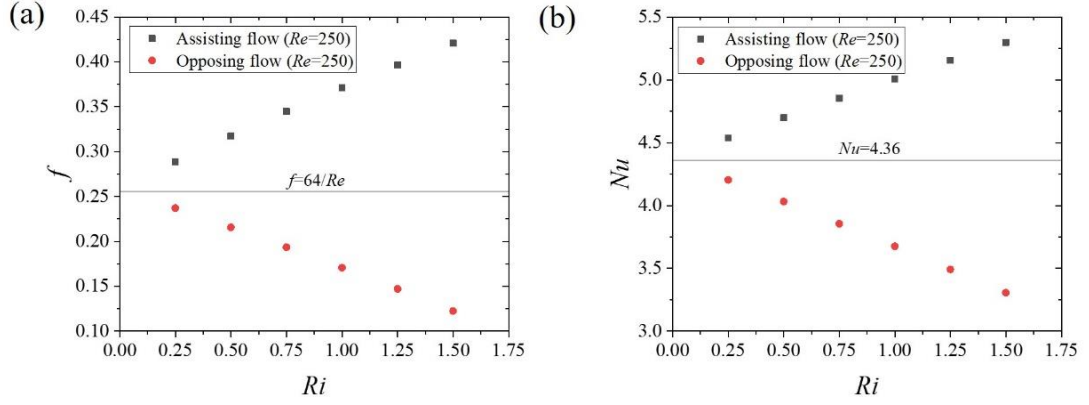


**Figure 5.24** Comparison between fully developed (a)  $f$  and (b)  $Nu$  for assisting and opposing flow at  $Re = 250$  and  $Ri = 0.125 - 1.5$ . Similar trends were observed at  $Re = 350, 500$  and  $750$  (See Figure A.13).

The hydrodynamic ( $L_h$ ) and thermal ( $L_t$ ) entry length for the mixed convection case is clearly different from the pure forced convection. In forced convection the entry length is a function of  $Re$ ,  $Pr$  and characteristic length only. Whereas in case of simultaneously hydrodynamic and thermally developing mixed convection flow the entry length is dependent on  $Gr$  also. This can be explained with the help of local  $C_f$  and local  $Nu$  plot along the length of the tube for different  $Ri$  as shown in Figures 5.6(a) & (b) and Figures 5.17(a) & (b). It has been observed that as the  $Ri$  increases, the local  $C_f$  and  $Nu$  both increases in assisting flow whereas it decreases in opposing flow. The criteria to be hydrodynamically fully developed is set as Eq. 5.1 and for thermally fully developed as Eq. 5.2. The hydrodynamic or thermal entry length either increases or decreases with the increase in  $Ri$ . It increases or decreases depending on the flow direction (buoyancy-assisting and opposing flows). This is indeed true that at higher  $Ri$ , fluid properties will vary and consequently the flow will suppress the turbulent motion. That situation leads to more ordered or laminar flow. It may approach a condition where it becomes fully developed in terms of velocity and temperature profiles. From Figure 5.25 it is evident that for assisting flow there is an increase in hydrodynamic entry length and decrease in thermal entry length whereas increase in both hydrodynamic and thermal entry length was observed in case of opposing flow with the increase of  $Ri$ . It is found that the nondimensional hydrodynamic entry length for laminar mixed convection at  $Re = 250$  and  $Pr = 7$  is relatively 5-15 times higher than the laminar tube flow and thermal entry length is 2-3 times higher as compared to pure forced convection within the specified range of  $Ri = 0.125 - 1.5$ .

## 5.4 Friction factor and Nusselt number correlations

$$d(C_f)/d(L/D) \leq 10^{-6} \quad (5.1)$$

$$d(Nu)/d(L/D) \leq 10^{-5} \quad (5.2)$$

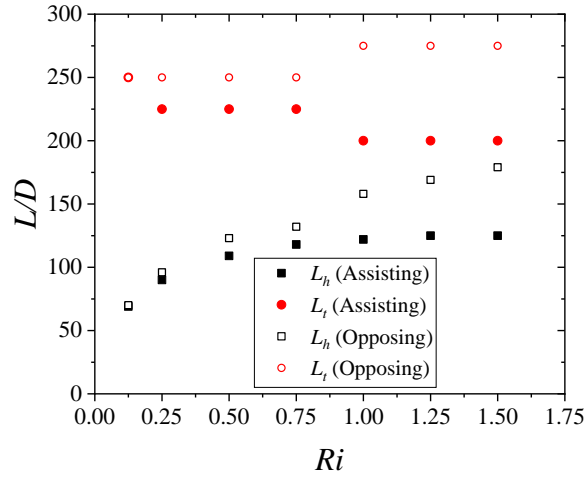


**Figure 5.25** Comparison of hydrodynamic and thermal entry length for assisting and opposing flow at  $Re = 250$  and different  $Ri$ .

## 5.4 Friction factor and Nusselt number correlations

With the available simulation data for  $f$  and  $Nu$ , different correlations have been produced. The decreasing logarithmic friction factor plot in Figures 5.26(a) and (b) accounts for decrease in pressure drop as the  $Re$  increases at a fixed  $Ri$ . A power curve fit has been employed to the data points, gives two correlations Eqs. (5.3) and (5.6) as  $f = CRe^m$  for assisting and opposing flow. Similarly, to account the relationship of  $f$  with  $Ri$ , a linear curve fit has been done through the data points as shown in Figures 5.26(c) and (d). The correlations with increasing slope for assisting flow and decreasing slope in opposing flow are obtained as mentioned in Eqs. (5.4) and (5.7). The  $Nu$  relationship with the  $Re$  and  $Gr$  can be formed in terms of  $Ri$ . Linear curve fit is best suited for this as shown in Figures 5.26(e) and (f) with positive slope in assisting flow and negative slope in opposing flow. Eqs. (5.5) and (5.8) correlates the fully developed  $Nu$  with the  $Ri$  which comprises  $Gr$  and  $Re$ .

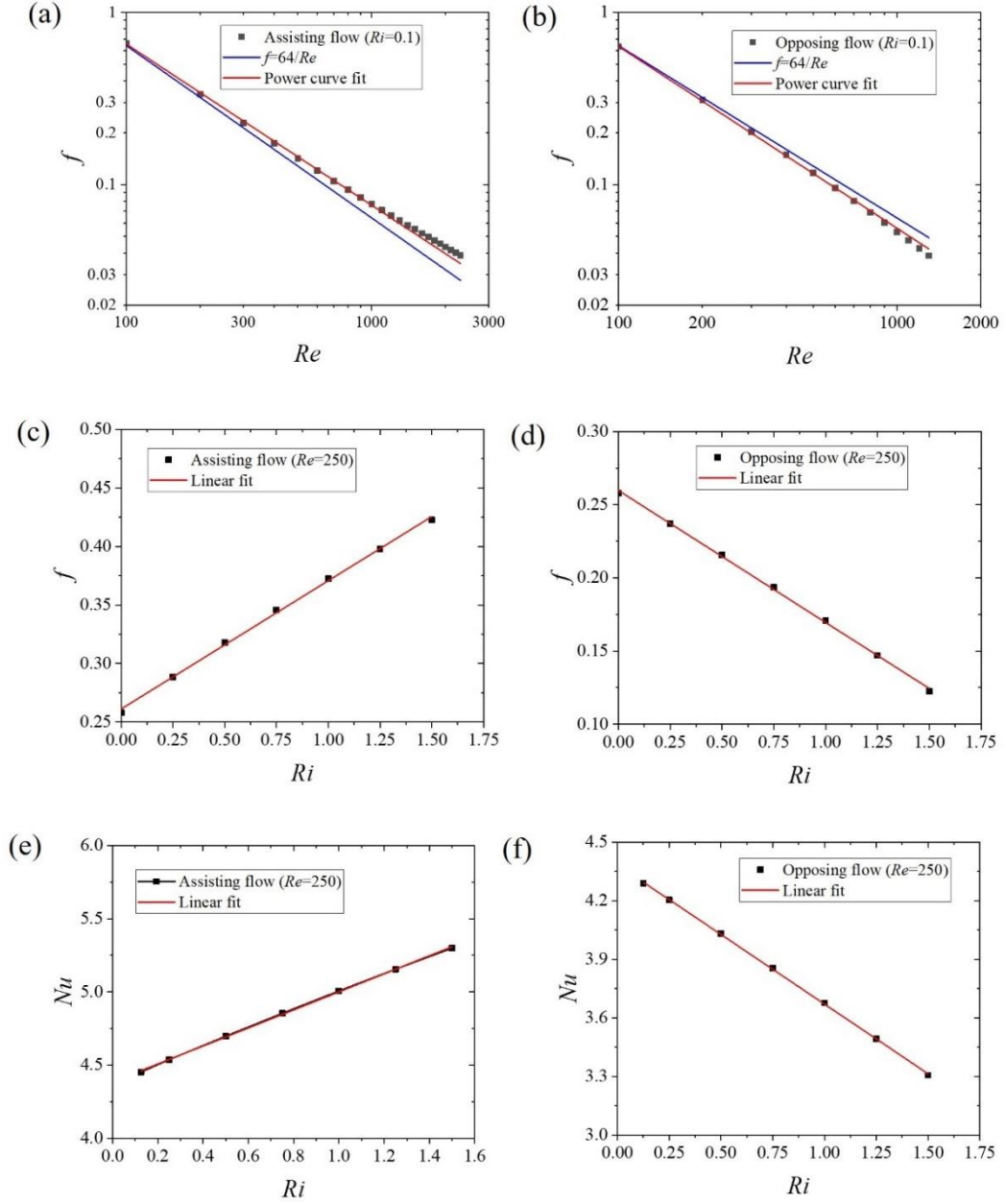


**Figure 5.26** (a) & (b) Fully developed friction factor correlation plot with  $Re$ , (c) & (d) fully developed friction factor correlation plot with  $Ri$ , and (e) & (f) fully developed  $Nu$  correlation plot with  $Ri$  for assisting and opposing flows, respectively

Buoyancy-assisted flow:

$$f = 48.37/Re^{0.93}; 100 \leq Re \leq 2300 \text{ and } Ri = 0.1 \quad (5.3)$$

$$f = 0.26 + 0.11Ri; 0.125 \leq Ri \leq 1.5 \text{ and } Re = 250 \quad (5.4)$$

$$Nu = 4.38 + 0.62Ri; 0.125 \leq Ri \leq 1.5 \text{ and } Re = 250 \quad (5.5)$$

Buoyancy-opposed flow:

$$f = 82.01/Re^{1.06}; 100 \leq Re \leq 1300 \text{ and } Ri = 0.1 \quad (5.6)$$

## 5.4 Friction factor and Nusselt number correlations

$$f = 0.26 - 0.09Ri; 0.125 \leq Ri \leq 1.5 \text{ and } Re = 250 \quad (5.7)$$

$$Nu = 4.38 - 0.71Ri; 0.125 \leq Ri \leq 1.5 \text{ and } Re = 250 \quad (5.8)$$

Furthermore, the  $Nu$  correlations with  $Gz$  has also been developed for developing ( $1/Gz < 0.10$ ) and fully developed ( $1/Gz \geq 0.10$ ) flows distinctly for both assisting as well as opposing flows. The developing data keeps on decreasing with  $1/Gz$  which fits to a power curve and the fully developed data fits with a best fit having an intercept and a power curve. The correlation has been obtained for  $Ri = 0.125$  to  $1.5$  at  $Re = 250$ . The lower and upper range of coefficients, constants, and the exponents ( $a, n, A$  and  $B$ ) mentioned in Eqs. (5.9) and (5.10) have been tabulated in Table 5.1 for assisting and opposing flows respectively.

$$Nu = a(1/Gz)^n; \text{ for } 1/Gz < 0.10 \quad (5.9)$$

$$Nu = A + B/(1/Gz); \text{ for } 1/Gz \geq 0.10 \quad (5.10)$$

**Table 5.1** Range of the coefficients, constants and exponents present in Eqs. (5.9) and (5.10)

$Ri = 0.125 \text{ to } 1.5$	$a$	$n$	$A$	$B$
Assisting flow	2.11 to 2.74	-0.26 to -0.22	4.45 to 5.30	0.0005 to 0.00005
Opposing flow	2.01 to 1.36	-0.27 to -0.33	4.28 to 3.30	0.00018 to 0.00034

To verify the performance of the correlations obtained, the values obtained through the correlation have been compared with the numerical results in a parity plot (Figures 5.27 and 5.28). The maximum deviation in between correlation and numerical values obtained from Eqs. 5.3 & 5.6 are found within  $\pm 15\%$  deviation. Eqs. 5.4 & 5.7 are within  $\pm 5\%$ , and Eqs. 5.5 & 5.8 are within  $\pm 5\%$ . Eqs. 5.3 and 5.6 are at fixed  $Ri (=0.1)$  and varying the  $Gr$  and  $Re$ . As the  $Re$  increases, consequently  $Gr$  also increases to keep the  $Ri$  constant. The higher  $Gr$  increases the free convection effect which changes the flow behaviour in mixed convection as compared to the forced convection. The trend of  $f$  vs  $Re$  and  $Nu$  vs.  $Re$  shows a substantial change in the mixed convection results. Hence, the correlations are well in agreement with the numerical data at lower value of  $Re$  and then it deviates as the  $Re$  increases. In contrast, Eqs. 5.2 and 5.5 are at fixed value of  $Re (=250)$  and varying the  $Gr, Ri$ . Because of the linear behaviour of the  $f$  and  $Nu$  with  $Ri$ , the correlations can predict close to the numerically obtained data. Additionally, the Eqs. 5.7 & 5.8 (Eqs. 5.9 & 5.10 in revised version) deviate by  $\pm 15\%$  and  $\pm 2\%$  respectively. In case of developing flow regime, the hydrodynamic and thermal boundary layers are in the developing phase. Since the velocity and



temperature variations in the developing region is more, the prediction by the correlations is having larger deviation whereas in the fully developed flow regime it can predict with an excellent agreement.

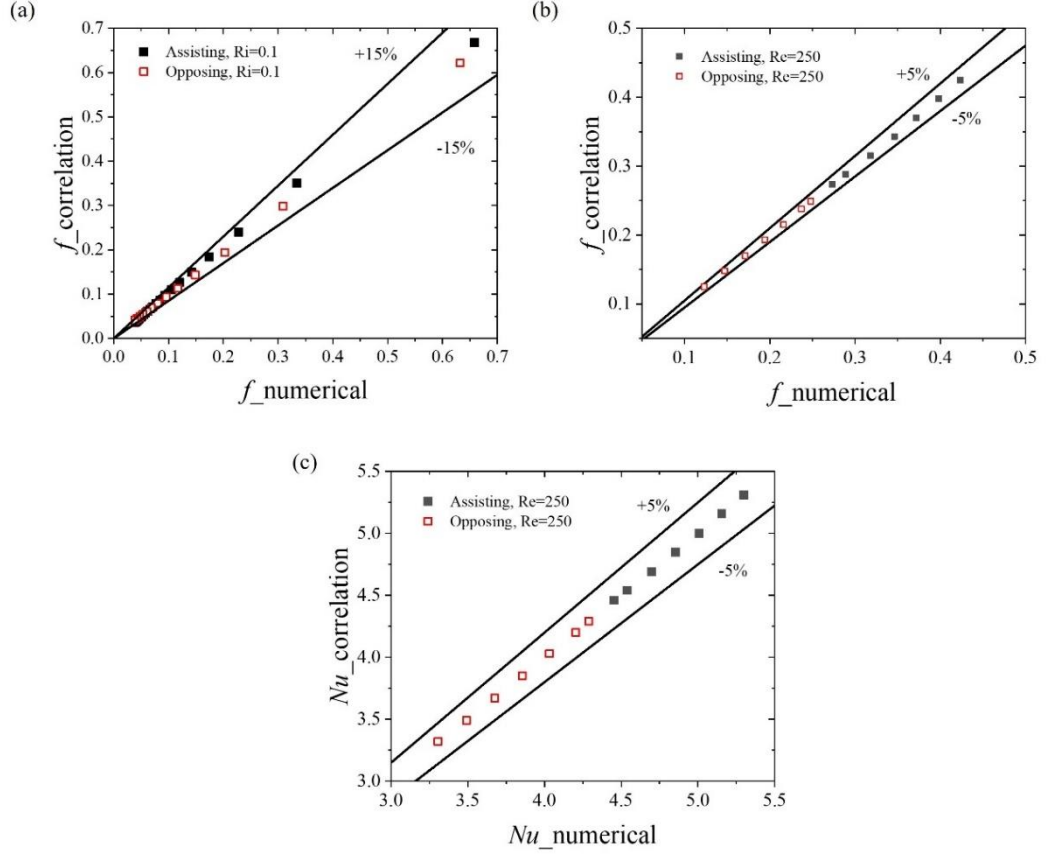


**Figure 5.27** Deviation of correlation and numerical data of  $f$  and  $Nu$  for (a) Eqs. 5.3 & 5.6 (b) Eqs. 5.4 & 5.7 and (c) Eqs. 5.5 & 5.8

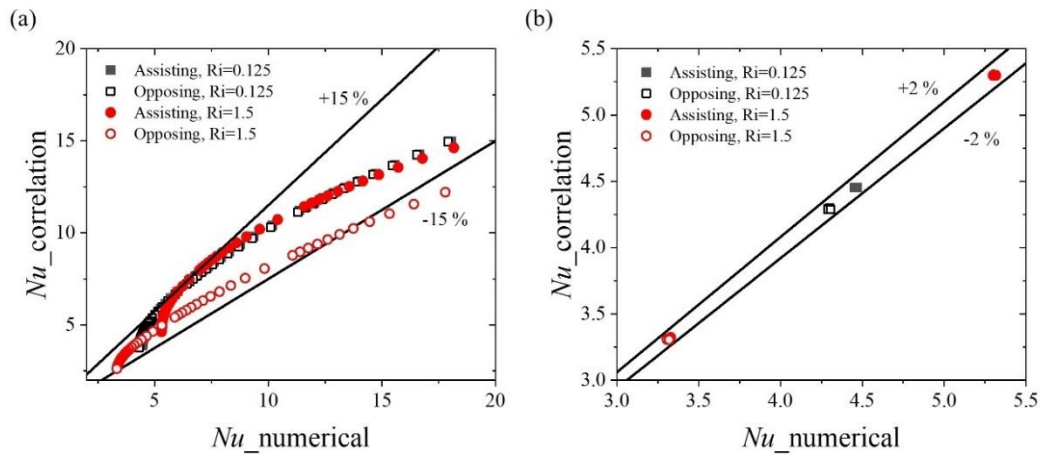


**Figure 5.28** Deviation of correlation and numerical data of  $Nu$  at fixed  $Re$  and varying  $Ri$  for Eq. 5.9 in (a) developing and Eq. 5.10 in (b) fully developed flows

## 5.5 Experimental results on laminar mixed convection

### 5.5 Experimental results on laminar mixed convection

Experiments were conducted for a variety of Reynolds numbers ( $539 \leq Re \leq 9621$ ), Grashof numbers ( $2.4 \times 10^4 \leq Gr \leq 1.3 \times 10^7$ ), Richardson numbers ( $0 \leq Ri \leq 0.3$ ), and Prandtl numbers ( $4.4 \leq Pr \leq 6.5$ ) in aiding flow and  $553 \leq Re \leq 9492$ ,  $3.6 \times 10^4 \leq Gr \leq 1.1 \times 10^7$ ,  $0 \leq Ri \leq 0.3$ , and  $5.2 \leq Pr \leq 6.4$  in opposing flow, respectively. The working fluid was normal water maintained at 20 °C and atmospheric pressure. The test section was heated using Joule heating with a low-voltage, high-current capacity DC power source. This high current is required for the Joule heating to achieve a high resistance. Positive and negative cables were attached to the test section's extremities. It is possible to arrange the experimental apparatus so that both supporting and opposing experiments can be conducted. The length ( $L$ )-to-diameter ( $D$ ) ratio i.e.,  $L/D$  was maintained at 130 to limit the scope of the study to the developing regime.  $Ri = 0$  represents the zero-heat flux condition. Consequently, a higher Reynolds number can be attained in the absence of a heat flux. As the heat flux and, consequently,  $Gr$  and  $Ri$  increase, the maximum achievable  $Re$  is limited to laminar or transitional flow regimes. The purpose is to maintain the outlet water temperature well below its saturation point. Thus, the highest achievable  $Ri$  is 1.5 for a  $Gr_b$  of  $8.1 \times 10^5$  and  $Re_b$  of 666 in aiding flows and  $Gr_b$  of  $7.5 \times 10^5$  and  $Re_b$  of 681 in opposing flows, respectively.

#### 5.5.1 Average pressure drop and heat transfer in simultaneously developing laminar flows

A log-log plot of average friction factor ( $\bar{f}$ ) vs. bulk Reynolds numbers ( $Re_b$ ) for different Richardson numbers is displayed in Figure 5.27 (a). At a given  $Ri$ , the  $Re_b$  is varied in between 500 and 10,000 depending on the amount of heat flux supplied. Correspondingly, the three flow regimes of laminar, transitional, and turbulent are demarcated as I ( $500 \leq Re \leq 2000$ ), II ( $2001 \leq Re \leq 4000$ ), and III ( $4001 \leq Re \leq 10000$ ). It is found that at a fixed  $Ri$ , the friction factor monotonically decreases in the laminar flow regime with an increase in  $Re$ . However, in transition region  $f$  increases with the increase in  $Re$ . The turbulence regime displays same decreasing trend of  $f$  vs.  $Re$  like the laminar regime.

In this section, we will confine the discussions relevant to zone I or laminar regime only. Further, with the increase of  $Ri$ , the friction factor shows a higher magnitude in aiding flow (Figure 5.29 (b)). The reason for this is that with the increase in  $Ri$ , the increase of free convection effect causes an increase in velocity near the wall. This increase in near-wall velocity is balanced by the decrease in velocity at the center of the tube to conserve mass. Due to this, the velocity gradient at the wall increases. Consequently, the shear stress and the pressure drop increase, which ultimately increases the friction factor. For buoyancy opposed flow, the friction factor reduces with increase in  $Ri$  at a given Reynolds number (Figure 5.29 (c)). In the case of opposing flow, the free convection effect decreases the velocity near the wall and increases the centreline velocity. As a result, the wall velocity gradient is decreased. As a result, the decreased shear stress and pressure drop lead to a lesser friction factor. Furthermore, a distinct trend has been observed in aiding flow that after  $Re=1413$  for  $Ri=0.1$ , the slope of  $f$  becomes lesser than the case when  $Ri=0.05$ . Also, the  $f$  follows a monotonically decreasing trend upto a higher value of  $Re=2332$  before the transition starts. Similarly, in opposing flow the  $f$  at  $Ri=0.1$  shows an increase in magnitude as compared to  $Ri=0.05$  in the entire laminar flow regime. The laminar flow is maintained till  $Re=2146$  before it enters the transitional flow.

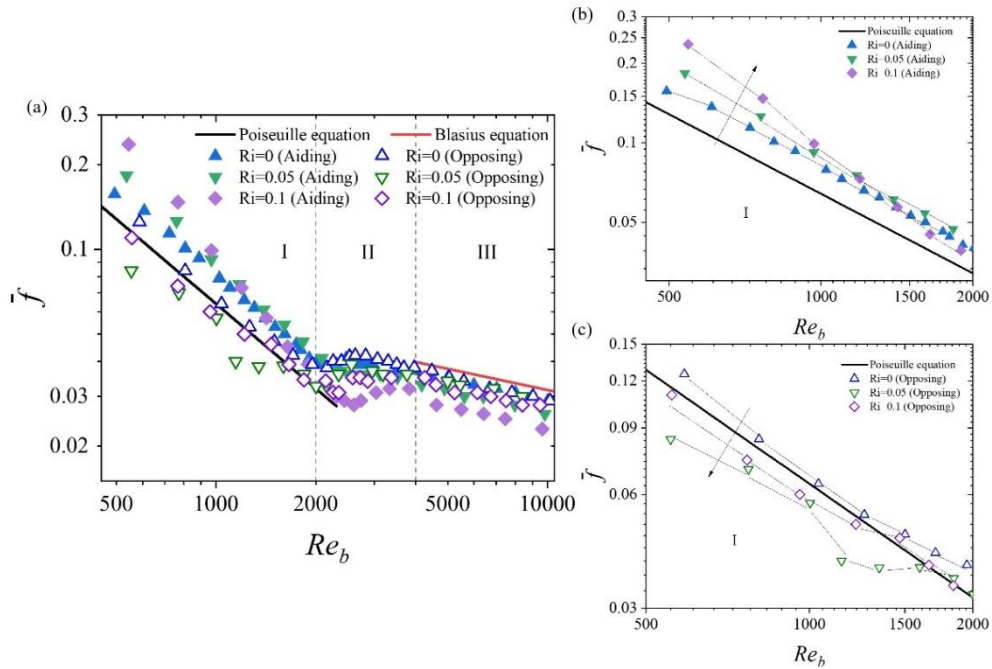


**Figure 5.29** (a) Average  $f$  vs.  $Re$  comparison plot with magnified plot for (b) aiding and (b) opposing flow of laminar mixed convection with varying  $Re$ ,  $Gr$  at different  $Ri$ .

## 5.5 Experimental results on laminar mixed convection

Figure 5.30(a) represents the average Nusselt number ( $\overline{Nu}$ ) vs.  $Re_b$  plot at different values of  $Ri$  for all the three regimes. Further, Figures 5.30(b) and (c) represents the buoyancy aided and opposed cases of laminar regime (zone I) respectively. In the laminar flow regime, the  $\overline{Nu}$  increases with the increase of  $Re_b$  because the flow lies in the developing flow instead of a fully developed flow, where  $Nu = 4.364$  for the uniform heat flux boundary condition. When the flow is still developing, the local  $Nu$  decreases along the length of the tube because of the development of the thermal boundary layer (TBL). Due to the growth of the TBL, the wall and fluid temperature differences increase resulting in a drop in local  $Nu$ . With the increase in  $Re$ , the thermal entrance length increases. Therefore, at an axial position the TBL thickness decreases and the  $Nu$  increases. However, the free convection effect increases with increasing thermal boundary layer thickness and may lead to an increase in  $Nu$ . When this decrease in  $Nu$  due to thermal boundary layer development is greater than the increase in  $Nu$  due to free convection effects, the Nusselt number increases with the increase in Reynolds number (Figures 5.30 (b) and (c)). In the present study of  $L/D$  of 130 and  $Re \geq 400$  the flow undergoes thermally developing (as per the thermal entry length correlation,  $L_t = 0.05RePrD = 140D$ ). Therefore, the entire study in laminar regime is for developing flow only. The magnified view in the laminar flow regime depicts that the  $Nu$  monotonically increases with the increase in flow rate for both buoyancy aided (Figure 5.30(b)) and buoyancy opposed (Figure 5.30(c)) flow respectively. At a fixed  $Re$ , the  $Nu$  increases with the increase in  $Ri$  for both buoyancy-aided and opposed flows. Further, the slope is more pronounced with the increase in  $Ri$ . The reason behind this is that due to the increase in flow rate and heat flux, the hydrodynamic as well as thermal boundary layers develop faster. This growth of the boundary layer helps diffusion take place, and more heat is being convected away by the fluid.

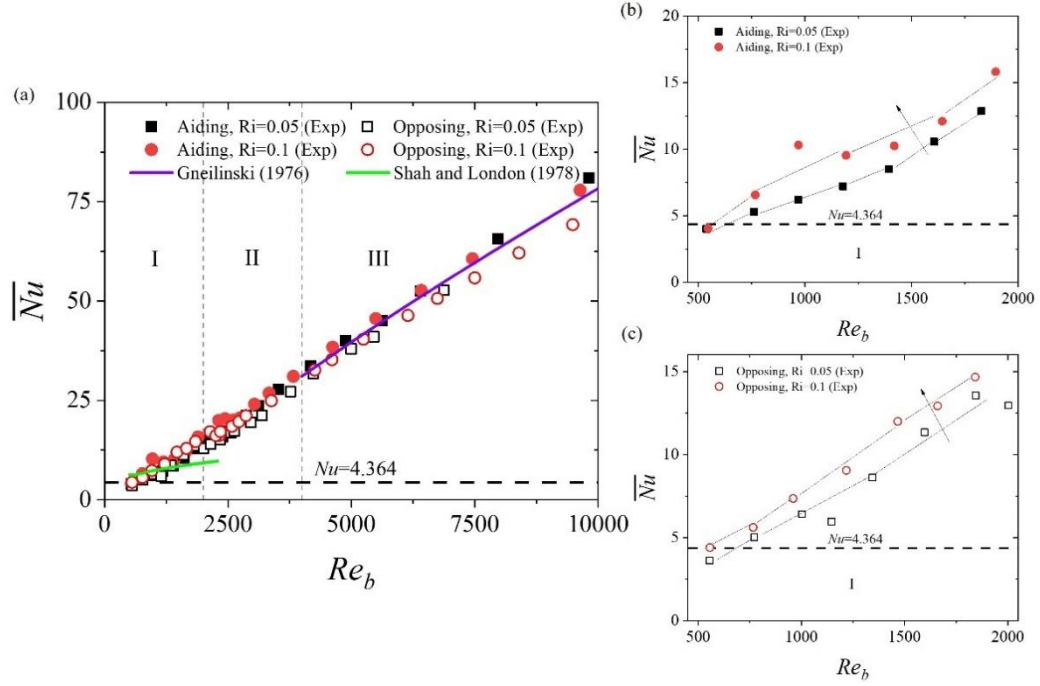


**Figure 5.30** Average  $Nu$  vs.  $Re$  comparison plot for laminar mixed convection with varying  $Re$ ,  $Gr$  at different  $Ri$

### 5.5.2 Local heat transfer in the developing laminar mixed convection flow

Figures 5.31(a) and (b) highlights the axial variation of  $Nu$  in terms of the  $Nu$  vs  $L/D$  and  $Nu$  vs  $Gz$  plot respectively in the buoyancy aided laminar regime. Results are analysed for both buoyancy-aiding as well as opposing flows (Figure 5.32) at same  $Ri = 0.1$ . In aiding flow, the  $Nu$  is higher in the developing flow regime and approaches a constant value as it progresses towards the fully developed flow. In addition, with the increase in  $Re$  at fixed  $Ri$ , the heat transfer ( $Nu$ ) also increases, as shown in the plot of  $Nu$  vs  $L/D$ . The standard plot of  $Nu$  with  $Gz$  (Figure 5.31(b)) shows that the flow is in the developing regime (Figure 5.8 (b) shows that the fully developed state reached at  $1/Gz > 0.10$ ). The local  $Nu$  decreases with the increase in axial length ensures the flow is still in developing state. This local  $Nu$  in developing laminar mixed convection regime is coinciding to a single value of  $Nu = 4.364$  for the fully developed case as the  $1/Gz$  increases.

## 5.5 Experimental results on laminar mixed convection

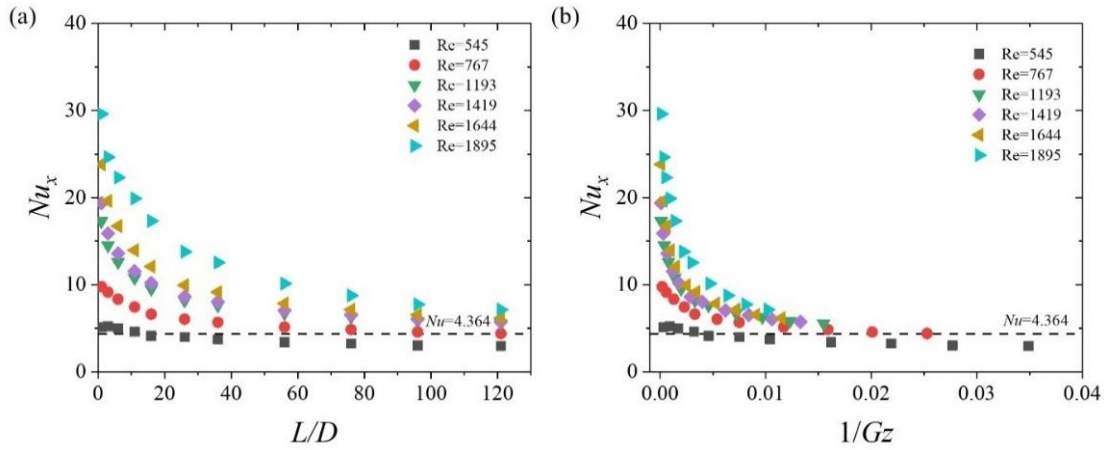


**Figure 5.31** Local (a)  $Nu$  vs.  $L/D$  and (b)  $Nu$  vs.  $Gz$  plot for laminar mixed convection at fixed  $Ri=0.1$  in aiding flow for different  $Re$ .

In opposing flow, the local  $Nu$  also converges to the fully developed  $Nu$  of 4.364, like it was seen in case of aiding flow. Furthermore, the heat transfer is quantitatively 14.51 % lower in the case of opposing flow as compared to aiding flow at  $Re=767$ . This decrement in heat transfer further reduces to 3.03% at higher  $Re=1200$ . The decrease in velocity gradient near the wall reduces the growth of the thermal boundary layer because of the opposing free convection effect (Figure 5.19 (b)), which reduces advection and results in a decrease in heat transfer.

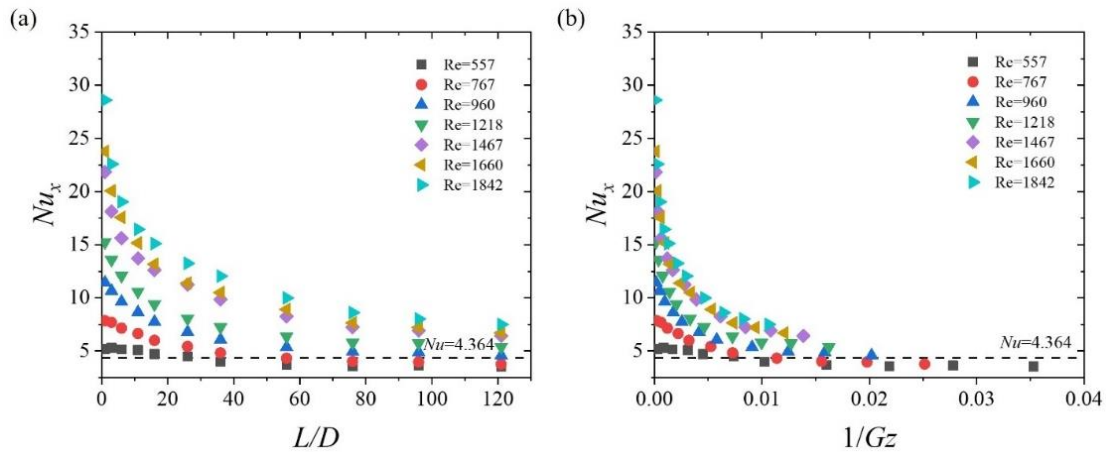


**Figure 5.32** Local (a)  $Nu$  vs.  $L/D$  and (b)  $Nu$  vs.  $Gz$  plot for laminar mixed convection at fixed  $Ri=0.1$  in opposing flow

### 5.5.3 Effect of $Ri$ on heat transfer

In this section, the effect of varying  $Ri$  from 0.1 to 1.5 at fixed  $Re$  of 500 and 700 is being analyzed with the help of local and average  $Nu$  variation plots by increasing heat

fluxes. Figure 5.33 displays the effect of  $Ri$  on the local Nusselt number ( $Nu_x$ ) at  $Re=500$ . From Figure 5.33(a), it is evident that in case of buoyancy aided flow,  $Nu_x$  initially increases with increase in  $Ri$  till  $Ri \leq 0.75$ . From  $Ri=0.75$  onwards, the magnitude of the  $Nu$  remains almost the same till  $Ri = 1.5$ . This is also true for opposing flows (Figure 5.33(b)).

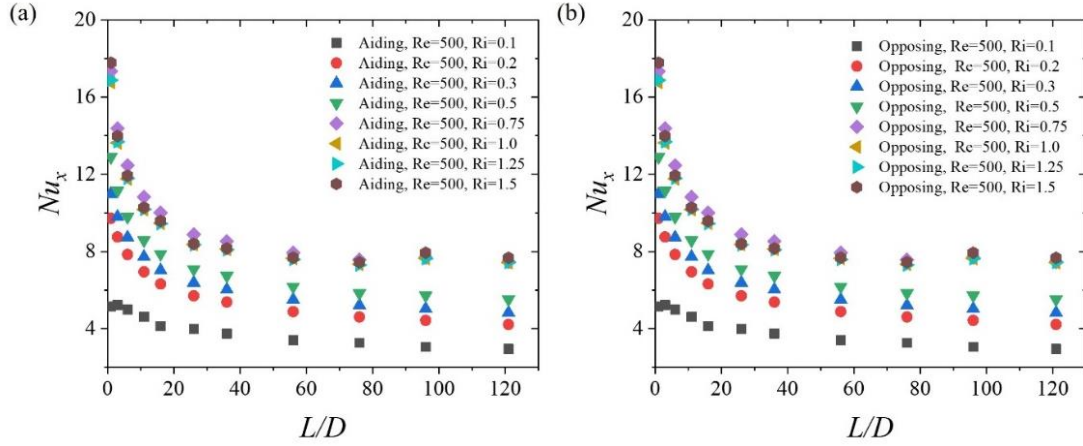


**Figure 5.33** Local  $Nu$  vs.  $L/D$  plot for laminar mixed convection at fixed  $Ri=0.1-1.5$  in (a) aiding and (b) opposing flow at  $Re=500$

Figure 5.34 displays the effect of  $Ri$  on the local Nusselt number ( $Nu_x$ ) at  $Re=700$ . In case of aiding flow (Figure 5.34(a)) the local  $Nu_x$  increases with increase in  $Ri$  upto 0.75. Further increase of  $Ri = 0.1$  results in a decrease in  $Nu_x$  and stays constant in the regime of  $Ri=1$  to 1.5. Unlike aiding flows, the  $Nu$  drops after  $Ri=0.5$  and then recovers and increases drastically for higher values of  $Ri$  in opposing flows (Figure 5.34(b)). One reason seems to be that because of the opposing inertia, the wall temperature becomes lower at the tube exit side, whereas the mean fluid temperature increases continuously due to the constant heat flux supply. Therefore, the wall and mean temperature difference decrease and result in a higher  $Nu$  at the tube outlet. The wall and mean fluid temperature plots in aiding and opposing flow have been shown here for one case  $Ri=0.75$  at  $Re=700$  (Figures 5.34 (c) and (d)).



## 5.5 Experimental results on laminar mixed convection

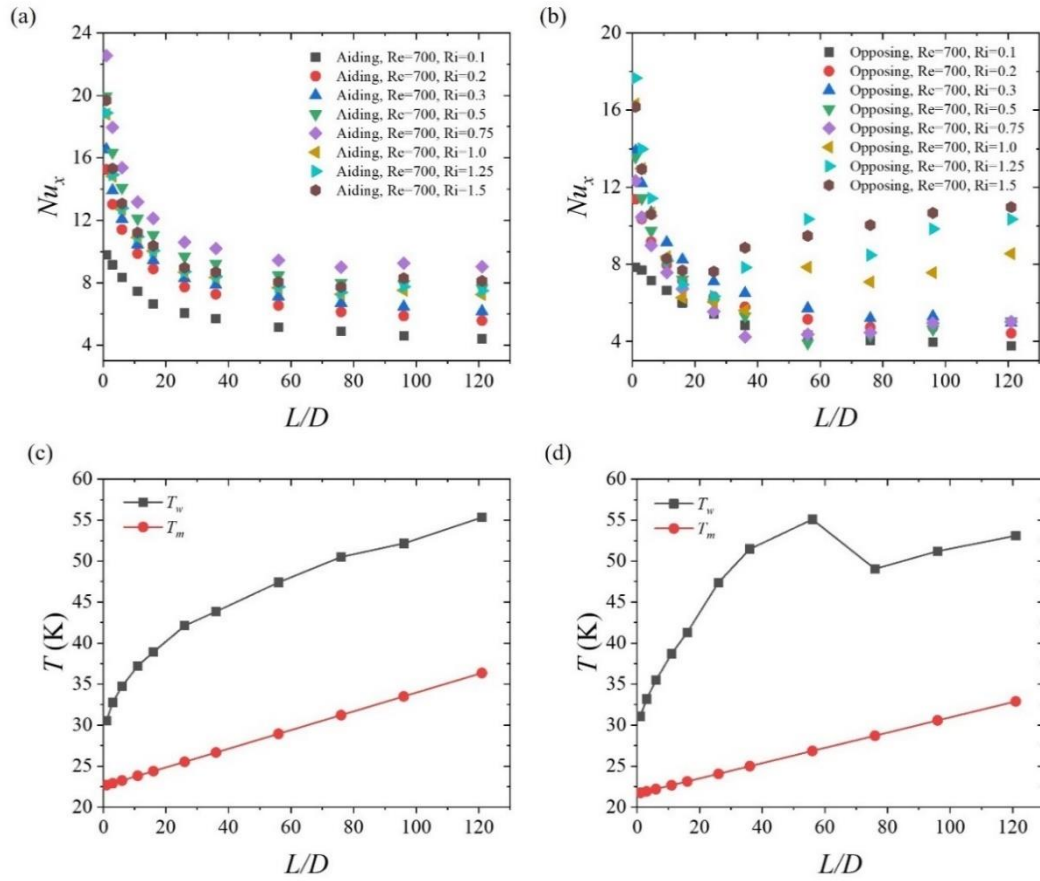


**Figure 5.34** Local  $Nu$  vs.  $L/D$  plot for laminar mixed convection at varying  $Ri=0.1-1.5$  in (a) aiding and (b) opposing flow at  $Re=700$  along with wall and mean fluid temperature variation in (c) aiding and (d) opposing flow for  $Ri=0.75$

To elucidate this trend, the average  $Nu$  is also plotted for increasing value of  $Ri$  (Figure 5.35). This also shows that the  $Nu$  before  $Ri=0.75$  increases in both aiding and opposing flow. Thereafter, it drops in aiding flow and rises in opposing flow.

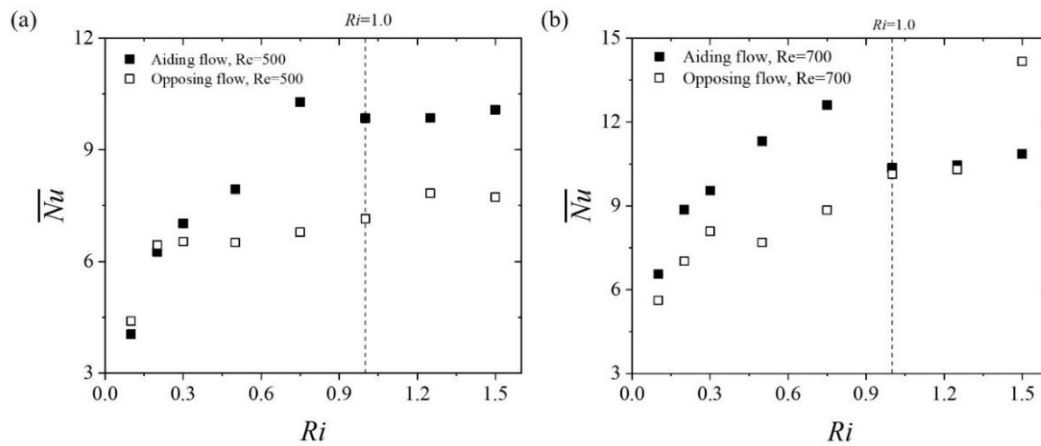


**Figure 5.35** Average  $Nu$  vs  $Ri$  plot for laminar mixed convection at fixed  $Re=500$  and  $700$  in (a) aiding and (b) opposing flow



### 5.5.3.1 Influence of $Ri$ through visualization

The increase in heat flux increases the  $Gr$  and hence  $Ri$  will increase. At a fixed mass flow rate, increase of the heat flux will alter the hydrodynamic and thermal features. It has been observed in the previous section, at  $Ri > 1$ , the flow behaves differently as compared to  $Ri < 1$ . The local  $Nu$  decreases with an increase in  $Ri=0.75$  onwards in aiding flow and increases in opposing flow. The effect of  $Ri$  on the flow features at a fixed  $Re=1000$  for buoyancy aiding and opposing flows are presented in Figures 5.36 and 5.37 respectively. Using flow visualization technique, the different flow patterns with variation in  $Ri$  is clearly evident (Figures 5.36 and 5.37). It has been observed that for a buoyancy aided flow (Figure 5.36) at a fixed mass flow rate, as we increase the heat flux, the flow gradually changes from laminar to transitional and eventually to turbulent. Due to the increase in heat flux, the fluid properties (viscosity and density) near the wall decrease. The change in viscosity due to the change in temperature is almost 20% higher as compared to the change in density. This increases the velocity, and hence  $Re$  which changes the flow regime even at a fixed mass flow rate. The flow patterns reveal that the flow remains laminar at  $Ri=0.1$ , it enters transition at  $Ri=0.5$ , becomes quasi-turbulent at  $Ri=1.0$  and becomes fully turbulent at  $Ri=1.5$  (Figure 5.36). The bulk Reynolds number ( $Re_b$ ) becomes 1212, 1391, 1655, and 1888 at  $Ri=0.1, 0.5, 1.0$ , and  $1.5$ , respectively. Similar behavior can be seen in the case of opposing flows (Figure 5.37). For fixed  $Re=1000$ , the flow is laminar at  $Ri=0.1$ , progresses towards transition at  $Ri=0.5$ , becomes quasi-turbulent at  $Ri=1.0$ , and ultimately turbulent at  $Ri=1.5$ . Here, the bulk Reynolds number obtained is 1223, 1437, 1600, and 1871 at  $Ri=0.1, 0.5, 1.0$ , and  $1.5$ , respectively. Comparing these flow patterns (Figures 5.36 and 5.37), it can be deduced that the laminar-turbulent transition is faster in opposing flow in comparison to aiding flow.

## 5.5 Experimental results on laminar mixed convection

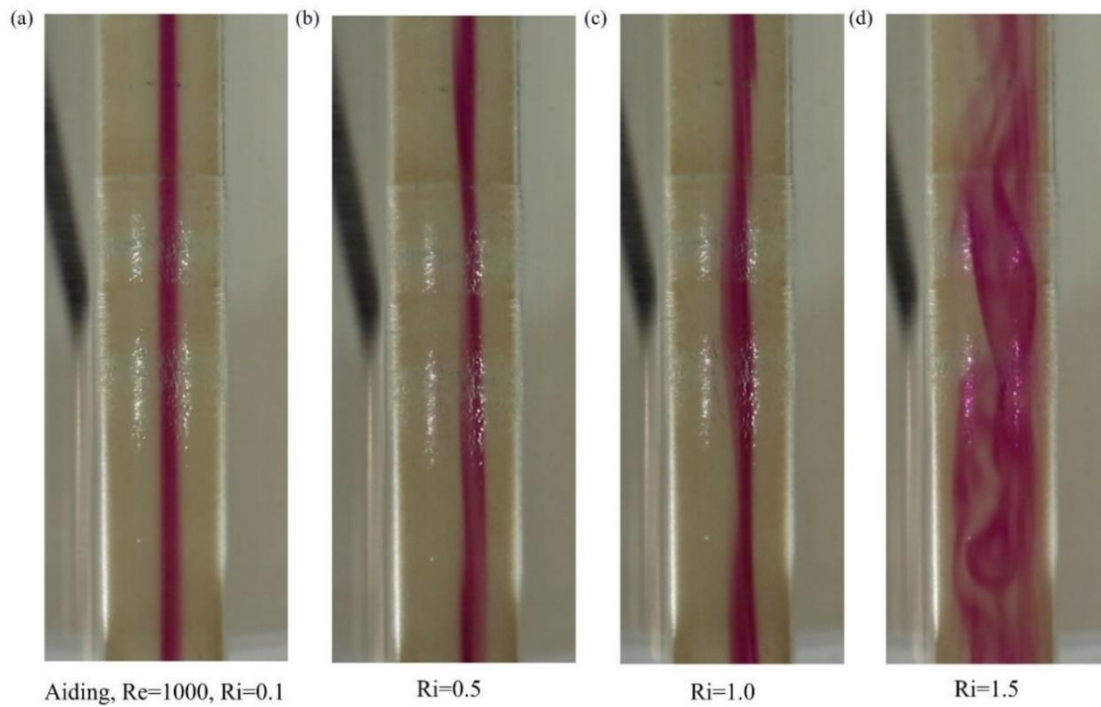


**Figure 5.36** Flow patterns at fixed  $Re=1000$  for (a)  $Ri=0.1$  (laminar) (b)  $Ri=0.5$  (transitional) (c)  $Ri=1.0$  (quasi-turbulent) and (c)  $Ri=1.5$  (turbulent) in aiding flow

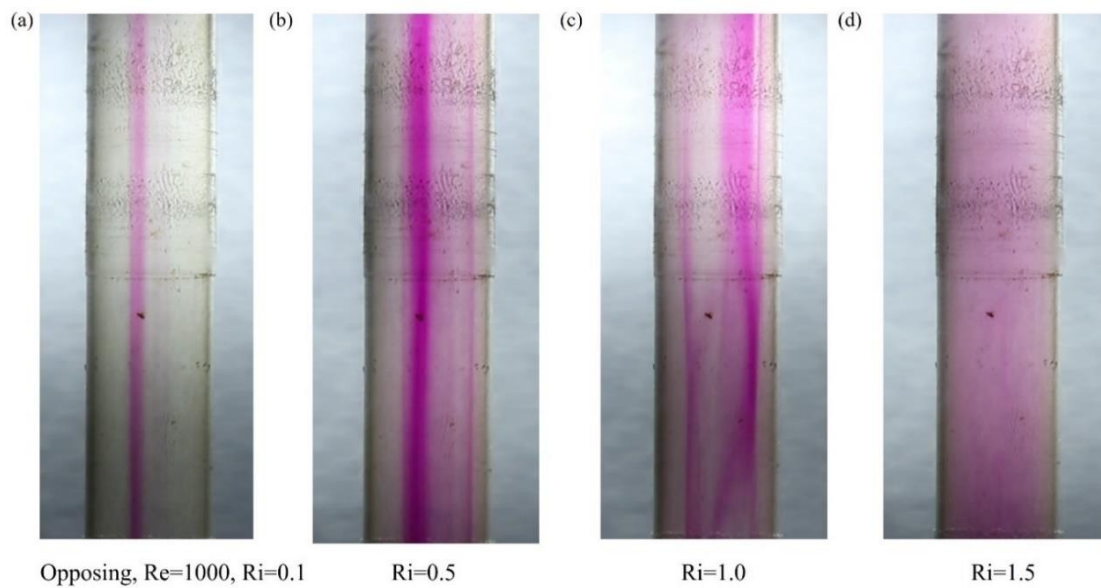


**Figure 5.37** Flow patterns at fixed  $Re=1000$  for (a)  $Ri=0.1$  (laminar) (b)  $Ri=0.5$  (transitional) (c)  $Ri=1.0$  (quasi-turbulent) and (c)  $Ri=1.5$  (turbulent) in opposing flow

## 5.6 Comparison between numerical and experimental laminar mixed convection results

In this section, the experimental results in the laminar regime were compared with my numerical simulation results to ensure the validity of the numerical results.

### 5.6.1 Pressure drop and heat transfer comparisons

The local friction factor and Nusselt number are compared for  $Re$  from 500 to 1500 at fixed  $Ri=0.1$  in both aiding and opposing flows of laminar mixed convection. Here, it is found that the friction factor is continuously decreasing with the increase in  $Re$  in a log-plot for both aiding (Figure 5.38 (a)) and opposing flows (Figure 5.38 (c)). In contrast to it, the  $Nu$  increases with the increase in  $Re$  in both aiding and opposing flows (Figures 5.38 (b) and (d)) as also observed in the numerical results. The trends in the experiment are similar, with some differences in the magnitudes. The difference in magnitudes can be due to the inadvertent inaccuracies in both the experimental and simulation aspects. The difference may be due to the presence of instrumental error and measurement uncertainty. In addition, the energy balance error was created due to the heat loss to the surroundings during the experiments. The heat loss is not a matter of concern in the case of numerical simulations of the friction factor and Nusselt number values. However, certain assumptions such as the Boussinesq approximation, were employed in the simulations to consider the buoyancy effect. It varies the density only in the body force term of the momentum equation, irrespective of the presence of density in convective terms as well. The other reason is that with the best possible effort, it is very difficult to maintain the water temperature at 20°C while performing the experiments at high heat fluxes, especially in the summer season in India. In the simulations, one can set the desired temperature for any case of high or low heat fluxes. Lastly, the two-dimensional approximation used in our simulations due to lack of computational resources may also be the reason of discrepancies.

## 5.6 Comparison between numerical and experimental laminar mixed convection results

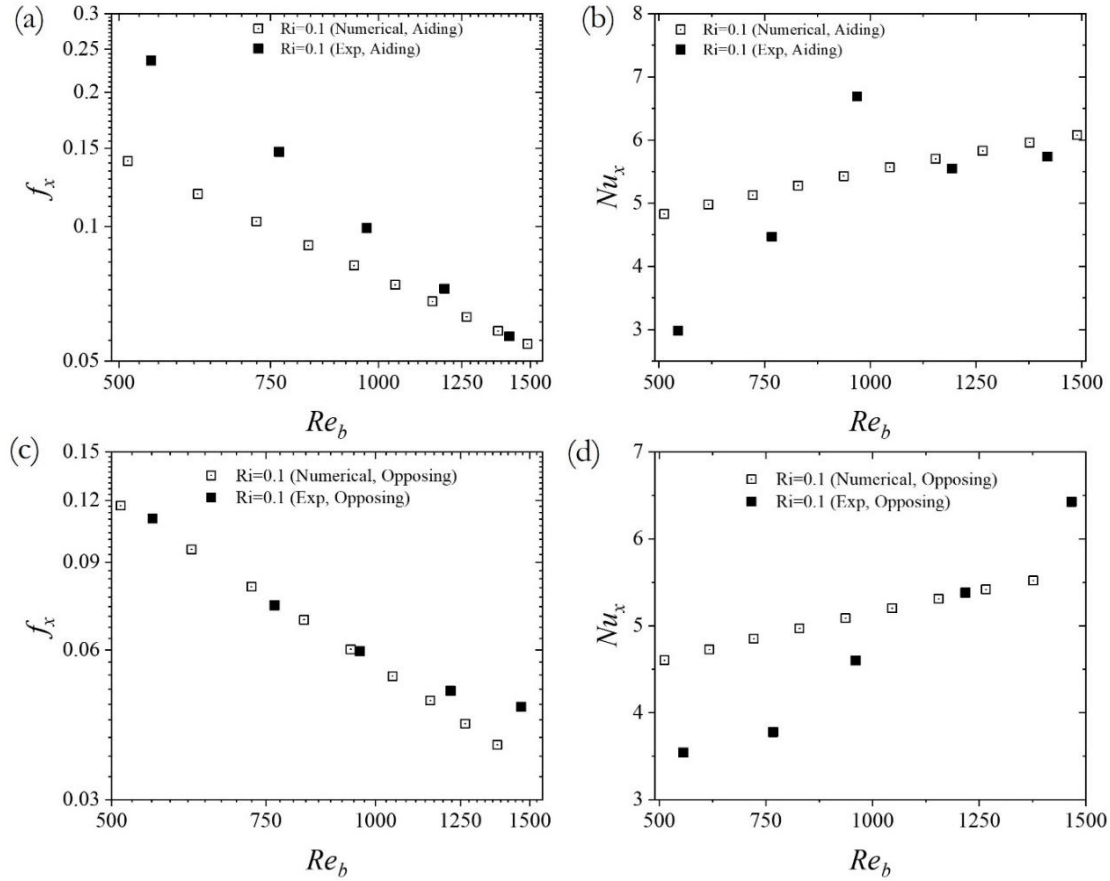


**Figure 5.38** Local  $f$  and  $Nu$  vs.  $Re$  comparison plot at  $L/D=121$  for (a) & (b) aiding and (c) & (d) opposing laminar mixed convection at fixed  $Ri=0.1$

Three specific cases of laminar mixed convection experiments at  $Re_b$  of  $\sim 500$ ,  $\sim 700$  and  $\sim 900$  is compared with the numerical results of local  $Nu$  vs.  $Gz$  plot (Figures 5.39 (a) and (b)). The  $1/Gz$  length is higher in the simulations because of greater length-to-diameter ratio ( $L/D \geq 500$ ) considered in the simulations as compared to the experiments ( $L/D \leq 130$ ). For the common Graetz length, the local  $Nu$  obtained in the experiments show similar trend to the numerical values. Furthermore, with the increase in  $Re$ , the increasing trend of  $Nu$  is found in both numerical as well as experimental results. At higher flow rates, the heat is being carried away by the flowing fluid, resulting in a higher Nusselt number. The deviation in the numerical and experimental results for  $Re = 545$  in aiding flow and  $Re = 557$  in opposing flow is due to the heat loss to the surroundings during experiments. Another reason can be that at low flow rates, the heat is being transferred by conduction rather than convection, which exhibits low heat transfer.

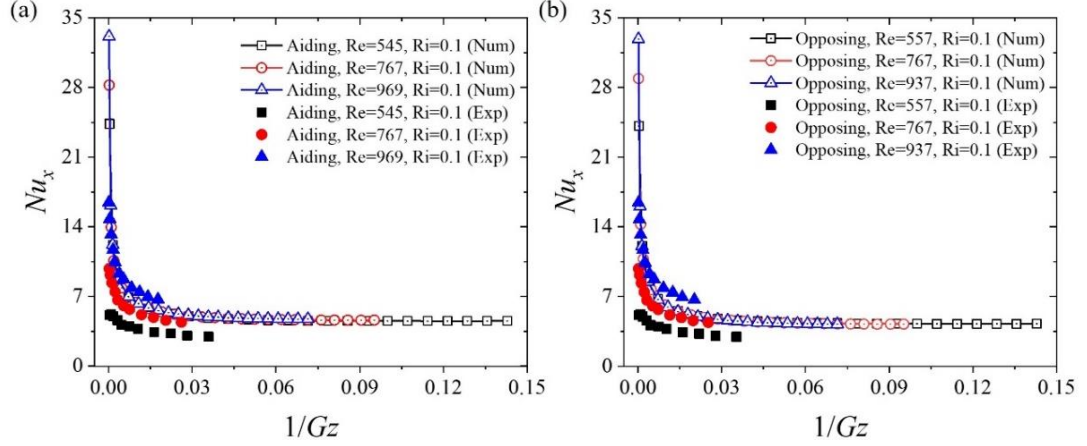


**Figure 5.39** Local  $Nu$  (numerical vs. experimental) comparison plots in (a) aiding and (b) opposing flow for laminar mixed convection at fixed  $Ri$

## 5.7 Conclusions

We have performed a comparative study of numerical simulations and experimental investigations of laminar mixed convection for buoyancy-assisted and buoyancy-opposed flows through a vertical tube.

- **Velocity profile:** In cases of assisting flow, it has been observed that the velocity is accelerated near the tube wall compared to the center of the tube. In contrast, velocity is accelerated at the center as compared to the tube wall in the case of opposing flow for same  $Re$  and  $Ri$ .
- **Effect of  $Ri$ , by varying  $Gr$  at constant  $Re$ :** With increasing  $Ri$ , both  $f$  and  $Nu$  exhibited increasing and decreasing trends for buoyancy-aided and opposed cases, respectively. It is worth mentioning that the developing region exhibits higher  $Nu$  compared to fully developed states for both aided and opposed flows.
- **Effect of  $Re$  at fixed  $Ri$ :** Furthermore, as the  $Re$  increases at a fixed  $Ri$ , the  $f$  decreases in both buoyancy-assisted and -opposed flow as believed, whereas the  $Nu$  increases in assisted flow and decreases in opposed flow.
- **Colburn  $j$ -factor:** The heat transfer results are also examined in terms of Colburn  $j$ -factor for developing and fully developed flows. The developing and fully developed Colburn  $j$ -factor both increases in case of buoyancy-assisting flow and decreases in buoyancy-opposed flow.

## 5.7 Conclusions

- **Entry length:** It is also confirmed from the results that the entry length is dependent on free convection effect for simultaneously hydrodynamically and thermally developing flows. The hydrodynamic development length increases with the increase the  $Ri$  for both assisting and opposing flow, but the thermal entry length decreases in case of assisting flow in contrast to the opposing flow.
- Finally, the correlations for fully developed  $f$  with  $Re$  as well as  $Ri$  and  $Nu$  with  $Ri$  are developed. Two independent correlations of local  $Nu$  with Graetz number ( $Gz$ ) for developing ( $1/Gz < 0.10$ ) and fully developed ( $1/Gz \geq 0.10$ ) regimes were developed to obtain the heat transfer for  $Ri = 0.125 - 1.5$  at a particular  $Re$  in both buoyancy-assisting and buoyancy-opposing flows.

This study is limited to the constant properties (except density) of water flow through vertical smooth tubes subjected to constant heat flux. Since it is also believed that viscosity will play an important role in the flow characteristics, the extreme cases have been studied further to see the effect of it on the results. The viscosity is varying according to the correlation of Popiel and Wojtkowiak [128], which is modified as per the Eq. (5.9). The results with varying the viscosity along with the density for  $Ri=0.1$  and  $Re=500$  for aiding and opposing flow are presented in Figures A.14-A.15 of Appendix-A.

$$\mu = 0.000000127 T^2 - 0.000023 T + 0.001399 \quad (5.9)$$

Where  $T$  is the temperature in °C.

The experimental investigations exhibited similar trends with the results obtained the numerical simulations. However, quantitatively the magnitudes of the experimentally obtained quantities like  $f$  and  $Nu$  were different from the numerical simulations due to the reasons discussed in preceding section. In addition to the quantities like  $f$  and  $Nu$ , the visualization of flow has been carried out in the experiments to identify the flow behaviour.

## APPENDIX A

### Additional plots related to laminar mixed convection numerical results

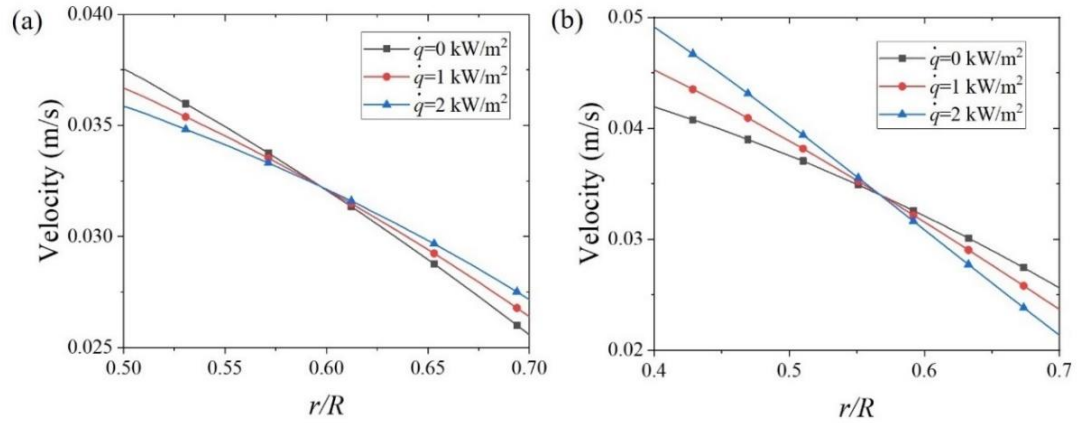


**Figure A.1** Magnified view of (a) Figure 5.1(b) and (b) Figure 5.12(b) within region  $0.5 \leq r/R \leq 0.70$

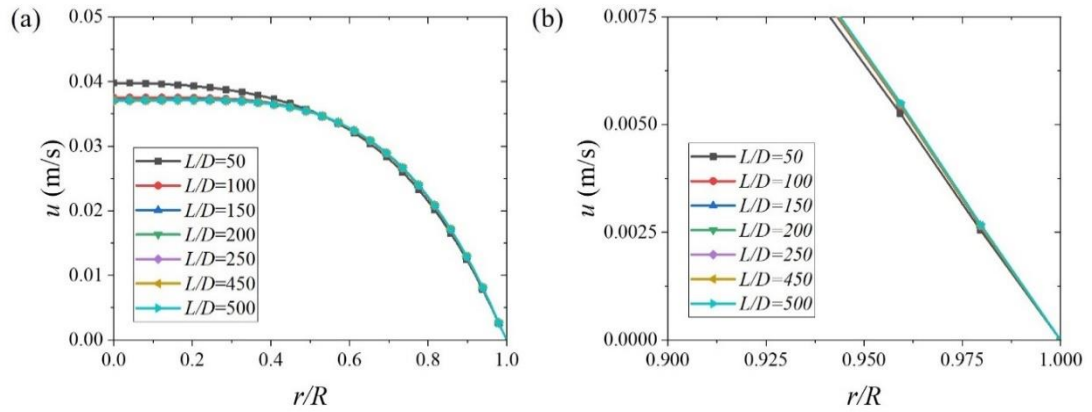


**Figure A.2:** (a) Velocity profile and (b) magnified velocity near the walls ( $0.95 \leq r/R \leq 1$ ) at different axial length (for Figure 5.1(b) at  $\dot{q} = 2$  kW/m<sup>2</sup>)

## Additional plots

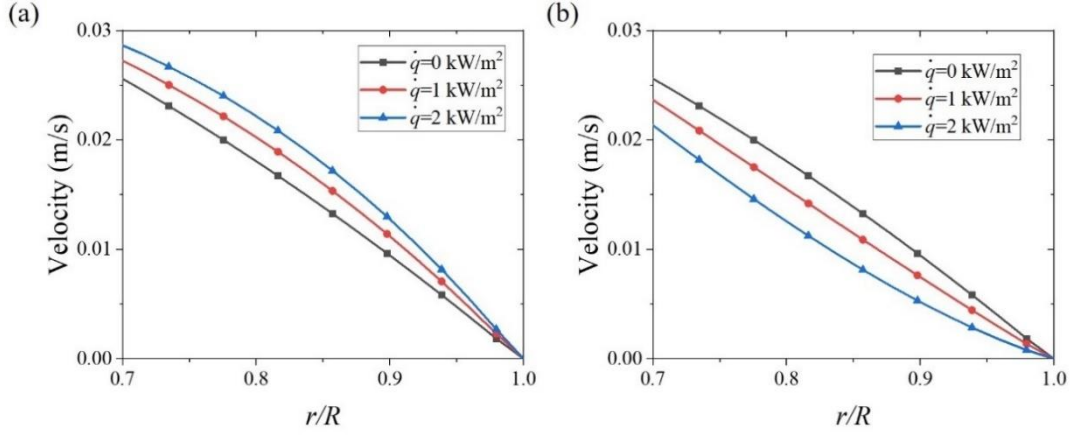


**Figure A.3:** Magnified view of (a) Figure 5.1 b) and (b) Figure 5.12(b) adjacent to the wall i.e.,  $0.7 \leq r/R \leq 1$ , based upon which the friction factor was defined

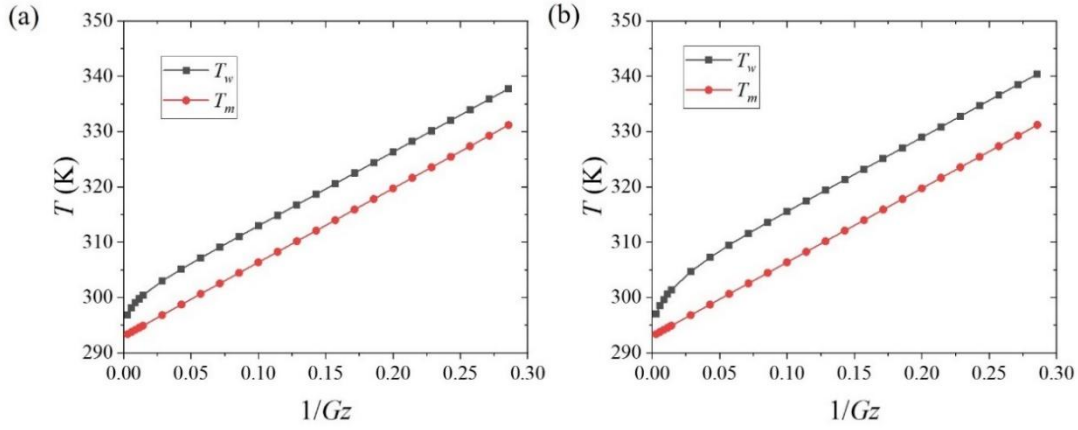


**Figure A.4:** Wall temperature ( $T_w$ ) and mean temperature ( $T_m$ ) variation at different axial length (for Figure 5.3(b) and 5.14(b) at  $\dot{q}=2$  kW/m<sup>2</sup>) for (a) assisting and (b) opposing flow

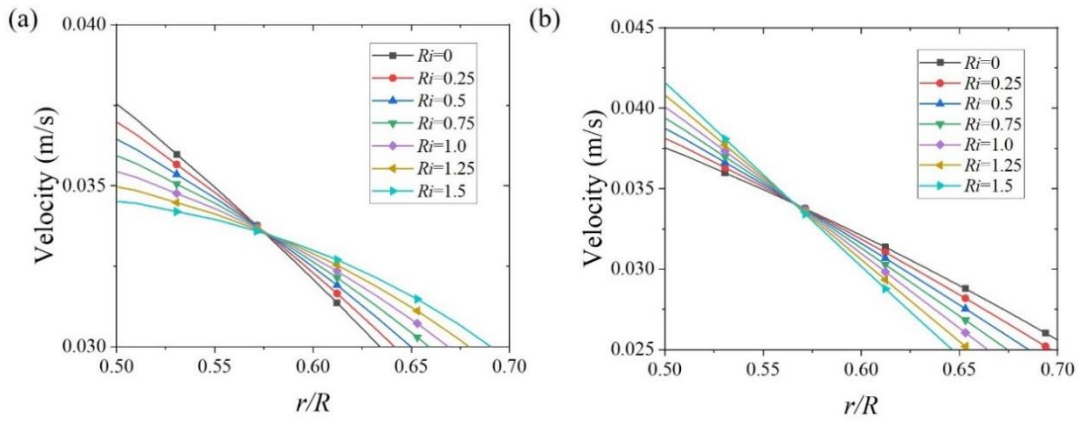


**Figure A.5:** Magnified view of (a) Figure 5.4(b) and (b) Figure 5.15(b)



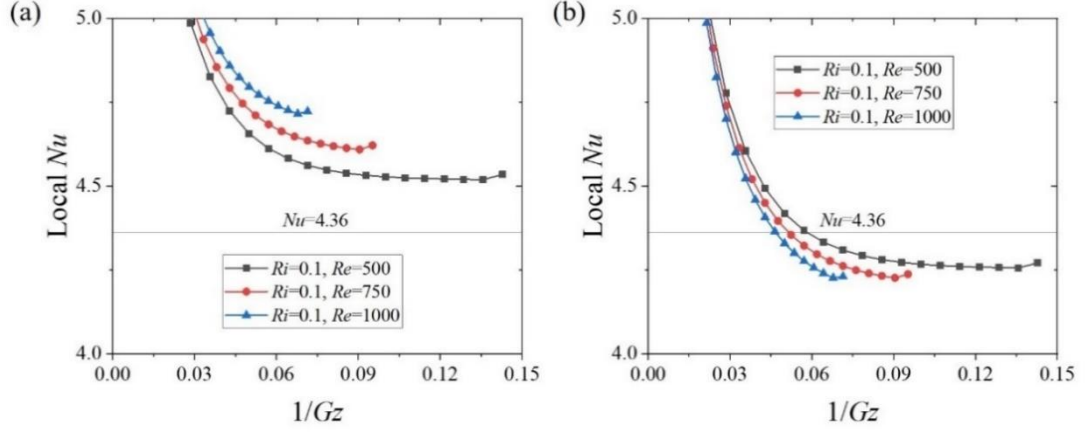


**Figure A.6:** Magnified view of (a) Figure 5.8(b) and (b) Figure 5.19(b)

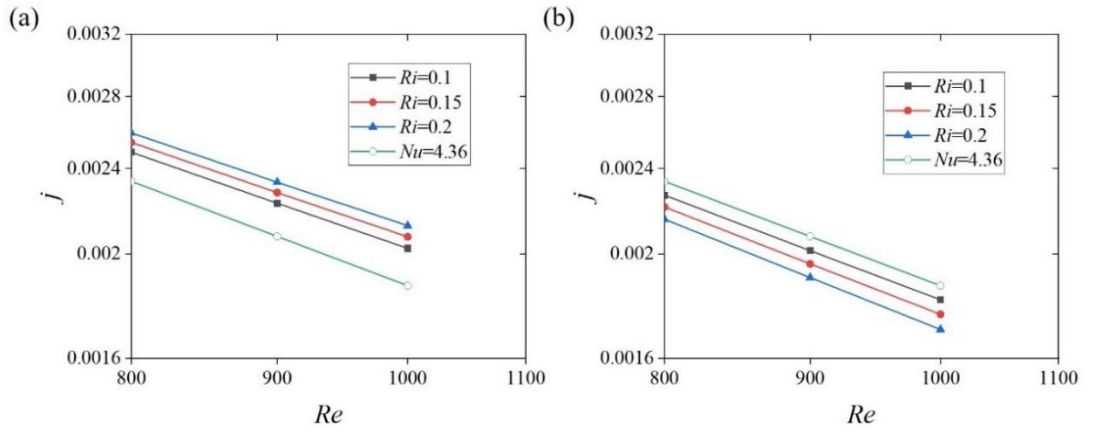


**Figure A.7:** Magnified view of (a) Figure 5.10 and (b) Figure 5.21

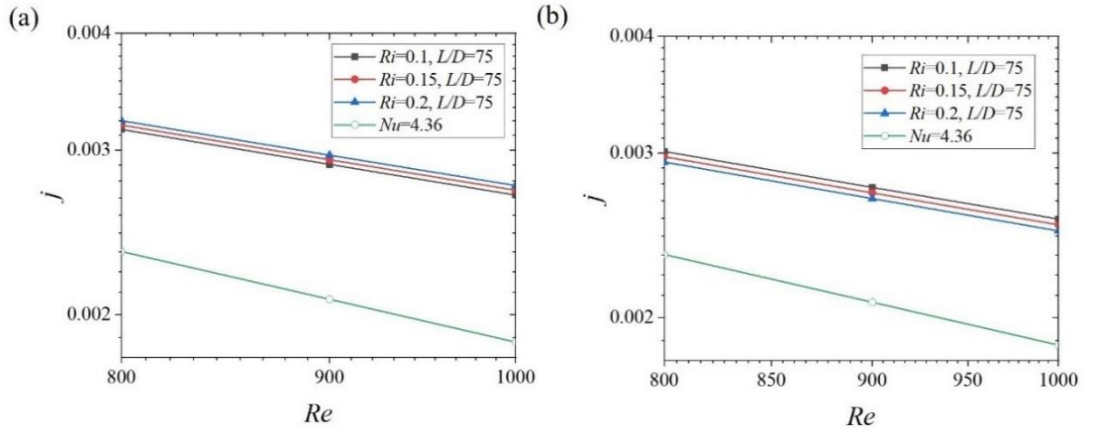


**Figure A.8:** Enlarged view of (a) Figure 5.11(b) and (b) Figure 5.22(b)

## Additional plots

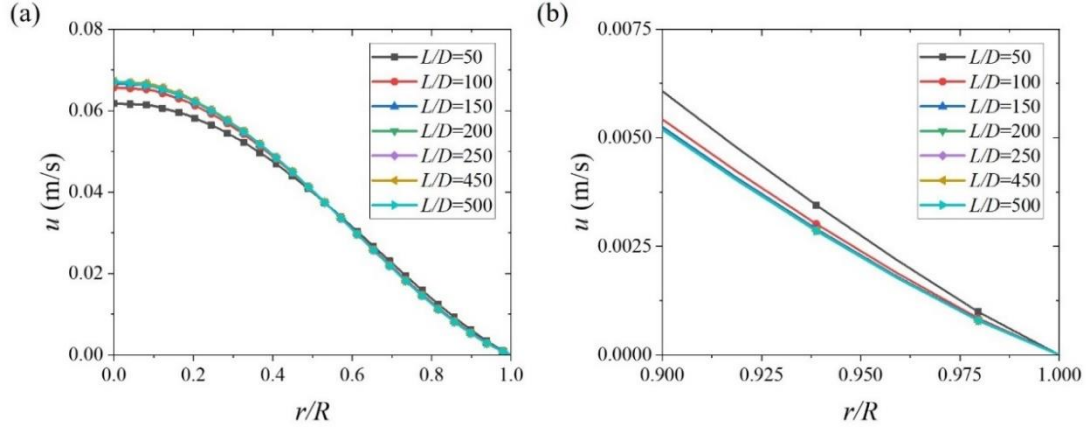


**Figure A.9:** (a) Velocity profile and (b) magnified velocity near the walls ( $0.95 \leq r/R \leq 1$ ) at different axial length (for Figure 5.12(b) at  $\dot{q} = 2 \text{ kW/m}^2$ )

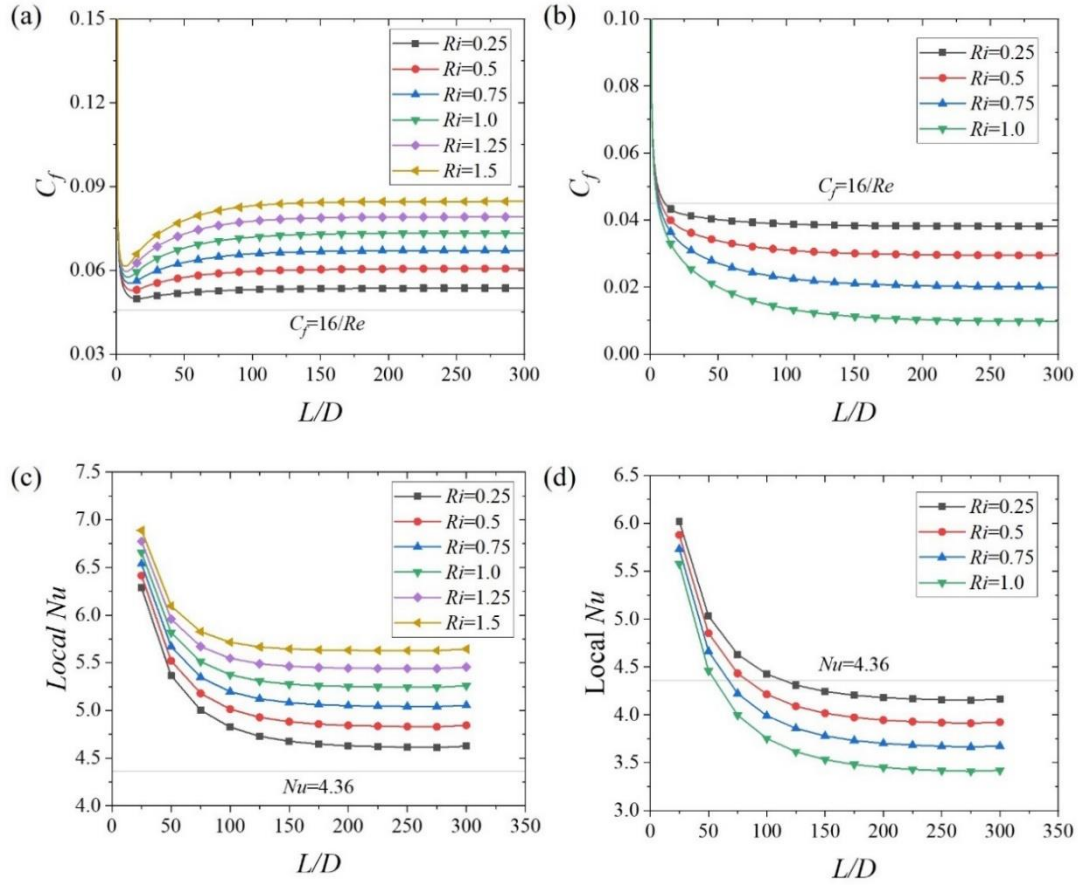


**Figure A.10:** Local  $C_f$  and  $Nu$  plot corresponding to different  $Ri$  at  $Re = 350$  for (a, c) assisting and (b, d) opposing flow (numerical instability observed after  $Ri = 1.0$ )

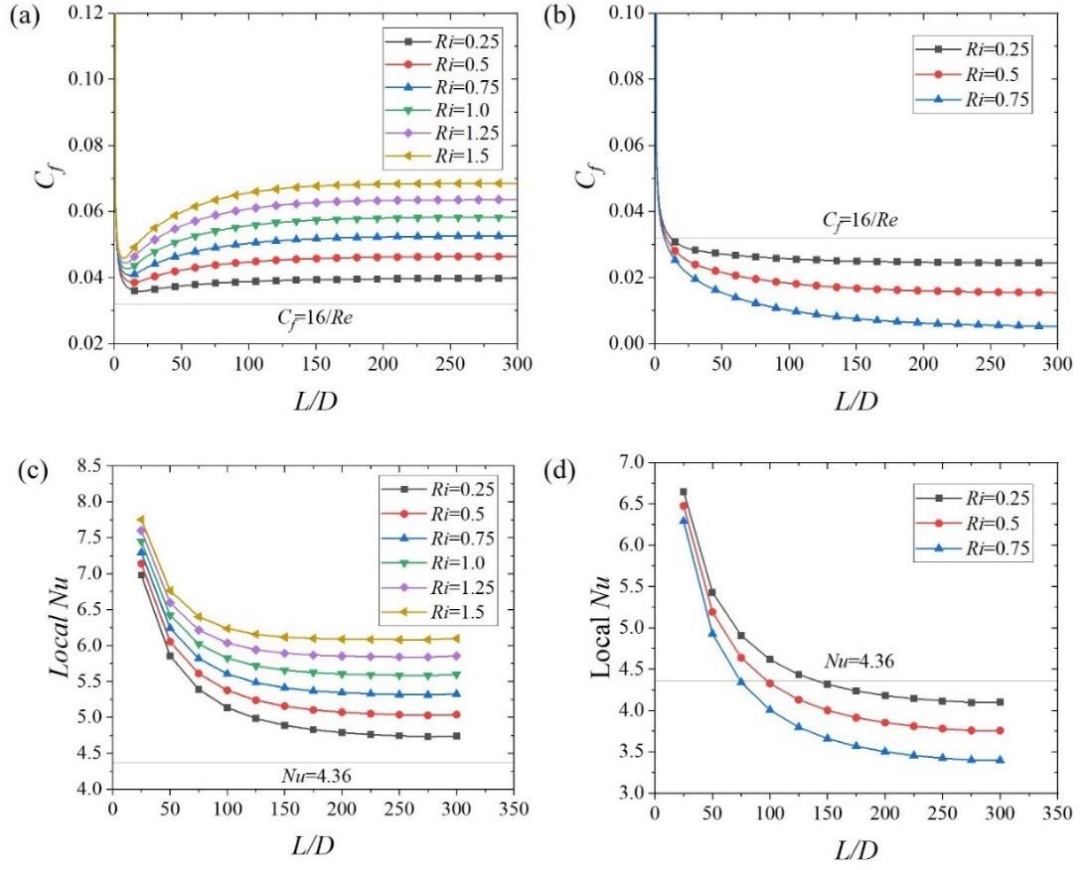


**Figure A.11:** Local  $C_f$  and  $Nu$  plot corresponding to different  $Ri$  at  $Re = 500$  for (a, c) assisting and (b, d) opposing flow (numerical instability observed after  $Ri = 0.75$ )

## Additional plots

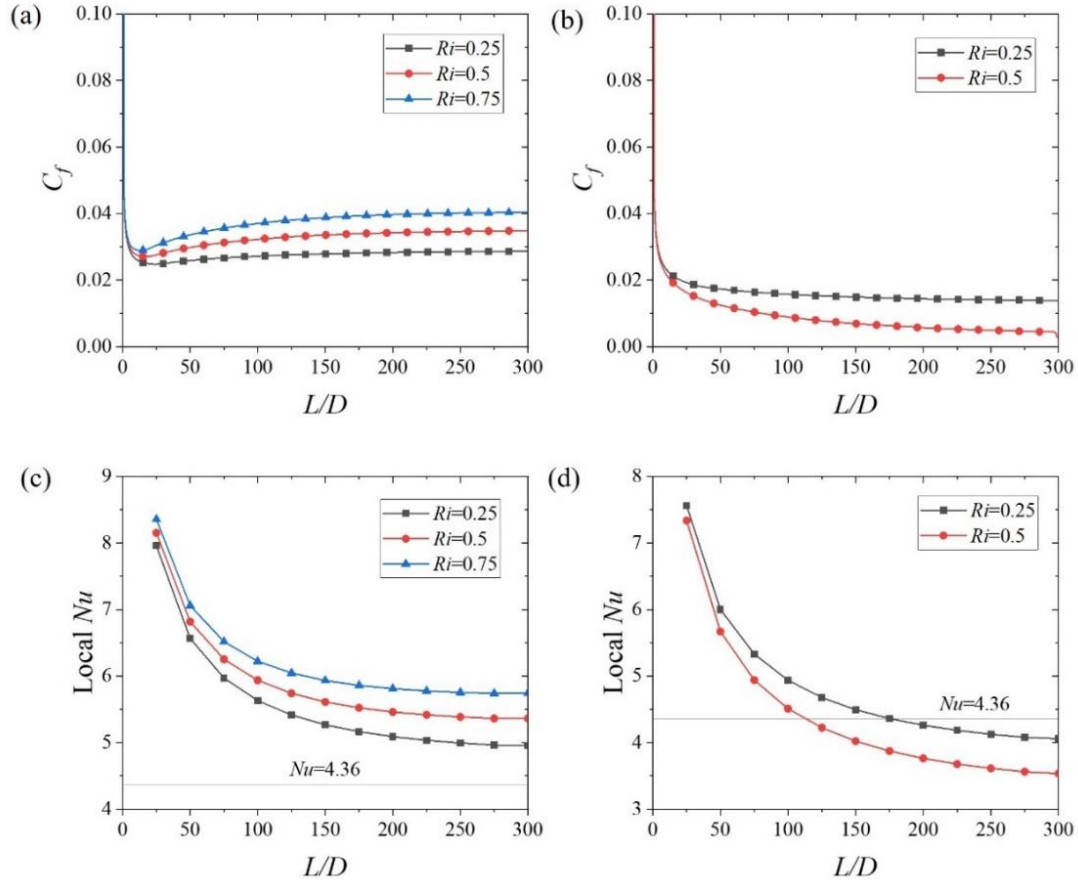


**Figure A.12:** Local  $C_f$  and  $Nu$  plot corresponding to different  $Ri$  at  $Re = 750$  for (a, c) assisting and (b, d) opposing flow (numerical instability observed after  $Ri = 0.5$ )

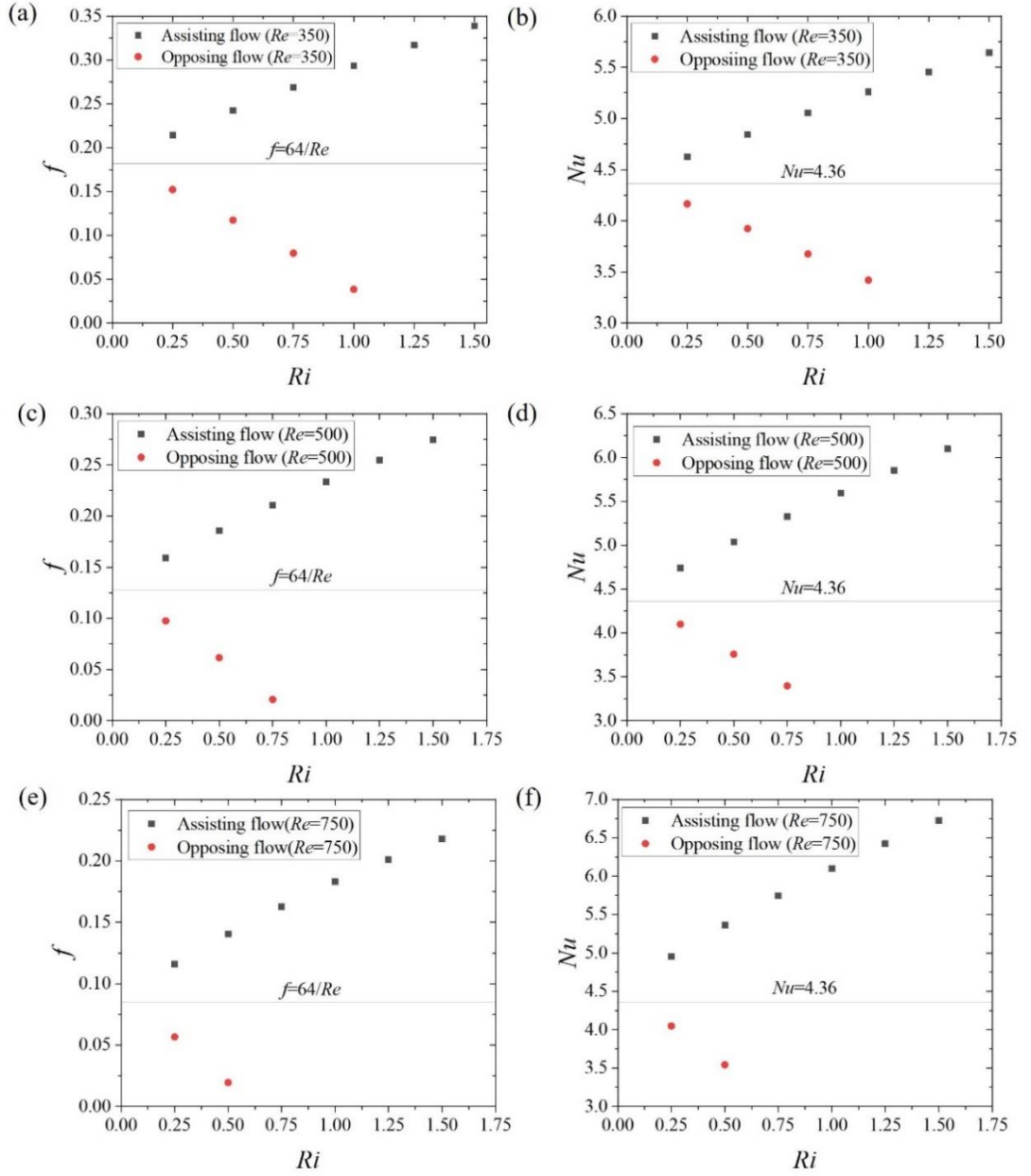


**Figure A.13:** Fully developed  $f$  vs.  $Ri$  and  $Nu$  vs.  $Ri$  plots corresponding to (a, b)  $Re = 350$  (c, d) 500 and (e, f) 750 for assisting and opposing flow (numerical instability observed after  $Ri = 1.0$  for  $Re = 350$ , after  $Ri = 0.75$  for  $Re = 500$  and after  $Ri = 0.5$  for  $Re = 750$ )

## Additional plots

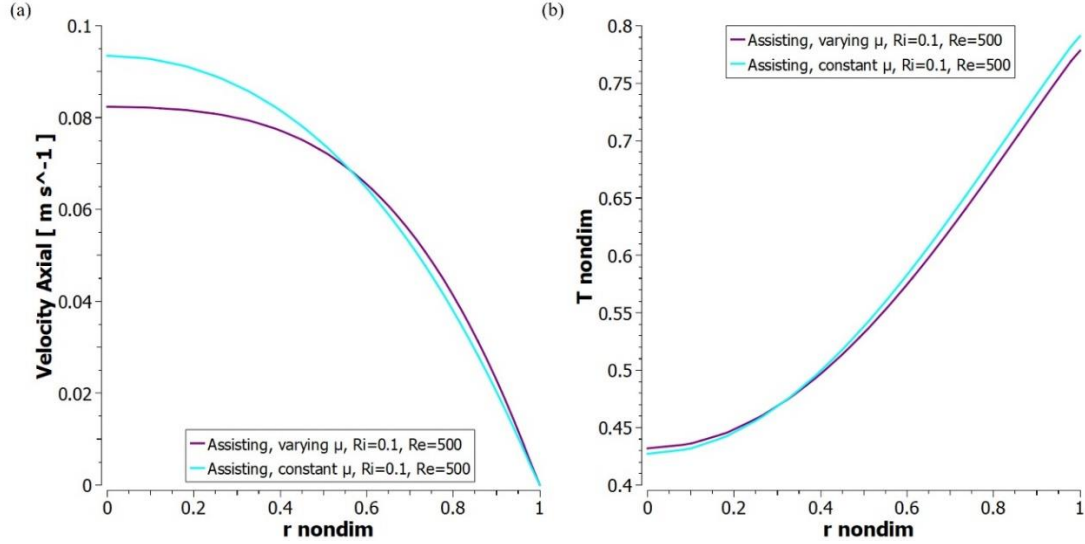


**Figure A.14:** Comparison of (a) velocity and (b) non-dimensional temperature ( $T_{nondim}=(T-T_i)/\dot{q}D/k$ ,  $r_{nondim}=r/R$ ) profiles for varying viscosity at  $Ri=0.1$  and  $Re=500$  in aiding flow. Due to the decrease in viscosity with the increase in temperature, velocity near the wall increases as compared to the velocity when the viscosity is constant. To conserve the mass the increase in velocity near the wall gets compensated with the decrease of it at the centre. Thus, the heat is being carried away by the fluid resulting in lower temperature gradient. This ultimately increases the friction factor and decreases the Nusselt number.

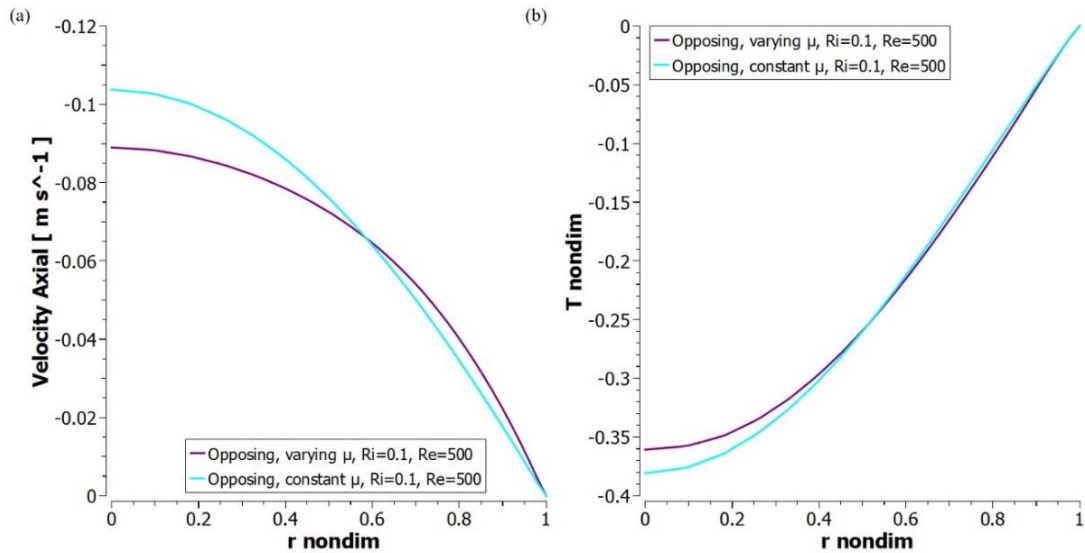


**Figure A.15:** Comparison of (a) velocity and (b) non-dimensional temperature profiles for varying viscosity at  $Ri=0.1$  and  $Re=500$  in opposing flow. Due to opposing effect of free convection the increase in the velocity near the wall and decrease at the centre is less as compared to aiding flow. Thus, the pressure drop also increases in opposing flow. The temperature gradient is indiscernible in case of varying viscosity with temperature

as compared to the constant viscosity. However, there is an increase of temperature at the core which results in decrease of heat transfer.





### Transitional Mixed Convection

---

#### 6.1 Introduction

Compared to transitional regime of mixed convection in horizontal tubes, transition regime of buoyancy-aided or -opposed mixed convection flow in vertical tubes is relatively lesser studied. In this present study, we have first performed the numerical simulations of the developing regime of laminar-turbulent transitional mixed convection in a vertical tube. In addition to the thermal and hydrodynamic features in the developing flow, the variation of hydrodynamic and thermal entry length with the variation of  $Gr$  is discussed for both buoyancy-assisted and opposed cases. In this present study, to avoid a two-phase at the tube outlet, the length-to-diameter ratio of the tube was chosen at 150 for the given heat flux. In real life heat exchangers, mostly the flow is developing because of shorter tube length. It has also been kept in mind that the mixed convection regime should be maintained. To achieve this, the  $Re$  was varied from 2000 to 5000 at a fixed value of  $Ri=0.1$ . Followed by the numerical work, experimental observations related to the laminar-turbulent transitional characteristics have been described for both the flows.

#### 6.2 Numerical results on transitional mixed convection

Mixed convection in a vertical pipe with test fluid water is characterized by different parameters like  $Re$ ,  $Gr$  and  $Ri$ . The  $Re$  range is 2000 to 5000 is based on the average inlet velocity and  $Gr$  range is  $4 \times 10^3$  to  $5 \times 10^7$  is based on the heat flux,  $Ri$  range is from 0.001 to 0.1, and  $Pr$  is 7 based on water at the inlet temperature of 20°C. The flow rate ( $Re$ ) has been decided based on the experimental evidence of Reynolds [10], and the heat flux ( $Gr$ ) was obtained from the flow regime map (Figure 1.3) applicable for mixed convection in a vertical tube [3]. The results are analysed in such a way that  $Ri$  is constant while varying  $Gr$ ,  $Re$ .

$$Ri = Gr/Re^2 \quad (6.1)$$

## 6.2 Numerical results on transitional mixed convection

Where  $Gr = g\beta D^4 \dot{q} / \nu^2 k$  and  $Re = \rho u_m D / \mu$

### 6.2.1 Buoyancy-assisting Flow

#### 6.2.1.1 Fixed $Ri$ and varying $Gr$ , $Re$

In this section, the effect of  $Re$  and  $Gr$  in the transitional regime of buoyancy-assisting flow have been quantified. Simulations were carried out by keeping  $Ri$  constant as 0.1 and varying  $Re = 2000 - 5000$  with appropriate changes in the  $Gr$ . Here the effect of  $Re$  on the flow as well as heat transfer has been explained with the plots of velocity, temperature, skin friction coefficient ( $C_f$ ), Nusselt number ( $Nu$ ), turbulent kinetic energy ( $\kappa$ ), and turbulent eddy frequency ( $\omega$ ), intermittency ( $\gamma$ ) and momentum thickness Reynolds number ( $Re_\theta$ ).

The centreline velocity in Figure 6.1(a) shows an increase in velocity at the entrance and then it decreases and becomes steady once the flow becomes fully developed. In the developing regime the boundary layer develops due to the no slip boundary condition which increases the velocity at centre. Further downstream, due to increase in free convection effect the velocity near the wall increases and to maintain the same flow rate the velocity at the centre reduces. Afterwards, the velocity becomes steady once the flow becomes fully developed. The velocity profiles in Figure 6.1(b) reflect the increase in velocity magnitude with an increase in  $Re$  at fixed  $Ri$ . The maximum velocity profiles at  $Re=2100$  ( $u_{max}/u_{avg} = 1.248$ ) and  $Re=2400$  ( $u_{max}/u_{avg} = 1.2556$ ) are deviating from the parabolic profile by 37.6% and 37.2% lower, respectively.

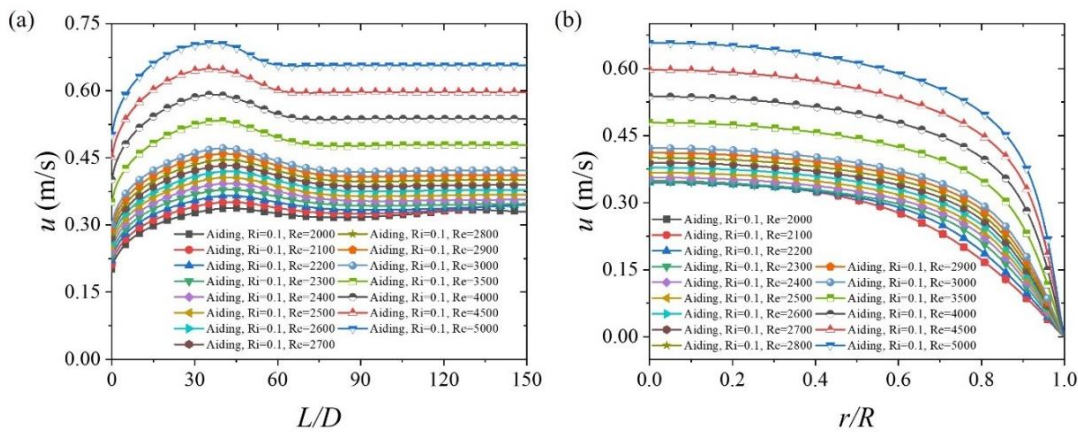


**Figure 6.1** (a) Centerline velocity and (b) velocity profile at  $L/D=150$  for fixed  $Ri=0.1$  and varying  $Re$  and  $Gr$  in aiding flow

Analogous to the axial variation analysis of centreline velocity, the axial variation of centreline temperature was represented in Figure 6.2(a). The centreline temperature

initially stays constant at ambient temperature of 20°C (293 K) upto  $L/D \sim 40$  because the thermal boundary layer was developing, and a small amount of heat is being diffused towards the centre. Further downstream, the boundary layer develops, and it increases with increase in axial length. The rate of increment of centreline temperature with axial length is initially higher due to the transition. Beyond the constant temperature region ( $L/D \geq 40$ ), at a given instant, the centreline temperature continuously increases with the increase in  $Re$ . The boundary layer was developed, and more heat gets diffused to the centre that results into higher centreline temperature. Apart from that, the wall temperature ( $T_w$ ) increases with the increase in  $Ri$  and reaches a peak value, drops at further downstream to the tube. Eventually the difference between wall and mean fluid temperature ( $T_m$ ) decreases which increases the temperature gradient near the wall can be seen in Figures 6.2(a) and (b).

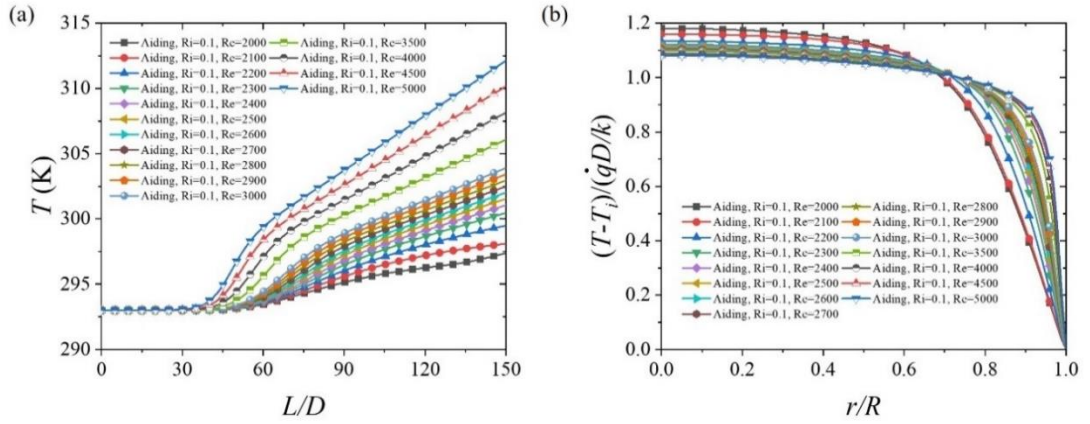


**Figure 6.2** (a) Centerline temperature and (b) non-dimensional temperature profile at  $L/D=150$  for fixed  $Ri=0.1$  and varying  $Re$  and  $Gr$  in aiding flow

Based on the velocity (Figure 6.1) and temperature profile (Figure 6.2), the skin friction coefficient ( $C_f$ ) and Nusselt number ( $Nu$ ) are shown in Figures 6.3(a) and (b) respectively. The  $C_f$  decreases initially with the increase of  $L/D$  because of the development of hydrodynamic boundary layer, and eventually achieves a higher constant value in fully developed state. The Nusselt number is higher in developing flow due to the development of thermal boundary layer. Thereafter,  $Nu$  decreases as the flow progresses. Then  $Nu$  is increased and becomes steady when flow becomes fully developed. In contrast,  $C_f$  increases with the increase in  $Re$  and attains an early peak before the flow is developed. Therefore, the hydrodynamic entry length decreases with the increase in  $Re$ , as indicated by A, B, C, D, E, F, G, H, I, J, and K (Figure 6.3(a)) and thermal entry length increases as indicated by an arrow (Figure 6.3(b)) with the increase in  $Re$ , at fixed  $Ri$ . However, from

## 6.2 Numerical results on transitional mixed convection

the plot, it is speculated that the points A, B, C, and D in the cases of  $Re=2000, 2100, 2200$ , and  $2300$  are the end of the developing flow, which may not be true. To find out the exact entry length and whether the flow is thermally fully developed or not, a higher  $L/D$  ratio is needed to be simulated.

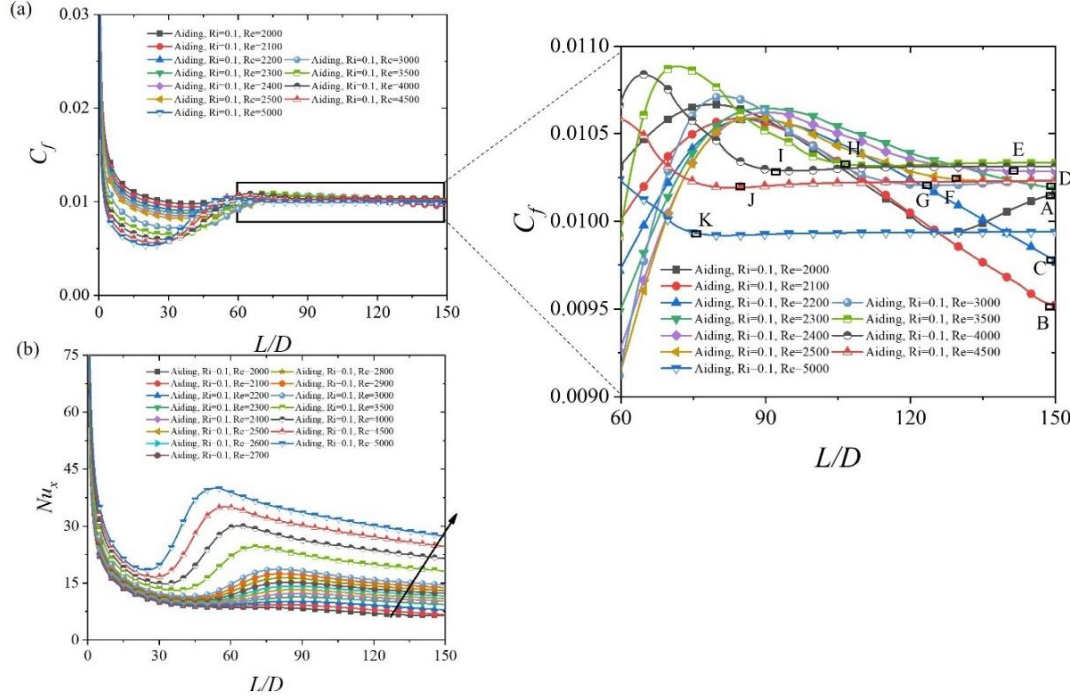


**Figure 6.3** (a) Coefficient of skin friction ( $C_f$ ) and (b) local  $Nu$  axial plot at fixed  $Ri=0.1$  and varying  $Re$  and  $Gr$  in aiding flow

Furthermore, to keep  $Ri$  constant, an increase in  $Re$  results in an increase of  $Gr$  and consequently an increase in heat flux. The higher  $Gr$  implies the increase in the free convection effect. Due to the increase in free convection effect and eventually the  $Re$ , the velocity fluctuations near the wall increases. Thus, the turbulent kinetic energy in Figure 6.4(a) increases with the increase in  $Re$  with a peak shifting towards the wall near at  $r/R \sim 0.8$ . In addition, the turbulence eddy frequency ( $\omega$ ) (Figure 6.4(b)) also increases with the increase in  $Re$ . The turbulence eddy frequency or specific dissipation rate is the relative variation of the turbulent kinetic energy which gets dissipated over the amount of turbulent kinetic energy that was generated. With the increase in  $Re$ , after a certain axial distance the  $\kappa$  increases and some of the energy gets dissipated. This ultimately increases the  $\omega$ , becomes steady for the rest of the tube length.

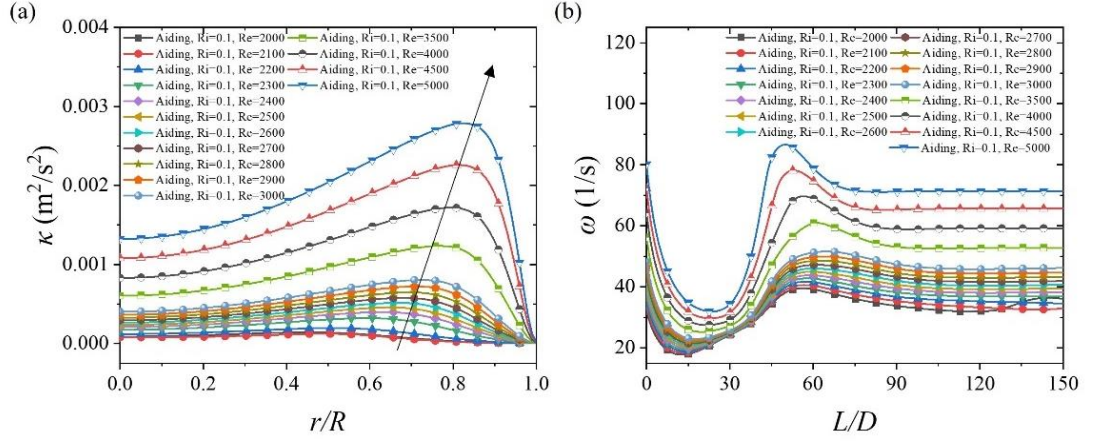


**Figure 6.4** (a) Radial turbulent kinetic energy ( $\kappa$ ) at  $L/D=150$  and (b) axial turbulent eddy frequency ( $\omega$ ) plot at fixed  $Ri=0.1$  and varying  $Re$  and  $Gr$  in aiding flow

The two important transitional transport parameters (section 3.4) intermittency ( $\gamma$ ) and momentum thickness ( $Re_\theta$ ) are highlighted in Figures 6.5(a) and (b) respectively. The intermittency factor  $\gamma$  represents the ratio of time duration of a flow in laminar and turbulent state respectively. Consistent with the previous studies [129]–[131], the intermittency factor increases as we increase  $Re$  from 2000 to 2700. With increase in  $Re$ , the flow tends to be predominantly in the turbulent regime. Naturally the intermittency factor is also of much lower magnitude than that of  $Re \leq 2700$  regime. The  $Re_\theta$  is the Reynolds number based on the momentum thickness ( $\theta$ ) which is a measure of the distance from the leading edge to the point where transition occurs. It is basically a function of turbulent intensity and a scale of measure of streamwise pressure gradient. Corresponding to the intermittency variation, the onset of transition delays with the increase in  $Re$ . The  $Re_\theta$  increases due to the decrease in intermittency near the entry. At higher mass flow rate, the  $Re_\theta$  increases indicating a delay in the onset of transition.

## 6.2 Numerical results on transitional mixed convection

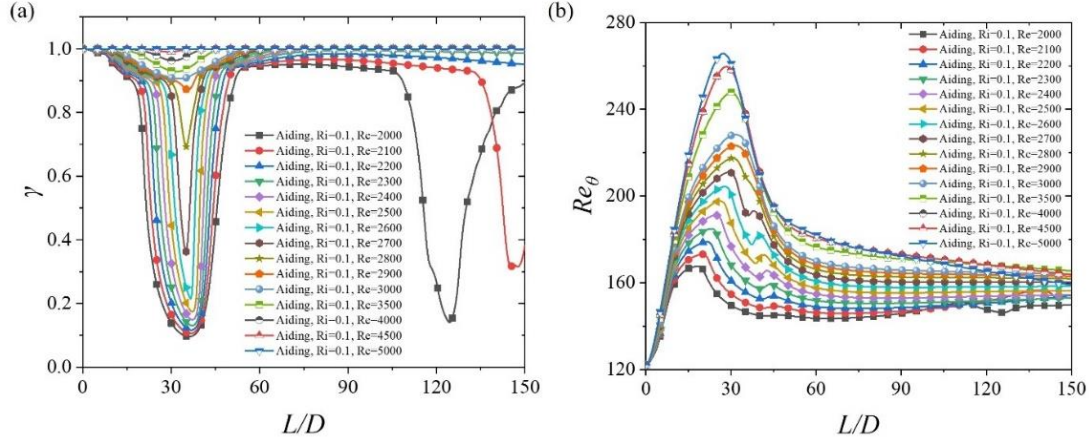


**Figure 6.5** Axial (a) intermittency ( $\gamma$ ) and (b) momentum thickness Reynolds number ( $Re_\theta$ ) plot at the centreline (i.e.,  $r/R=0.5$ ) for fixed  $Ri=0.1$  and varying  $Re$  and  $Gr$  in aiding flow

### 6.2.2 Buoyancy-opposing Flow

#### 6.2.2.1 Fixed $Ri$ and varying $Gr$ , $Re$

In this section, like buoyancy-assisted case the effect of  $Re$  and  $Gr$  have been quantified in the transitional regime of buoyancy-opposing flow. Keeping the  $Ri$  constant at 0.1, simulations are carried out by varying  $Re$  from 2000 to 5000 with appropriate changes in the  $Gr$ . The results are similar in trend but different in magnitude in buoyancy-opposed flow as compared to the buoyancy-assisted flow (Figures 6.1-6.5). The centreline velocity in Figure 6.6(a), like buoyancy assisting flow shows an increase in velocity at the entrance and then it decreases and becomes steady once the flow becomes fully developed. The velocity profiles in Figure 6.6(b) reflect the increase in velocity magnitude with an increase in  $Re$  at fixed  $Ri$ . The maximum velocity profiles at  $Re=2100$  ( $u_{max}/u_{avg} = 1.283$ ) and  $Re=2400$  ( $u_{max}/u_{avg} = 1.252$ ) deviate by 35.8% and 37.3% respectively, from the parabolic profile.



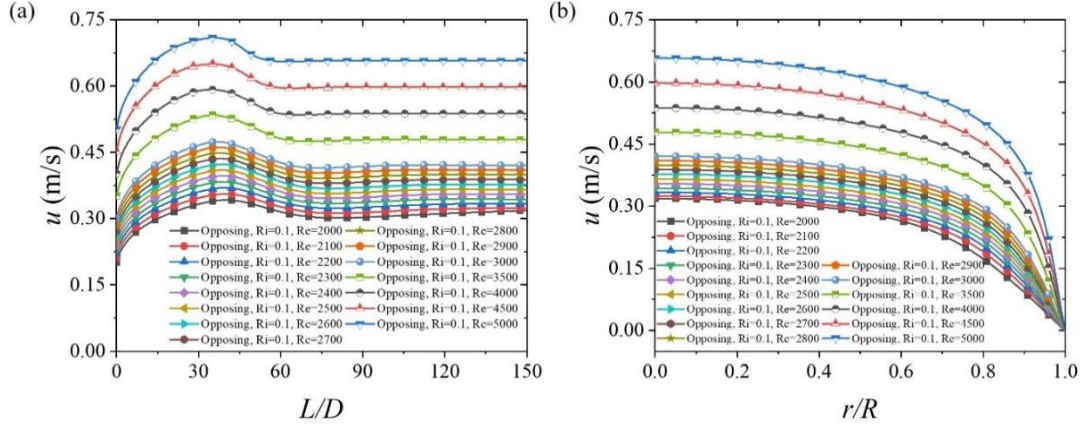


**Figure 6.6** (a) Centerline velocity and (b) velocity profile at  $L/D=150$  for fixed  $Ri=0.1$  and varying  $Re$  and  $Gr$  in opposing flow

The centreline temperature remains almost constant until  $L/D \leq 40$ ; it increases continuously with the increase in  $Re$ . The wall temperature also increases initially, reaches a peak value, and drops down before its slope increases. Eventually the difference between wall and mean fluid temperature decreases which increases the temperature gradient near the wall as shown in Figures 6.7(a) and (b).

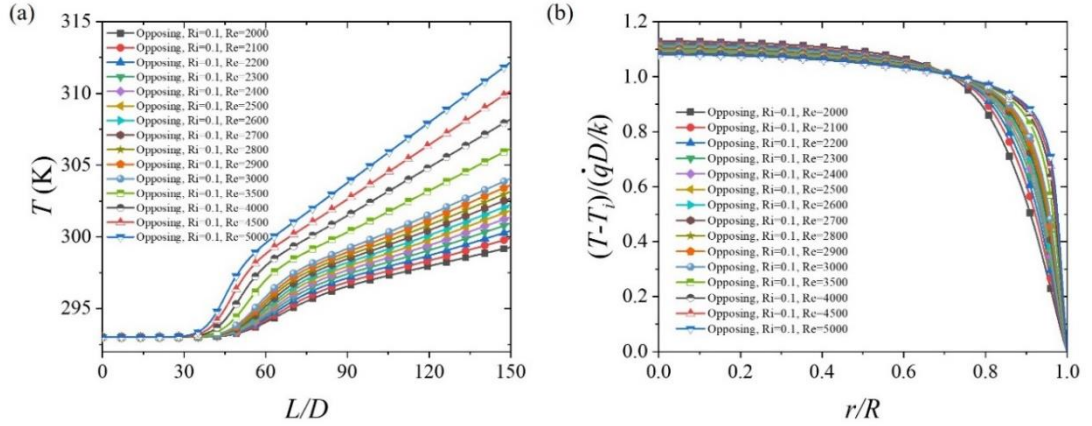


**Figure 6.7** (a) Centerline temperature and (b) non-dimensional temperature profile at  $L/D=150$  for fixed  $Ri=0.1$  and varying  $Re$  and  $Gr$  in opposing flow

The local  $C_f$  in Figure 6.8(a) decreases in the developing region, increases in the downstream and attains a peak then attains a steady value when flow becomes fully developed. The local  $Nu$  variation in Figure 6.8(b) shows a decrease at the entry due to developing thermal boundary layer and then jumps to a peak like plateau shape indicating the transition. The magnified plots show that the local  $C_f$  decreases and the local  $Nu$  increases with the increase in  $Re$  value at fixed  $Ri$ . Hence the hydrodynamic entrance length decreases as indicated by A, B, C, D, E, F, G, H, I, J, and K in Figure 6.8(a), and thermal entrance length increases with the increase in  $Re$ , at fixed  $Ri$  as indicated by an

## 6.2 Numerical results on transitional mixed convection

arrow in Figure 6.8(b). The points A, B, C, and D for  $Re=2000$ , 2100, 2200, and 2300 are hypotheses for a fully developed state which may not be true because the flow may switch from laminar to turbulent and vice versa. If the tube length had been longer, a fully developed state may have been obtained.

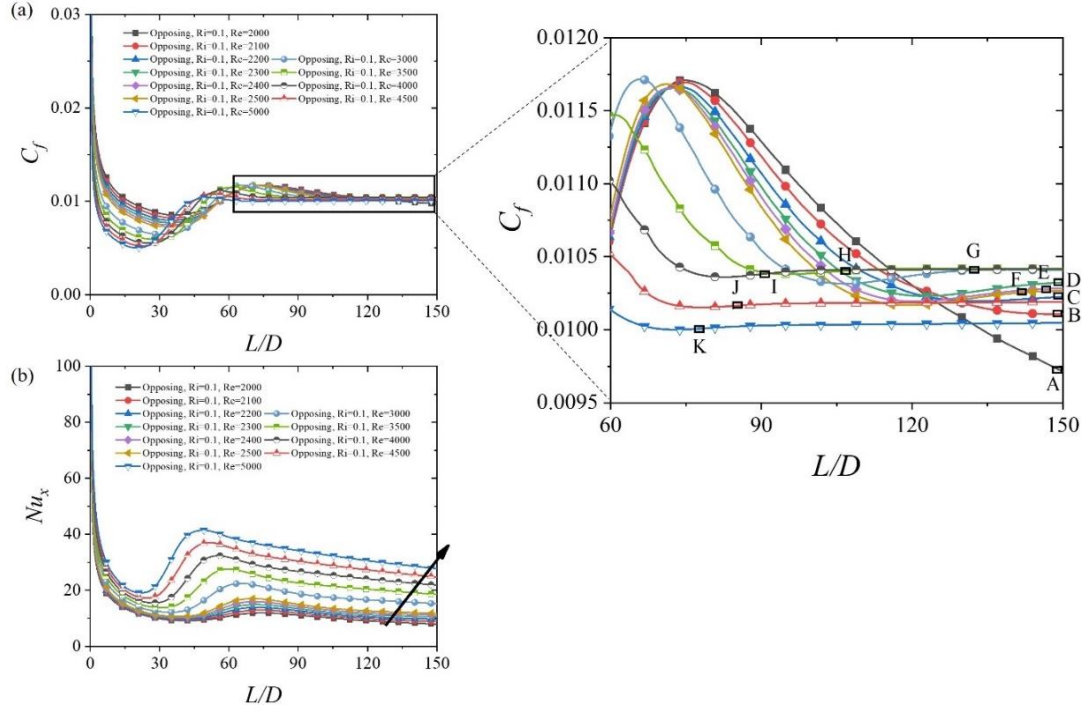


**Figure 6.8** (a) Coefficient of skin friction ( $C_f$ ) and (b) local  $Nu$  plot at fixed  $Ri=0.1$  and varying  $Re$  and  $Gr$  in opposing flow

For  $Ri$  constant, an increase in  $Re$  results in an increase of  $Gr$  and in the heat flux. This higher  $Gr$  increases the free convection effect and hence the velocity fluctuations near the wall increases. Therefore, the turbulent kinetic energy profile shown in Figure 6.9(a) increases with the increase in  $Re$  with a peak shifting towards the wall near at  $r/R \sim 0.85$ . In addition to it the axial turbulence eddy frequency in Figure 6.9(b) which represents the specific turbulence dissipation rate also increases with the increase in  $Re$ .



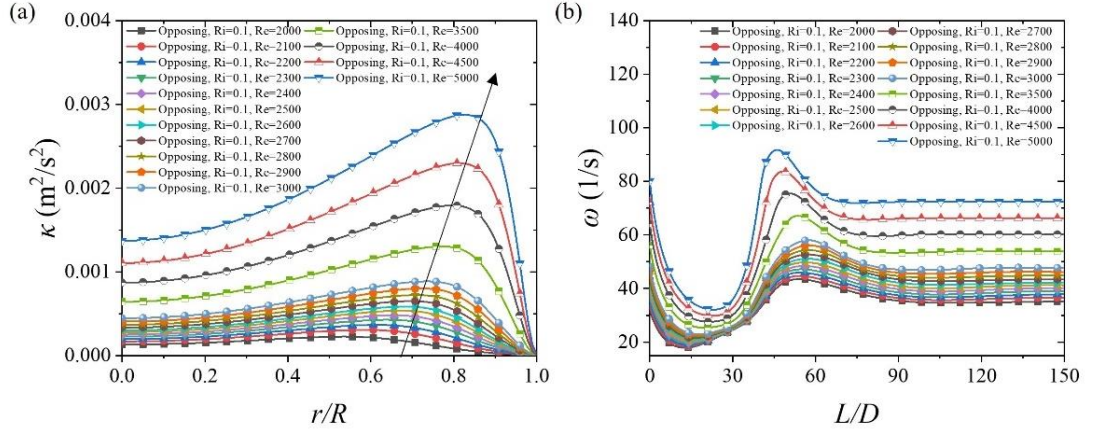


**Figure 6.9** (a) Radial turbulent kinetic energy at  $L/D=150$  ( $\kappa$ ) and (b) axial turbulent eddy frequency ( $\omega$ ) plot at fixed  $Ri=0.1$  and varying  $Re$  and  $Gr$  in opposing flow

The transport parameters  $\gamma$  and  $Re_\theta$  in Figures 6.10(a) and (b) show the flow behaviour and the onset of transition in an opposing flow. At the entry the fluctuation of intermittency represents that the flow is in transition (laminar as well as turbulent for some duration of time) and as the flow progresses, it becomes fully turbulent. The transport equation (Eq. 3.12 of section 3.4) for intermittency comprises of production as well as destruction terms. The production term controls the length of the transition region, and the destruction term allows the boundary layer to laminarise by dissipating the fluctuations. This fluctuation in velocity is prominent at lower transitional region ( $2000 < Re < 3000$ ) as that of the upper transitional region ( $3000 < Re < 5000$ ). The  $Re_\theta$  which is basically a function of turbulent intensity and a scale of measure of streamwise pressure gradient shows an increase soon after the entry due to the transition. This  $Re_\theta$  increases with the increase in  $Re$  at fixed  $Ri$ , which ultimately delays the transition onset.

### 6.3 Comparison between buoyancy-assisting and opposing flows

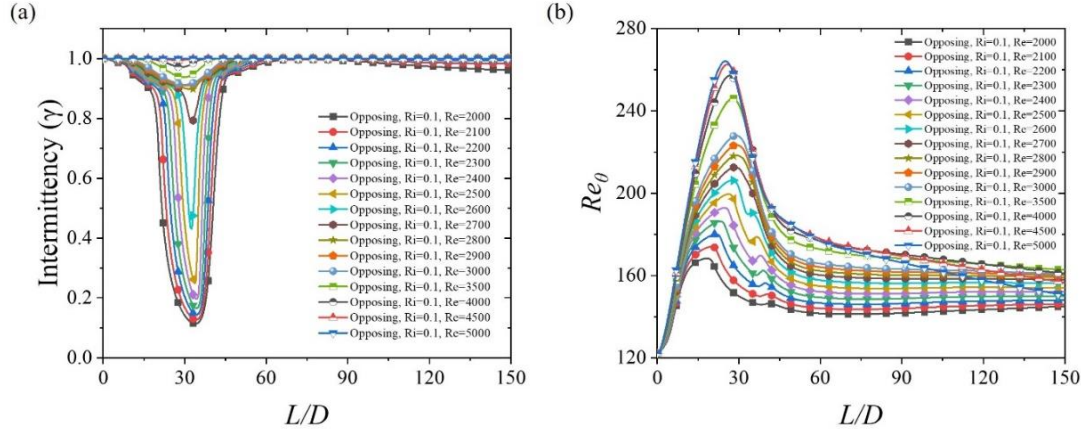


**Figure 6.10** Axial (a) intermittency ( $\gamma$ ) and (b) momentum thickness Reynolds number ( $Re_\theta$ ) plot at the centreline (i.e.,  $r/R=0.5$ ) for fixed  $Ri=0.1$  and varying  $Re$  and  $Gr$  in opposing flow

### 6.3 Comparison between buoyancy-assisting and opposing flows

The trend of results is almost same in both assisting and opposing flow case, but the difference can be seen in their magnitude. In this section, the difference is shown by comparing the results at same  $Re=2500$  and  $Ri=0.1$ . It can be seen in Figures 6.11(a) and (b) that the centerline velocity and the velocity gradient near the wall is marginally higher in buoyancy-opposing flow as that of the assisting flow. Because of opposing free convection effect, the momentum transfer is higher in opposing flow as compared to the aiding flow. This ultimately tries to acquire a non-laminar flow velocity profile and reduces the velocity at the centre and increases near the wall. The centerline temperature and the non-dimensional temperature gradient in Figures 6.12(a), (b) depicts similar trends as that of velocity. The reduction in velocity near the wall in opposing flow causes less heat is being convected towards the tube centre which increases the temperature gradient near the wall.

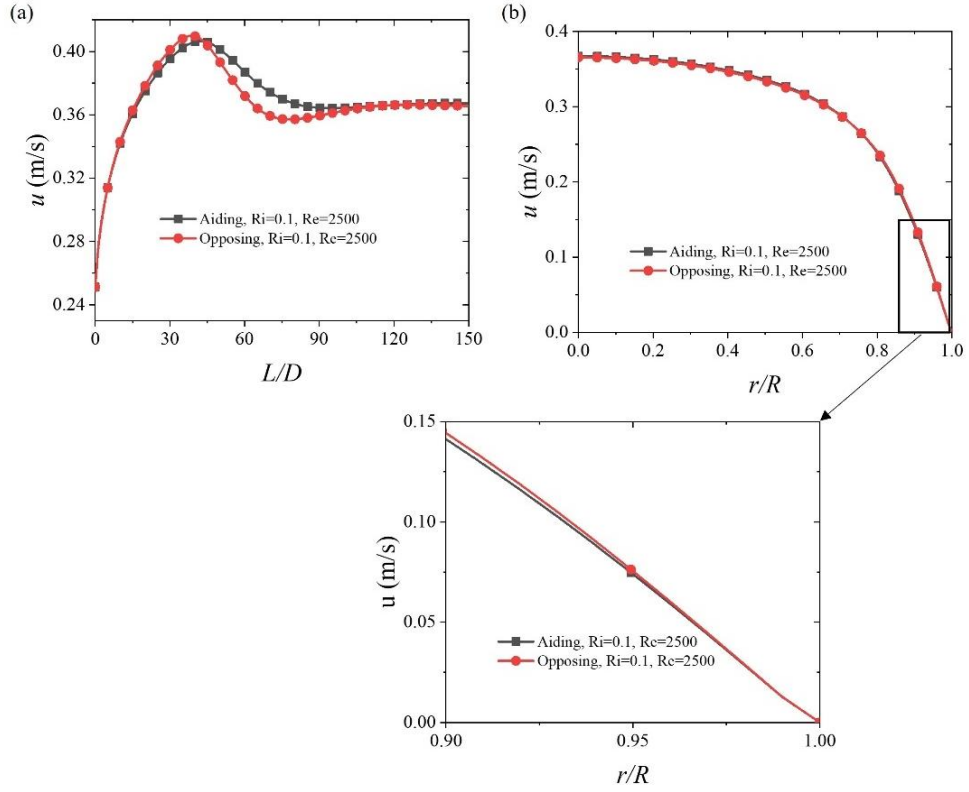


**Figure 6.11** Comparison of (a) centerline velocity and (b) outlet velocity profile in assisting and opposing case at  $Re=2500$  and  $Ri=0.1$

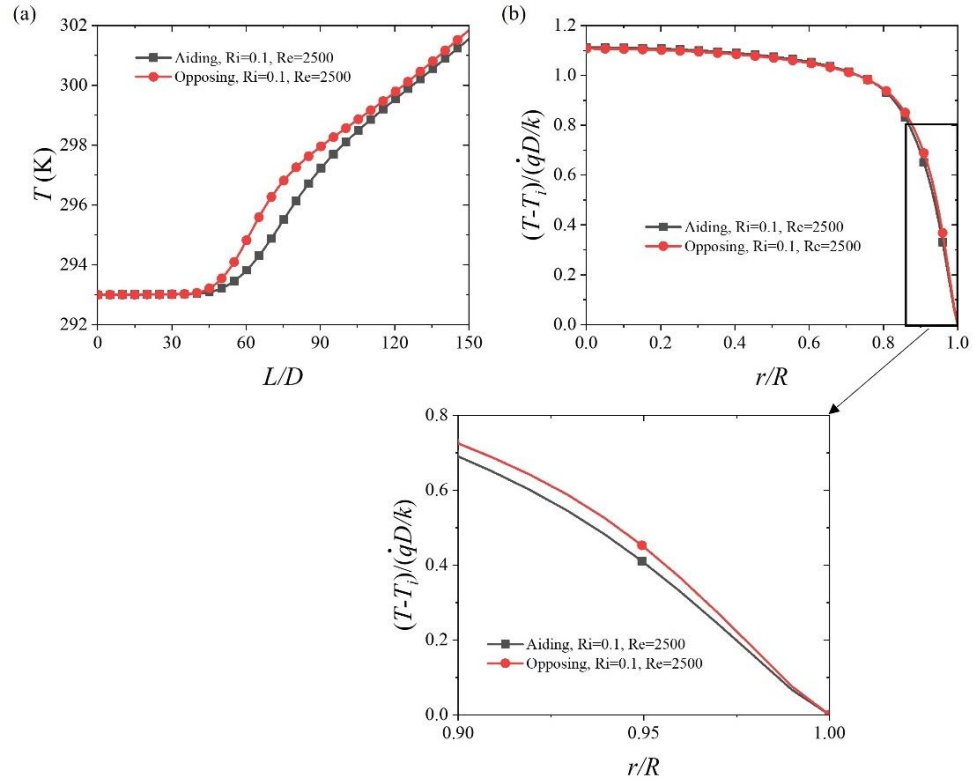


**Figure 6.12** Comparison of (a) centerline temperature and (b) outlet non-dimensional temperature profile in assisting and opposing case at  $Re=2500$  and  $Ri=0.1$

### 6.3 Comparison between buoyancy-assisting and opposing flows

Due to the greater velocity and temperature gradient in opposing flow, the local  $C_f$  and  $Nu$  plot in Figures 6.13(a), (b) show both are higher in opposing flow as that of the assisting flow. The hydrodynamic entry length seems to be smaller in case of opposing flow than the aiding flow. The velocity and temperature fluctuations are higher in opposing flow due to the opposing free convection effect. Therefore, the turbulent kinetic energy and the turbulent eddy frequency are also greater in opposing flow as can be seen in Figures 6.14(a), (b). The intermittency is little longer in assisting flow as compared to the opposing flow as shown in Figure 6.15(a). Because of higher average value of  $Re_\theta$ , the onset of transition is also delayed in aiding flow as compared to the opposing flow as shown in Figure 6.15(b). It exhibits that the transition is earlier in opposing flow as compared to aiding flow for same  $Re$  and  $R$ .

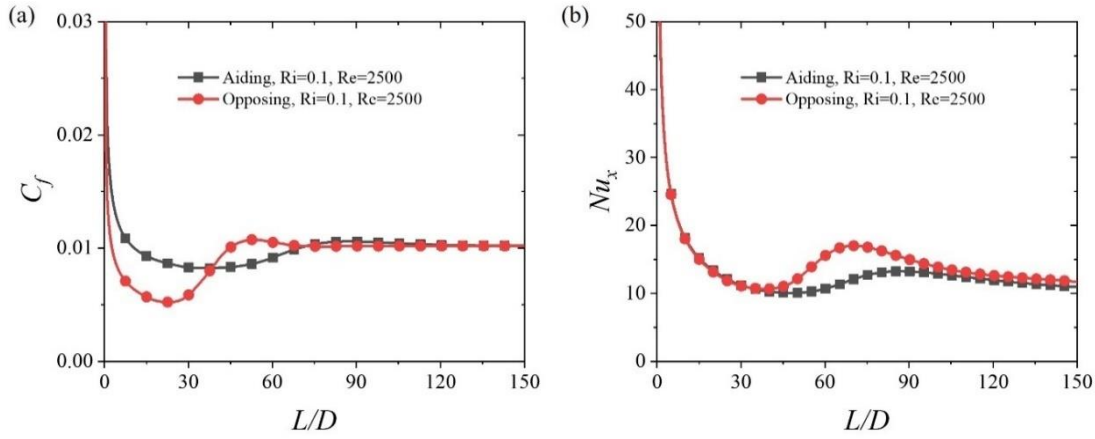


**Figure 6.13** Comparison local  $C_f$  and  $Nu$  in assisting and opposing case at  $Re=2500$  and  $Ri=0.1$

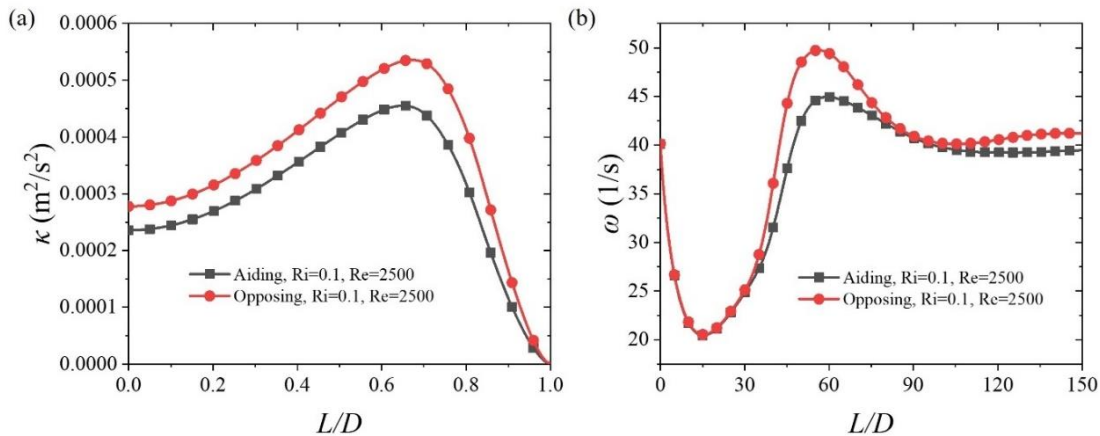


**Figure 6.14** Comparison of turbulent kinetic energy at  $L/D=150$  and turbulent eddy frequency profile at outlet in assisting and opposing case at  $Re=2500$  and  $Ri=0.1$

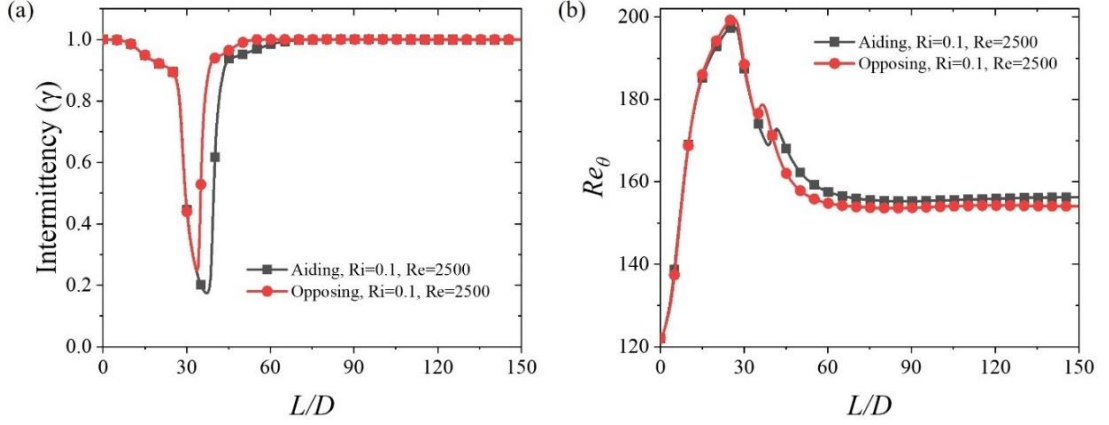


**Figure 6.15** Comparison of intermittency and  $Re_\theta$  in assisting and opposing case at  $Re=2500$  and  $Ri=0.1$

#### 6.4 Experimental results on transitional mixed convection

Experiments were carried out throughout a broad spectrum of Reynolds numbers ( $539 \leq Re \leq 9621$ ), Grashof numbers ( $2.4 \times 10^4 \leq Gr \leq 1.3 \times 10^7$ ), Richardson numbers ( $0 \leq Ri \leq 0.3$ ), and Prandtl numbers ( $4.4 \leq Pr \leq 6.5$ ) in aiding flow and  $553 \leq Re \leq 9492$ ,  $3.6 \times 10^4 \leq Gr \leq 1.1 \times 10^7$ ,  $0 \leq Ri \leq 0.3$ , and  $5.2 \leq Pr \leq 6.4$  in opposing flow, respectively. The working fluid was normal water, which was kept at a temperature of 20 °C and under atmospheric pressure. The Joule heating method, which utilizes a DC power source with low voltage and a high current capacity, was used to warm the testing portion. It is necessary to have such a large current for the Joule heating to achieve a high resistance in the testing section. Experiment that assists and opposes free and forced convection one another can be carried out using the same apparatus if it is set up in a way that allows for this. To limit the scope of the investigation within the developmental regime, the length-to-diameter ratio is maintained at 130.  $Ri = 0$  indicates that there is no heat flux being supplied, and because there is no heat flux, it is possible to reach a higher Reynolds number. When we increase the heat flux, which in turn raises the  $Gr$ , ultimately raises the  $Ri$ , the maximum  $Re$  that may be attained thereafter drops. The reason for this is to maintain a temperature for the output water that is lower than its saturation temperature. This means that the highest achievable  $Ri$  is 0.3, with  $Gr$  values of  $1.9 \times 10^7$  and  $1.2 \times 10^7$  and a  $Re_b$  value of 6240 and 5302 in aiding and opposing flows, respectively.

## 6.4 Experimental results on transitional mixed convection

### 6.4.1 Average pressure drop and heat transfer in the transitional mixed convection flow

In an experimental run when the steady state is reached, the pressure drop across the tube and surface temperature data at different axial locations are logged. Thereafter, the friction factor and Nusselt number at different axial locations are obtained. Then the average quantities are obtained by length integral over the entire tube length (as explained in section 4.3). The average friction factor ( $\bar{f}$ ) vs. bulk Reynolds numbers ( $Re_b$ ) are compared for different Richardson numbers. At a given  $Ri$ , the  $Re$  is varied in between 500 to 10000 depending on the limit of heat flux supplied. The laminar, transitional, and turbulent regimes are distinguished with zone I ( $500 \leq Re \leq 2000$ ), II ( $2001 \leq Re \leq 4000$ ), and III ( $4001 \leq Re \leq 10000$ ) respectively. It is found that the friction factor monotonically decreases in the laminar flow regime, increases in the transitional flow regime and then with further increase of  $Re$ , it decreases continuously in the turbulent flow regime. The effect of an increase in  $Ri$  to the friction factor, particularly in the transitional regime, has been investigated. In the laminar-turbulent transitional flow regime (zone II), it has been shown in the magnified view of the region. The magnified plot reveals that the increase in  $Ri$  from 0 to 0.1, decreases the friction factor. Hence the decrease in  $f$ , ultimately delaying the transition in both aiding and opposing flows. In addition to it, the critical Reynolds number ( $Re_c=2159$ , 2195, and 2264 at  $Ri=0$ , 0.05, and 0.1 respectively) at which transition takes place (indicated in Figure 6.16(c)) in opposing flow is smaller than the  $Re_c=2193$ , 2271, and 2438 at  $Ri=0$ , 0.05, and 0.1 respectively obtained in the case of aiding flow (as indicated in Figure 6.16(b)).

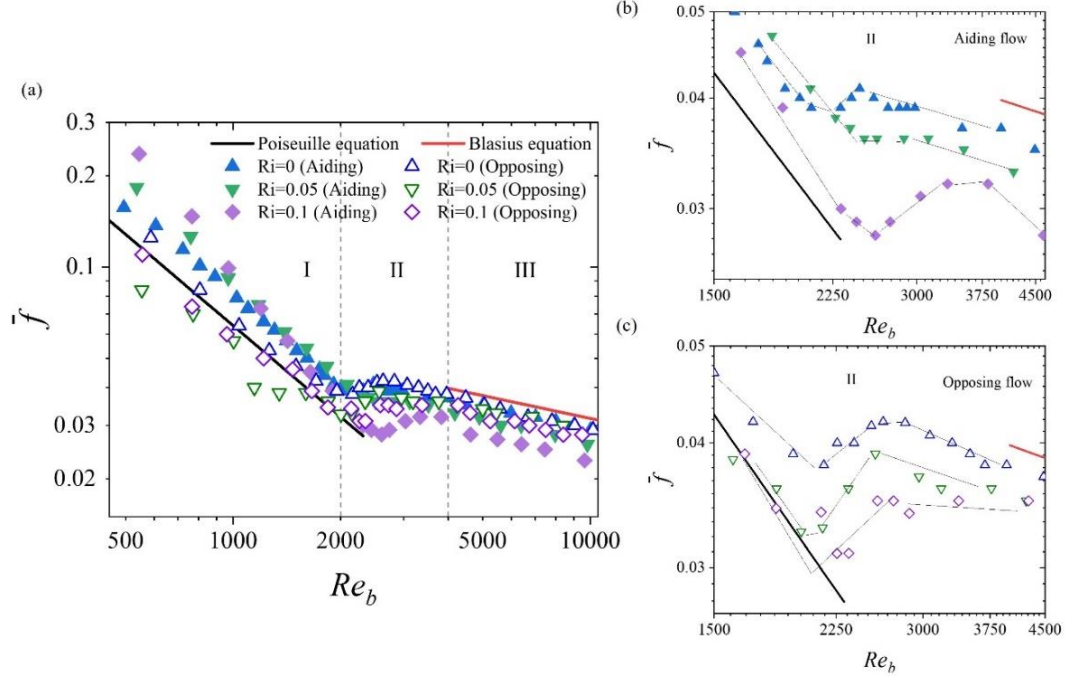


**Figure 6.16** (a) Average  $f$  vs.  $Re$  comparison plot and magnified view for (b) aiding and opposing flow of transitional mixed convection with varying  $Re$ ,  $Gr$  at different  $Ri$

Similar to friction factors, the average Nusselt number ( $\overline{Nu}$ ) vs.  $Re_b$  plot in Figure 6.17 demonstrates the variation of  $\overline{Nu}$  with the increase of  $Re_b$  at fixed  $Ri$ . In the laminar flow regime, it has been shown that the  $\overline{Nu}$  increases with the increase of  $Re_b$  because the flow lies in the developing flow instead of a fully developed flow, where thermal boundary layer develops. In the present study of the transitional flow regime, the flow switches in between laminar and turbulent flow. The  $\overline{Nu}$  remains stagnant for the regime of  $Re=2313$  to  $2737$  in aiding flow and  $Re=2139$  to  $2345$  in opposing flow respectively at  $Ri=0.1$ . Afterwards, the  $Nu$  continuously increases with further increase in  $Re$  at a fixed  $Ri$ . The magnified view in the transitional flow regime (zone II) depicts that the change in slope from laminar to turbulent flow is more pronounced with an increase in  $Ri$  (Figures 6.17(b) and (c)). This also resembles a delay in the transition due to the increase in  $Ri$  in both aiding and opposing flows. Apart from that, it can also be concluded that the critical Reynolds number ( $Re_c$ ) at which the transition takes place is a little earlier in the case of opposing flow ( $Re_c = 2264$ , at  $Ri = 0.1$ ) as compared to aiding flow ( $Re_c = 2438$ , at  $Ri = 0.1$ ). This indicates that for same  $Ri$ , the transition in opposing flow is earlier than that in aiding flow. The disturbance generated in the flow due to the opposing effect of free convection in the opposing flow leads to an early transition.



## 6.4 Experimental results on transitional mixed convection

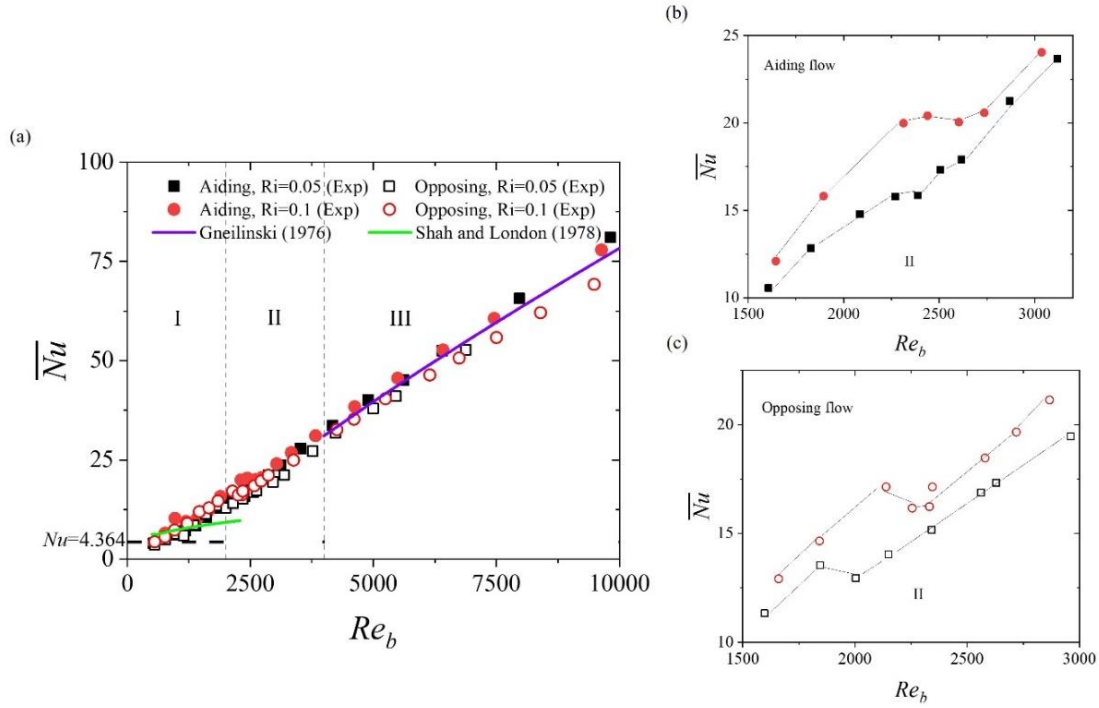


**Figure 6.17** (a) Average  $Nu$  vs.  $Re$  comparison plot and magnified plot for (b) aiding and opposing flow of transitional mixed convection with varying  $Re$ ,  $Gr$  at different  $Ri$

### 6.4.2 Friction factor and Nusselt number correlations

With the available experimental data for  $f$  and  $Nu$ , correlations have been produced for buoyancy-assisting and opposing flows. The range of parameters for which the correlations are applicable is  $2255 \leq Re \leq 4174$ ,  $0.05 \leq Ri \leq 0.2$  and  $3.5 \leq Pr \leq 6.6$ . To quantitatively determine the pressure drop and heat transfer, a correlation for average friction factor has been generated with the variation of  $Re$  as mentioned in Eq. (6.2). A power curve with best fit with an average  $R^2$  value of 0.7263. It states that more data points are required to get a better fit. Similarly, the correlation of average  $Nu$  has been obtained with  $Re$  at fixed  $Ri$ . The Eq. (6.3) produces  $Nu$  in terms of  $Re$  with a power curve best fit with an average  $R^2$  value of 0.9636. The coefficients and the exponents range for  $Ri = 0.05 - 0.2$  for both buoyancy-assisting and opposing flows are tabulated in Table 6.1. It has been observed that the coefficients and exponents are significantly varying with the increase of  $Ri$ . With the increase in  $Ri$ , the  $f$  and  $Nu$  both are decreasing and increasing in aiding and opposing flows respectively.

$$f = p(Re)^q \quad (6.2)$$

$$Nu = r(Re)^s \quad (6.3)$$



**Table 6.1** Range of the coefficients and exponents present in Eqs. (6.2) and (6.3)

Flow	$Ri$	$p$	$q$	$r$	$s$
Assisting flow	0.05	0.155	-0.183	0.0008	1.320
	0.1	0.0026	0.307	0.0135	0.935
	0.2	0.0055	0.214	0.008	0.997
Opposing flow	0.05	0.00007	0.808	0.048	0.743
	0.1	0.00006	0.797	0.0077	0.992
	0.2	0.0028	0.324	0.0136	0.928

### 6.4.3 Local heat transfer in the developing transitional mixed convection flow

Based on the results shown earlier (section 6.4.1), the transitional regime is separated, and the axial variation of  $Nu$  is produced in terms of the  $Nu$  vs.  $L/D$  and  $Nu$  vs.  $Gz$  plot. Results have been analysed for both buoyancy-aiding as well as opposing flows at the same  $Ri$ . In aiding flow, the local  $Nu$  in laminar mixed convection regime is coincided to a single line to the magnitude of the fully developed  $Nu$  of 4.364. Thereafter, with an increase in  $Re$  in the transitional flow regime,  $Nu$  is no longer converges but rather increases gradually with the increase in axial distance (Figure 6.18). This is due to the increase in velocity fluctuations, which is responsible for the higher rate of heat being convected away in the flow as compared to the laminar case. The average  $Nu$  in the transitional regime is more than twice as that of the average  $Nu$  in a laminar flow.

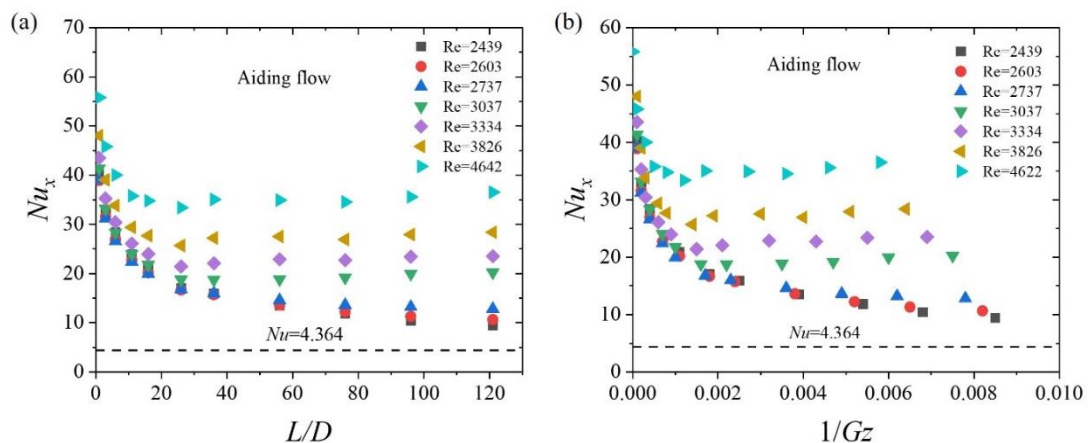


**Figure 6.18** Local (a)  $Nu$  vs.  $L/D$  and (b)  $Nu$  vs.  $Gz$  plot for transitional mixed convection at fixed  $Ri=0.1$  in aiding flow

In opposing flow, the local  $Nu$  in transitional flow regime is also higher, like it was in aiding flow. In the transitional flow regime, the local  $Nu$  starts increasing after a certain axial length (Figure 6.19) due to the higher thermal diffusivity in the thermal boundary

## 6.4 Experimental results on transitional mixed convection

layer. The transition is also fast in opposing flow ( $Re \sim 2345$ ) as compared to aiding flow ( $Re \sim 2439$ ) due to the opposing free convection effect. However, it is interesting to note that the average heat transfer is higher in aiding flow in the laminar regime, but as the flow enters the transitional regime and then the turbulent regime, heat transfer becomes higher in opposing flows. This signifies that there is a cross-over from a decreasing trend in laminar flow to an increasing trend in turbulent flow in buoyancy-opposing flows. The reason for the decrease in heat transfer in laminar flow is explained in section 5.5.2, whereas the increase of heat transfer in a turbulent flow will be explained in the next chapter (section 7.3.2).

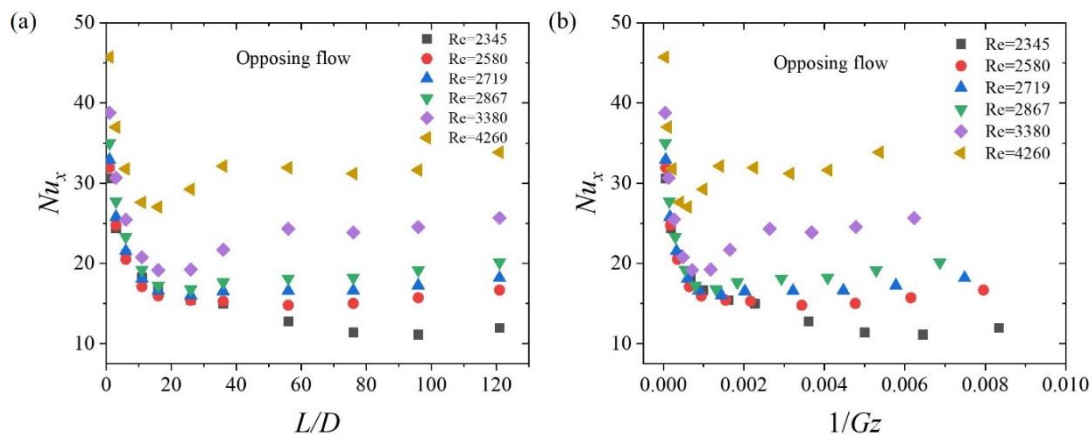


**Figure 6.19** Local (a)  $Nu$  vs.  $L/D$  and (b)  $Nu$  vs.  $Gz$  plot for transitional mixed convection at fixed  $Ri=0.1$  in opposing flow

### 6.4.4 Flow visualization in laminar, transitional, and turbulent mixed convection flow

To ensure and understand the laminar-turbulent transition in simultaneously developing mixed convection flow through a vertical tube, a provision to visualize has been made to the experimental set-up. A transparent section (section 4.2.4 in Chapter 4) has been provided at the tube exit to see whether the flow is laminar or is transition or in a turbulent regime. To visualize the transition phenomena, potassium permanganate ( $KMnO_4$ ) solution is used as a dye. The solid potassium permanganate crystals were mixed with normal water to form a 0.1 M to 0.2 M solution so that the weight density of the solution would remain the same as that of the working fluid (water). The dye flow rate is also maintained equal to the main line flow rate to avoid any relative velocity between the flows. The dye is sent through a needle of diameter 20 gauge (ID= 0.6mm and OD=0.9 mm) with a length of 110 mm bent at  $90^\circ$ . The needle is placed exactly at

the center of the tube so that the heating effect on the dye will be uniform. When the flow reaches a steady state, the dye is sent through the syringe pump set at the desired flow rate. Once the dye passes through the test section, its flow behavior will depend on the flow rate ( $Re$ ) and the heat flux ( $\dot{q}$ ) supplied through the walls. In the laminar mixed convection flow, the streak of dye remains straight and reaches the tube exit without mixing with the fluid. This can be seen in Figure 6.20(a) for aiding flow at  $Re=969$  and  $Ri=0.1$ , when the flow is in laminar mixed convection regime. Thereafter, with the increase in mass flow rate ( $Re_c=2438$ ), the flow is always no longer straight and becomes wavy in nature for some time and again becomes straight. This indicates that the flow switches between laminar and turbulent. This phenomenon is nothing but the laminar-turbulent transition (Figure 6.20(b)) and the corresponding Reynolds number can be said as critical Reynolds number. Further, at higher mass flow rates ( $Re=3814$ ), the flow becomes turbulent, and the dye is mixed completely (Figure 6.20(c)). This fills the whole tube with a light purple color.

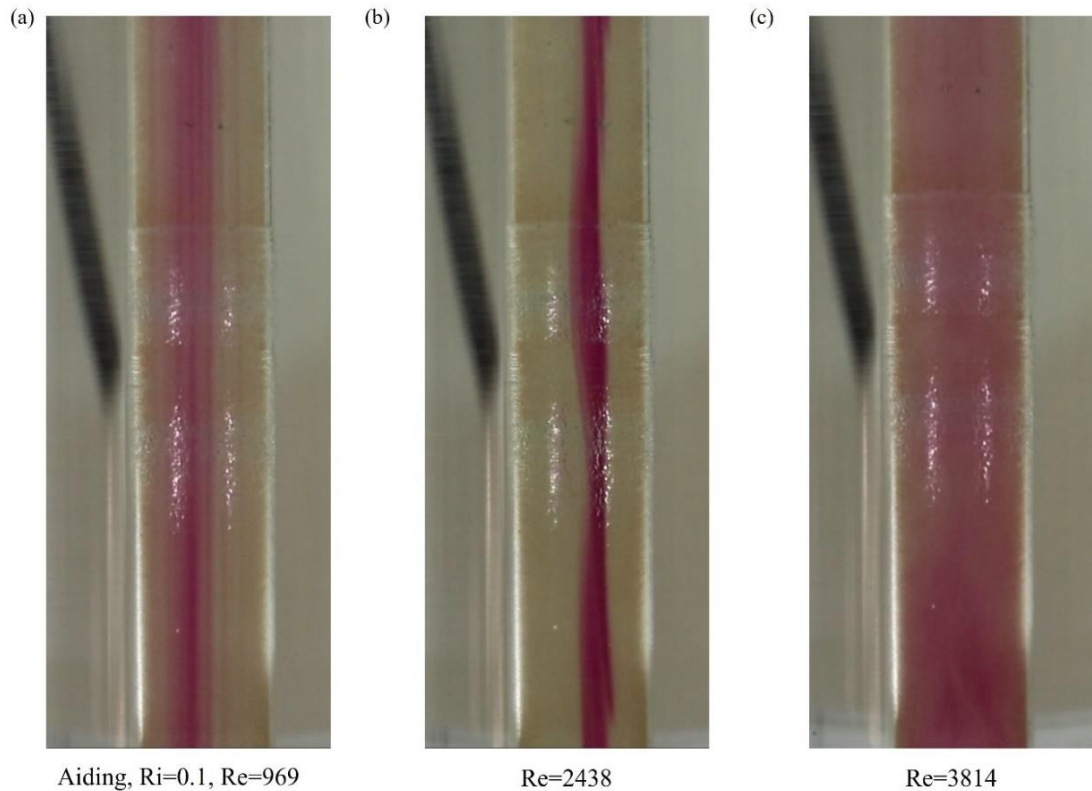


**Figure 6.20** Flow patterns for (a) laminar ( $Re=969$ ) (b) transitional ( $Re=2438$ ) and (c) turbulent ( $Re=3814$ ) mixed convection at fixed  $Ri=0.1$  in aiding flow

Similarly, in opposing flows, the flow pattern is visualized, as demonstrated in Figure 6.21. The flow remains laminar for  $Re=977$  at  $Ri=0.1$ . Thereafter, it enters the transition

## 6.4 Experimental results on transitional mixed convection

with an increase in flow rate to  $Re=2264$  and then enters the turbulent flow regime with a further increase in flow rate to  $Re=3394$ .

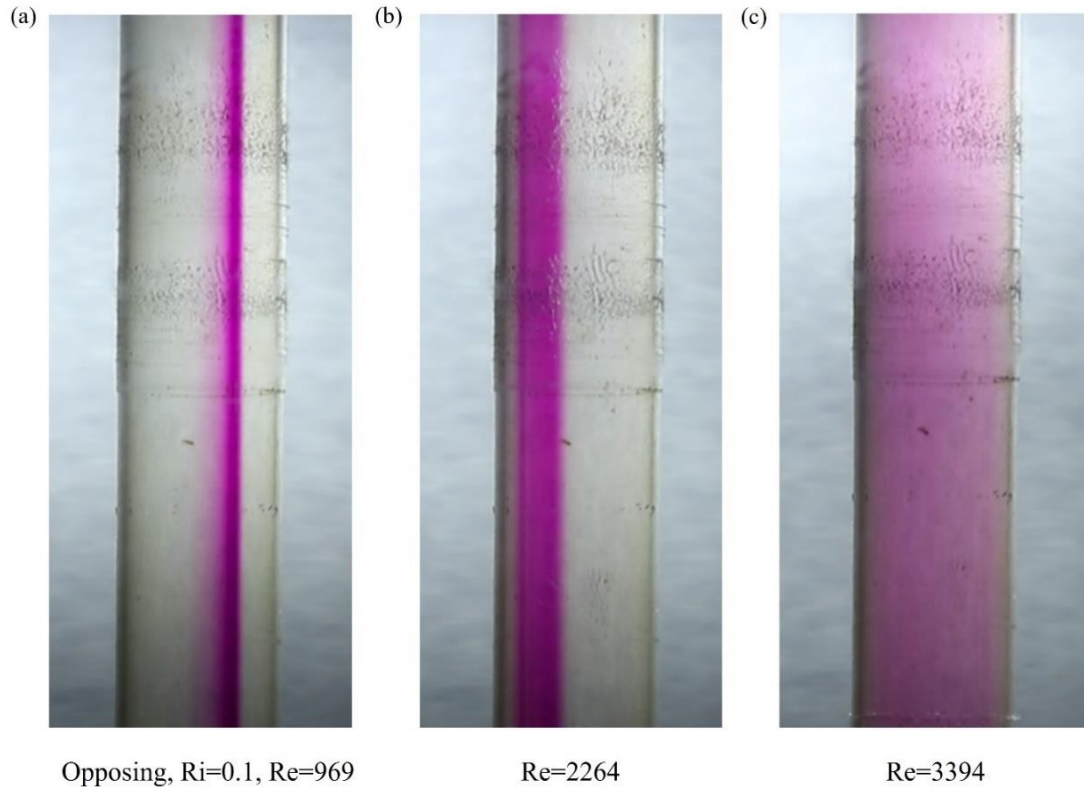


**Figure 6.21** Flow patterns for (a) laminar ( $Re=977$ ) (b) transitional ( $Re=2264$ ) and (c) turbulent ( $Re=3394$ ) mixed convection at fixed  $Ri=0.1$  in opposing flow

## 6.5 Comparison between numerical and experimental transitional mixed convection results

### 6.5.1 Heat transfer in the developing regime of transitional mixed convection flows

The laminar-turbulent transition in a pipe flow depends on one parameter, which is the Reynolds number ( $Re$ ). The  $Re$  can be increased either with the increase in fluid velocity or due to reduction in fluid viscosity by heating. In my experiments it has been observed that at high heat fluxes, the flow becomes transitional or turbulent, even at  $Re < 2300$ . In simulations, one can't observe this by applying either a laminar, transitional, or turbulent model, which is applicable for one flow regime. There are a few works by Abraham *et al.* [109], Abraham *et al.* [132], and We and Abraham [133] in which the authors claim that their single model is capable of performing in all three flow regimes. However, the results they have obtained are either Poiseuille flow or forced convection through a pipe and not for mixed convection. The local  $Nu$  plot of the present

experiments for  $Re \sim 2300$  and  $\sim 3000$  at  $Ri=0.1$  is compared to the numerical results obtained for the same parameters as shown in Figure 6.22. The experimental results are in good agreement with the present simulations within the uncertainty limit (Table 4.1) for both aiding and opposing flows.

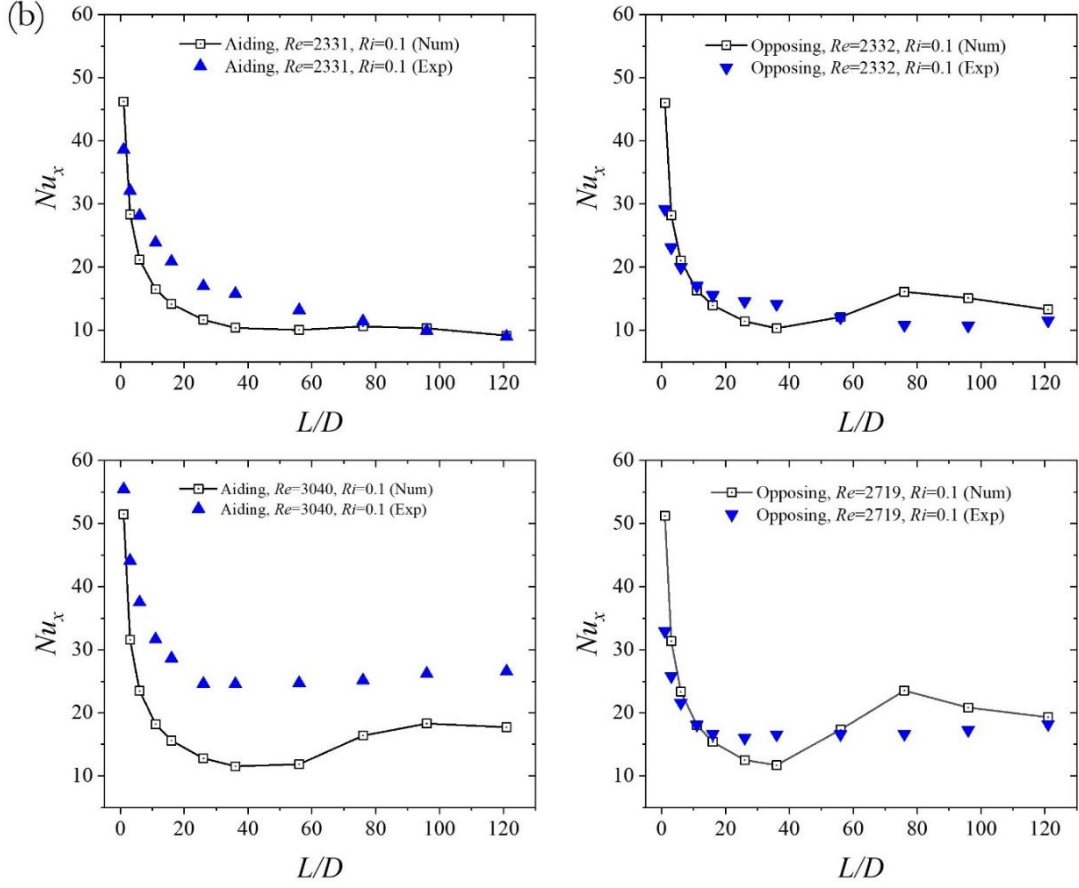


**Figure 6.22** Local  $Nu$  (numerical vs. experimental) comparison plots for transitional mixed convection at fixed  $Ri$

## 6.6 Conclusions

This chapter gives a numerical and experimental comparison of laminar-turbulent transitional mixed convection for buoyancy-assisted and buoyancy-opposed flows through a vertical tube with a constant heat flux boundary condition. The numerical results lead to the following conclusions:

1. The increase in  $Re$  and  $Gr$  keeping  $Ri$  constant, increases both  $C_f$  (hence pressure drop) and  $Nu$  (hence heat transfer) in buoyancy assisting and opposing flow. But at a given  $Ri$ , the magnitude of  $C_f$  and  $Nu$  is higher in the opposing flow as compared to the assisting flow.

## 6.6 Conclusions

2. The hydrodynamic entrance length decreases with the increase of  $Re$  and  $Gr$  keeping  $Ri$  constant in both buoyancy assisting and opposing flows.
3. The thermal entrance length increases with the increase of  $Re$  and  $Gr$  keeping  $Ri$  constant in both buoyancy assisting and opposing flows.
4. The intermittent plot shows higher velocity fluctuations of turbulent and laminar flow in lower transitional zones ( $2000 < Re < 3000$ ) as that of higher transitional zones ( $3000 < Re < 5000$ ).
5. At fixed  $Re$  and  $Ri$ , the comparison plots (Figures 6.11-6.15) illustrate that the onset of transition and turbulent characteristics are more likely to have in the opposing flow as compared to the assisting flow.

The experimental outcome furnishes the following conclusions:

1. With the increase in  $Ri$ , the average friction factor decreases and the average Nusselt number increases in aiding and opposing flows, respectively.
2. The start of transition depends on the heat flux supplied, and it occurs earlier in the opposing flow as compared to the assisting flow for same  $Ri$ .
3. In the transitional mixed convection flow regime, the local  $Nu$  increases after an axial length instead of remaining constant like in fully developed flow because of the decrease in the difference between the inner wall and mean fluid temperature.

### Turbulent Mixed Convection

---

#### 7.1 Introduction

From the existing literature, it has been concluded that when  $Re$  is in a pure turbulent and  $Ra$  is in a pure laminar regime, the flow state is in mixed convection regime. The hydrodynamic and thermal features for turbulent mixed convective regime in a vertical tube have not been explored in previous studies. This chapter explains a numerical and experimental investigation to analyse the flow characteristics and heat transfer behaviour for simultaneously developing as well as the developed regime of turbulent mixed convection in a vertical tube, considering the buoyancy-assisting and buoyancy-opposing effects. The aim is to investigate the effect of  $Gr$ ,  $Re$ , and  $Ri$  on the friction factor ( $f$ ) and Nusselt number ( $Nu$ ) in a vertical tube subjected to constant heat flux conditions. The variation of hydrodynamic and thermal entry length with the variation of  $Gr$ ,  $Re$ , and  $Ri$  is also studied for both buoyancy-aided and opposed flows. Finally, the correlations of friction factor ( $f$ ), Colburn factor ( $j$ ), and Nusselt number ( $Nu$ ) with the governing parameters like  $Re$ ,  $Gr$ , and  $Pr$  are developed.

#### 7.2 Numerical results on turbulent mixed convection

Mixed convection in a vertical pipe with test fluid water is characterized by different parameters like  $Re$ ,  $Gr$ , and  $Ri$ . The  $L/D$  ratio was decreased from 150 to 50 in further simulations for two reasons. 1. Since, the entry length is usually short in turbulent flow,  $L/D = 50$  is adequate for the analysis of developing as well as fully developed flow. 2. The  $L/D$  was reduced to avoid the possibility of the fluid temperature at the pipe exit exceeding boiling temperature at ambient atmospheric pressure. The results are analysed in three different ways: I.  $Gr$  is constant and varying  $Re$ ,  $Ri$ , II.  $Ri$  is constant and varying  $Gr$ ,  $Re$ , and III.  $Re$  is constant and varying  $Gr$ ,  $Ri$ . The results of the case when  $Re$  is constant is presented in Figures B.1, B.2, and B.3 of Appendix B. It is a similar study, and all the result plots show that the flow characteristics are invariant of varying the  $Gr$  and  $Ri$  at constant  $Re$ .

## 7.2 Numerical results on turbulent mixed convection

### 7.2.1 Flow regime plot

The mixed convection regime for flow through a vertical tube can be validated with the plot proposed by Metais and Eckert [3] based on experimental results applicable for vertical tubes subjected to uniform heat flux as well as uniform wall temperature conditions. The plot is redrawn specifying the boundaries between free, forced, and mixed convections which is valid for both buoyancy-assisting and -opposing flows in circular tubes with a condition of  $0.01 < PrD/L < 1$ . In Figure 7.1, most of the present data ( $0.05 < PrD/L < 0.14$ ) lie in the pure turbulent mixed convection regime except a few in the forced turbulent regime. Comparing the Richardson number i.e. the ratio of buoyancy forces to viscous forces ( $Ri = Gr/Re^2$ ), also confirms that  $\sim 97\%$  of the present study ( $0.05 \leq Ri \leq 0.25$ ) lies in the mixed convection range ( $0.1 \leq Ri \leq 10$ ) [13].

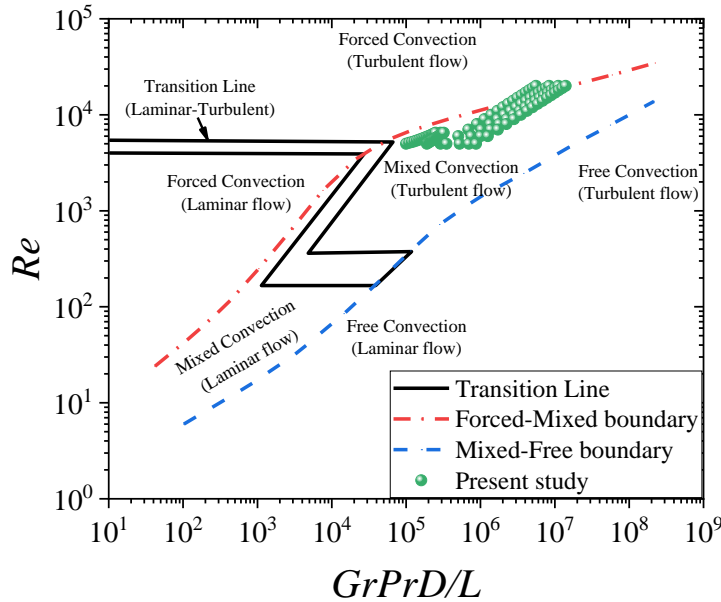


**Figure 7.1** Comparison of the present mixed convection data on the flow regime map of Metais and Eckert [3] applicable for a vertical tube ( $0.01 < PrD/L < 1$ )

### 7.2.2 Buoyancy-assisted flow

In buoyancy-assisted flow with heating from side walls, the fluid flow assists the buoyancy. Here the bulk properties are calculated once the simulations are performed based on the bulk fluid temperature obtained in each case. Also, the changes in the results for constant and varying viscosity is compared and illustrated in the next sections for the II case. The correlation used for the variation of viscosity has been adopted from Popiel and Wojtkowiak [128]. The viscosity in terms of temperature with a best fit of piecewise polynomial (Eq. (5.9)) was modelled accordingly in the materials section of



the solution set-up. As per the definition of mixed convection, the II case is sufficient to explain the effect of varying the viscosity in the results.

### 7.2.2.1 Fixed $Gr$ and varying $Re$ , $Ri$

The effect of varying the  $Re$  from 5000 to 6500 at fixed  $Gr = 4.07 \times 10^6$  leads to the variation of  $Ri$  from 0.16 to 0.10. Here, the bulk Reynolds number ( $Re_b$ ) becomes 7291, 7758, 8246, and 8746 for  $Ri_b=0.17, 0.14, 0.12, 0.10$  for the bulk fluid temperature ( $T_b$ ) of 37.3 °C, 35.6°C, 34.3 °C, and 33.2 °C at fixed  $Gr_b$  of  $9.05 \times 10^6$ ,  $8.39 \times 10^6$ ,  $7.96 \times 10^6$ , and  $7.66 \times 10^6$ . The bulk fluid temperature ( $T_b$ ) is the mean of inlet ( $T_i$ ) and outlet ( $T_o$ ) fluid temperature. With increase in  $Re$ , the flow rate will increase. The effect of variation of  $Re$  on natural convection in buoyancy-aided flow has been analyzed with the velocity profile, temperature profile, friction factor, and Nusselt number plots. The velocity gradient in Figure 7.2(a) is steeper near the wall as the  $Re$  increases. To keep the  $Gr$  constant, increase in  $Re$  is accompanied with decrease in  $Ri$ . Consequently, compared to Blasius equation, the friction factors are lesser in case of buoyancy assisted flows as shown in Figure 7.2(b). The reason is that in case of buoyancy assisted flow, the fluid near the wall accelerates the flow. This increases the distribution of shear stress across the wall layer. At high heat flux a situation may arise when the shear stress acting upward to the buoyant layer is lower than the downward acting wall shear stress. Hence the friction factor is lesser as compared to the friction factor of no buoyancy flow.

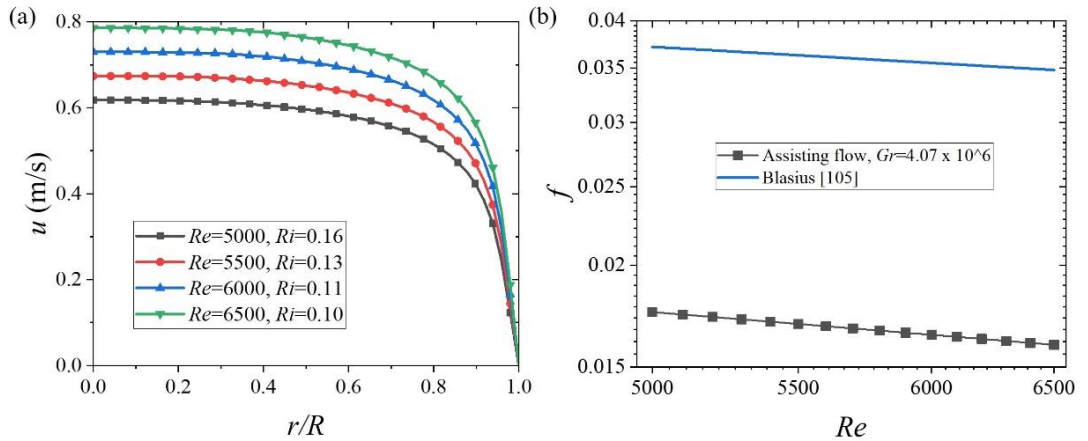


**Figure 7.2** (a) Outlet velocity profile and (b) fully developed  $f$  at  $L/D = 150$  for varying  $Re$ ,  $Ri$  at fixed  $Gr=4.07 \times 10^6$

In Figure 7.3(a), the temperature gradient near the wall becomes steeper. This results in higher heat transfer ( $Nu$ ) as shown in Figure 7.3(b). The  $f$  is as much as 55 % lower and the corresponding  $Nu$  is as much as 12 % higher compared to the classical

## 7.2 Numerical results on turbulent mixed convection

correlations of Blasius [105] and Dittus-Boelter [9] respectively. Figures 7.4(a) and (b) describe the variation of  $\kappa$  and  $\varepsilon$  respectively across the cross-section at  $L/D = 150$ . In both Figures 7.4(a) and (b), the magnitude of peak  $\kappa$  and  $\varepsilon$  increases with increase in  $Re$ . The  $\kappa$  or  $\varepsilon$  attains the peak value at  $r/R \sim 0.9$  and then decreases to a saturated value in the centreline region ( $0 \leq r/R \leq 0.4$ ). The axial variation of the transport quantities ( $\kappa$  and  $\varepsilon$ ) at centerline with the increase in  $Re$  is plotted. These quantities increase at the entry and then become steady once the flow is developed. The centerline  $\kappa$  and  $\varepsilon$  both increase with the increase of  $Re$  at a constant  $Gr$ . However, there is a decrease in both  $\kappa$  and  $\varepsilon$  at the entry in case of  $Re=5000$  as the flow is in transition or quasi-turbulent.

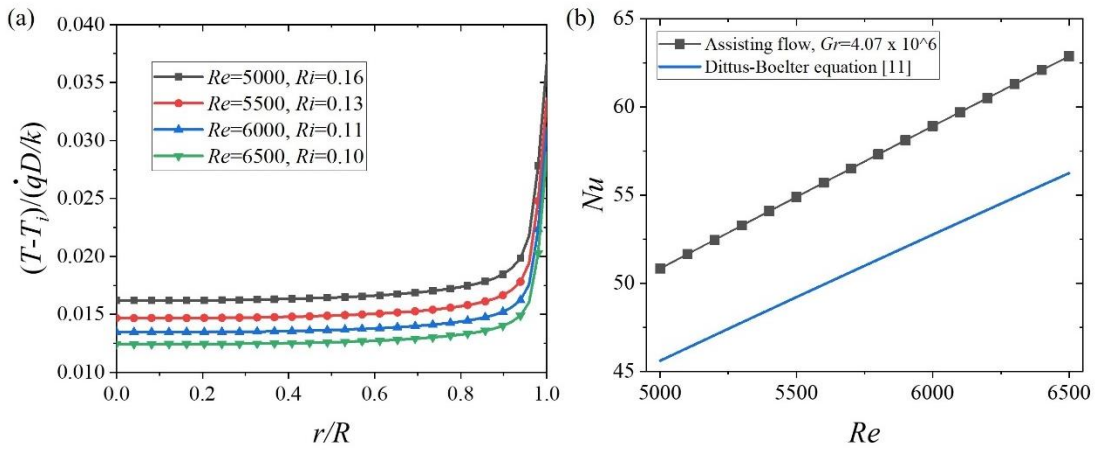


**Figure 7.3** Non-dimensional outlet temperature profile and (b) fully developed  $Nu$  plot at fixed  $Gr=4.07 \times 10^6$  and varying  $Re, Ri$

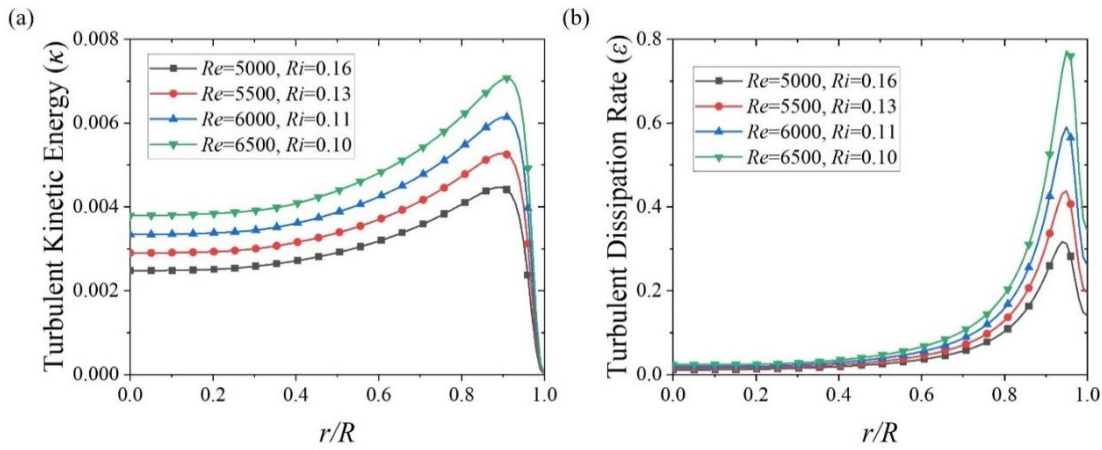


**Figure 7.4** Radial variation of (a)  $\kappa$  and (b)  $\varepsilon$  profile at a fixed  $L/D = 150$  for varying  $Re, Ri$  at fixed  $Gr=4.07 \times 10^6$

### 7.2.2.2 Fixed $Ri$ and varying $Re, Gr$

In this section, the effect of  $Re$  and  $Gr$  in the turbulent regime have been quantified. Simulations are performed keeping the  $Ri$  constant as 0.16, varying  $Re = 5000, 5500, 6000$ , and 6500 with appropriate changes in the  $Gr$  as  $4.07 \times 10^6$ ,

$4.93 \times 10^6$ ,  $5.86 \times 10^6$ , and  $6.88 \times 10^6$  respectively. The bulk nondimensional numbers obtained are  $Re_b=7229, 8215, 9252, 10341$  and  $Gr_b=1.42 \times 10^7, 1.9 \times 10^7, 2.49 \times 10^7, 3.21 \times 10^7$  for the  $T_b$  of  $36.8^\circ\text{C}, 38.5^\circ\text{C}, 40.2^\circ\text{C}$ , and  $41.9^\circ\text{C}$  at fixed  $Ri_b$  of  $0.27, 0.28, 0.29$ , and  $0.30$ . Here the effect of  $Re$  on the flow as well as heat transfer has been explained with the plots of velocity, temperature, friction factor, Nusselt number, turbulent kinetic energy, and turbulent dissipation rate. The velocity profiles in Figure 7.5(a) reflect the increase in velocity magnitude with an increase in  $Re$  at fixed  $Ri$ . The figure also depicts the difference in the velocity profile with constant and varying viscosity with temperature. It is evident that the velocity gradient near the wall becomes more steeper with varying viscosity. At fixed  $Ri$ , with the increase of  $Re$  and correspondingly  $Gr$ , increases the bulk fluid temperature resulting in the decrease of viscosity. This accelerates the flow at faster rate near to the wall that leads to the sharp velocity gradient. The friction factor drops with the increase in  $Re$  from 5000 to 6500, however it is not significant ( $\sim 10\%$ ) as shown in Figure 7.5(b). This is because of the negligible difference in velocity gradient near to the wall as can be seen in Figure 7.5(a). However, it is clear from the plot that the friction factor is quite less ( $\sim 53\%$ ) compared to the Blasius equation when the viscosity is constant. There is a  $\sim 83\%$  rise in friction factor due to the variation of viscosity with temperature compared to the constant viscosity as shown in Figure 7.5(b) which was expected. To keep  $Ri$  constant, an increase in  $Re$  results in an increase of  $Gr$  and consequently an increase in heat flux. This higher  $Gr$  increases the free convection effect and the temperature difference between the inlet and bulk fluid. Hence, the temperature gradient in Figure 7.6(a) is also increasing for higher  $Re$ . The magnified view of the non-dimensional temperature profile ( $0.9 \leq r/R \leq 1$ ) clearly demonstrate the increase in temperature gradient near the wall. Therefore, the  $Nu$  increases with the increase in  $Re$  as shown in Figure 7.6(b) and it is  $\sim 8\%$  higher than that of the Dittus-Boelter estimation. Furthermore, the  $Nu$  increases by  $\sim 56\%$  when varying the viscosity with temperature than the constant viscosity as compared in Figure 7.6(b). The  $Nu$  increases because of the increase in  $Re_b$  and  $Gr_b$  as it is a strong function of both in case of turbulent mixed convection.

## 7.2 Numerical results on turbulent mixed convection

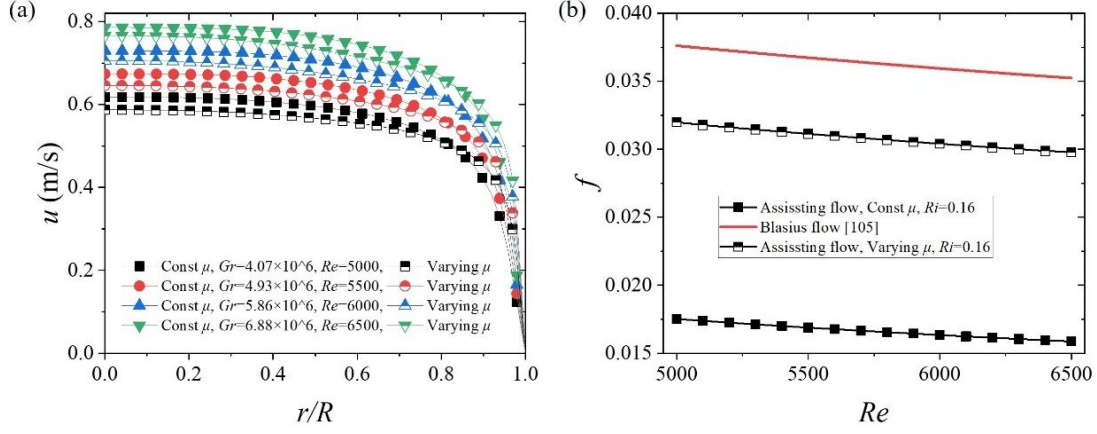


**Figure 7.5** (a) Velocity profile at  $L/D = 150$  and (b) fully developed  $f$  plot for varying  $Re, Gr$  at fixed  $Ri = 0.16$

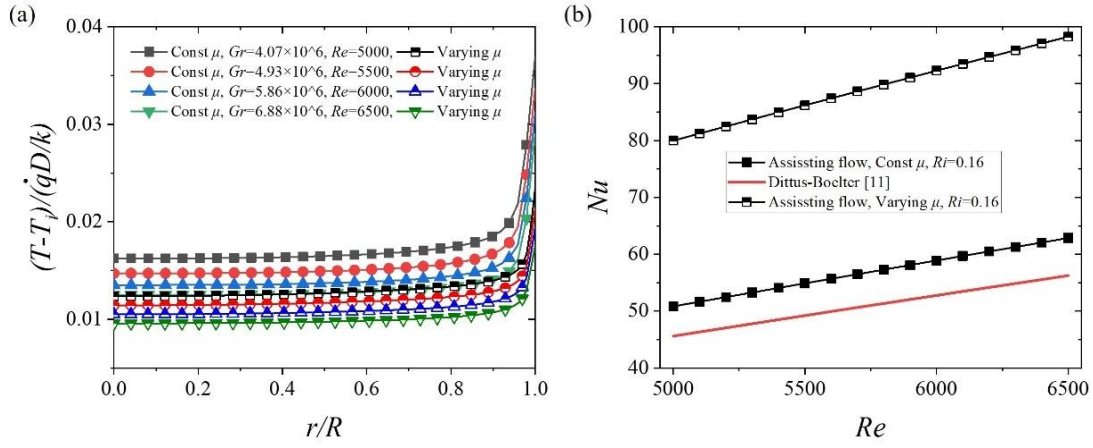


**Figure 7.6** (a) Non-dimensional outlet temperature profile and (b) fully developed  $Nu$  plot for varying  $Re, Gr$  at fixed  $Ri = 0.16$

Further, Figures 7.7(a) and (b) describes that the  $\kappa$  and  $\varepsilon$  profile at a cross-section increases with the increase in  $Re$  at fixed  $Ri$ . The variable viscosity drops the  $\kappa$  and increases the  $\varepsilon$  near the wall as that of constant viscosity. The decrease in viscosity due to rise in temperature causes the decrease in  $\kappa$  and rise in  $\varepsilon$  near the wall.

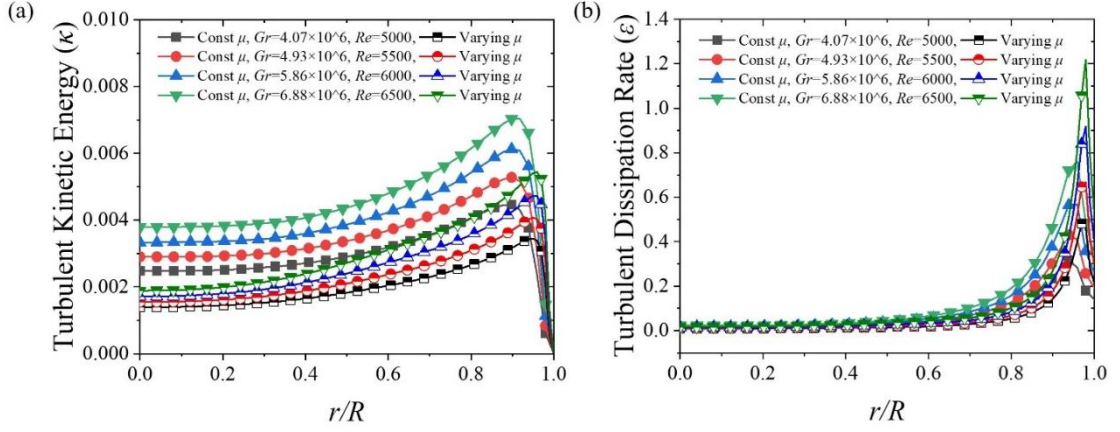


**Figure 7.7** Variation of radial (a)  $\kappa$  and (b)  $\varepsilon$  profile at a fixed  $L/D = 150$  for varying  $Re, Gr$  at fixed  $Ri = 0.16$

### 7.2.3 Buoyancy-opposed flow

In case of buoyancy-opposed flow, the fluid is flowing exactly in opposite to the direction of buoyancy. Here the bulk properties are considered same as that of the buoyancy-assisted flow because of very minor changes in the bulk fluid temperature. However, the changes in the results for constant and varying viscosity with temperature are compared and illustrated here for the II case as like the buoyancy-assisted flow.

#### 7.2.3.1 Fixed $Gr$ and varying $Re, Ri$

Like buoyancy-assisted flow, the effect of  $Re$  can be understood by varying the inlet velocity at a fixed  $Gr$  value. This will ultimately vary the  $Ri$ . The  $Re$  has been varying from 5000 to 6500 to ensure that the flow is in a pure turbulent regime. The corresponding  $Ri$  decreases from 0.16 to 0.10 with the increase of  $Re$  at fixed  $Gr = 4.07 \times 10^6$ . The centerline velocity increases in the entrance region and afterward becomes steady as the flow becomes fully developed. That's why the velocity profile becomes steeper at higher  $Re$  and lower  $Ri$ . However, in the case of centreline temperature, it decreases with the increase of  $Re$  as the heat is carried away by the fluid. Because of this reason the outlet fluid average temperature decreases with the increase of  $Re$  hence the temperature gradient is becoming steeper near the tube wall.

Therefore, due to increase in  $Re$  at constant  $Gr$  as explained in the above paragraph results in a lower friction factor and higher  $Nu$  as observed in Figures 12(a) and (b). The friction factor decreases due to the higher value of  $Re$  and the  $Nu$  increases because of the heat carried away by the fluid at a higher velocity. In case of turbulent mixed convection in a vertical tube, the effects of buoyancy on  $f$  and  $Nu$  contrast with what have been found in the laminar mixed convection simulations. In laminar mixed

## 7.2 Numerical results on turbulent mixed convection

convection, at fixed  $Gr$  with the increase in  $Re$ , the friction factor and  $Nu$  both increases in the assisting flow and decreases in the opposing flow. The main reason for this is the turbulence production due to the buoyancy effect. The transport quantities such as  $\kappa$  and  $\varepsilon$  increase for varying  $Re$  and  $Ri$  at fixed  $Gr$  in their radial profile. However, the axial variation of  $\kappa$  and  $\varepsilon$  does not show much influence for varying  $Re$  and  $Ri$  at fixed  $Gr$ . The reason is that by increasing the  $Re$ ,  $Ri$  decreases for a fixed  $Gr$ . This facilitates that the turbulence suppresses the free convection effect and hence the heat is being carried away by the eddies itself.

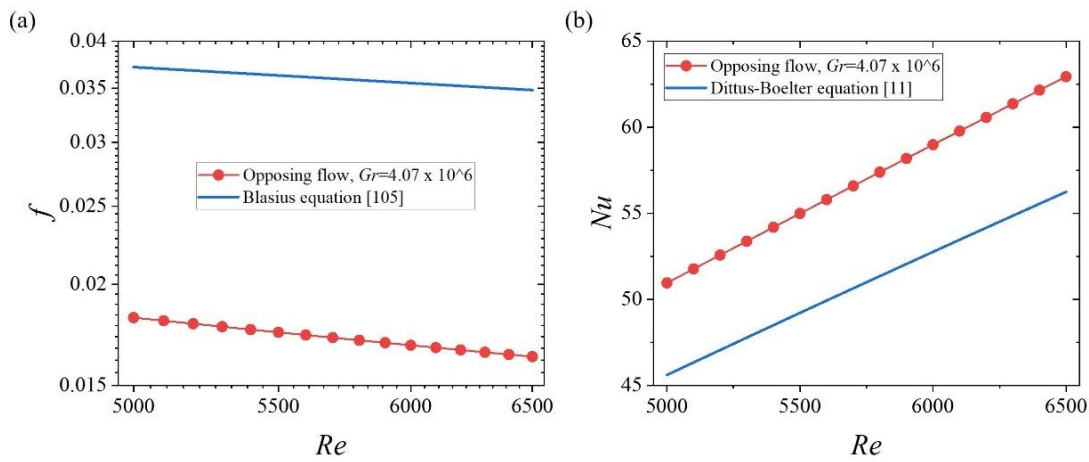


**Figure 7.8** (a) Fully developed  $f$  (b)  $Nu$  variation for varying  $Re$ ,  $Ri$  at fixed  $Gr = 4.07 \times 10^6$

### 7.2.3.2 Fixed $Ri$ and varying $Re$ , $Gr$

In buoyancy-opposing flow, the influence of  $Re$  can be identified with the hydrodynamic and thermal plots for a range of  $Gr$  from  $4.07 \times 10^6$  to  $6.88 \times 10^6$  and  $Re$  from 5000 to 6500 at fixed  $Ri = 0.16$ . The results are opposite in buoyancy-opposed flow as compared to the buoyancy-assisted flow (Figure 7.6(a)). The fluid velocity increases as the  $Re$  increases from 5000 to 6500 at a fixed  $Ri$ . The centreline velocity increases in the development length and then becomes steady once the flow is fully developed. The corresponding velocity profiles show the increase in velocity magnitude with an increase in  $Re$ . For a fixed  $Ri$ , an increase in  $Re$  results in an increase of  $Gr$  and consequently an increase in heat flux. This higher  $Gr$  increases the free convection effect and the temperature difference between the inlet and bulk fluid. Hence, the centreline temperature and the temperature gradient near the wall increases for higher  $Re$ .

The friction factor plot in Figure 7.9(a) resembles the drop in  $f$  whereas the local  $Nu$  plot in Figure 7.9(b) increases by increasing  $Gr$  and the corresponding  $Re$  at fixed



$Ri$ . At higher  $Re$ , the heat is being carried away by the working fluid at a faster rate. Hence the temperature gradient near the wall also increases resulting in enhancement of  $Nu$ . Further, by varying the viscosity with temperature leads to the increase in  $f$  (~105 %) because of the increase in velocity gradient near the wall (like Figure 7.5(a)) and rise in  $Nu$  (~56 %) due to the increase in  $Re_b$ . The  $\kappa$  and  $\varepsilon$  profile radially at  $L/D = 150$ , the peak near the wall increases with the increase in  $Re$  at fixed  $Ri$  with varying  $Gr$  and  $Re$ . The similar feature of increase of peak in  $\kappa$  and decrease of peak in  $\varepsilon$  was reflected by varying the viscosity on their radial profile. The axial dependence is prominent in case of  $\kappa$  whereas the axial dependence of  $\varepsilon$  is discernible. It is also found that the  $\kappa$  increases with the increase in  $Re$  and  $Gr$  but there is no effect of varying  $Re$  and  $Gr$  at fixed  $Ri$  on  $\varepsilon$ .

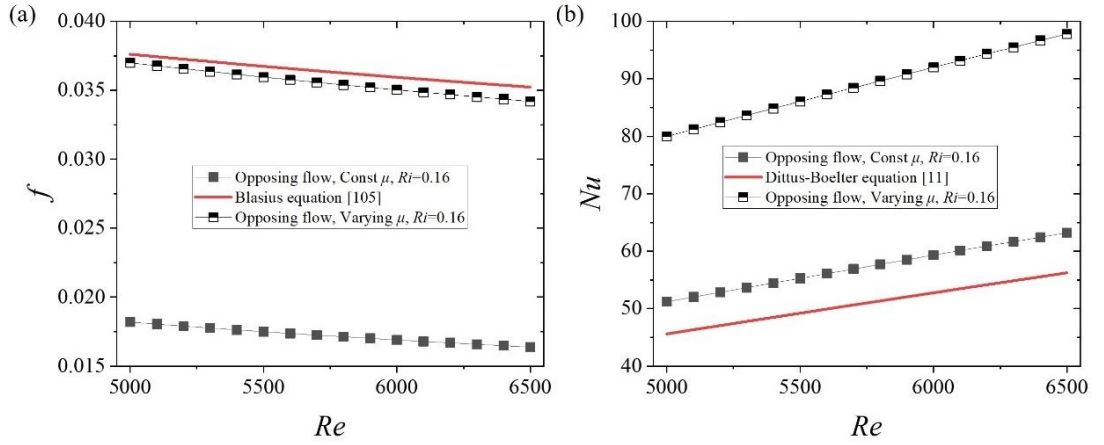


**Figure 7.9** Variation of fully developed (a)  $f$  and (b)  $Nu$  at fixed  $Ri = 0.16$  and varying  $Re, Gr$

## 7.2.4 Comparison between buoyancy-assisted and buoyancy-opposed flow

In this section, the comparative analysis of the buoyancy-assisting and opposing flows in the turbulent regime of mixed convection has been described for a particular range of  $Gr, Re$ , and  $Ri$ .

### 7.2.4.1 Fixed $Gr$ and varying $Re, Ri$

Figures 7.10(a) and (b) represent the comparison plots of average  $f$  and  $Nu$  variation in the fully developed regime for  $Re = 5000 - 6500$ ,  $Ri = 0.10 - 0.16$  at fixed  $Gr = 4.07 \times 10^6$ . The values of  $Ri$  are chosen in such a way that the free convection effect is comparable to that of the forced convection effect and at the same time, the outlet fluid temperature is well below its saturation temperature. The  $f$  and  $Nu$  plot clearly explain

## 7.2 Numerical results on turbulent mixed convection

that there is a small difference in the friction factor and even less difference in Nusselt number for assisting and opposing flows while varying  $Re$  and  $Ri$  at fixed  $Gr$ . It seems that the  $f$  and  $Nu$  both are slightly higher in the case of opposing flow than that of the assisting flow. The difference in effect of buoyancy in aiding and opposing case is very less because of turbulence in which the flow features characterise by the eddies. These eddies diminish the effect of buoyancy. The only difference has been found, in aiding flow the centreline velocity increases a bit at the entry then it drops and becomes steady once the flow becomes fully developed which is not in case of opposing flow where it continuously increases at the entry and becomes constant at fully developed condition.

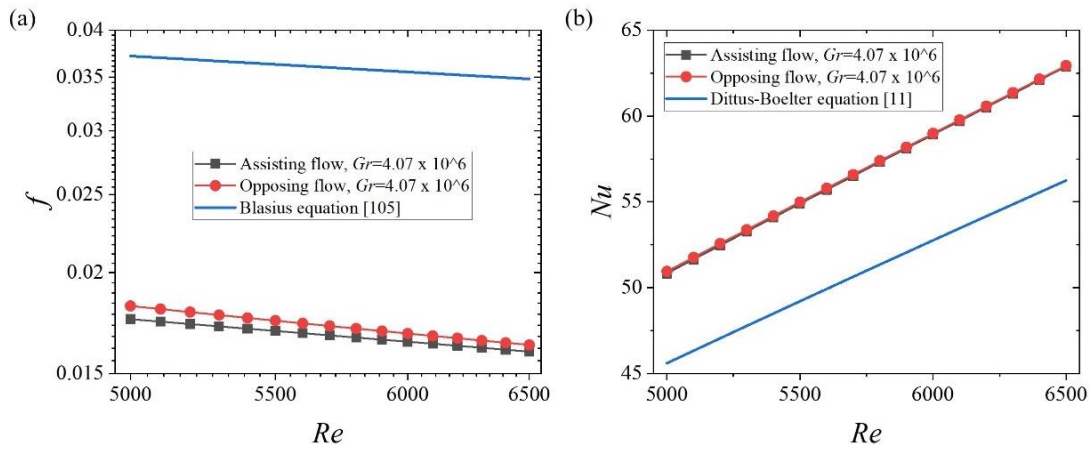


**Figure 7.10** Comparison between fully developed (a)  $f$  and (b)  $Nu$  for varying  $Re$  and  $Ri$  at fixed  $Gr$  in assisting and opposing flow

### 7.2.4.2 Fixed $Ri$ and varying $Gr$ , $Re$

The comparisons are made for varying  $Re = 5000 - 6500$ ,  $Gr = 4.07 \times 10^6 - 6.88 \times 10^6$  at fixed  $Ri = 0.16$ . Because of the higher velocity and temperature gradients near the wall, the  $f$  and  $Nu$  in opposing flow become a bit higher than that of the assisting flow. Thereafter, to cover the entire range of  $Re$  from 5000 to 20000, the  $L/D$  ratio had been reduced from 150 to 50 to avoid the outlet temperature well below the saturation temperature and then the effect of varying  $Gr$  was analysed in Figure 7.11. It has been found that the fully developed  $f$  as well  $Nu$  at a particular  $Re$  increases in the opposing flow and decreases in the assisting flow with the increase in  $Ri$ . In another way of analysis, the non-dimensional term popularly known as Buoyancy parameter ( $Bo$ ) has been introduced to see the effect of buoyancy on friction factor and Nusselt number. In Figure 7.12, the ratio of mixed and forced convection friction factor ( $f/f_o$ ) and the Nusselt number ( $Nu/Nu_o$ ) has been plotted against  $Bo$ . Here,  $f_o$  is the friction factor and  $Nu_o$  is the Nusselt number in case of pure forced convection. It is found that



the present range of parameters are for  $Bo < 10^{-5}$ , for which the friction factor and Nusselt number ratio both are higher in opposing flow. Quantitatively the friction factor in opposing flow is 5-10 % higher and Nusselt number is 2-3 % higher as that of the assisting flow.

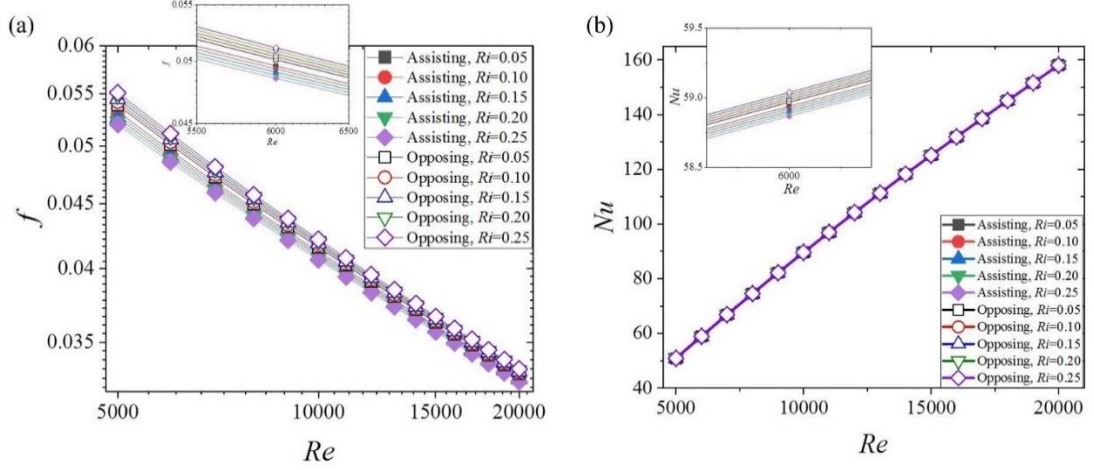


**Figure 7.11** Comparison between fully developed (a)  $f$  and (b)  $Nu$  at  $L/D = 50$  for varying  $Gr$  and  $Re = 5000 - 20000$  at fixed  $Ri$  in assisting and opposing flow

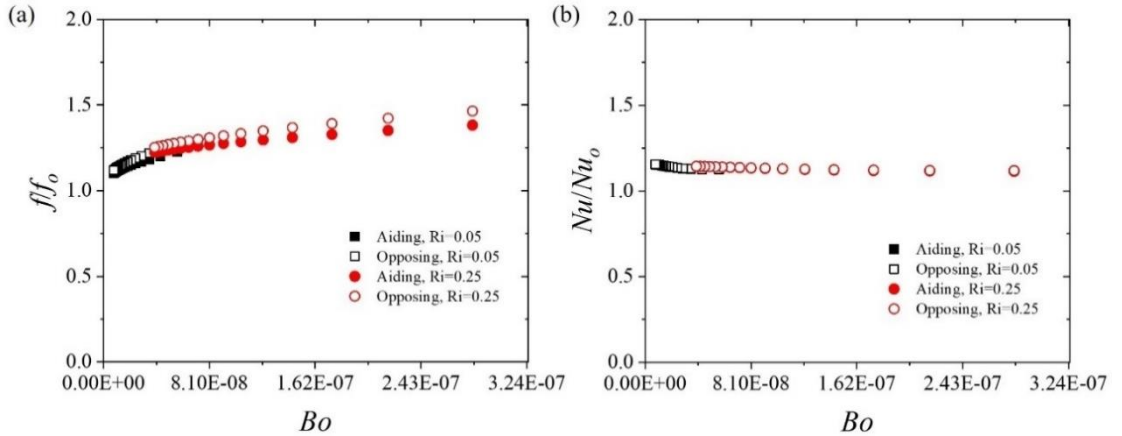


**Figure 7.12** Comparison of the ratio of (a) friction factor ( $f/f_o$ ) and (b) Nusselt number ( $Nu/Nu_o$ ) of mixed and forced convection in assisting and opposing flow

### 7.2.5 Entry length comparison

The hydrodynamic ( $L_h$ ) and thermal ( $L_t$ ) entry length for the turbulent mixed convection case is no longer varying as it varies in the case of the laminar mixed convection. A detailed study by [106] on the entry length of laminar mixed convection flow through a vertical tube subjected to uniform heat flux conditions shows an increase in hydrodynamic and thermal entry length with the increase of  $Ri$  in buoyancy-assisting and opposing flows. The reason for short entry length in turbulent mixed convection is the development of hydrodynamic and thermal boundary layer development, which is

## 7.2 Numerical results on turbulent mixed convection

quick in case of a turbulent flow as compared to the laminar case. This can be explained with the help of local  $C_f$  and local  $Nu$  plot along the length of the pipe for different  $Ri$  (Figure 7.13). The local plot shows that the local  $C_f$  as well as  $Nu$  both are higher in the developing region and gradually decreases and then becomes constant once the flow progresses to fully developed.

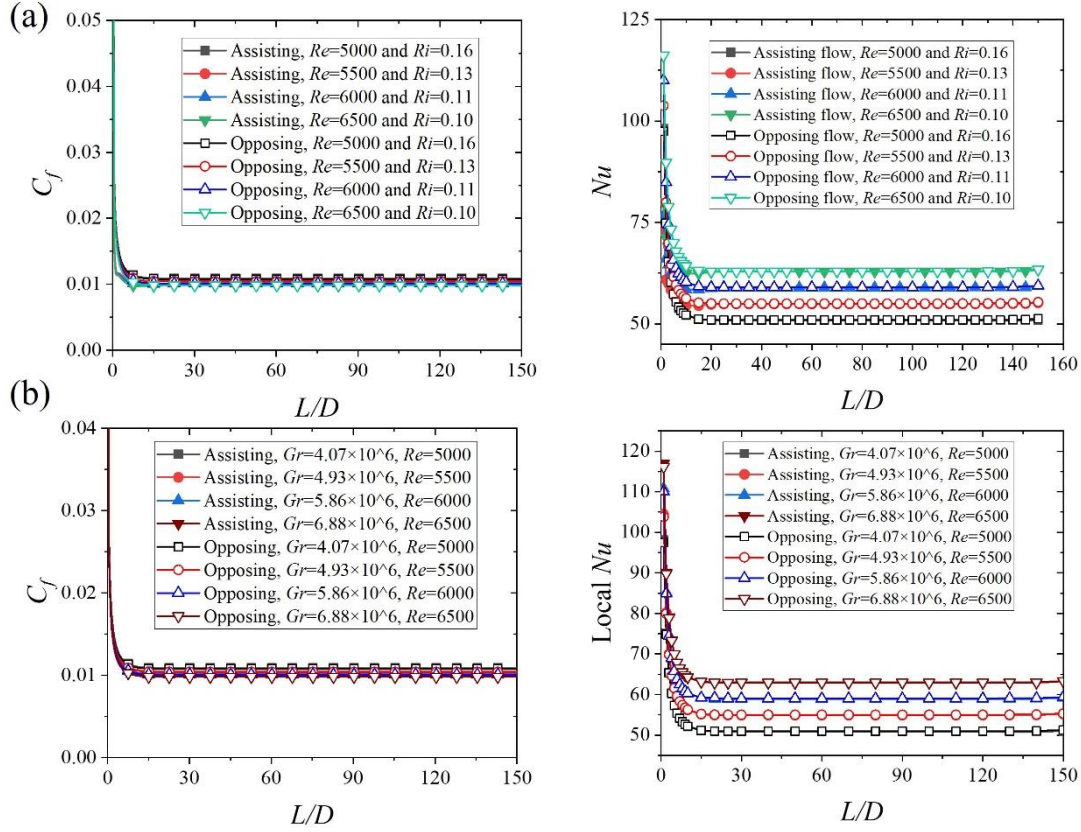


**Figure 7.13** Local skin friction coefficient ( $C_f$ ) and Nusselt number ( $Nu$ ) variation axially for assisting and opposing flow (a) at fixed  $Gr$  and varying  $Re$ ,  $Ri$  (b) at fixed  $Ri$  and varying  $Re$ ,  $Gr$

The criteria to be hydrodynamically fully developed are set as  $d(C_f)/d(L/D) \leq 10^{-5}$  and for thermally fully developed as  $d(Nu)/d(L/D) \leq 10^{-2}$  based on their axial gradient. By this approach, the hydrodynamic fully developed condition is achieved in buoyancy-aiding flows at  $L/D \sim 21$  and in the case of buoyancy-opposing flows it is approximately at  $L/D \sim 17$  whereas the thermally fully developed condition is achieved in buoyancy-aiding flows at  $L/D \sim 25$  and in case of buoyancy-opposing flows it is approximately at  $L/D \sim 20$  as shown in Figure 7.14. For the present range of parameters, it can be inferred that with the increase of  $Ri$ , the entry length (hydrodynamic) increases marginally in assisting flows whereas the thermal entry length either remains constant or hardly decreases in opposing flows. In contrast to it, the trend is different when  $Ri$  is

fixed and both  $Gr$ ,  $Re$  increases, the thermal entry length remains same in both the flows whereas the hydrodynamic entry length decreases in assisting flow and increases in opposing flow. The reason for this is the increase in buoyancy effect first decreases and then increases the velocity near the wall which grows the boundary layer faster and reaches fully developed earlier which doesn't happen in the opposing flow because of not much change in the velocity.

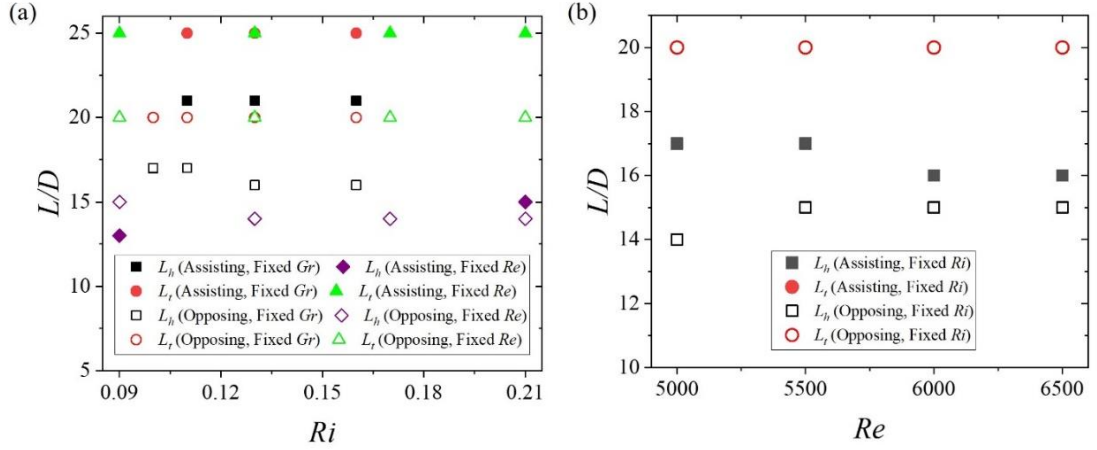


**Figure 7.14** Comparison of hydrodynamic and thermal entry length for assisting and opposing flow (a) at fixed  $Gr$  and varying  $Re$ ,  $Ri$  and fixed  $Re$  and varying  $Gr$ ,  $Ri$  (b) at fixed  $Ri$  and varying  $Re$ ,  $Gr$

### 7.2.6 Friction factor and Nusselt number correlations

With the available simulation data for  $f$  and  $Nu$ , different correlations have been produced for buoyancy-assisting and opposing flows. The range of parameters for which the correlations are applicable is  $5000 \leq Re \leq 20000$ ,  $0.05 \leq Ri \leq 0.25$ , and  $Pr = 7$ . To quantitatively examine the relationship between pressure drop and heat transfer, a plot of  $f/j$  has been obtained with  $Re$ . It will make possible to determine either  $f$  or  $j$  when the other variable is known. Eq. (7.1) represents the correlation between  $f$  and  $j$  in terms of  $Re$ . The log-plot of  $f/j$  shows it monotonically decreases with the increase in  $Re$ . A power curve fit employed in the data points, gives the correlation with the best fit with a trendline of  $R^2$  (is a measure of goodness of fit, it is represented in percentage and higher the value, the better the line gives a fit to the data points) value of 0.99565. A separate correlation for friction factor has been generated with the variation of  $Re$  as mentioned in Eq. (7.2). A power curve with decreasing trend is best fitted with a  $R^2$  value of 0.9988. It deviates a little from Blasius equation due to the combined free and forced convection effect. Similarly, the correlation of fully developed  $Nu$  has been obtained with  $Re$  at fixed  $Ri$ . The Eq. (7.2) have been substituted in Eq. (7.1) and

## 7.2 Numerical results on turbulent mixed convection

representing  $j$  in terms of  $Re$  produces Eq. (7.3) the correlation of  $Nu$  in terms of  $Re$  and  $Pr$ . The  $Pr = 7$ , throughout the simulations based on the inlet temperature of the water. The coefficient ( $c$ ) and exponent ( $o$ ) of Eq. (7.3) can also be obtained as ' $b/a$ ' and ' $1+n-m$ '. The coefficients and the exponents range for  $Ri = 0.05 - 0.25$  for both buoyancy-assisting and opposing flows are tabulated in Table 7.1. It has been observed that the coefficients and exponents are significantly varying with the increase of  $Ri$ . To verify the performance of the correlations obtained, it compared with the numerical results in a parity plot and found that the maximum deviation in between correlation and numerical data are within  $\pm 5\%$  of deviation (Figure 7.15). The deviation in the turbulent regime is comparatively less than laminar regime. The reason is that the fully developed flow condition is more prevailing in turbulent flow as compared to the developing flow.

$$\frac{f}{j} = a(Re)^m \quad (7.1)$$

$$f = b(Re)^n \quad (7.2)$$

$$Nu = c(Re)^o(Pr)^{1/3} \quad (7.3)$$

**Table 7.1** Range of the coefficients and exponents present in Eqs. (7.1), (7.2), and (7.3)

Flow	$Ri$	<b>a</b>	<b>b</b>	<b>c</b>	<b>m</b>	<b>n</b>	<b>o</b>
Assisting flow	0.05	26.35	0.51	0.019	-0.13	-0.3	0.83
	0.25	44.19	0.88	0.0199	-0.15	-0.33	0.82
Opposing flow	0.05	31.16	0.5	0.016	-0.15	-0.3	0.85
	0.25	56.25	1.15	0.0204	-0.18	-0.36	0.82

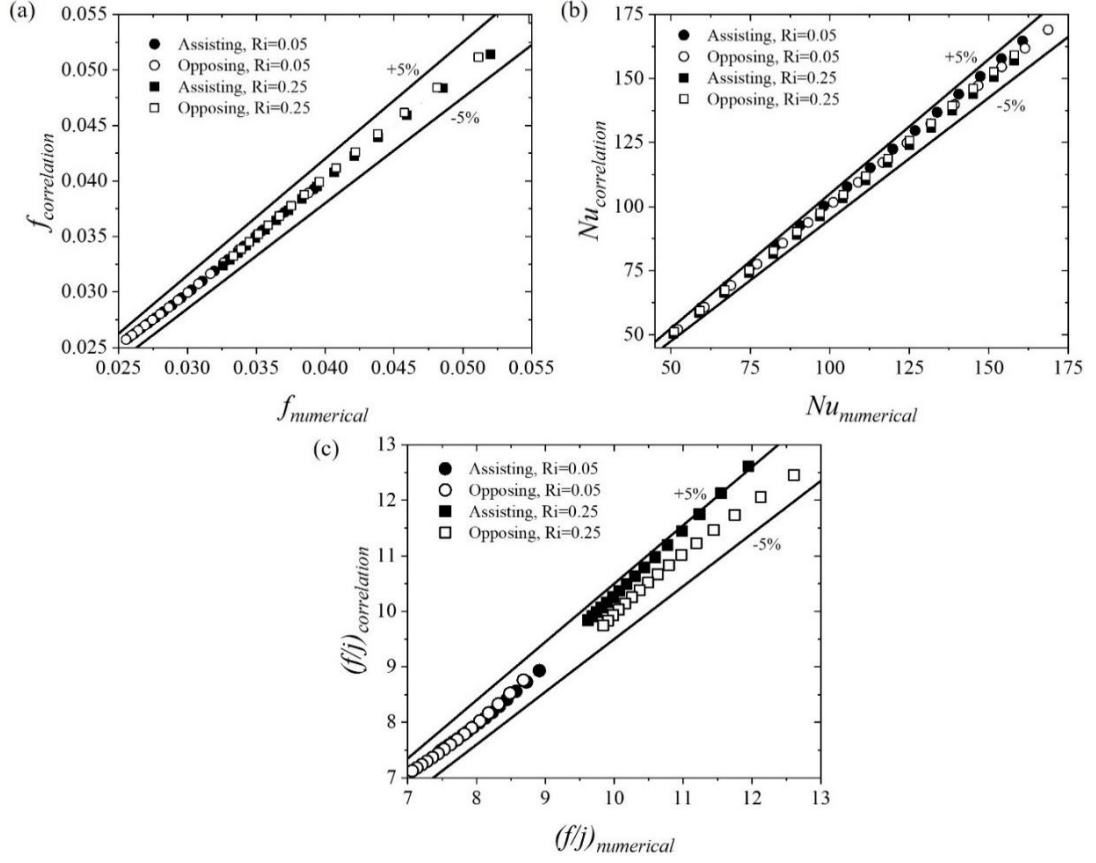


**Figure 7.15** Deviation of correlation and numerical data for (a)  $f$  (b)  $Nu$  and (c)  $f/j$

### 7.3 Experimental results on turbulent mixed convection

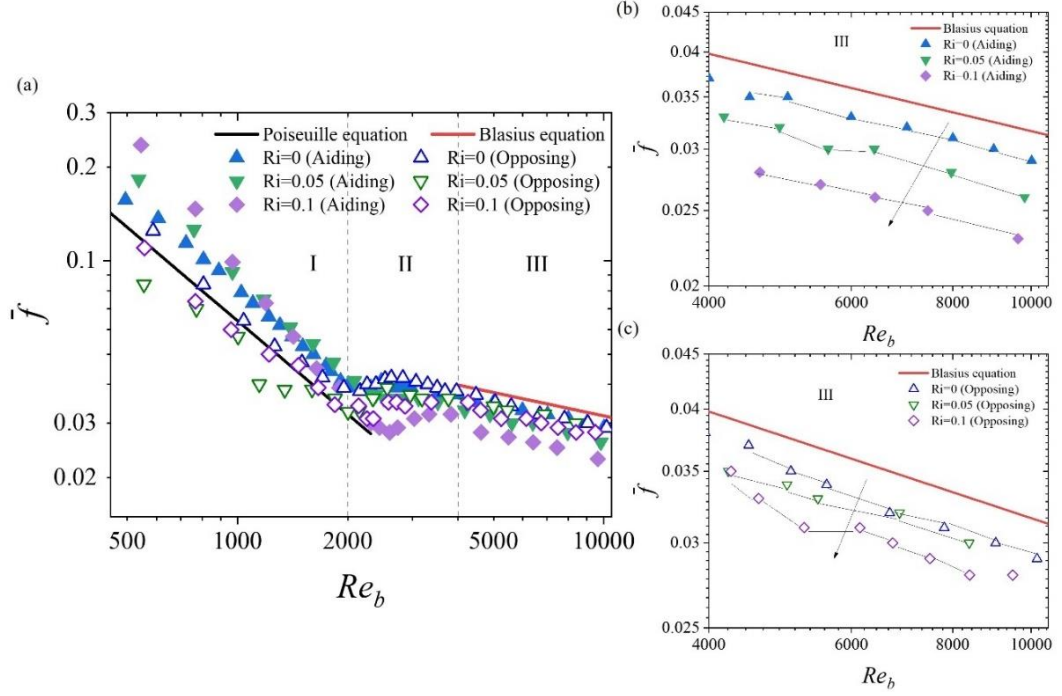
The experiments were carried out for a variety of Reynolds numbers ( $539 \leq Re \leq 9621$ ), Grashof numbers ( $2.4 \times 10^4 \leq Gr \leq 1.3 \times 10^7$ ), Richardson numbers ( $0 \leq Ri \leq 0.3$ ), and Prandtl numbers ( $4.4 \leq Pr \leq 6.5$ ) in aiding flow and  $553 \leq Re \leq 9492$ ,  $3.6 \times 10^4 \leq Gr \leq 1.1 \times 10^7$ ,  $0 \leq Ri \leq 0.3$ , and  $5.2 \leq Pr \leq 6.4$  in opposing flow, respectively. Normal water was used as the working fluid, which was maintained at  $20^\circ\text{C}$  at atmospheric pressure. The test part was heated using Joule heating and a low voltage, high current capacity DC power source. The experimental setup can be configured so that both assisting and opposing tests can be carried out. To study in the developing and fully developed regime, the length-to-diameter ratio is preserved at 130.  $Ri=0$  indicates that zero heat flux case, and when there is no heat flow, it is possible to achieve a higher Reynolds number. For a mixed convection flow, the buoyancy effect depends on the amount of heat flux supplied. With the addition of heat flux, the  $Gr$  increases, and, as a result, the outlet water temperature also increases. This limits the present mixed convection study to such a value of  $Gr$  so that a lower  $Ri$

### 7.3 Experimental results on turbulent mixed convection

may be obtained. The rationale for this is to keep the temperature of the output water below its saturation point. This means that the highest achievable  $Ri$  is 0.3, with  $Gr$  values of  $4.5 \times 10^7$  and  $1.7 \times 10^7$  and a  $Re_b$  value of 8870 and 6354 in aiding and opposing flow, respectively.

#### 7.3.1 Average pressure drop and heat transfer in the fully developed turbulent flow

The log-log plot (Figure 7.16(a)) of average friction factor ( $\bar{f}$ ) vs. bulk Reynolds numbers ( $Re_b$ ) highlights the role of Richardson numbers on  $\bar{f}$  for both aiding and opposing flow. At a given  $Ri$ , the  $Re$  was varied in between 500 and 10,000 depending on the amount of heat flux supplied. The zone III in Figure 7.16(a) denotes the turbulent regime where the friction factor decreases with  $Re$  for the range of  $Ri$  tested in our experimental studies. Magnified versions of Figure 7.16(a) turbulent aided and opposed regimes are presented in Figure 7.16(b) and (c) respectively. It is readily evident that at any fixed  $Ri$ , the friction factor follows the same trend as Blasius scaling for fully turbulent heat flow with no heat flux ( $f \propto Re^{-0.25}$ ). In the turbulent flow regime, Figures 7.16 (b) and (c) show there is significant effect of buoyancy on aiding and opposing flows respectively. The magnified view reveals that the increase in  $Ri$ , decreases the friction factor in both aiding and opposing flows respectively. This ensures that the  $f$  is also function of  $Gr$  along with  $Re$  in a mixed convection flow regime. However, the decrease in  $f$  with the increase in  $Gr$  in opposing flow is comparatively less than that in aiding flow.



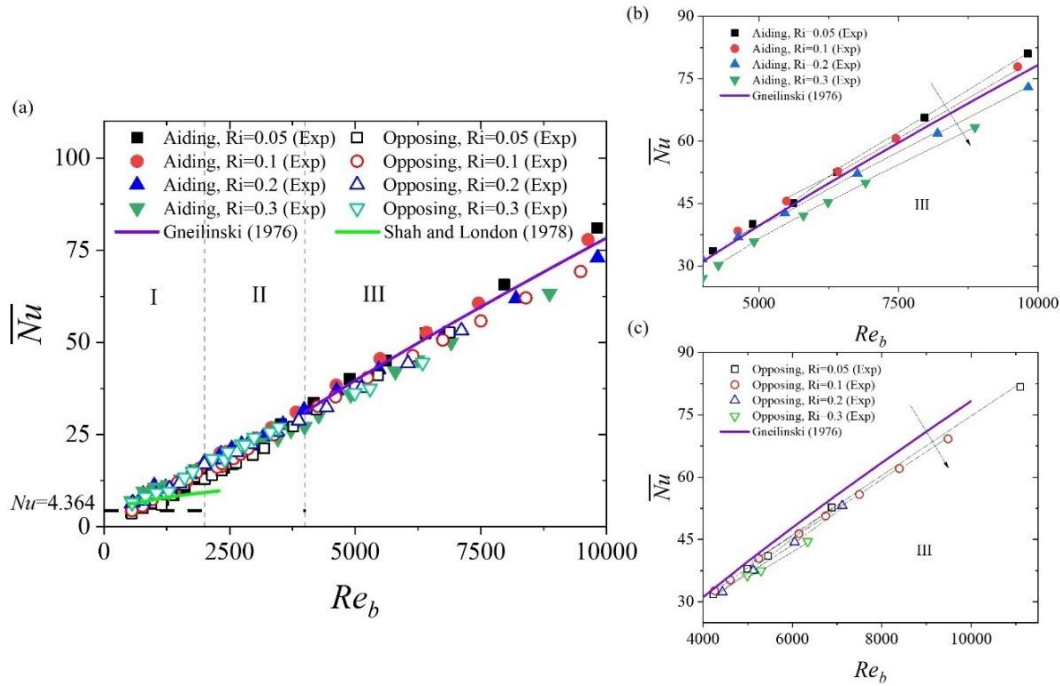
**Figure 7.16** Average  $f$  vs.  $Re$  comparison plot in turbulent mixed convection with varying  $Re$ ,  $Gr$  at different  $Ri$

Figure 7.17(a) zone III highlights the variation of average Nusselt number  $\overline{Nu}$  with the increase of  $Re_b$  at fixed  $Ri$ . In laminar flow regime (Figure 7.17(a) zone I) the  $\overline{Nu}$  increases with the increase of  $Re_b$  because the flow lies in the developing flow instead of a fully developed flow where  $Nu=4.364$  for uniform heat flux boundary condition. Afterwards, in the transitional flow regime (Figure 7.17(a) zone II) the flow switches between laminar and turbulent flow and the  $Nu$  remains stagnant (Figure 6.17, section 6.4.1) for next few  $Re$  and then continuously increases with further increase in  $Re$  at a fixed  $Ri$ . The magnified view of the turbulent flow regime in Figures 7.17(b) and (c) shows that the average  $Nu$  decreases with the increase in  $Ri$  for both aiding and opposing flows respectively. In aiding flow, acceleration of the flow near the wall decreases the shear stress across the wall. Based on the physical explanation given by Jackson [42], I have hypothesised the probable reason for the heat transfer behaviour in a turbulent flow. The buoyancy force of fluid near wall helps to overcome the shear force exerted by the wall. This buoyant thermal layer is mainly confined to the viscous-sub-layer and buffer layer regions, and the reduction in shear stress is experienced where the turbulence production is concentrated. As a result of this the turbulence is likely to be diminished and hence heat transfer decreases. In opposing flow, the effect of buoyancy in the opposite direction increases the shear stress and hence the turbulence



### 7.3 Experimental results on turbulent mixed convection

is enhanced. The higher buoyancy leads to more turbulence that results into higher heat transfer compared to the aiding flow.



**Figure 7.17** Average  $Nu$  vs.  $Re$  comparison plot in turbulent mixed convection with varying  $Re$ ,  $Gr$  at different  $Ri$

#### 7.3.2 Local heat transfer in the turbulent mixed convection flow

Based on the results shown in the above section, the turbulent regime is categorized into aiding and opposing flows. Fig. 7.18 (a) and (b) highlights the axial variation of  $Nu$  i.e.,  $Nu$  vs  $L/D$  and  $Nu$  vs  $Gz$  plot presented respectively. In buoyancy aided turbulent mixed convection, with increase in  $Re$ , the effect of turbulent eddies dominates the free convection effect. These turbulent eddies convected away the heat at a faster rate than laminar flows which ultimately resulted in higher heat transfer. Because of the short entry length ( $L/D \sim 20$ ) in turbulent flows [134], the difference between inner wall and bulk mean fluid temperature decreases after the inlet which increases the local  $Nu$ . In a turbulent flow, the  $Gz$  is not an important parameter to decide the entry length in comparison to the laminar flow. The  $Nu$  vs.  $Gz$  plot shows that the Nusselt number increases with the increase in  $Re$  at a fixed  $Ri=0.1$ .



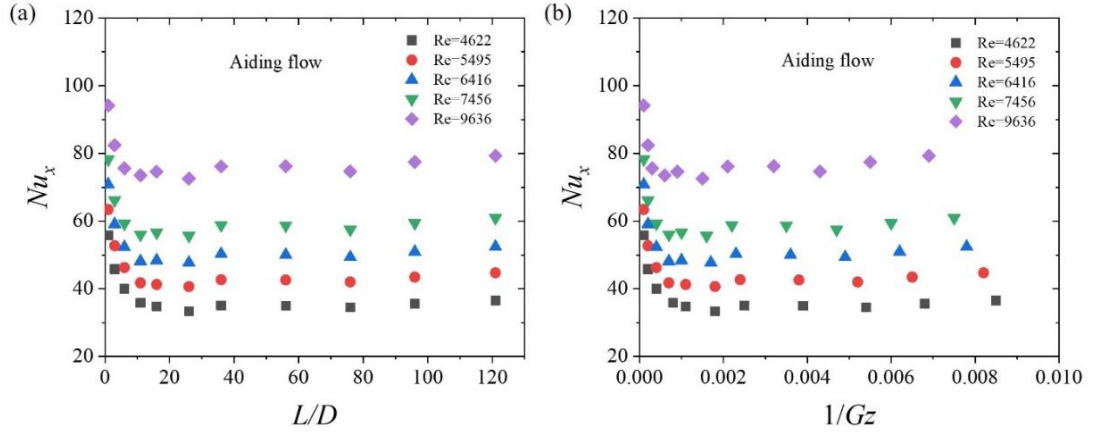


**Figure 7.18** Local (a)  $Nu$  vs.  $L/D$  and (b)  $Nu$  vs.  $Gz$  plot for turbulent mixed convection at fixed  $Ri=0.1$  in aiding flow

In opposing turbulent flow, Figure 7.19(a) exhibits the axial variation of  $Nu$ . Initially the local  $Nu$  starts increasing till  $L/D \sim 20$  and then starts increasing till  $L/D \sim 40$ . Eventually the local  $Nu$  assumes almost a steady state value after  $L/D > 40$ . In fully developed state, after a small axial length due to higher thermal diffusivity in the thermal boundary layer, the  $Nu$  becomes high. In Figure 7.19(b), which is a similar plot of  $Nu$  vs.  $L/D$  shows that  $Nu$  increases after  $1/Gz \geq 0.0005$  and becomes steady once the flow is developed. The rate of heat transfer further increases with the increase in  $Re$ . However, it is interesting to note that the heat transfer is higher in opposing flows in comparison to the aiding flows. As the flow progresses, in the fully developed flow condition, the wall and mean fluid temperature difference in opposing flow become even smaller than the wall and mean temperature difference in aiding flow. This signifies that the turbulence and mixing is more in opposing flow as compared to the aiding flow. In the study of opposing flow, it has been speculated that the heated fluid near the wall tends to sink toward the walls. This can disrupt the typical near-wall turbulent structures and increase the mixing between different fluid layers [66].

## 7.4 Comparison between numerical and experimental turbulent mixed convection results

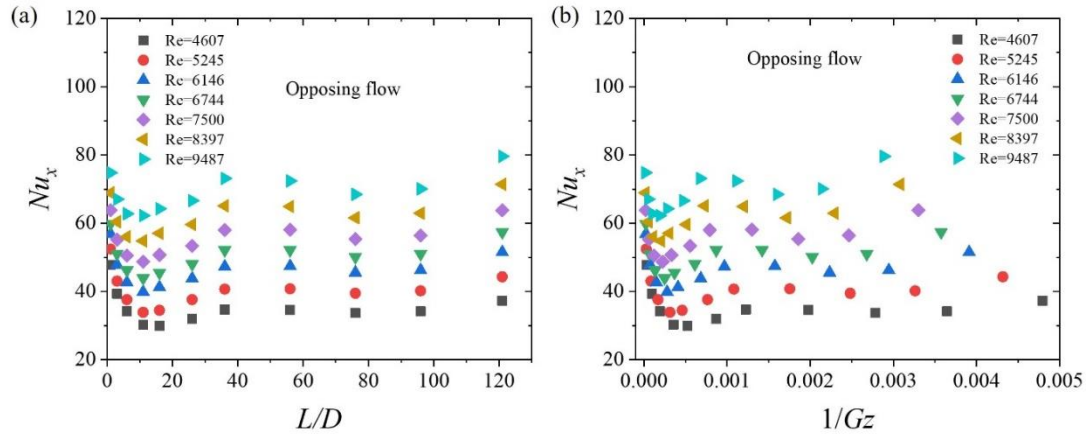


**Figure 7.19** Local (a)  $Nu$  vs.  $L/D$  and (b)  $Nu$  vs.  $Gz$  plot for turbulent mixed convection at fixed  $Ri=0.1$  in opposing flow

## 7.4 Comparison between numerical and experimental turbulent mixed convection results

### 7.4.1 Heat transfer comparison in turbulent mixed convection

The local  $Nu$  axial variation in the experiments has been compared with the numerical results as illustrated in Figure 7.20. It is found that there is qualitative similarity in the trend, but quantitatively there is difference in magnitude, and it is higher in the experiments. One reason for this is that in turbulent mixed convection flows, at a given  $Ri$  for higher  $Re$ , the corresponding  $Gr$  is also higher. Because a higher  $Gr$ , results in a greater heat flux that leads to the higher bulk fluid temperature. Consequently, it decreases the fluid properties such as viscosity and density to a greater extent. Because of this the bulk  $Re$  increases and the bulk  $Pr$  decreases, which ultimately increases the  $Nu$ . In case of aiding flows, the wall and mean fluid temperature difference is higher at the entry region which causes decrease in  $Nu$ . At further downstream, the wall and mean fluid temperature decreases resulting into higher  $Nu$ . This is also true in case of opposing flow which results into higher heat transfer.

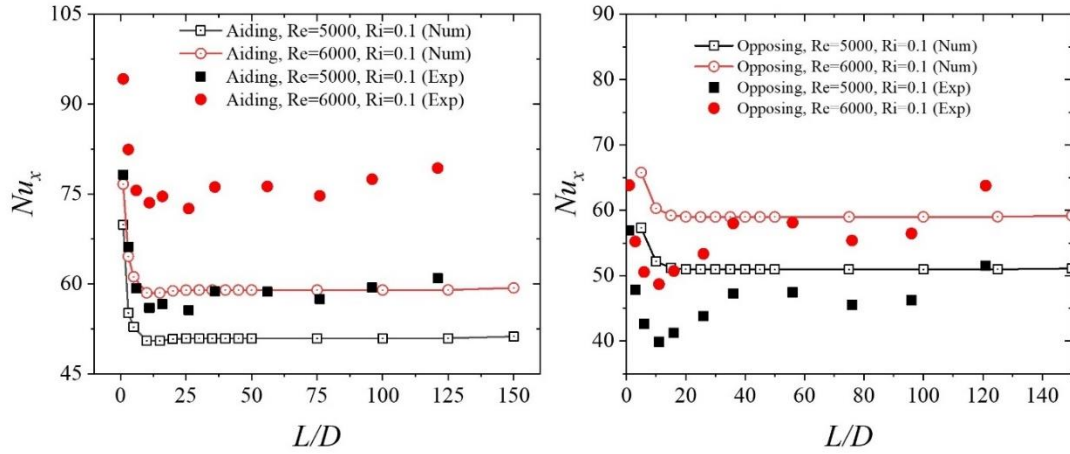


**Figure 7.20** Local  $Nu$  (numerical vs. experimental) comparison plots in (a) aiding and (b) opposing flow of turbulent mixed convection at fixed  $Ri$

## 7.5 Conclusions

A comparative analysis of turbulent mixed convection for buoyancy-assisted and -opposed water flow through a vertical tube have been presented numerically and experimentally. The results were validated with the available correlations and existing experimental studies. It has been found that the realizable  $\kappa - \varepsilon$  model with enhanced wall treatment was the most suitable as compared to the other turbulence models. Thereafter, the effect of parameters such as  $Gr$ ,  $Re$ , and  $Ri$  were analyzed by keeping one of them fixed and then varying others. It has been observed that the pressure drops (quantified by  $f$ ) and heat transfer (quantified by  $Nu$ ) both are higher in buoyancy-opposing flow than in the buoyancy-assisting flow. It has also been observed that the fully developed friction factor,  $f$  is lower as compared to the Blasius equation and Nusselt number,  $Nu$  is higher as compared to the Dittus-Boelter equation for both assisting and opposing flows. The turbulent quantities such as turbulent kinetic energy, and turbulent dissipation rate were also analysed radially and axially in the tube. The  $\kappa$  and  $\varepsilon$  profile attains a peak near the wall at  $r/R \sim 0.9$  and comes down at the centre of the tube. The axial variation of  $\kappa$  and  $\varepsilon$  shows that it decreases at the entry, becomes steady when the flow is fully developed. Further, the entry length was also examined for simultaneously hydrodynamically and thermally developing turbulent mixed convection flows. The hydrodynamically developed condition in buoyancy-assisting and opposing flow are achieved by  $L/D \sim 21$  and  $\sim 17$  respectively and the thermally developed condition by  $L/D \sim 25$  and  $\sim 20$  respectively. Correlations were developed

## 7.5 Conclusions

to quantify the friction factor,  $f = f(Re)$ , Colburn  $j$ -factor,  $f/j = f(Re)$ , and Nusselt number,  $Nu = f(Re, Pr)$ , for a range of  $Re$ ,  $Ri$  and  $Pr$  in both the flows. It has been concluded that in case of assisting flow the heat transfer is lower than that of opposing flow due to the lower turbulence production because of the laminarization of the flow in assisting case. From literature [42], it has been postulated that in cases of strong buoyancy flows, the flow can become laminar from turbulent due to the damping effect of buoyancy on turbulence. From the experiments, it has been found that the  $f$  and  $Nu$  both decreases with the increase of  $Ri$ . The local  $Nu$  plot shows that in turbulent flows the heat transfer increases after a small axial distance due to the decrease in inner wall and bulk fluid temperature.

### Summary and Conclusions

---

#### 8.1 Introduction

The present chapter outlines the aim, methodology and the results chapter wise. Followed by the major outcome from the study are summarized. Finally, the future work and recommendations are discussed.

#### 8.2 Summary of the present work

The present study comprises both numerical and experimental investigations. For numerical study, the Computational Fluid Dynamics (CFD) tool based on the Finite Volume Method (FVM) and commercially available software ANSYS-Fluent has been used. This is efficient and robust software that uses laminar, transitional, and various turbulence models to deal with different flow regimes. The 2D axisymmetric geometry was modeled in the Design Modular (DM), and structured meshing was done with fine grids near the tube walls to account for sharp velocity and temperature gradients. The solution was set up for a steady-state, axisymmetric model with a pressure-based solver. The governing equations were solved by using the SIMPLE/coupled scheme for pressure-velocity coupling in the momentum equations and the UPWIND scheme for the convective terms. Grids were optimized after the Grid Independency Test (GIT) for further simulations. A laminar model was used for the laminar regime, Transition Shear Stress Transport (SST) model was used for the transitional regime, and two equation Reynolds-Averaged-Navier-Stokes (RANS) models were used for the turbulence modeling simulations. The residuals were set at least one order less than the default values for the continuity, momentum, and energy equations. The introduction, organization of the thesis, literature survey, and objectives are discussed in Chapters 1–2. The numerical procedure, grid independence test, and validation of the numerical model for laminar, turbulent, and transitional mixed convection are analyzed in Chapter 3. The detailed experimental set-up design, procedure, data reduction technique, uncertainty analysis, and validation of results are explained in Chapter 4. The numerical and experimental results and their comparisons in laminar, transitional, and turbulent

## 8.2 Summary of the present work

mixed convection flows are discussed in Chapters 5, 6, and 7, respectively. The summary of the present work, concluding remarks, and its future scope are briefly discussed in Chapter 8.

In Chapter 3, the numerical procedure to deal with the laminar regime of mixed convection flow through a vertical tube has been explained in detail. The GIT, followed by the validation of the laminar model with theory and experiments, was presented. The results were investigated in terms of local and average  $f$ , Colburn  $j$ -factor, and  $Nu$  plots in developing and fully developed flows. The effect of governing parameters on the flow characteristics and the entrance length was also explained for both buoyancy-assisted and opposed flows. In laminar mixed convection, it has been observed that  $f$  and  $Nu$  are higher in buoyancy-assisted flows as compared to buoyancy-opposed flows. In addition to that, it has been found that the entry length is greater in mixed convection than in pure forced convection. Furthermore, at a given flow rate, the increase in the heat flux increases the pressure drop (quantified by  $f$ ) and heat transfer (quantified by  $Nu$ ) in buoyancy-assisted flow and decreases in buoyancy-opposed flow.

Further, like the laminar mixed convection, grid optimization, validation of the turbulence model with the existing correlations, and experiments were presented for the turbulent mixed convection flows in a vertical tube. Here, the results were explored for the developing and fully developed flows. It was found that the entry length is short in turbulent flows, and no significant difference was observed for buoyancy-assisted and opposed flows. This indicates that the effect of buoyancy is not commendable in turbulent flows.

Furthermore, the transition SST model was used for the transitional mixed convection simulations. The results were compared with the existing Direct Numerical Simulations (DNS) and experimental data. The local  $C_{f_x}$  and  $Nu$  plots describe that the transition is dependent on heat flux and gets delayed in buoyancy-assisting flow and advances in buoyancy-opposing flow with the increase of heat flux.

Chapter 4 explained the experimental set-up design, procedure, uncertainty analysis in detail, and validation for the heating with upward (aiding) and heating with downward (opposing) flows in the laminar, transitional, and turbulent flow regimes.

Chapters 5, 6, and 7 presented the results in detail for the simultaneously developing laminar, transitional, and turbulent mixed convection flow regimes. The effect of heat flux on these three flow regimes was investigated for both buoyancy-assisted and opposed flows. The average friction factor ( $\bar{f}$ ) and Nusselt number ( $\overline{Nu}$ ) variations at fixed  $Ri$  have been analyzed. It has been observed that in laminar mixed convection, the pressure drop and heat transfer both are higher in the assisting flow as compared to the opposing flow. In contrast to it, the pressure drop and heat transfer both higher in the opposing flow as compared to the assisting flow in the case of turbulent mixed convection. In turbulent flow, the effect of buoyancy is insignificant. Furthermore, it has also been observed that the increase in heat flux causes the transition in the opposing flow to occur faster as compared to the assisting flow. At the end of each individual chapter, the numerical and experimental results were compared and discussed for the laminar, transitional, and turbulent flows.

In Chapter 8, all the results are summarized, major conclusions are mentioned, and the future scope of the present research work is highlighted. This section also highlights a few limitations pertaining to the present work.

### 8.3 Major conclusions

The investigations concentrated on the developing regime of mixed convection flows through a vertical tube. The effect of governing parameters was analysed in terms of friction factor and Nusselt number. A comparative analysis of laminar, transitional, and turbulent mixed convection has been presented in buoyancy-assisted and buoyancy-opposed flows subjected to constant heat flux boundary conditions. The major conclusions from the present work are as follows:

#### Laminar mixed convection:

- ✓ In the case of assisting flow, the velocity is accelerated near the tube wall compared to the centre of the tube. In contrast, velocity is accelerated at the centre as compared to the tube wall in the case of opposing flow for same  $Re$  and  $Ri$ .
- ✓ With increasing  $Ri$ , both  $f$  and  $Nu$  exhibited increasing and decreasing trends for buoyancy-aided and opposed cases, respectively. It is worth mentioning that the developing region exhibits higher  $Nu$  compared to fully developed states for both aided and opposed flows. The hydrodynamic development length ( $L_h$ )

### 8.3 Major conclusions

increases with the increase of  $Ri$  for both assisting and opposing flow, but the thermal entry length ( $L_t$ ) decreases in the case of assisting flow in contrast to the opposing flow.

#### Transitional mixed convection:

- ✓ The increase in  $Re$  and  $Gr$  keeping  $Ri$  constant, increases both  $C_f$  (hence  $f$ ) and  $Nu$  in buoyancy assisting and opposing flow. But at a given  $Ri$ , the magnitude of  $C_f$  and  $Nu$  is higher in the opposing flow as compared to the assisting flow.
- ✓ The hydrodynamic entrance length decreases, and the thermal entrance length increases with the increase of  $Re$  and  $Gr$  keeping  $Ri$  constant in both buoyancy-assisting and opposing flows.
- ✓ The start of transition depends on the heat flux supplied, and it occurs earlier in the opposing flow as compared to the assisting flow for the same  $Re$  and  $Gr$ .

#### Turbulent mixed convection:

- ✓ Even though the effect of heat flux is not commendable due to turbulence, it has been observed that the pressure drop (quantified by  $f$ ) and heat transfer (quantified by  $Nu$ ) both higher in buoyancy-opposing flow than buoyancy-assisting flow.
- ✓ The hydrodynamically fully developed condition in buoyancy-assisting and opposing flow was achieved by  $L/D \sim 21$  and  $\sim 17$  respectively, and the thermally developed condition by  $L/D \sim 25$  and  $\sim 20$  respectively.

Finally, correlations were developed to quantify the friction factor,  $f = f(Re)$ , Colburn  $j$ -factor,  $f/j = f(Re)$ , and Nusselt number,  $Nu = f(Ri, Gr)$  in laminar, transitional, and turbulent flow regimes for a range of  $Re$ ,  $Gr$ ,  $Ri$  and  $Pr$  in both the flows.

### 8.4 Future scope and recommendations

To further extend the present work, the following future work can be recommended:

1. The present work is restricted to mixed convection in a vertical tube with a constant heat flux boundary condition. The study of the tube inclination and its effect on pressure drop and heat transfer can be a potential area to investigate. Because the tube inclination will play a crucial role in heat transfer to mixed convection flows through a vertical tube. The other boundary condition of constant wall temperature can also be a challenging area to explore.
2. The working fluid used for the present work was water, and the  $Pr$  for water varies with temperature in the present study is from 3 to 7. Other fluids with a



Prandtl number higher than water, such as ethylene glycol-water mixture and lower than water, for example air, molten metal can be used in the simulations as well as experiments to discover the flow characteristics.

3. Further, the test section diameter can be varied considerably, such as of 20 mm and 30 mm, so that the effect of an increase of diameter can be investigated in the results. The increase in diameter will decrease the heat flux, and hence the Grashof number ( $Gr$ ) will also decrease. At the same time, it will increase the Reynolds number ( $Re$ ), consequently the Richardson number ( $Ri$ ) will increase and it will be an important parameter for the design of a heat exchanger.
4. The present experiments were conducted with a smooth stainless-steel circular tube of grade 316 L to avoid any corrosion while conducting the experiments. The surface roughness can be varied intentionally, and the changes in velocity as well as temperature profiles and the growth of hydrodynamic and thermal boundary layers to determine the entry length of the flow will be interesting to work on further.



## REFERENCES/BIBLIOGRAPHY

- [1] J. D. Jackson, M. A. Cotton, and B. P. Axcell, "Studies of mixed convection in vertical tubes," *Int. J. Heat Fluid Flow*, vol. 10, no. 1, pp. 2–15, 1989, doi: 10.1016/0142-727X(89)90049-0.
- [2] J. P. Meyer, A. I. Bashir, and M. Everts, "Single-phase mixed convective heat transfer and pressure drop in the laminar and transitional flow regimes in smooth inclined tubes heated at a constant heat flux," *Exp. Therm. Fluid Sci.*, vol. 109, no. July, p. 109890, 2019, doi: 10.1016/j.expthermflusci.2019.109890.
- [3] B. Metais and E. R. G. Eckert, "Forced, Mixed, and Free Convection Regimes," *J. Heat Transfer*, vol. 86, no. 2, p. 295, 1964, doi: 10.1115/1.3687128.
- [4] M. Everts and J. P. Meyer, "Relationship between pressure drop and heat transfer of developing and fully developed flow in smooth horizontal circular tubes in the laminar, transitional, quasi-turbulent and turbulent flow regimes," *Int. J. Heat Mass Transf.*, vol. 117, pp. 1231–1250, 2018, doi: 10.1016/j.ijheatmasstransfer.2017.10.072.
- [5] N. Galanis and A. Behzadmehr, "Mixed convection in vertical ducts," in *Proceedings of 6th IASME/WSEAS International Conference on Fluid Mechanics and Aerodynamics*, 2008, pp. 35–43.
- [6] J. P. Meyer and M. Everts, "A review of the recent developments in laminar, transitional, quasi-turbulent and turbulent forced and mixed convective flow through horizontal tubes," *Adv. Heat Transf.*, vol. 51, pp. 131–205, 2019, doi: 10.1016/bs.aiht.2019.07.001.
- [7] A. J. Ghajar, "Heat transfer and pressure drop in the transition region of smooth horizontal circular tubes with different inlet configurations," in *Advances in heat transfer*, vol. 51, Elsevier, 2019, pp. 1–53. [Online]. Available: <https://doi.org/10.1016/bs.aiht.2019.05.001>
- [8] S. Gorai and S. K. Das, "Studies on Mixed Convection and Its Transition to Turbulence—A Review," in *50 Years of CFD in Engineering Sciences: A Commemorative Volume in Memory of D. Brian Spalding*, A. Runchal, Ed., Singapore: Springer Singapore, 2020, pp. 317–361. doi: 10.1007/978-981-15-2670-1\_10.
- [9] Y. A. Cengel and A. J. Ghajar, *Heat and mass transfer*, 5th ed. McGraw-Hills, 2007.
- [10] O. Reynolds, "An Experimental Investigation of the Circumstances which determine whether the Motion of Water shall be Direct or Sinuous, and of the Law of Resistance in Parallel Channels," *R. Soc.*, vol. 174, 1883, doi: <https://doi.org/10.1098/rstl.1883.0029>.
- [11] P. G. Drazin, *Introduction to hydrodynamic stability*, vol. 32. Cambridge university press, 2002.
- [12] M. Everts and J. P. Meyer, "Laminar hydrodynamic and thermal entrance lengths for simultaneously hydrodynamically and thermally developing forced and mixed convective flows in horizontal tubes," *Exp. Therm. Fluid Sci.*, vol. 118, no. February, p. 110153, 2020, doi: 10.1016/j.expthermflusci.2020.110153.
- [13] M. Everts and J. P. Meyer, "Flow regime maps for smooth horizontal tubes at a constant heat flux," *Int. J. Heat Mass Transf.*, vol. 117, pp. 1274–1290, 2018, doi: 10.1016/j.ijheatmasstransfer.2017.10.073.
- [14] A. J. Ghajar and L. M. Tam, "Flow regime map for a horizontal pipe with uniform wall heat flux and three inlet configurations," *Exp. Therm. Fluid Sci.*, vol. 10, no. 3, pp. 287–297, 1995, doi: 10.1016/0894-1777(94)00107-J.
- [15] R. C. Martinelli and L. M. K. Boelter, "Analytical Prediction of Superimposed Free and Forced Convection in a Vertical Pipe, 5. University of California," *Publ. Eng.*, pp. 23–58, 1942.
- [16] T. M. Hallman, "Combined forced and free-laminar heat transfer in vertical tubes with uniform internal heat generation," *Trans. ASME*, vol. 78, no. 8, pp. 1841–1851, 1956.
- [17] T. J. Hanratty, E. M. Rosen, and R. L. Kabel, "Effect of heat transfer on flow field at low Reynolds numbers in vertical tubes," *Ind. Eng. Chem.*, vol. 50, no. 5, pp. 815–820, 1958.
- [18] B. R. Morton, "Laminar convection in uniformly heated vertical pipes," *J. Fluid Mech.*, vol. 8, no. 2, pp. 227–240, 1960, doi: 10.1017/S0022112060000566.
- [19] E. M. Rosen and T. J. Hanratty, "Use of boundary-layer theory to predict the effect of heat transfer on the laminar-flow field in a vertical tube with a constant-temperature wall," *AIChE J.*, vol. 7, no. 1, pp. 112–123, 1961, doi: 10.1002/aic.690070126.
- [20] R. L. Pigford, *Non-isothermal flow and heat transfer inside vertical tubes*. Chemical Engineering Progress Symposium Series, 51, 79-92, 1955.
- [21] T. S. Chen, B. F. Armaly, and N. Ramachandran, "Correlations for laminar mixed convection flows on vertical, inclined, and horizontal flat plates," *J. Heat Transfer*, vol. 108, no. 4, pp. 835–840, 1986.

- [22] K. Boulama and N. Galanis, "Analytical solution for fully developed mixed convection between parallel vertical plates with heat and mass transfer," *J. Heat Transfer*, vol. 126, no. 3, pp. 381–388, 2004, doi: 10.1115/1.1737774.
- [23] C. Cheng, H. Kou, and W. Huangt, "Flow Reversal and Heat Transfer of Fully Developed Mixed Convection in Vertical Channels," vol. 4, no. 3, pp. 375–383, 1990.
- [24] A. A. Avramenko, A. I. Tyrinov, I. V. Shevchuk, N. P. Dmitrenko, A. V. Kravchuk, and V. I. Shevchuk, "Mixed convection in a vertical flat microchannel," *Int. J. Heat Mass Transf.*, vol. 106, pp. 1164–1173, 2017.
- [25] D. Bradley and A. G. Entwistle, "Developed laminar flow heat transfer from air for variable physical properties," *Int. J. Heat Mass Transf.*, vol. 8, no. 4, pp. 621–638, 1965, doi: 10.1016/0017-9310(65)90049-9.
- [26] W. T. Lawrence and J. C. Chato, "Heat-Transfer Effects on the Developing Laminar Flow Inside Vertical Tubes," *J. Heat Transfer*, vol. 88, no. 2, pp. 214–222, 1966, doi: 10.1115/1.3691518.
- [27] W. J. Marnier and H. K. McMillan, "Combined free and forced laminar convection in a vertical tube with constant wall temperature," *J. Heat Transfer*, vol. 92, no. 3, pp. 559–562, 1970.
- [28] B. Zeldin and F. W. Schmidt, "Developing Flow with Combined Forced-Free Convection in an Isothermal Vertical Tube," *J. Heat Transfer*, vol. 94, pp. 211–223, 1972, doi: 10.1115/1.3449899.
- [29] H. Tanaka, M. Shigeo, and H. Shunichi, "Combined forced and natural convection heat transfer for upward flow in a uniformly heated, vertical pipe," *Int. J. Heat Mass Transf.*, vol. 30, no. 1, pp. 165–174, 1987.
- [30] D. D. Joye, "Pressure drop correlation for laminar, mixed convection, aiding flow heat transfer in a vertical tube," *Int. J. Heat Fluid Flow*, vol. 24, no. 2, pp. 260–266, 2003, doi: 10.1016/S0142-727X(02)00238-2.
- [31] O. O. Onyejekwe, "Combined effects of shear and buoyancy for mixed convection in an enclosure," *Adv. Eng. Softw.*, vol. 47, no. 1, pp. 188–193, 2012, doi: 10.1016/j.advengsoft.2011.11.002.
- [32] N. Sharma, A. K. Dhiman, and S. Kumar, "Mixed convection flow and heat transfer across a square cylinder under the influence of aiding buoyancy at low Reynolds numbers," *Int. J. Heat Mass Transf.*, vol. 55, no. 9–10, pp. 2601–2614, 2012, doi: 10.1016/j.ijheatmasstransfer.2011.12.034.
- [33] M. T. Al-Asadi, H. A. Mohammed, A. S. Kherbeet, and A. A. Al-Aswadi, "Numerical study of assisting and opposing mixed convective nanofluid flows in an inclined circular pipe," *Int. Commun. Heat Mass Transf.*, vol. 85, pp. 81–91, 2017.
- [34] C. Balaji, M. Hölling, and H. Herwig, "A general methodology for treating mixed convection problems using asymptotic computational fluid dynamics (ACFD)," *Int. Commun. Heat Mass Transf.*, vol. 34, no. 6, pp. 682–691, 2007, doi: 10.1016/j.icheatmasstransfer.2007.03.006.
- [35] K. Gersten and H. Herwig, "Strömungsmechanik, Grundlagen der Impuls-, Wärme- und Stoff-Übertragung aus Asymptotischer Sicht," *Vieweg-Verlag, Braunschweig/Wiesbaden. Google Sch.*, 1992.
- [36] T. Mare, N. Galanis, I. Voicu, J. Miriel, and O. Sow, "Experimental and numerical study of mixed convection with flow reversal in coaxial double-duct heat exchangers," *Exp. Therm. Fluid Sci.*, vol. 32, no. 5, pp. 1096–1104, 2008, doi: 10.1115/1.3449722.
- [37] W.-S. Fu, Y.-C. Lai, Y. Huang, and K.-L. Liu, "An investigation of flow reversal of mixed convection in a three dimensional rectangular channel with a finite length," *Int. J. Heat Mass Transf.*, vol. 64, pp. 636–646, 2013.
- [38] T. M. Hallman, *Experimental study of combined forced and free laminar convection in a vertical tube, N.A.S.A.T.N. D-1104*. 1961.
- [39] D. D. Joye, "Comparison of correlations and experiment in opposing flow, mixed convection heat transfer in a vertical tube with Grashof number variation," *Int. J. Heat Mass Transf.*, vol. 39, no. 5, pp. 1033–1038, 1996.
- [40] J. D. Jackson, M. A. Cotton, and B. P. Axcell, "Studies of mixed convection in vertical tubes," *Int. J. heat fluid flow*, vol. 10, no. 1, pp. 2–15, 1989.
- [41] H. A. Mohammed and Y. K. Salman, "Experimental investigation of mixed convection heat transfer for thermally developing flow in a horizontal circular cylinder," *Appl. Therm. Eng.*, vol. 27, no. 8–9, pp. 1522–1533, 2007, doi: 10.1016/j.applthermaleng.2006.09.023.
- [42] J. D. Jackson, "Studies of buoyancy-influenced turbulent flow and heat transfer in vertical passages," in *International Heat Transfer Conference 13, KN-24*, 2006. doi: 10.1615/IHTC13.p30.240.
- [43] A. F. Polyakov, "Development of secondary free-convection currents in forced turbulent flow in horizontal tubes," *J. Appl. Mech. Tech. Phys.*, vol. 15, no. 5, pp. 632–637, 1974.

- [44] T. J. Craft, S. E. Gant, A. V. Gerasimov, H. Iacovides, and B. E. Launder, "Development and application of wall-function treatments for turbulent forced and mixed convection flows," vol. 38, pp. 127–144, 2006, doi: 10.1016/j.fluiddyn.2004.11.002.
- [45] K. Suga, Y. Ishibashi, and Y. Kuwata, "An analytical wall-function for recirculating and impinging turbulent heat transfer," *Int. J. Heat Fluid Flow*, vol. 41, pp. 45–54, 2013.
- [46] T. J. Craft, A. V. Gerasimov, H. Iacovides, and B. E. Launder, "Progress in the generalization of wall-function treatments," *Int. J. Heat Fluid Flow*, vol. 23, pp. 148–160, 2002.
- [47] M. E. Shitsman, "Natural convection effect on heat transfer to a turbulent water flow in intensively heated tubes at supercritical pressures," *Arch. Proc. Inst. Mech. Eng. Conf. Proc. 1964-1970 (vols 178-184), Var. titles Label. Vol. A to S*, vol. 182, no. 39, pp. 36–41, 2006, doi: 10.1243/PIME\_CONF\_1967\_182\_265\_02.
- [48] J. W. Ackerman, "Pseudoboiling Heat Transfer to Supercritical Pressure Water in Smooth and Ribbed Tubes," *J. Heat Transfer*, vol. 92, no. 3, p. 490, 1970, doi: 10.1115/1.3449698.
- [49] J. D. Jackson, K. E. Lutterodt, and R. Weinberg, "Experimental Studies of Buoyancy-influenced Convective Heat Transfer in Heated Vertical Tubes at Pressures Just Above and Just Below the Thermodynamic Critical Value," *Proc. Int. Conf. Glob. Environ. Adv. Nucl. Power Plants*, vol. 36, no. 4, p. Paper No. 1177, 2003.
- [50] W. B. Hall and P. H. Price, "Mixed forced and free convection from a vertical heated plate to air," in *International Heat Transfer Conference 4*, 1970.
- [51] A. Steiner, "On the reverse transition of a turbulent flow under the action of buoyancy forces," *J. Fluid Mech.*, vol. 47, no. 3, pp. 503–512, 1971.
- [52] D. B. R. Kenning, J. Y. Poon, and R. A. W. Shock, *Local Reductions in Heat Transfer Due to Bouyancy Effects in Upward Turbulent Flow*. Atomic Energy Research Establishment, 1973.
- [53] J. Fewster, "Mixed forced and free convective heat transfer to supercritical pressure fluids flowing in vertical pipes," The University of Manchester, 1976.
- [54] Y.-Y. Hsu and J. M. Smith, "The Effect of Density Variation on Heat Transfer in the Critical Region," *J. Heat Transfer*, vol. 83, p. 176, 1961, doi: 10.1115/1.3680510.
- [55] H. Tanaka, T. Ayao, H. Masaru, and N. Nuchi, "Effects of buoyancy and of acceleration owing to thermal expansion on forced turbulent convection in vertical circular tubes—criteria of the effects, velocity and temperature profiles, and reverse transition from turbulent to laminar flow," *Int. J. Heat Mass Transf.*, vol. 16, no. 6, pp. 1267–1288, 1973.
- [56] P. J. Walklate, "A comparative study of theoretical models of turbulence for the numerical prediction of boundary-layer flows," Ph.D Thesis, University of Manchester, Manchester, 1976. doi: <https://ethos.bl.uk/OrderDetails.do?uin=uk.bl.ethos.482533>.
- [57] A. D. Carr, M. A. Connor, and H. O. Buhr, "Velocity, Temperature, and Turbulence Measurements in Air for Pipe Flow With Combined Free and Forced Convection," *J. Heat Transfer*, vol. 95, no. 4, p. 445, 1973, doi: 10.1115/1.3450087.
- [58] B. E. Launder and D. B. Spalding, "The Numerical Computation of Turbulent Flows," *Comput. Methods Appl. Mech. Engg.*, vol. 3, pp. 269–289, 1974, doi: <https://doi.org/10.1016/B978-0-08-030937-8.50016-7>.
- [59] D. Skiadaressis and D. B. Spalding, "Prediction of combined free and forced convection in turbulent flow through horizontal pipes," *Lett. heat mass Transf.*, vol. 4, no. 1, pp. 35–39, 1977.
- [60] A. M. Abdelmeguid and D. B. Spalding, "Turbulent flow and heat transfer in pipes with buoyancy effects," *J. Fluid Mech.*, vol. 94, no. 2, pp. 383–400, 1979.
- [61] B. S. Petukhov and B. K. Strigin, "Experimental investigation of heat transfer with viscous-inertial-gravitational flow of a liquid in vertical tubes. Teplofizika Vysokikh Temperatur, 6, 933-937," vol. 6, no. 5. pp. 933–937, 1968.
- [62] B. S. Petukhov, "Turbulent flow and heat transfer in pipes under considerable effect of thermogravitational forces," *Heat Transf. Turbul. Buoyant Convect. Int. Cent. Heat Mass Transf. Dubrovnik, Yugosl. Hemisph. Publ. Corp. Washingt. D.C.*, vol. 2, pp. 701–717, 1976.
- [63] B. E. Launder and B. I. Sharma, "Application of the energy-dissipation model of turbulence to the calculation of flow near a spinning disc," *Lett. heat mass Transf.*, vol. 1, no. 2, pp. 131–137, 1974.
- [64] D. P. Mikielewicz, "Comparative studies of turbulence models under conditions of mixed convection with variable properties in heated vertical tubes," Ph.D Thesis, University of Manchester, Manchester, 1994. doi: <https://ethos.bl.uk/OrderDetails.do?uin=uk.bl.ethos.493293>.
- [65] N. Kasagi and M. Nishimura, "Direct numerical simulation of combined forced and natural turbulent convection in a vertical plane channel," *Int. J. Heat Fluid Flow*, vol. 18, no. 96, pp. 88–99, 1997.
- [66] J. You, J. Y. Yoo, and H. Choi, "Direct numerical simulation of heated vertical air flows in fully

- developed turbulent mixed convection,” *Int. J. Heat Mass Transf.*, vol. 46, no. 9, pp. 1613–1627, 2003, doi: 10.1016/S0017-9310(02)00442-8.
- [67] W. S. Kim, S. He, and J. D. Jackson, “Assessment by comparison with DNS data of turbulence models used in simulations of mixed convection,” *Int. J. Heat Mass Transf.*, vol. 51, no. 5–6, pp. 1293–1312, 2008, doi: 10.1016/j.ijheatmasstransfer.2007.12.002.
- [68] E. R. G. Eckert and A. J. Diaguila, “Convective Heat Transfer for Mixed, Free, and Forced Flow Through Tubes,” *Trans. ASME*, no. 53, 1954, doi: 10.1115/1.4014885.
- [69] C. K. Brown and W. H. Gavvin, “Combined free-and-forced convection: II. Heat transfer in opposing flow,” *Can. J. Chem. Eng.*, vol. 43, no. 6, pp. 313–318, 1965.
- [70] J. V. Vilemas, P. S. Poškas, and V. E. Kaupas, “Local heat transfer in a vertical gas-cooled tube with turbulent mixed convection and different heat fluxes,” *Int. J. Heat Mass Transf.*, vol. 35, no. 10, pp. 2421–2428, 1992.
- [71] Y. Parlattan, N. E. Todreas, and M. J. Driscoll, “Buoyancy and Property Variation Effects Turbulent Mixed Convection of Water in Vertical Tubes,” *J. Heat Transfer*, vol. 118, no. 2, pp. 381–387, 1996, doi: 10.1115/1.2825855.
- [72] J. D. Jackson, B. P. Axcell, and A. Walton, “Mixed-convection heat transfer to sodium in a vertical pipe,” *Exp. Heat Transf.*, vol. 7, no. 1, pp. 71–90, 1994, doi: 10.1080/08916159408946473.
- [73] G. P. Celata, F. D’Annibale, A. Chiaradia, and M. Cumo, “Upflow turbulent mixed convection heat transfer in vertical pipes,” *Int. J. Heat Mass Transf.*, vol. 41, no. 24, pp. 4037–4054, 1998, [Online]. Available: [https://doi.org/10.1016/S0017-9310\(98\)00177-X](https://doi.org/10.1016/S0017-9310(98)00177-X)
- [74] A. J. Ghajar and K. F. Madon, “Pressure Drop Measurements in the Transition Region for a Circular Tube with Three Different Inlet Configurations,” *Exp. Therm. Fluid Sci.*, vol. 5, no. 1, pp. 129–135, 1992, doi: 10.1016/0894-1777(92)90062-A.
- [75] A. J. Ghajar and L.-M. Tam, “Heat Transfer Measurement and Correlations in the Transition Region for a Circular Tube with Three Different Inlet Conditions,” *Exp. Therm. Fluid Sci.*, vol. 8, pp. 79–90, 1994.
- [76] L. Tam and A. J. Ghajar, “Effect of Inlet Geometry and Heating on the Fully Developed Friction Factor in the Transition Region of a Horizontal Tube,” *Exp. Therm. Fluid Sci.*, vol. 1777, no. 97, pp. 52–64, 1997, doi: 10.1016/S0894-1777(97)00035-6.
- [77] H. K. Tam, L. Mou, and A. J. Ghajar, “Effect of inlet geometries and heating on the entrance and fully-developed friction factors in the laminar and transition regions of a horizontal tube,” *Exp. Therm. Fluid Sci.*, vol. 44, pp. 680–696, 2013, doi: 10.1016/j.expthermflusci.2012.09.008.
- [78] T. Aicher and H. Martin, “New correlations for mixed turbulent natural and forced convection heat transfer in vertical tubes,” *Int. J. Heat Mass Transf. Vol. 40, No. 15, 3617-3626.*, 1997.
- [79] A. J. Ghajar, L. M. Tam, and S. C. Tam, “Improved heat transfer correlation in the transition region for a circular tube with three inlet configurations using artificial neural networks,” *Heat Transf. Eng.*, vol. 25, no. 2, pp. 30–40, 2004.
- [80] L. M. Tam, A. J. Ghajar, and H. K. Tam, “Contribution Analysis of Dimensionless Variables for Laminar and Turbulent Flow Convection Heat Transfer in a Horizontal Tube Using Artificial Neural Network,” *Heat Transf. Eng.*, vol. 29, no. 9, pp. 793–804, 2008, doi: 10.1080/01457630802053827.
- [81] J. P. Meyer and S. M. Abolarin, “Heat transfer and pressure drop in the transitional flow regime for a smooth circular tube with twisted tape inserts and a square-edged inlet,” *Int. J. Heat Mass Transf.*, vol. 117, pp. 11–29, 2018, doi: 10.1016/j.ijheatmasstransfer.2017.09.103.
- [82] A. I. Bashir and J. P. Meyer, “Experimental investigation of convective heat transfer in the transitional flow regime of an inclined smooth tube,” in *International Heat Transfer Conference Digital Library*, 2018, pp. 3127–3133. doi: 10.1615/IHTC16.cov.023461.
- [83] J. P. Meyer, M. Everts, N. Coetzee, K. Grote, and M. Steyn, “Heat transfer coefficients of laminar, transitional, quasi-turbulent and turbulent flow in circular tubes,” *Int. Commun. Heat Mass Transf.*, vol. 105, pp. 84–106, 2019, doi: 10.1016/j.icheatmasstransfer.2019.03.016.
- [84] A. Behzadmehr, N. Galanis, and A. Laneville, “Laminar-turbulent transition for low Reynolds number mixed convection in a uniformly heated vertical tube,” *Int. J. Numer. Methods Heat Fluid Flow*, vol. 12, no. 7, pp. 839–854, 2002, doi: 10.1108/09615530210443052.
- [85] A. Behzadmehr, N. Galanis, and A. Laneville, “Low Reynolds number mixed convection in vertical tubes with uniform wall heat flux,” *Int. J. Heat Mass Transf.*, vol. 46, no. 25, pp. 4823–4833, 2003, doi: 10.1016/S0017-9310(03)00323-5.
- [86] L. M. Tam and A. J. Ghajar, “Transitional heat transfer in plain horizontal tubes,” *Heat Transf. Eng.*, vol. 27, no. 5, pp. 23–38, 2006, doi: 10.1080/01457630600559538.
- [87] S. W. Churchill, “Comprehensive Correlating Equations for Heat, Mass and Momentum Transfer

- in Fully Developed Flow in Smooth Tubes,” *Ind. Eng. Chem. Fundam.*, vol. 16, no. 1, pp. 109–116, 1977, doi: 10.1021/i160061a021.
- [88] P. Poskas, R. Poskas, and A. Gediminskas, “Numerical investigation of the opposing mixed convection in an inclined flat channel using turbulence transition models,” *J. Phys. Conf. Ser.*, vol. 395, no. 1, p. 012098, 2012, doi: 10.1088/1742-6596/395/1/012098.
- [89] P. Poskas, R. Poskas, A. Sirvydas, and A. Smaizys, “Experimental investigation of opposing mixed convection heat transfer in the vertical flat channel in a laminar-turbulent transition region,” *Int. J. Heat Mass Transf.*, vol. 54, no. 1–3, pp. 662–668, 2011, doi: 10.1016/j.ijheatmasstransfer.2010.09.004.
- [90] M. Abdollahzadeh, M. Esmailpour, R. Vizinho, A. Younesi, and J. C. Páscoa, “Assessment of RANS turbulence models for numerical study of laminar-turbulent transition in convection heat transfer,” *Int. J. Heat Mass Transf.*, vol. 115, pp. 1288–1308, 2017, doi: 10.1016/j.ijheatmasstransfer.2017.08.114.
- [91] G. A. Kemeny and E. V Somers, “Combined free and forced-convective flow in vertical circular tubes-experiments with water and oil,” *J. Heat Transfer*, vol. 84, no. 4, pp. 339–345, 1962, doi: 10.1115/1.3684389.
- [92] G. S. Barozzi, A. Dumas, and M. W. Collins, “Sharp entry and transition effects for laminar combined convection of water in vertical tubes,” pp. 235–241, 1984.
- [93] W. Grassi and D. Testi, “Developing upward flow in a uniformly heated circular duct under transitional mixed convection,” *Int. J. Therm. Sci.*, vol. 45, no. 9, pp. 932–937, 2006, doi: 10.1016/j.ijthermalsci.2005.11.007.
- [94] A. Behzadmehr, A. Laneville, and N. Galanis, “Experimental study of onset of laminar-turbulent transition in mixed convection in a vertical heated tube,” *Int. J. Heat Mass Transf.*, vol. 51, no. 25–26, pp. 5895–5905, 2008, doi: 10.1016/j.ijheatmasstransfer.2008.04.005.
- [95] R. Poskas, A. Sirvydas, J. Kolesnikovas, and R. Kilda, “Experimental Investigation of Opposing Mixed Convection Heat Transfer in a Vertical Flat Channel in the Transition Region. 1. Analysis of Local Heat Transfer,” *Heat Transf. Res.*, vol. 44, no. 7, pp. 589–602, 2013, doi: 10.1615/HeatTransRes.v44.i7.10.
- [96] M. Everts and J. P. Meyer, “Heat transfer of developing flow in the transitional flow regime,” in *ASTFE Digital Library*, 2015, pp. 1051–1063. doi: 10.1615/TFESC1.fnd.012660.
- [97] A. I. Bashir, “Single-phase forced and mixed convection in the laminar and transitional flow regimes of inclined smooth tubes with inlet disturbances,” Ph.D Thesis, University of Pretoria, 2019. [Online]. Available: <http://hdl.handle.net/2263/77852>
- [98] A. I. Bashir, M. Everts, R. Bennacer, and J. P. Meyer, “Single-phase forced convection heat transfer and pressure drop in circular tubes in the laminar and transitional flow regimes,” *Exp. Therm. Fluid Sci.*, vol. 109, no. July, p. 109891, 2019, doi: 10.1016/j.expthermflusci.2019.109891.
- [99] J. P. Meyer, A. I. Bashir, and M. Everts, “Single-phase mixed convective heat transfer and pressure drop in the laminar and transitional flow regimes in smooth inclined tubes heated at a constant heat flux,” *Exp. Therm. Fluid Sci.*, vol. 109, p. 109890, 2019.
- [100] P. Poskas and R. Poskas, “Mixed Convection in Channel Flows,” *Heat Transf. Res.*, vol. 40, no. 1, pp. 31–56, 2009, doi: 10.1615/HeatTransRes.v40.i1.30.
- [101] H. K. Dawood, H. A. Mohammed, N. A. C. Sidik, K. M. Munisamy, and M. A. Wahid, “Forced, natural and mixed-convection heat transfer and fluid flow in annulus: A review,” *Int. Commun. Heat Mass Transf.*, vol. 62, pp. 45–57, 2015, doi: <https://doi.org/10.1016/j.icheatmasstransfer.2015.01.006>.
- [102] ANSYS-Fluent, “ANSYS Fluent 12.0 user’s guide,” *Ansys Inc*, vol. 15317, pp. 1–2498, 2009.
- [103] D. John and J. R. Anderson, *Computational fluid dynamics: the basics with applications*. 1995.
- [104] B. Kotresha and N. Gnanasekaran, “Numerical Simulations of Fluid Flow and Heat Transfer through Aluminum and Copper Metal Foam Heat Exchanger – A Comparative Study,” *Heat Transf. Eng.*, vol. 41, no. 6–7, pp. 637–649, 2020, doi: 10.1080/01457632.2018.1546969.
- [105] F. M. White, *Fluid Mechanics*, McGraw-Hill, 6th ed. 1994.
- [106] S. Gorai, S. K. Das, and D. Samanta, “Numerical investigations on the difference between aiding and opposing flows in the developing regime of laminar mixed convection in vertical tubes,” *Numer. Heat Transf. Part A Appl.*, vol. 84, no. 4, pp. 1–25, 2022, doi: 10.1080/10407782.2022.2105600.
- [107] D. K. Walters and D. Cokljat, “A three-equation eddy-viscosity model for Reynolds-averaged Navier--Stokes simulations of transitional flow,” 2008.
- [108] R. B. Langtry, F. R. Menter, S. R. Likki, Y. B. Suzen, P. G. Huang, and S. Volker, “A correlation-based transition model using local variables: Part II—test cases and industrial applications,” in

- Turbo Expo: Power for Land, Sea, and Air*, 2004, pp. 69–79.
- [109] J. P. Abraham, E. M. Sparrow, and J. C. K. Tong, “Heat transfer in all pipe flow regimes : laminar , transitional / intermittent , and turbulent,” *Int. J. Heat Mass Transf.*, vol. 52, no. 3–4, pp. 557–563, 2009, doi: 10.1016/j.ijheatmasstransfer.2008.07.009.
  - [110] A. Bejan, *Convection heat transfer*. John Wiley & sons, 2013.
  - [111] R. Poskas, R. Zujus, and A. Gediminskas, “Modelling of the aiding mixed convection in a vertical rectangular channel,” in *HEFAT*, International Conference on Heat Transfer, Fluid Mechanics and Thermodynamics, 2012, pp. 1741–1746. doi: <http://hdl.handle.net/2263/44305>.
  - [112] B. Kotresha, N. Gnanasekaran, and C. Balaji, “Numerical Simulations of Flow-Assisted Mixed Convection in a Vertical Channel Filled with High Porosity Metal Foams Numerical Simulations of Flow-Assisted Mixed Convection in a Vertical Channel Filled with High Porosity Metal Foams,” *Heat Transf. Eng.*, vol. 41, no. 8, pp. 739–750, 2020, doi: 10.1080/01457632.2018.1564208.
  - [113] P. Spalart and S. Allmaras, “A one-equation turbulence model for aerodynamic flows,” in *30th aerospace sciences meeting and exhibit*, 1992, p. 439.
  - [114] B. E. Launder and D. B. Spalding, “Lectures in mathematical models of turbulence,” (*No Title*), 1972, [Online]. Available: <https://cir.nii.ac.jp/crid/1130282273069118208>
  - [115] S. A. Orszag, “Renormalisation group modelling and turbulence simulations,” *Near-wall Turbul. flows*, 1993.
  - [116] T.-H. Shih, W. W. Liou, A. Shabbir, Z. Yang, and J. Zhu, “A new k- $\epsilon$  eddy viscosity model for high reynolds number turbulent flows,” *Comput. Fluids*, vol. 24, no. 3, pp. 227–238, 1995.
  - [117] R. W. Allen and E. R. G. Eckert, “Friction and Heat-Transfer Measurements to Turbulent Pipe Flow of Water ( $Pr=7$  and 8) at Uniform Wall Heat Flux,” *J. Heat Transf. Asme*, vol. 86, pp. 301–310, 1964.
  - [118] M. Everts, “Single-phase mixed convection of developing and fully developed flow in smooth horizontal tubes in the laminar, transitional, quasi-turbulent and turbulent flow regimes,” Ph.D Thesis, University of Pretoria, Pretoria, 2017. doi: <http://hdl.handle.net/2263/64045>.
  - [119] S. P. Venkateshan, *MECHANICAL MEASUREMENTS*, 2nd Editio. John Wiley & Sons Ltd., 2015.
  - [120] R. K. Shah, “A Correlation for Laminar Hydrodynamic Entry Length Solutions for Circular and Noncircular ducts,” *J. Fluids Eng.*, vol. 100, no. June, pp. 177–179, 1978, doi: <https://doi.org/10.1115/1.3448626>.
  - [121] R. J. Phillips, “Forced-convection, liquid-cooled, microchannel heat sinks,” Ph.D Thesis, Massachusetts Institute of Technology, 1987.
  - [122] R. K. Shah and A. L. London, “Rectangular ducts,” *Laminar Flow Forced Convect. Ducts*, pp. 196–222, 1978.
  - [123] V. Gnielinski, “New equations for heat and mass transfer in turbulent pipe and channel flow,” *Int. Chem. Eng.*, vol. 16, no. 2, pp. 359–367, 1976.
  - [124] H. Hausen, *Heat transfer in counterflow, parallel-flow, and cross-flow*. McGraw-Hill, 1983. [Online]. Available: <https://lccn.loc.gov/81011772>
  - [125] D. Bertsche, P. Knipper, and T. Wetzel, “International Journal of Heat and Mass Transfer Experimental investigation on heat transfer in laminar , transitional and turbulent circular pipe flow,” *Int. J. Heat Mass Transf.*, vol. 95, pp. 1008–1018, 2016, doi: 10.1016/j.ijheatmasstransfer.2016.01.009.
  - [126] D. Taler, “A new heat transfer correlation for transition and turbulent fluid flow in tubes,” *Int. J. Therm. Sci.*, vol. 108, pp. 108–122, 2016, doi: <https://doi.org/10.1016/j.ijthermalsci.2016.04.022>.
  - [127] V. Gnielinski, “On heat transfer in tubes,” *Int. J. Heat Mass Transf. heat Transf. tubes*, vol. 63, pp. 134–140, 2013, doi: <http://dx.doi.org/10.1016/j.ijheatmasstransfer.2013.04.015>.
  - [128] C. O. Popiel and J. Wojtkowiak, “Simple formulas for thermophysical properties of liquid water for heat transfer calculations (from 0 °C to 150 °C),” *Heat Transf. Eng.*, vol. 19, no. 3, pp. 87–101, 1998.
  - [129] M. Nishi, B. Ünsal, F. Durst, and G. Biswas, “Laminar-to-turbulent transition of pipe flows through puffs and slugs,” *J. Fluid Mech.*, vol. 614, pp. 425–446, 2008, doi: 10.1017/S0022112008003315.
  - [130] F. Durst and B. Unsal, “Forced laminar-to-turbulent transition of pipe flows,” *J. Fluid Mech.*, vol. 560, pp. 449–464, 2006, doi: 10.1017/S0022112006000528.
  - [131] V. Mukund and B. Hof, “The critical point of the transition to turbulence in pipe flow,” *J. Fluid Mech.*, no. 2018, pp. 76–94, 2018, doi: 10.1017/jfm.2017.923.
  - [132] J. P. Abraham, “Application of an Intermittency Model for Laminar , Transitional , and Turbulent Internal Flows,” vol. 141, no. July, pp. 1–8, 2019, doi: 10.1115/1.4042664.



- [133] T. Wei and J. Abraham, “Heat transfer regimes in fully developed circular tube flows , a map of flow regimes,” *Int. Commun. Heat Mass Transf.*, vol. 104, no. March, pp. 147–152, 2019, doi: 10.1016/j.icheatmasstransfer.2019.02.006.
- [134] S. Gorai, D. Samanta, and S. K. Das, “Heat Transfer in Simultaneously Developing Turbulent Mixed Convection Flows in Vertical Tubes,” *Heat Transf. Eng.*, 2023, doi: 10.1080/01457632.2023.2289226.



## Uncertainty Analysis and Calibration of Instruments

### B.1 General form of uncertainty analysis equation

If  $R$  is a function of several variables such as  $R = f(x_1, x_2, x_3, \dots, x_n)$  and  $\sigma_{x_i}$  is the uncertainty of each measured quantity  $x_i$ , the uncertainty ( $\sigma$ ) of the variable  $R$  will be,

$$\sigma_R = \sqrt{\sum_1^n \left( \frac{\partial R}{\partial x_i} \times \sigma_{x_i} \right)^2} \quad (A)$$

For friction factor,  $f = \frac{\Delta p(D/L)}{\rho u^2/2} = f(\Delta p, D, \rho, u, L)$ , the uncertainty can be obtained as

$$\sigma_f = \sqrt{\left( \frac{\partial f}{\partial p} \times \sigma_{\Delta p} \right)^2 + \left( \frac{\partial f}{\partial D} \times \sigma_D \right)^2 + \left( \frac{\partial f}{\partial \rho} \times \sigma_\rho \right)^2 + \left( \frac{\partial f}{\partial u} \times \sigma_u \right)^2 + \left( \frac{\partial f}{\partial L} \times \sigma_L \right)^2} \quad (B)$$

Similarly, for Nusselt number,  $Nu = \frac{hD}{k} = f(h, D, k)$ , the uncertainty can be obtained as

$$\sigma_{Nu} = \sqrt{\left( \frac{\partial Nu}{\partial h} \times \sigma_h \right)^2 + \left( \frac{\partial Nu}{\partial D} \times \sigma_D \right)^2 + \left( \frac{\partial Nu}{\partial k} \times \sigma_k \right)^2} \quad (C)$$

The uncertainties based on the above formulae used of the measured and derived quantities are tabulated in Table 4.1.

### B.2 Calibration of RTD and thermocouples

The thermocouples (T-type) and RTD (PT 100) used in the present study have been calibrated in the thermal technical calibration unit of the Central Electronic Center (CEC) at IIT Madras, following National Institute of Standards and Technology (NIST) standards. The calibration of all thermal sensors is completed along with the data-logger as a single unit after attaching the sensors to the data-logger multiplexer (Figure B.1). This is to avoid the minor errors that appear due to the data-logger. Fluke Calibration 9142 Field Metrology Well of operating range of -25°C to 210°C, Super DAQ, and a Fulke 5609 8PRT Probe are used for the calibration. The detailed calibration report is generated for each sensor, was used to compute the gain (M) and offset (B) for each thermocouple/RTD. Thermocouples were calibrated in the range of 20°C to 160°C with

## B.2 Calibration of RTD and thermocouples

a step of 10°C and PT 100 were calibrated in the range of 10°C to 100°C with a step of 10°C. A sample of the data is shown in Table B.1 and Table B.2. It shows their five reference and measured values along with the average quantity at different temperatures.



**Figure B.1:** Calibration of T-type thermocouples and PT 100

**Table B.1:** Sample data generated from the calibration report of a T-type thermocouple

Set Point	Reference values (R)					R-Avg	Measured values (M)					M-Avg
	R-1	R-2	R-3	R-4	R-5		M-1	M-2	M-3	M-4	M-5	
20	20.33	20.33	20.33	20.33	20.33	<b>20.33</b>	20.75	20.72	20.72	20.71	20.74	<b>20.73</b>
30	30.34	30.34	30.34	30.34	30.34	<b>30.34</b>	30.74	30.77	30.75	30.75	30.75	<b>30.75</b>
40	40.36	40.36	40.36	40.36	40.36	<b>40.36</b>	40.76	40.75	40.75	40.74	40.74	<b>40.75</b>
50	50.39	50.39	50.39	50.39	50.39	<b>50.39</b>	50.60	50.61	50.62	50.63	50.62	<b>50.61</b>
60	60.63	60.62	60.66	60.65	60.65	<b>60.64</b>	60.63	60.62	60.66	60.65	60.65	<b>60.64</b>
70	70.43	70.43	70.43	70.43	70.43	<b>70.43</b>	70.85	70.84	70.86	70.86	70.86	<b>70.85</b>
80	80.47	80.47	80.47	80.47	80.47	<b>80.47</b>	81.00	81.05	81.06	81.06	81.06	<b>81.05</b>
90	90.49	90.49	90.49	90.49	90.49	<b>90.49</b>	90.98	91.00	90.99	91.02	91.03	<b>91.00</b>
100	100.52	100.52	100.52	100.52	100.52	<b>100.52</b>	101.04	101.06	101.05	101.06	101.06	<b>101.05</b>
110	110.54	110.54	110.54	110.54	110.54	<b>110.54</b>	111.10	111.10	111.08	111.09	111.10	<b>111.09</b>
120	120.58	120.58	120.58	120.58	120.58	<b>120.58</b>	121.00	120.99	121.00	121.02	120.99	<b>121.00</b>
130	130.60	130.60	130.60	130.60	130.60	<b>130.60</b>	131.04	131.08	131.08	131.08	131.06	<b>131.07</b>
140	140.60	140.60	140.60	140.60	140.60	<b>140.60</b>	141.13	141.14	141.14	141.13	141.14	<b>141.13</b>
150	150.60	150.60	150.60	150.60	150.60	<b>150.60</b>	151.14	151.16	151.17	151.19	151.20	<b>151.17</b>
160	160.21	160.21	160.21	160.21	160.21	<b>160.21</b>	160.87	160.87	160.87	160.86	160.87	<b>160.87</b>

**Table B.2:** Sample data generated from the calibration report of a PT100

Set Point	Reference values (R)					R-Avg	Measured values (M)					M-Avg
	R-1	R-2	R-3	R-4	R-5		M-1	M-2	M-3	M-4	M-5	
10	10.29	10.29	10.29	10.29	10.29	<b>10.29</b>	10.44	10.44	10.44	10.44	10.44	<b>10.44</b>
20	20.32	20.32	20.32	20.32	20.32	<b>20.32</b>	20.43	20.43	20.43	20.43	20.43	<b>20.43</b>
30	30.34	30.34	30.34	30.34	30.34	<b>30.34</b>	30.43	30.43	30.43	30.43	30.43	<b>30.43</b>
40	40.37	40.37	40.37	40.37	40.37	<b>40.37</b>	40.41	40.42	40.42	40.42	40.42	<b>40.42</b>
50	50.40	50.40	50.40	50.40	50.40	<b>50.40</b>	50.41	50.41	50.42	50.42	50.43	<b>50.42</b>
60	60.40	60.40	60.40	60.40	60.40	<b>60.40</b>	60.43	60.43	60.43	60.43	60.42	<b>60.43</b>
70	70.46	70.46	70.46	70.46	70.46	<b>70.46</b>	70.43	70.43	70.43	70.43	70.43	<b>70.43</b>
80	80.48	80.48	80.48	80.48	80.48	<b>80.48</b>	80.44	80.44	80.44	80.44	80.44	<b>80.44</b>
90	90.50	90.50	90.50	90.50	90.50	<b>90.50</b>	90.45	90.44	90.44	90.44	90.44	<b>90.44</b>
100	100.49	100.50	100.50	100.50	100.50	<b>100.49</b>	100.42	100.41	100.41	100.41	100.41	<b>100.41</b>

### B.3 Calibration of DPT

A differential pressure transmitter (Yokogawa, Model No. EJA110E-JHS4J-912EB) of the diaphragm type is used for the pressure drop measurements. The span of measurement was set from 0 Pa (LRV) to 5000 Pa (URV). The accuracy of the differential pressure transducer was  $\pm 0.055\%$  of the span. The differential pressure transmitter and the digital manometer was connected simultaneously, and the readings were compared (Figure B.2). At a mass flow rate of 141.9 kg/hr, for which the  $Re$  is 5000, the pressure drop from the inlet to the outlet obtained in the differential pressure transducer was 594 Pa.

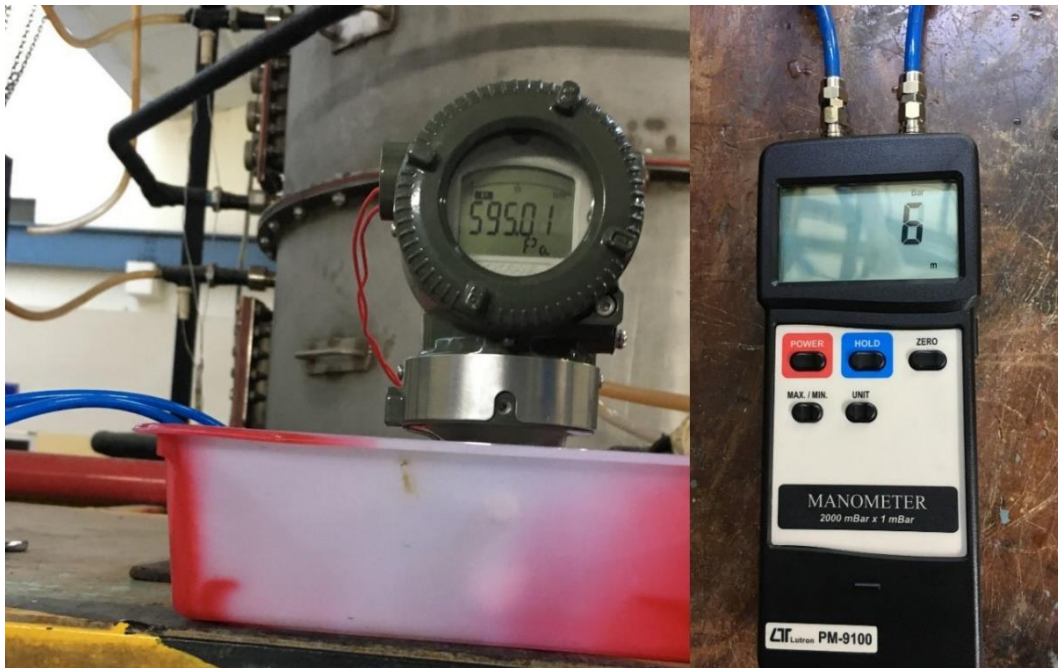


**Figure B.2:** Comparison of Differential Pressure Transmitter (DPT) with digital manometer

## B.4 Calibration of Coriolis mass flowmeter

### B.4 Calibration of Coriolis mass flowmeter

A Coriolis mass flow meter (EMERSION, Model: 1700R12ABFEZCZ) with a flow range of 0 to 450 kg/hr is used for the present experiments. The micro motion mass flow meter was calibrated by stopwatch and bucket method and the accuracy found was 1.54 % in the laminar range ( $Re=0-2300$ ), 2.54 % in the transitional range ( $Re=2300-5000$ ) and 1.10 % in the turbulent regime ( $Re=5000-15000$ ). The graphical plot of the reading from the flowmeter and the manually measured value is plotted in Figure B.3.

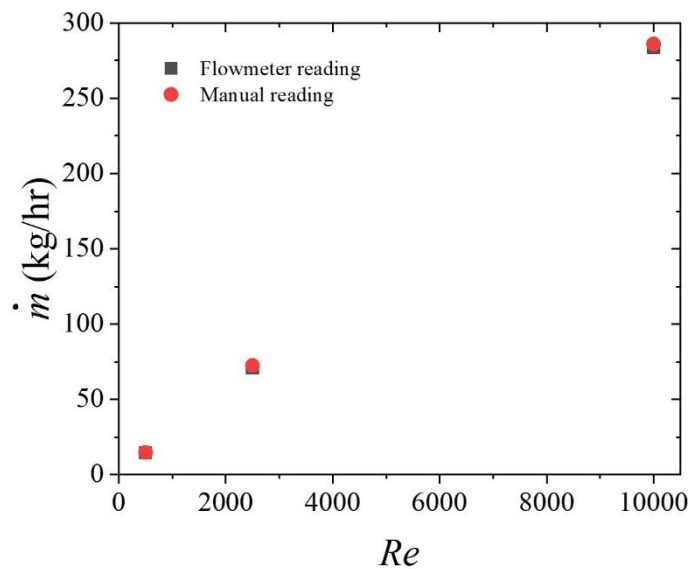


**Figure B.3:** Flowmeter vs. manual readings calibration plot

### B.5 Calibration of alignment of the set-up

The most important aspect of mixed convection through a vertical tube is the vertical and horizontal alignment of the experimental test rig. To get the free convection effect in a vertical tube, the vertical alignment is an essential measurement. The alignment has been verified by the spirit level meter before fixing the setup rigidly as shown in Figure B.4.



**Figure B.4:** Vertical and horizontal alignment of the experimental test-rig

### B.6 Measurement of surface roughness

The surface roughness ( $R_a$ ) was measured (Figure B.5) by a surface roughness tester (BRUKER) in micro-electro-mechanical-system (MEMS) laboratory at IIT Madras. The readings were taken at ten different locations on the inside surface of the circular tube. The tube was cut in half radially so that the probe could measure the surface roughness inside the tube. The average of the ten different measured roughness values obtained is  $1.12 \mu\text{m}$  for which the relative roughness ( $\varepsilon/D$ ) is 0.000112 m and can be fairly considered a smooth surface.

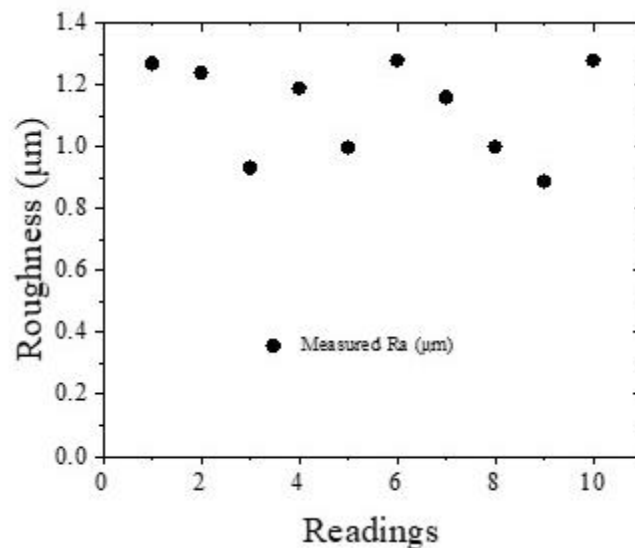


**Figure B.5:** Surface roughness measured at ten different locations of inside surface of the SS 316 L tube





## **CURRICULUM VITAE**

**NAME:** Somenath Gorai

**DOB:** 26<sup>th</sup> Jan 1987

### **EDUCATION:**

#### **Bachelor of Technology (2005–2009)**

CGPA : 7.8/10

Institute : Seemanta Engineering College, Biju Patnaik University of  
Technology, Odisha, India

Specialization : Mechanical Engineering

#### **Master of Technology (2011–2013)**

CGPA : 9.35/10

Institute : National Institute of Technology Jamshedpur, Jharkhand, India

Specialization : Thermal and Fluids Engineering

#### **Doctor of Philosophy (Jan 2018–Jan 2024)**

CGPA : 8.25/10

Institute : Indian Institute of Technology Ropar, Rupnagar, Punjab, India

Specialization : Thermal and Fluids Engineering